

INDUCED FISSION TRACK MEASUREMENTS OF
CARBONACEOUS CHONDRITE Th/U RATIOS
AND Th/U MICRODISTRIBUTIONS IN ALLENDE INCLUSIONS

Thesis by
Maritza Irene Stapanian

In Partial Fulfillment of the Requirements
for the Degree of
Doctor of Philosophy

California Institute of Technology
Pasadena, California

1981

(Submitted August 22, 1980)

Acknowledgments

This work was done under the guidance of Dr. Donald S. Burnett. Special thanks to Dr. R. Eggars, Dr. N. Namboodiri, and the staff at the Texas A&M cyclotron facility. Thanks also to Mike Carr for his expert machining, Jan Mayne for the illustrations, and Mickey McConnell, Joanne Clark, and Joana Vizgirda for helping me put this thesis together. Funding was provided by N.S.F. Grant EAR 76-84402.

ABSTRACT

A double irradiation fission track radiography technique has been developed to measure Th/U ratios in carbonaceous chondrites and map Th/U microdistributions in Ca-Al-rich inclusions. (Th + ^{238}U) fission is induced by high dose 35-40 MeV proton irradiations. These irradiations are coupled with reactor ^{235}U thermal neutron fission measurements to obtain the corresponding Th/U ratios.

The average solar system Th/U ratio is important in the theoretical modelling of the time scales for heavy element r-process nucleosynthesis. Earlier measurements (Morgan & Lovering, 1967, 1968) indicated CC Th/U ratios ranging from 2-6. This is in sharp contrast to ordinary chondrite, terrestrial, and lunar sample measurements which are tightly constrained to present day values of 3.8 ± 0.5 . An objective of this study was to check the 2-6 spread in CC ratios. The fission track technique, while not a high precision technique, can give individual meteorite measurements to within 12-20%. This is adequate to verify the existence of highly fractionated (relative to terrestrial) CC Th/U ratios. The results of our analyses of six bulk samples mainly type C2, but also including the Ivuna type C1 chondrite, show within the errors of the measurements that bulk CC Th/U ratios lie within the normal 3.8 ± 0.5 range.

The real strength of the fission track technique lies in the ability to map Th/U microdistributions in-situ. Our technique has the sensitivity to make U measurements within 10% counting statistics errors on 100μ grains with 20 ppb. Th+U measurements of similar precision can be made on 100μ grains with 1 ppm Th+U. We have focussed

our Th/U mapping experiments on the Allende meteorite- in particular, the calcium-aluminum-rich inclusions (CAI). The chemical and mineralogical composition of these CAI conform to model predictions for the earliest forming nebular condensates. Because of the refractory nature of Th and U, location and identification of Th,U-rich carrier phases can test solar nebula condensation models. Our major results are: (1) The high concentrations of Th and U in the rims of two Type A coarse-grained CAI attests to the importance of rims in understanding Th,U condensation and perhaps other refractory trace elements as well. (2) Analysis of a compact Type A inclusion shows that incorporation of rim material into total inclusion values is necessary to obtain Th and particularly U enrichments over Cl levels on par with the uniform enrichment of other refractory elements (Grossman et al., 1977). (3) The highly fractionated Th/U ratios observed in Type A perovskite (~ 20), and the general tendency for our CAI bulk measurements which show fractionated Th/U ratios to give high ratios suggests support of the Boynton (1978) proposal of higher U volatility compared to Th under the conditions of the early condensing nebula. Alternatively, our Type A inclusions may be atypical, having formed from a reservoir (gas?) of high Th/U. One mechanism for preferential depletion in the early stages of condensation could be alloying of U with Pt metals as discussed by Jones & Burnett (1980), although there is no strong evidence to support this specific mechanism. (4) The Th/U fractionations observed in Type A CAI suggest the strong likelihood for $^{244}\text{Pu}/^{238}\text{U}$ fractionations as well. Such inclusions would probably not be appropriate for determining the solar system Pu/U or Pu/Th ratios.

TABLE OF CONTENTS

Acknowledgements	ii
Abstract	iii
I. Introduction	1
A. Actinide Nucleosynthesis and Cosmochronology	2
1. Th/U	2
2. ^{244}Pu /actinide ratios	7
B. Th/U microdistributions--tests for solar nebula condensation models and Allende inclusion petrogenesis	8
C. Research Scope	19
II. Experimental	
A. Basic Physics of the Double Irradiation Technique	21
1. Thermal Neutron Irradiation	21
2. High Energy Irradiation	23
3. Fission Track Radiography	27
4. Th/U by Double Irradiation Experiments	30
B. Samples/Standards	
1. Meteorites	33
2. Standards	33
3. Blanks and Micas	36
C. Reactor Experiments	
1. Packaging	37
2. Irradiations	43
D. Cyclotron Experiments	
1. Packaging	45
2. Irradiation Requirements	51

3. On-line Experimental Set Up	51
4. Irradiations	57
E. Analysis	61
1. Reactor- [U]	61
a. Mica etch and track counts	61
b. Track counting efficiency factor (SMI)	62
c. Dosimetry	64
d. Range	68
2. Cyclotron- (Th+U)	
a. Interaction tracks and pre-etch mica annealing	71
b. Mica etch and track counts	72
c. Dosimetry	76
d. Fission cross-section corrections	83
e. Fission of other elements	86
f. Fission track annealing during irradiation	88
3. Blank Corrections	
a. Reactor	90
b. Cyclotron	90
F. Technique Evaluation	
1. Sensitivity	92
2. Error estimates	92
3. Reproducibility	94
4. NBS Standard Glasses	95
III. Bulk Carbonaceous Chondrite Th/U Ratios	
A. Results	97
Ivuna	105

Orgueil	107
Murchison	109
Mighei	110
Mokoia	111
Lance	112
Allende	113
B. Accuracy of the Data	
1. Internal Reproducibility	115
2. Comparison with Isotopic Dilution Measurements	120
C. Summary of Bulk Sample Results	129
IV. Review of Allende Inclusions	133
A. Coarse-grained CAI	134
B. Fine-grained CAI	139
C. Amoeboid Olivine Aggregates	142
D. Olivine and Pyroxene-Rich Chondrules	143
E. CAI Rims	144
V. Allende Inclusion Results	
A. Remarks on Allende Inclusion Analysis	149
B. Allende Inclusion Descriptions and Th/U Results	
1. Allende C-5-A	154
2. Allende C-5-B	158
3. Allende C-5-E	164
4. Allende D-2-A	165
5. Allende D-2-E	170
6. Allende A-5-A	173
7. Allende A-5-B	179

8. Allende D-2-C	182
9. Allende D-2-D	182
VI. Discussion of Allende Th/U Results	
A. Discussion	184
B. Inclusion Summary Statement	201
VII. Conclusions	
A. Bulk Carbonaceous Chondrites	203
B. Allende Inclusions	204
Appendix I: U,Th Relative Fission Cross Section Correction	207
Appendix II: Sample/Standard Preparation	210
A. Bulk Sample Pellets	210
B. Polished Section Preparation	212
C. Standards	216
Appendix III: Relative Track Counting Efficiencies at High and Low Density: The SMI Factor	217
Appendix IV: Small Angle Scattering	226
Appendix V: Cyclotron Dosimetry	229
Appendix VI: Interaction and Fission Track Registration and Annealing in Cyclotron-Irradiated Mica	238
A. Interaction Tracks	238
B. Fission Track in Irradiation-Damaged Mica	248
Appendix VII: Differential Fission Track Annealing of Mica during Cyclotron Irradiation	257
Appendix VIII: Uranium Isotopic Variations	260
References	266

I. Introduction

In trying to understand how our solar system formed many studies have focussed on the carbonaceous chondrites. Bulk elemental abundances for the C1 subclass match observed solar abundances, thus the carbonaceous chondrites (CC) are thought to represent a total nonvolatile condensate of the solar system's precursor, the solar nebula (Anders, 1971; Holweger, 1977). This study focusses on the actinide elements thorium and uranium, and more explicitly, the ratio of Th/U in CC material. As will be discussed, the solar system value for the Th/U ratio is crucial for modelling the time-scale for heavy element r-process nucleosynthesis. Use of actinide element ratios as chronometers requires the knowledge that fractionation of the elements has not occurred or that proper correction for fractionation has been done. The determination of CC Th/U ratios on a micro-scale can give invaluable insight toward the interpretation of bulk measurements. Knowledge of Th/U fractionations could also aid in the use of other actinide chronometers- in particular the use of measured meteoritic $^{244}\text{Pu}/\text{U}$ and $^{244}\text{Pu}/\text{Th}$ ratios as chronometers. Relative abundance measurements of the extinct actinide ^{244}Pu ($t_{1/2}=82$ my) are made via its fission products. Documentation of fractionation of Th relative to U in meteoritic materials as well as the magnitude of fractionation could lead to judicious selection or discrimination of Pu/actinide measurements as appropriate for chronometric usage.

In 1969 the fall of the several ton Allende C3 meteorite (King et al., 1969; Clarke et al., 1970) opened the way for an exciting burst of scientific research. Calcium-aluminum rich inclusions were

found in this meteorite that appeared to be excellent candidates for early formed high temperature condensates (Marvin et al., 1970; Larimer & Anders, 1970) proposed in some solar system condensation models (Lord, 1965; Grossman, 1972). The opportunity for detailed exhaustive geochemical and petrographic work to test and develop solar system formation theories had fortuitously "fallen at our feet".

Thorium and uranium are considered refractory elements (Grossman & Ganapathy, 1977) and, as such, could have histories intimately associated with the earliest stages of solar system condensation. Identification of the Th and U bearing phases and the determination of their Th/U ratios is important for the interpretation of the petrogenesis of the Ca-Al-rich inclusions as well as for testing theories of the solar nebula.

A. Actinide Nucleosynthesis and Cosmochronology

1. Th/U

The actinide elements are the heaviest elements known, disregarding the hypothetical superheavy elements. Because of a region of short-lived alpha emitting nuclei between $Z=83$ and $Z=90$, the synthesis of these elements must have required very specialized conditions for rapid neutron capture on seed nuclei to build heavier nuclei on a time scale faster than the competing beta decays (Burbidge et al. 1957). Supernovae are thought to be the best astrophysical candidates for the site of r-process nucleosynthesis. This study focusses on the most abundant actinide elements uranium and thorium. In nature today, for all practical purposes, there are only two isotopes of uranium,

^{235}U and ^{238}U , which are radioactive with half-lives of 0.70×10^9 yr and 4.47×10^9 yr respectively (Jaffey et al., 1971). The relative $^{238}/^{235}$ isotopic abundance ratio for terrestrial materials is 137.88 ($\pm 0.1\%$) (Shields, 1960; Cowan & Adler, 1976) with lunar values indistinguishable from the terrestrial ratio (Rosholt & Tatsumoto, 1971; Barnes et al., (1972)). Until recently (Arden, 1977), the terrestrial $^{238}/^{235}$ ratio has been undisputed as the general meteoritic value as well. We reserve full discussion of meteoritic U isotopic variations to Appendix VIII in this thesis. For the purposes of the present discussion we accept the terrestrial U isotopic ratio as a solar system value in accord with very persuasive evidence (Chen & Wasserburg, 1980). Thorium is monoisotopic with the ^{232}Th half-life equal to 14×10^9 yr (LeRoux & Glendenin, 1963).

Fowler & Hoyle (1960) illustrated the importance of knowing the solar system $^{232}\text{Th}/^{238}\text{U}$ ratio to determine the duration of nucleosynthesis. Schramm & Wasserburg (1970) developed "model-independent" chronologies and showed that the ratio of a long-lived and an essentially stable nuclide would allow a "mean age" of the elements to be determined independent of the time-dependent element production model used. The concept of a solar system Th/U ratio and its determination are fundamental in determining meaningful numerical solutions for these cosmochronological quantities.

Solar spectroscopic data are able to give only an upper limit to the solar U abundance and what may be only a lower limit to the Th abundance due to thermal and gravitational diffusion at the bottom of the solar convective zone (Grevesse, 1969). Thus, it is through

analysis of meteorite, lunar and terrestrial material that a solar system Th/U value must be determined. Many terrestrial and lunar igneous rocks give Th/U ratios within a restricted range. Following the arguments presented in Schramm & Wasserburg (1970) terrestrial Pb measurements on a wide variety of rock types indicate evolution from a $^{232}\text{Th}/^{238}\text{U}$ atomic ratio of 3.9 ± 0.2 or alternatively a ratio by weight of 3.8. All Th/U ratios henceforth will be given as weight ratios, because in later sections we will be discussing U and Th abundances in terms of concentrations by weight. Lunar rock measurements give $^{232}\text{Th}/^{238}\text{U}$ values near 4 (e.g., see Toksoz & Johnston, 1978). Murthy & Patterson (1962) found that the lead isotopes from a carefully selected suite of ordinary chondrites, as well as the eucrite Nuevo Laredo, evolved from a $^{232}\text{Th}/^{238}\text{U}$ ratio of 3.8. Morgan & Lovering (1968) measured Th and U concentrations on a large suite of chondritic meteorites by neutron activation analysis. Th/U ratios for twenty ordinary chondrites were determined. Averaging these analyses gives a Th/U ratio of 3.5 ± 0.4 for this chondrite group. Thus analysis of a wide range of terrestrial, lunar, and non-CC meteoritic material strongly suggests that indeed a solar system Th/U ratio does exist with "normal" defined as 3.8 ± 0.5 .

In this context the Morgan & Lovering (1967, 1968) (herein referred to as M&L) analyses of carbonaceous chondrite Th/U ratios proved puzzling. Ratios ranging from as low as ~ 2 to as high as ~ 6 were observed. There was also observed a high degree of variability in measured ratios for different samples of the same CC meteorite--especially in the C1 group. Ivuna samples had Th/U ratios ranging from 2.3 to 3.7,

and Orgueil ratios ranged from 2.2 to 4.3. This variability is hard to reconcile with the model of Cl elemental abundances reflecting solar system abundances as total nonvolatile condensates. One might ask whether this range in CC Th/U ratios is indicative of differences in the chemical properties of the two elements under the nebular conditions at the time of their condensation. The primitiveness of the CC's can also be questioned. McSween (1979) presents evidence for thermal metamorphism and aqueous alteration. To what extent bulk CC Th/U ratios could be affected is unclear.

Following the model-dependent nucleosynthesis model calculations of Fowler (1972, updated 1977), which are similar to those of many other authors, there is still a large enough uncertainty in the value for a "normal" Th/U ratio of 3.8 ± 0.5 that widely different (a factor of 4) time scales for nucleosynthesis are implied. More general conclusions were given by Schramm and Wasserburg (1970), but for simplicity the Fowler (1972) calculations will be discussed. These consider element production from two types of nucleosynthesis, continuous and sudden spike. Nucleosynthesis of the elements (post big-bang) comes from discrete stellar events. In the long term context these discrete events can be approximated in an average sense as a "continuous" process of element production. Based on arguments concerning star formation and disruption, Fowler favors an exponential form for this continuous nucleosynthesis of the form $\exp(-t/T_R)$. When the characteristic exponential decay constant $T_R = \infty$ the result is a uniform element production rate over time. When $T_R = 0$, elements are synthesized in a single event, referred to by Fowler as an "early spike". In the event of any significant local

late-stage (i.e., just prior to solar system formation) injection of freshly synthesized material into the solar nebula, Fowler considers the concept of "late spike" nucleosynthesis. Short-lived nuclide abundances in particular are sensitive to a late spike event(s).

In order to obtain a self-consistent solution Fowler (1972) uses as input to his model the initial solar system $^{232}\text{Th}/^{238}\text{U}$ ratio for determining the long-term continuous nucleosynthesis component, short-lived/long-lived(or stable) nuclide ratios ($^{244}\text{Pu}/^{238}\text{U}$, $^{129}\text{I}/^{127}\text{I}$) for determining the contribution from last-minute spike nucleosynthesis and the intermediate/long-lived $^{235}\text{U}/^{238}\text{U}$ ratio for intermediate time scales. A present day solar system Th/U ratio equal to 3.9 is consistent with having essentially all (>92%) r-process nucleosynthesis accomplished in a continuous exponential synthesis process of 6 b.y. duration [$T_R=3$ b.y. for $^{244}\text{Pu}/^{238}\text{U}=0.03$, and $T_R=10$ b.y. for $^{244}\text{Pu}/^{238}\text{U}=0.015$]. Higher Th/U ratios indicate a more uniform (large T_R) continuous nucleosynthesis over longer times and a negligible need to invoke a last minute spike. In contrast, a present day solar system Th/U value equal to 3.4 is compatible with a model where essentially all (>88% assuming $^{244}\text{Pu}/^{238}\text{U}<0.03$) the synthesis occurred in an "early" spike ~3 b.y. before meteorite formation. As can be seen the CC Th/U ratio range of 2 to 6 observed by Morgan & Lovering (1968) [herein referred to as M&L(1968)] implies even greater differences in r-process nucleosynthesis models and their associated time scales.

Because of the above implications of the 2 to 6 range in Th/U ratios, as well as possible inferences as to the environmental conditions during CC condensation or later alteration, a prime goal of this thesis study was to see if we could confirm these values.

2. ^{244}Pu /actinide ratios

Positive identification of the presence of now-extinct nuclides has shown that nucleosynthesis was occurring immediately prior to solar nebula condensation. These also constrain time scales for early nebular condensation itself (for ^{129}I , ^{244}Pu , ^{26}Al see review in Podosek, 1978; for ^{107}Pd see Kelly & Wasserburg, 1978 and Kaiser et al., 1980). $^{129}\text{I}/^{127}\text{I}$ and $^{244}\text{Pu}/^{238}\text{U}$ (^{129}I has $t_{1/2}=17$ m.y. and the actinide ^{244}Pu has $t_{1/2}=82$ m.y.) are incorporated with the abundance ratios for $^{235}\text{U}/^{238}\text{U}$ and $^{232}\text{Th}/^{238}\text{U}$ to obtain self-consistent solutions for r-process nucleosynthesis (Wasserburg et al., 1969 ; Schramm & Wasserburg, 1970). However, $^{244}\text{Pu}/^{238}\text{U}$ ratios ranging from 0.015 to 0.087 have been measured on meteoritic materials(see review in Burnett et al., 1980). Depending on which ratio is taken as the solar system value at the time of solar system formation, different r-process nucleosynthesis models are implied. For example, values of 0.03 and higher necessitate a late spike of r-process nucleosynthesis $1-3 \times 10^8$ yr prior to solar system formation which would contribute $>8\%$ of the total r-process nucleosynthesis. This spike will produce essentially all of the ^{244}Pu as well as 80% of the ^{235}U (Wasserburg et al., 1969). Kelly & Wasserburg (1978) present arguments against any major late injection of ^{244}Pu in the last minute nucleosynthesis "event" 1-3 m.y. prior to solar system formation, associated with ^{26}Al and ^{107}Pd production. Measurements of actinide/actinide fractionation in terms of Th/U can aid in making judicious selection of a $^{244}\text{Pu}/^{238}\text{U}$ value that is not strongly affected by chemical fractionation.

B. Th/U microdistributions--tests for solar nebula condensation models and Allende inclusion petrogenesis

Cristophe Michel-Levy (1968) was the first to suggest that a coarse-grained calcium-aluminum rich inclusion (CAI) from the C3 meteorite Vigarano was a high temperature nebular condensate. This suggestion was based on a comparison of the theoretical calculations for condensation of a cooling solar nebula (Lord, 1965; Larimer, 1967) with the observed inclusion mineralogy. After the 1969 fall of the C3 Allende meteorite, similar CAI were recognized. Marvin et al. (1970) and Larimer & Anders (1970) also proposed an early nebular condensate origin based on the observed Ca-Al-Ti-rich mineralogy predicted by theory. CAI have subsequently been recognized in other CC's as well (e.g., Kurat, 1970; Frost & Symes, 1970; Grossman et al., 1977). The preservation of what may be the earliest nebular condensates provided an exciting opportunity to test and develop condensation theories. Because of the abundance of material and diversity of inclusions the Allende meteorite has been the focus for a wide range of meteoritic research.

Gray et al. (1973) measured the $^{87}\text{Sr}/^{86}\text{Sr}$ ratio for Allende Ca-Al rich chondrules. Correction for in-situ ^{87}Rb decay is minimized by selecting samples with low $^{87}\text{Rb}/^{86}\text{Sr}$. The $^{87}\text{Sr}/^{86}\text{Sr}$ measured (0.69877 ± 0.00002) was the lowest observed in any meteorite to date and supported the view of these inclusions as early condensates isolated from a high Rb environment. Although a well-defined age was not observed, $^{129}\text{I}/^{127}\text{I}$ measurements on a mixture of CAI (Podosek & Lewis, 1972), however, gave no evidence for an age for the CAI any older than the ages of recrystallized chondrites. Evidence for

in-situ decay of the extinct nuclide ^{26}Al ($t_{1/2}=0.7$ m.y.) in some Allende CAI (Lee et al., 1976; Papanastassiou et al., 1977; Wasserburg et al., 1976) attests to a link of at least some fraction of these inclusions with the first ~ 1 m.y. of solar system history.

Beginning with a gas of solar composition Grossman (1972) calculated an equilibrium condensation sequence for a cooling gas at constant pressure. Incorporation of solid solution processes and revised thermodynamic and solar abundance data led to a series of papers (see Grossman, 1980 for complete reference list).

Analogous to the thermodynamic calculations used by astronomers in predicting compositions of stellar condensate grains, the theoretical equilibrium condensation models for a cooling solar nebula are useful as a framework to interpret meteorite observations. Solar condensation models should be able to predict the phases and sequence of nebular condensation. Grossman & Larimer (1974) begin with a nebula of solar composition at average total pressure of 10^{-3} atm. (Cameron & Pine, 1973). Table 1 lists the calculated equilibrium gas to solid condensation sequence of Grossman & Larimer (1974). As can be seen the first major mineral phases to condense out are corundum, perovskite, melilite, spinel, and diopside. For the most part these are the major phases observed in the coarse-grained CAI. The exceptions are that hibonite is observed rather than corundum and that a Ti-Al pyroxene (fassaite) is the abundant pyroxene phase observed rather than diopside. The lack of thermodynamic data makes it difficult to incorporate these phases into the theoretical calculations. Arguments have been made, however, to support these phases as high temperature

TABLE 1

RELATIONSHIPS BETWEEN THE CONDENSATION TEMPERATURES
OF THE REFRACTORY TRACE ELEMENTS
AND THOSE OF THE MAJOR HIGH-TEMPERATURE MINERALS **

Gaseous Species	Crystalline Phases	Condensation Temperature* °K	
		10 ⁻³ atm	10 ⁻⁴ atm
Os	Os	1925	1840
WO, W	W	1885	1798
ZrO, ZrO ₂ , Zr	Zr, ZrO ₂	1840	1789
Re	Re	1839	1759
	Corundum (Al ₂ O ₃)	1758	1679
HfO ~ HfO ₂ , Hf	Hf, HfO ₂	1719	1652
YO, Y	Y, Y ₂ O ₃	1719	1646
ScO, Sc	Sc, Sc ₂ O ₃	1715	1644
Mo, MoO	Mo, MoO ₃	1684	1603
	Perovskite (CaTiO ₃)	1647	1571
ReO, RE ⁺	RE, RE ₂ O ₃	1647	1571
Ir	Ir	1629	1555
	Gehlenite (Ca ₂ Al ₂ SiO ₇)	1625	1544
Ru	Ru	1614	1541
VO, V	VO ₂ , V, VO, V ₂ O ₃	1534	1458
	Spinel (MgAl ₂ O ₄)	1513	1444
TaO, Ta	Ta, Ta ₂ O ₅	1499	1452
ThO ₂ , ThO, Th	Th, ThO ₂	1496	1429
	Diopside (CaMgSi ₂ O ₆)	1450	1387

* The condensation temperature of the italicized crystalline phase.
For each element, this is the highest-condensing phase of those listed.

† Rare earth.

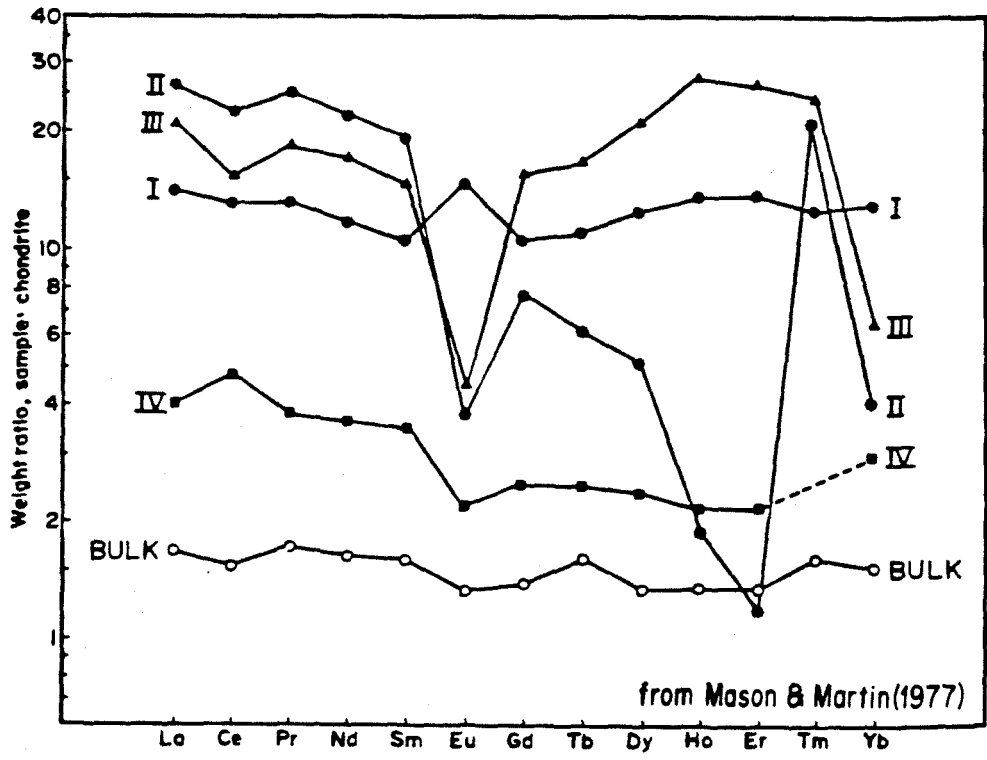
** Table taken from Grossman and Larimer (1974).

condensates (Grossman & Clarke, 1973; Lattimer & Grossman, 1978). The melilite-spinel-perovskite assemblage is the predicted equilibrium assemblage of a gas of solar composition at temperatures between 1533-1438°K at 10^{-3} atm. (Grossman & Larimer, 1974; Lattimer & Grossman, 1978). There is a 75°K drop in the condensation temperature scale for each order of magnitude drop in pressure.

Trace element analysis has played an important part in testing the early condensate theory. Pure metal nuggets and various multiple-metal alloys of Os, Ir, Pt, W, Mo, Ru, and Rh have been observed (e.g., Wark & Lovering, 1976; El Goresy et al., 1977) in coarse-grained CAI. The lanthanide or rare earths (REE) and thorium are also predicted to be early condensing elements. Following Grossman & Larimer (1974), condensation can be in the form of the pure element, oxides or as solid solution with the early condensing major mineral phases. The REE are similar in size and electronic structure leading to similar chemical behavior. Usually any variations in chemical behavior show up as smooth variations with atomic number. This is attributed to the small systematic decreases in ionic radius with atomic number (lanthanide contraction) due to the progressive filling of the 4f electron level. The possibility of multiple valence states for Eu and Ce can cause their fractionation relative to the other REE. Martin & Mason (1974) defined four basic REE element distribution patterns for Allende inclusions (see Fig. 1 taken from Mason & Martin, 1977). The majority of Ca-Al rich inclusions fall into the Group I or Group II REE patterns. Most coarse-grained CAI exhibit a Group I pattern, a relatively flat distribution showing an enrichment

FIGURE 1

This plot taken from Mason & Martin (1977, figure 1) shows the chondrite-normalized rare earth element patterns observed in Allende. A Group I pattern exhibits essentially uniform enrichment in the REE as do most coarse-grained Ca-Al-rich inclusions. Most fine-grained Ca-Al-rich inclusions have the highly fractionated Group II pattern which shows general higher enrichment of the light REE over the heavy REE. Group III patterns with a negative Eu anomaly are reported for Ca-Al-rich aggregates. The flat Group IV pattern is observed in Mg-rich chondrules and aggregates. The bulk Allende pattern is included for reference.



~15- 17 times Cl chondritic (Mason & Martin, 1977; Grossman & Ganapathy, 1976a). In contrast many fine-grained CAI have a group II pattern which, barring details, shows a uniform enrichment of the light REE (~20-40 times chondritic) with irregular depletion in the heavy REE at levels still higher than chondritic (Grossman & Ganapathy, 1976b; Mason & Martin, 1977).

Table 2 (Ganapathy & Grossman, 1976) lists the actinide species for which thermodynamic data are available to allow incorporation into the condensation models. ThO_2 is the only actinide crystalline phase considered which reaches saturation in the solar nebula above 1450°K (at 10^{-3} atm.). The pure elemental phases and oxides of U and Pu would not begin to condense out until $\sim 1300^\circ\text{K}$ and $\sim 1200^\circ\text{K}$ respectively. Grossman (1980) states that none of the purely crystalline phases of Th, U, Pu for which thermodynamic data are available are capable of condensing these elements above the postulated 1438°K (at 10^{-3} atm) coarse-grained CAI equilibrium condensation temperature. Grossman et al.(1977), however, illustrated that U is enriched over chondritic levels in the CAI. This is strong evidence that U did not condense in the oxide phase but rather initially condensed in solid solution with previously formed phases. Whether or not complete condensation of U occurred in these early phases is a subject of much contention. Although individual U abundances in CAI can easily vary by a factor of two, Grossman et al., (1977) contend that, on the average, U, along with 20 other refractory elements which include the REE, exhibit a uniform mean enrichment factor of 17.5 ± 0.4 relative to Cl bulk chondritic levels. (See

TABLE 2

ELEMENTAL AND OXIDE SPECIES OF Th, U and Pu
FOR WHICH FREE ENERGIES OF FORMATION ARE AVAILABLE*

<u>Element</u>	<u>Gaseous Molecules</u>	<u>Crystalline Phases</u>	<u>Condensation Temperature of Pure Phase (°K)</u>
Th	Th, ThO, ThO ₂	Th, ThO ₂	ThO ₂ : 1555
U	U, UO, UO ₂ , UO ₃	U, UO, U ₂ O ₃ , UO ₂ , U ₃ O ₈	UO ₂ : ~1300
Pu	Pu, PuO, PuO ₂	Pu, PuO, Pu ₂ O ₃ , PuO ₂	PuO ₂ : ~1200

* Table taken from Ganapathy and Grossman (1976)

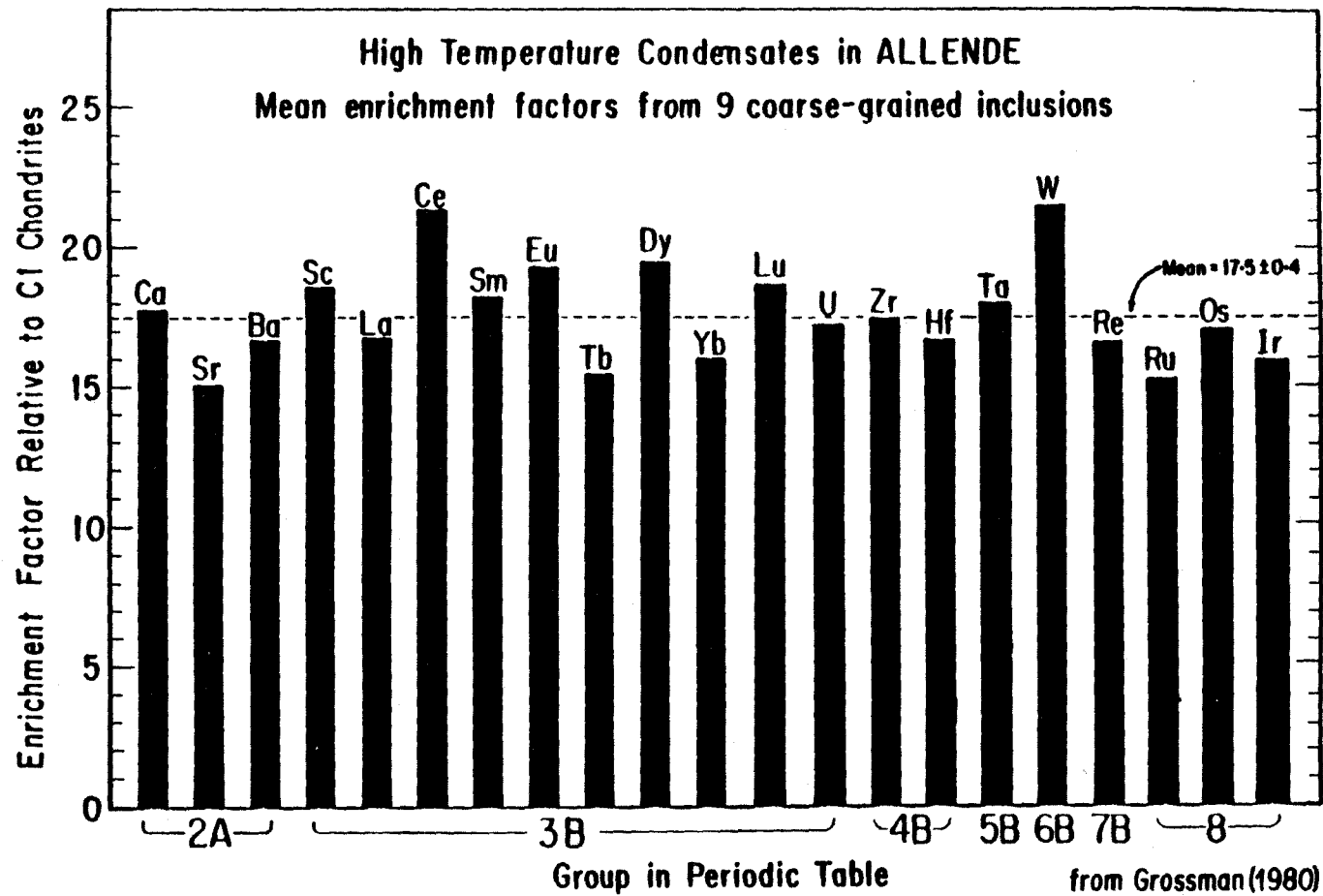
Fig. 2 taken from Grossman, 1980.) Taking the "normal" range to be 3.8 ± 0.5 , Boynton (1977), however, points to bulk CAI measurements of $\text{Th}/\text{U} > 5$ as evidence for incomplete U condensation (Tatsumoto et al., 1976; Chen & Tilton, 1976). His contention is that at the T and P conditions of CAI condensation U is more volatile than Th. Grossman et al. (1977) counterargue that CAI with ratios below 3.5 are also measured (Tatsumoto et al., 1976; Chen & Tilton, 1976) so that even though the Th/U ratio is apparently quite variable from inclusion to inclusion, the mean ratio for a group of CAI gives a value close to "normal" chondritic (~ 4).

Valence state can be a crucial factor in causing relative actinide fractionations. In contrast to the single +4 valence state of Th, +3,+4,+5,+6 U has been observed in natural systems. Valence state could also be important for Pu/actinide fractionation. Pu occurs primarily in the +3 and +4 valence states. The +6 state can be reached only under very oxidizing conditions. Fractionation studies of the extant actinides (Th/U) can guide judgements in the use of ^{244}Pu /actinide ratios from the same meteoritic material.

A major aim of this thesis is to determine Th/U ratios not only for bulk inclusions, but also on a micro-scale within a single inclusion, identifying the carrier phases when possible. Th/U variations between coexisting mineral phases in terrestrial (e.g. Silver, 1976), lunar (Burnett et al., 1971), and ordinary chondrite (Croaz, 1979) material is documented. Shirck (thesis, 1975) observes variations in inferred $^{244}\text{Pu}/^{238}\text{U}$ coexisting melilite and clinopyroxene grains in Allende coarse-grained inclusions. Th/U ratio microdistribution analysis put in

FIGURE 2

This figure is taken from Grossman (1980). Abundances of 21 refractory elements, including U, were determined for 9 coarse-grained inclusions (Grossman et al. 1977). The mean enrichment factors relative to C1 chondritic for these elements indicates a uniform refractory element enrichment factor of 17.5 ± 0.4 in coarse-grained Ca-Al-rich inclusions.



a petrographic context could give valuable insight into conditions during inclusion formation and, if relevant, conditions of subsequent alteration.

C. Research Scope

The goal of this work was to develop and implement an induced fission track radiography technique with the sensitivity to measure bulk carbonaceous chondrite Th/U ratios and map CAI Th/U micro-distributions. The technique was initially developed and tested using the bulk samples. Typical bulk Th concentrations in carbonaceous chondrites are ~40 ppb and U concentrations are ~10 ppb. Because of the non-destructive nature of the track technique, isotopic dilution comparison measurements on selected samples could be made. The prime scientific motivation for our bulk meteorite measurements was to check the 2-6 spread in CC Th/U ratios obtained by Morgan & Lovering (1968).

The real strength of the induced fission track method lies in the ability to map elemental abundances in-situ on a micro-scale. With track maps to define areas of element localizations, mineral phase identifications can be made on polished section samples with an electron microprobe or SEM. The mapping experiment in this study focusses on Allende, in particular the refractory-enriched CAI. Determination of bulk inclusion Th/U as well as the distribution and identification of the major Th and U carriers within an individual

inclusion was the primary goal of our Allende mapping study. Because our mapping experiments were done on polished sections which contained a wide variety of inclusions, we have the flexibility to identify some U,Th rich inclusions that otherwise would have gone unnoticed.

II. Experimental

A. Basic Physics of the Double Irradiation Technique

Our experimental technique takes advantage of the unique property of the heavy elements to fission under particle bombardment. As will be discussed, our two-irradiation technique uses the particular fission properties of the uranium isotopes and thorium to measure Th/U ratios.

1. Thermal Neutron Irradiation

Neutron capture on a ^{235}U nucleus (which makes up 0.7 atomic % of terrestrial uranium) creates the compound nucleus ^{236}U . Calculation of the difference in binding energy between the two nuclides gives an excitation energy of $B.E.(^{236}\text{U}) - B.E.(^{235}\text{U}) = 6.8 \text{ MeV}$ for a thermal neutron (refer Glasstone & Edlund(1966), pp.77-78). In comparison neutron capture on ^{238}U (~99.3% of terrestrial uranium) creating ^{239}U gives $B.E.(^{239}\text{U}) - B.E.(^{238}\text{U}) = 5.5 \text{ MeV}$. This 1.3 MeV difference in compound nucleus excitation energies is due mainly to the odd-even pairing energy term in the liquid drop model mass equation (see e.g., Glasstone & Edlund(1966), Chapt.1, or Vandenbosch & Huizenga (1973), Chapt.2). Because the compound nucleus ^{236}U has an even number of neutrons the pairing energy gives a positive contribution to the binding energy as opposed to the zero contribution for ^{235}U which has an unpaired neutron. The reverse situation occurs in the neutron capture on ^{238}U where an unpaired neutron is added to an even-even nucleus. This effect explains most of the 1.3 MeV difference in excitation energies. Because the fission barrier of ^{238}U is

about 6.5 MeV, an incident neutron needs $7 - 5.5 = 1.5$ MeV kinetic energy to induce fission; i.e., neutron induced fission of ^{238}U can be accomplished only with fast neutrons or any other particle which can supply the additional excitation energy. The fission barrier for ^{235}U is also 6.5 MeV. However, because of the spin-pairing effect described above, 6.8 MeV is available in excitation energy alone from capture of a neutron with zero kinetic energy. Thus, ^{235}U induced fission can occur with thermal neutron (.025 eV) bombardments.

Natural thorium is monoisotopic, and ^{232}Th is an even-even nuclide like ^{238}U . As such the basic rationale which prohibited ^{238}U thermal induced fission applies to prohibiting ^{232}Th thermal neutron fission as well.

The favorable condition of ^{235}U thermal n-fission is reflected in the ~ 600 barn ($1 \text{ barn} = 10^{-24} \text{ cm}^2$) fission cross section (see Neutron Cross Sections, BNL-325, 1965, Brookhaven Natl. Lab.) By comparison the cross-section for neutron fission of ^{238}U doesn't reach 0.5 b until neutron energies are close to 2 MeV. Similarly, it takes neutron bombarding energies of ~ 2 MeV to bring the ^{232}Th fission cross section just up to 0.1 b. Thus fission by thermal neutrons in natural materials can be uniquely ascribed to ^{235}U .

Taking advantage of the large thermal neutron fission cross section for ^{235}U , uranium measurements can be done on samples of normal or known isotopic composition in nuclear reactor irradiations. This has become a standard technique of fission track and xenology experimenters (Xe isotopes being among fission products) to measure

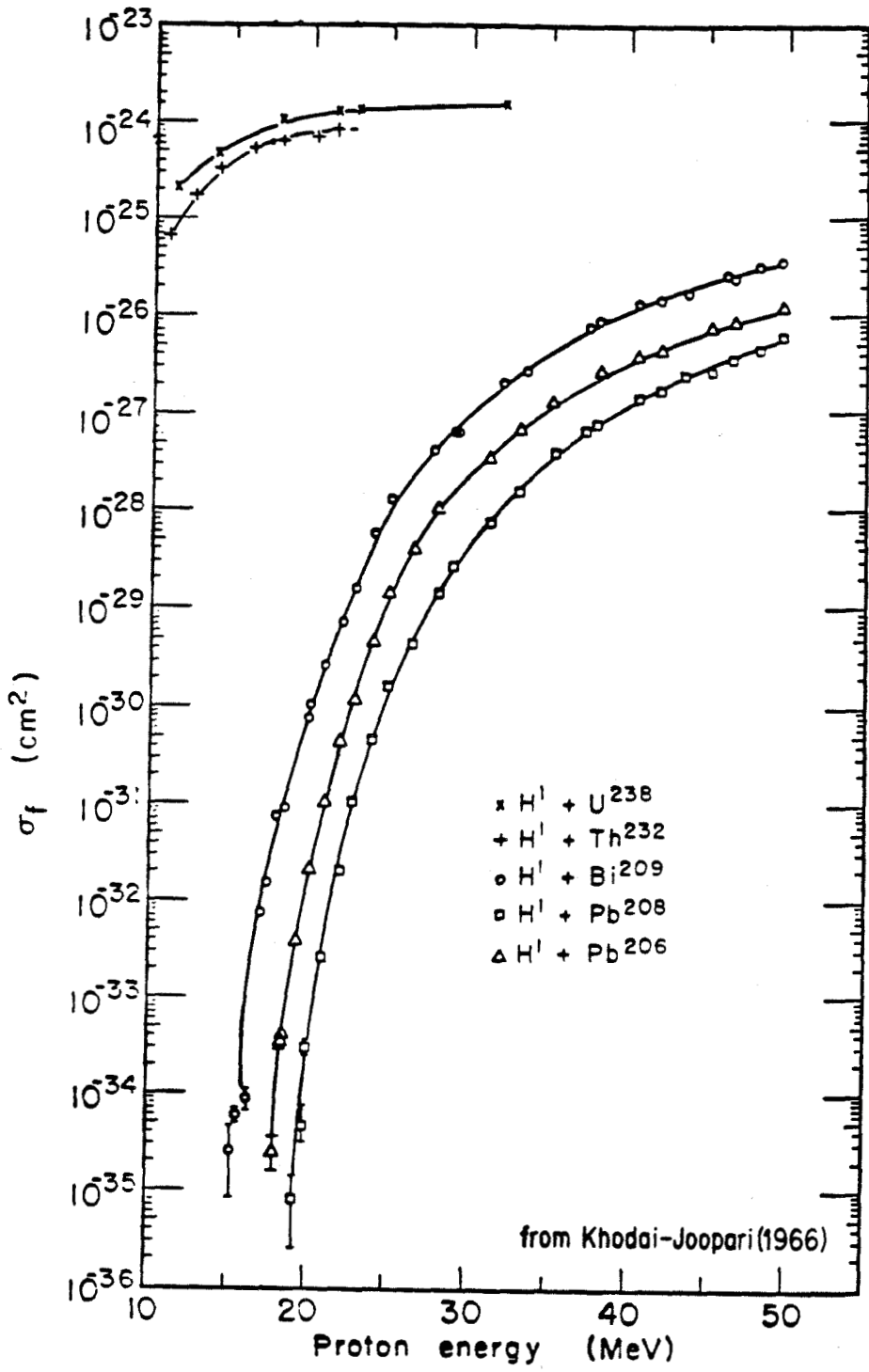
uranium concentrations. Our reactor irradiations were carried out at the University of Missouri Reactor Facility in Columbia, Missouri. This facility will often be referred to as Columbia in this study. Samples were irradiated in reflector positions I3(0-4) and I3(26-30). Neutrons with energies above 1 MeV composed only about 0.33% of the total neutron flux. Thus at maximum the contribution of ^{238}U and ^{232}Th fission to the total number of ^{235}U fission events would be 7 events in 10^4 .

2. High Energy Irradiation

To fission ^{232}Th requires bombardment by fast neutrons, high energy charged particles, or high energy photons (the photo-fission thresholds for Th and ^{238}U are ~ 5.5 MeV [e.g. see Haissinsky (1964) p.150]). The option chosen by us was determined by available beams, inferred cross-section ratios, fluxes, as well as availability to an outside user of the irradiation facility. The result of these considerations led to our use of charged particle beam irradiations at the Texas A&M cyclotron facility, College Station, Texas. During the development of the technique we have used the cyclotron's 100 MeV alpha, 50 MeV deuteron, and 35-40 MeV proton beams--all of which fission Th and U at comparable rates. As will be discussed later, the greatest success was accomplished with the 35 MeV proton irradiations. Proton-induced fission cross sections are presented in Figure 3 (taken from Khodai-Joopari, 1966). Smooth extrapolation of the measurements reveals that for proton energies above ~ 20 MeV the Th,U fission cross-sections are essentially energy independent, both

FIGURE 3

This figure is taken from Khodai-Joopari (1966) to illustrate the proton-induced fission cross-sections for ^{238}U , ^{232}Th , ^{209}Bi , ^{208}Pb , and ^{206}Pb . Over the energy interval of interest for our experiment (~25-40 MeV) the Th and U fission cross-sections appear essentially energy independent. In contrast, the fission cross-sections for Pb and Bi at 40 MeV are 2-3 orders of magnitude smaller than Th and U, and continue to decrease with decrease in proton energy.



with values close to 1 barn. In contrast, the fission cross sections for Pb and Bi are 2-4 orders of magnitude lower, drop an order of magnitude in going from 40 to 30 MeV, and continue to drop at an increasingly steeper rate for lower proton energies.

3. Fission Track Radiography

The technique used in this study to detect and record fission events is that of fission track radiography. A sheet of mica placed flush against the surface of a sample being irradiated intercepts the recoiling fission fragments and records their passage as tracks.

In slow neutron irradiation, ^{235}U fissions asymmetrically into a heavy (most probable $A\sim 138$) and light (most probable $A\sim 95$) fragment with accompanying emission of on the average 2.5 neutrons (see Vandebusch & Huizenga, 1973). Of the ~ 200 MeV released in the fission event, approximately 170 MeV is released as kinetic energy of the fission fragments. The ratio of the initial kinetic energies of the fragments goes as the inverse ratio of the masses of the fragments, i.e., a factor of 1.5. Thus, the light fragment will have an initial most probable kinetic energy of 96 MeV and the heavy fragment 64 MeV with velocities of 96/95 and 64/138 MeV/amu respectively.

As discussed in Fleischer, Price and Walker (1975, p.24), herein referred to as FPW, a high energy atom will quickly become ionized as its orbital electrons interact with the surrounding medium. An equation for the effective positive charge of the ion (Heckman et al., 1960) is $z_{\text{eff}} = Z(1 - \exp(-130\beta/Z^{2/3}))$, where β is the ratio of the ion speed to the speed of light. Taking $Z\sim 45$ for a fission fragment and energy ~ 100 MeV, a z_{eff} of 23 is calculated. Along their flight path these ions lose energy rapidly as they interact with the atomic electrons of the surrounding medium. At a given velocity the rate of energy loss of the penetrating ion (i.e., the dE/dx or in different units the specific ionization) is

proportional to z_{eff}^2 . Electrons of atoms within range of the electric force of the ion are excited and ions produced. This creates a channel of primary ionization in the medium along the ion's path of movement. If the ejected electrons themselves have high enough energy they too can cause excitation of secondary ionization. Calculations show, however, the secondary processes are fairly tightly constrained nearby to the primary ionization [FPW,p.24 refer to Katz & Kobetich,1968].

In dielectric media, these paths of ionization-caused dislocation damage, i.e. tracks, can be chemically etched out to be visible under the optical microscope. This process has many practical applications, although the details of track formation mechanisms are to date still not well understood(see FPW, Chapt. 1 for discussion of various proposed theories). Ruby muscovite mica is used in our experiments as the track detector. Fission tracks can be etched in mica using HF up to maximum lengths of ~10 microns. Prolonged etching increases the track diameter and, for mica, results in a characteristic diamond shape.

As mentioned above, the process of recordable track formation is dependent on the primary specific ionization rate. For each material to record observable tracks (1 micron or larger) there is a so-called critical ionization threshold. Although the concept of a sharp threshold has been disputed (Price et al., 1973) the model proves useful in visualizing the limits of various materials as track detectors. For each material there is a minimum ionization rate an ion must have to leave a path of ionization damage in the material that can be etched as a track. Thus the charge and velocity of a particle

determine whether a track is formed or not. One of the reasons mica was chosen as the track detector in our experiments is because the least ionizing particle that can make a track in muscovite mica is a 2 MeV ^{20}Ne ion (FPW, table 12, p.19). Thus, fission fragments which recoil from the sample into the mica will be recorded as tracks but the charged particle beams used to induce the U and Th fission leave no etchable ionization damage in the micas they pass through.

4. Th/U by Double Irradiation Experiments

The idea behind the double irradiation experiment is that the high energy irradiation fissions both Th and U allowing essentially [Th+U] concentrations to be measured. With the U determinations independently obtained from a reactor irradiation, (Th+U)/U ratios and hence Th/U ratios can be obtained.

A glass of known Th and U content accompanying the irradiation of an unknown is used as the standard by which fission track measurements can be converted to elemental concentrations (by weight). We will denote ρ as the measured track density, subscript L as the reactor irradiation, subscript H as the high energy irradiation, and subscript o as the standard. Assuming a sample size larger than fission fragment ranges, the same U isotopic composition in standards and samples, and neglecting small differential range corrections, uranium measurements are obtained from the reactor irradiation by the relation:

$$[U] \cong (\rho / \rho_o) [U]_o$$

The high energy irradiation fissions both Th and U. For the case of equal fission cross sections:

$$[\text{Th+U}]^* \cong (\rho / \rho_o) [\text{Th+U}]_o^*$$

In this way the combination of the two irradiations permits [Th+U]/U ratios and hence Th/U ratios to be measured. In Appendix XX the correction factor for deriving a [Th+U]/U ratio for unequal Th and U fission cross sections is derived:

$$\left[\frac{(\text{Th+U})}{U} \right] - \left[\frac{(\text{Th+U})}{U} \right]^* = \left\{ \left[\frac{(\text{Th+U})}{U} \right]^* \left[\frac{(\text{Th+U})}{U} \right]^{-1} C \right\} - C$$

where superscript * means the value obtained assuming equal U and Th fission cross sections and $C \cong [(\sigma_U/\sigma_{Th})-1]$ where σ_U/σ_{Th} is

the ratio of the fission cross-section for U relative to Th. In the technique we developed using 40 MeV protons, $\sigma_{\text{Th}}/\sigma_{\text{U}} = 0.87 \pm 0.01$

The same standard is used in the low and high energy irradiations. In principle, to obtain a $[\text{Th}+\text{U}]/\text{U}$ ratio requires knowledge of only the Th/U ratio in the standard. Thus, sensitivity to Th,U inhomogeneities in the standard is reduced if these elements are correlated. Similarly, in the analysis of a small grain Th/U ratios can be determined even though absolute concentrations cannot.

The first double irradiation experiments were reported by Bimbot et al.(1967) using 85 MeV protons and Hair et al.(1971) using 30 MeV alpha particles but these involved only test irradiations of standard glasses at high Th concentration. Burnett et al.(1971) used 30 MeV alphas to measure U,Th distributions for lunar rock 12013 which has granitic levels of U and Th. Reactor fast neutron measurements of Th and U in glasses and minerals are described in Berzina et al.(1968,1971) and Reimer and Carpenter (1973) but only a small (<10%(?)) fraction of the observed fissions are due to Th. Crozaz(1974,1979) made U,Th measurements on a suite of ordinary chondrites and achondrites using fission neutrons from a thermal converter for which $\sigma_{\text{Th}}/\sigma_{\text{U}} = 0.4$. The major difficulty that discouraged previous application of these techniques to chondrites was the low (~50 ppb) bulk concentrations of Th and U. The required high dose particle irradiations needed to obtain enough fission events for good statistics creates challenging problems to surmount besides reactor/cyclotron access, in particular the thermal and irradiation damage to samples, standards and detectors. Full description of these problems and how they were dealt with

follow as the experimental details are discussed.

In contrast to this study's reactor/cyclotron irradiation technique Shirck (1975) has proposed a three stage thermal neutron high dose irradiation method to measure low level U and Th concentrations. The first irradiation (nominal fluence= 10^{18} - $10^{19}/\text{cm}^2$) uses ^{235}U fission as already discussed to measure U in samples of known isotopic ratio. A second and third high dose irradiation permit Th+U measurements to be made. Th+U measurements are made by the transmutation of ^{232}Th into the thermal neutron fissionable ^{233}U and ^{238}U into thermal neutron fissionable ^{239}Pu . The $^{232}\text{Th} + n$ reactions during the second irradiation (nominal fluence= $10^{20}/\text{cm}^2$) require a subsequent ~ 30 day free decay (β) for the transmutation. The ^{238}U transmutation requires a ~ 2.5 day period after the second irradiation. The third irradiation (nominal fluence= 10^{18} - $10^{19}/\text{cm}^2$) then allows fission events to be recorded either directly or indirectly from a combined [$^{232}\text{Th} + ^{238}\text{U} + ^{235}\text{U}$] concentration of a sample. For samples with Th/U=4, approximately 0.44 of the total tracks are expected to be from Th, i.e. $\sigma_{\text{Th}}/\sigma_{\text{U}} \sim 0.2$. The proposed sensitivity of this technique permits measurements of Th concentrations as low as 20 ppb in a $70\mu \times 70\mu$ inclusion. This is ~ 40 times more sensitive than the level obtained with the technique described in this study. No successful meteorite analysis has been achieved using the Shirck (1975) technique to date. The total fluence levels required are \sim a factor of 100 higher than the combined reactor + cyclotron fluences obtained in our experiments (typical reactor nominal fluence = $1.8 \times 10^{18}/\text{cm}^2$; maximum cyclotron fluence = $2 \times 10^{17}/\text{cm}^2$).

B. Samples/Standards

1. Meteorites

Table 3 lists the meteorites and their sources used in this study. Bulk Th/U analyses were performed on 30 mg homogenized pressed powder pellets. The Th,U microdistribution mapping was done on Allende polished sections. Details of the sample preparation are given in Appendix II.

2. Standards

A microscope glass slide (Gold Seal micro-slide A-1458, Clay Adams, Inc., N.Y., N.Y.) designated CT served as the U,Th standard by which to make the relative meteorite concentration measurements. All CT standards used in our experiments come from a single slide from which isotopic dilution analyses were done. Isotopic dilution analysis by Oberli & Wasserburg (Caltech) of the CT glass gives $U = 374.3 \pm 1.9$ ppb, $Th = 338.0 \pm 3.5$ ppb, hence $Th/U = 0.903 \pm 0.010$. Independent analysis by M. Tatsumoto (USGS, Denver) gives $U = 362$ ppb, $Th = 319$ ppb, and $Th/U = 0.881$. Since we cannot rule out U,Th inhomogeneities in the glass of the order of the differences in measurements observed, we use the average of the two analyses. Thus our average CT glass has a $U = 368 \pm 6$ ppb, $[Th+U] = 697 \pm 16$ ppb, and $Th/U = 0.892 \pm 0.011$.

Uranium isotopic analysis by Tatsumoto gives a normal $^{238}/^{235}$ ratio for this glass.

TABLE 3

LIST OF METEORITES AND THEIR IRRADIATIONS

Sample	Pellet	Reactor (COLMS-#)	Cyclotron (TA+M-#)	Source/ID
Ivuna:	a	3	8, Layer A	Smithsonian/USNM 2478 (0.5g)
	e1	3	8, Layer A	"
	e2	3	9	"
Orgueil:	a	3	9	Smithsonian/USNM 2216 (0.5g)
Orgueil:	CII-1	2	7	UCLA/OII-U. Chicago *
	CII-2	3	8, Layer A	"
Orgueil:	I	2	7	UCLA/Montalban, Fr. *
Mighei:	C-1	2	7	UCLA/U. Chicago *
	C-2	3	8, Layer B	"
Mighei:	FM-1	3	8, Layer A	Field Museum/ME 1456 (1.5g)
	FM-2	3	10, Layer A	"
Murchison:	5	1	6-I	G. J. Wasserburg/J. F. Lovering
	5II	2	6-I	"
	5s	2	7	"

TABLE 3 (continued)

Sample	Pellet	Reactor (COLMS-#)	Cyclotron (TA+M-#)	Source/ID
Murchison:	7	1	6-I	G. J. Wasserburg/J. F. Lovering
Murchison:	M	3	8, Layer B	"
Murchison:	T	1		ASU, Tempe
Murray:	I	1	6-I	ASU, Tempe/#635.2(2.5g)
	II	2	6-II	"
Mokoia:	I	1	6-I	ASU, Tempe/#75.1(0.9g)
	II	2	6-II	"
Lance:	I	3	8, Layer A	NHM Wein (2g)
	II	3	8, Layer A	"
	9	3	10	"
Allende:	1	1		G. J. Wasserburg
Allende:	3	1	6-I	"
Allende:	NWT	1	6-II	NMNH 3512

* Received as crushed powder

3. Blanks and Micas

A high purity low Pb-U-Th quartz (T-21 Suprasil) was used in making the necessary blank measurements for our pressed pellet samples. (lead analysis by F. Tera gives 0.5 ppb total Pb, $206/204 = 18.9$, $207/204 = 15.6$).

Track detectors in the irradiations were low U,Th ruby muscovite micas. Mica is used because it records tracks only for heavy ions, can withstand high temperatures (decomposes 630°C), can be cleaved thin without worry of fracture, and is transparent. Mica also etches anisotropically. This results in a characteristic diamond shape surface expression allowing easy track recognition.

C. Reactor Experiments

1. Packaging

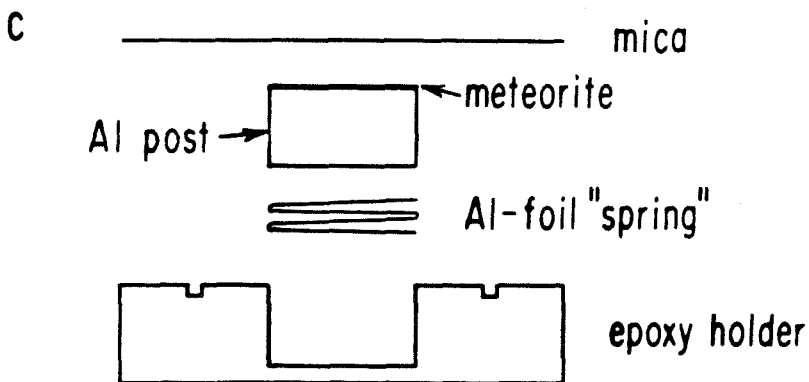
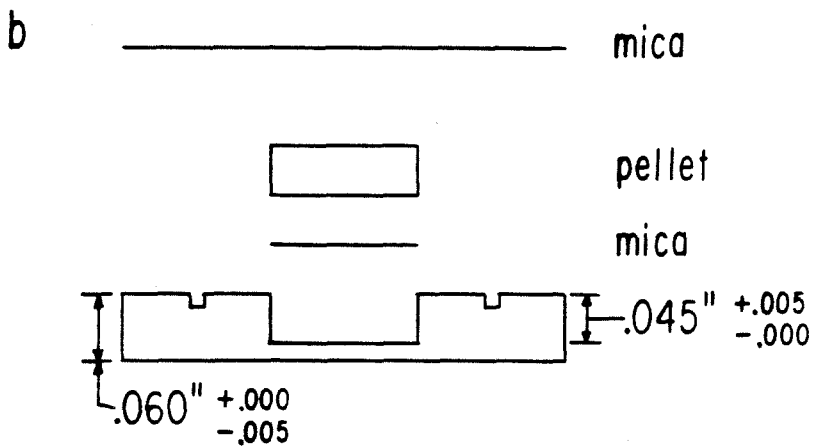
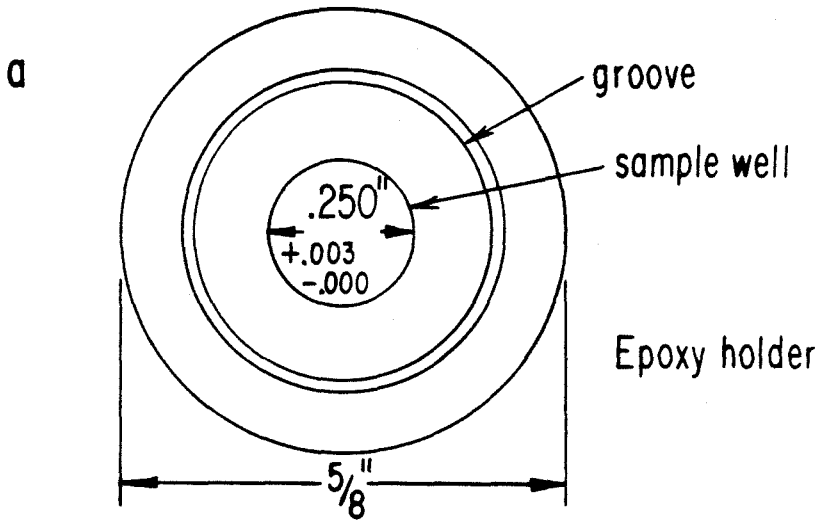
Figure 4 illustrates the individual sample mounts used in our reactor runs (identified as Col MS-1,2,3,4). Most steps in the packaging process were done on a laminar air flow bench. The holders are made from Colpot 3501 epoxy 5/8 inch diameter rods sliced to the desired thickness. Epoxy is used because it is clean (low U and Th), easily machinable, and produces low activation levels. Colpot epoxy is used because it can best withstand the high neutron doses necessitated in our experiments (Shirck, pers. comm.). Because our reactor irradiations were carried out in sealed aluminum cans, epoxy de-gassing limits the total amount of epoxy in a single run to 4-7 grams.

A sample well of highly constrained dimensions is milled into the center of the epoxy disks. Before a pellet sample is loaded into its mount, a freshly cleaved mica, which serves as the detector for the bottom surface of the pellet is dropped into place (Fig. 4 b). For polished sections, a "spring" made of high purity 3/4 mil aluminum foil is placed in the bottom of the sample well (Fig. 4 c). This "spring" is made by loosely folding the foil accordion style. The small bit of flexibility the spring adds could help offset any minor wedging of a sample resulting from the grinding stage of section-making (See Appendix II on sample prep.) In all cases, the sample well depths were chosen so that the top surface of a sample would sit above the holder by about .002 inch. This is done to insure flush contact of the surface against the top detector mica when it is

FIGURE 4

- a. Illustrates the meteorite sample holder used in our reactor irradiations. The holder is made from 5/8" diameter Colpot 3501 epoxy rod.
- b. Illustrates the mounting of a pellet sample. A 1/4" diameter mica is first placed in the bottom of the well to serve as a bottom pellet surface detector. After the pellet sample is loaded, the top detector mica is fastened in place onto the holder with a few dabs of E-7 epoxy placed between the groove and outside edge of the sample holder. This prevents E-7 epoxy running onto the sample surface. Depth of the sample well results in the pellet surface sitting ~.001" above the holder with the bottom detector mica underneath.
- c. Illustrates the mounting of a meteorite section sample. First, a "spring", made by folding a .00075" Al foil accordion-style, is placed into the well. The meteorite sample on its Al post is placed gently on top. Compression occurs only when the top detector mica is fastened into place to insure flush meteorite/mica surface contact. The well depth, allowing for the length of the Al post, permits ~.001" clearance of the meteorite surface above the epoxy holder.

REACTOR SAMPLE MOUNT



epoxied down to the holder. A few dabs of E-7 epoxy (Techkits, N.J.) placed outside the groove machined in the mount holds the mica down. The groove serves as a moat to prevent E-7 epoxy flow onto the sample. E-7 epoxy is used at this point because it cures at room temperature overnight. Also mica removal after the irradiation is no problem with this epoxy. A small weight is placed on top of the assembly during curing. It should be noted that since the aluminum foil "spring" is not a true spring, care is taken not to compress the mica-sample assembly before this last stage of top detector mica fastening.

The CT glass fragments used in the reactor irradiations as standards (~5 mm fragments) are mounted in 5/8 inch diameter Colpot epoxy disks. Both the top and bottom glass surfaces were polished. Detector micas are fastened down directly on the epoxy disk with E-7 epoxy. Weight is placed on top of the mica-sample-holder assemblies and the E-7 allowed to cure at room temperature overnight.

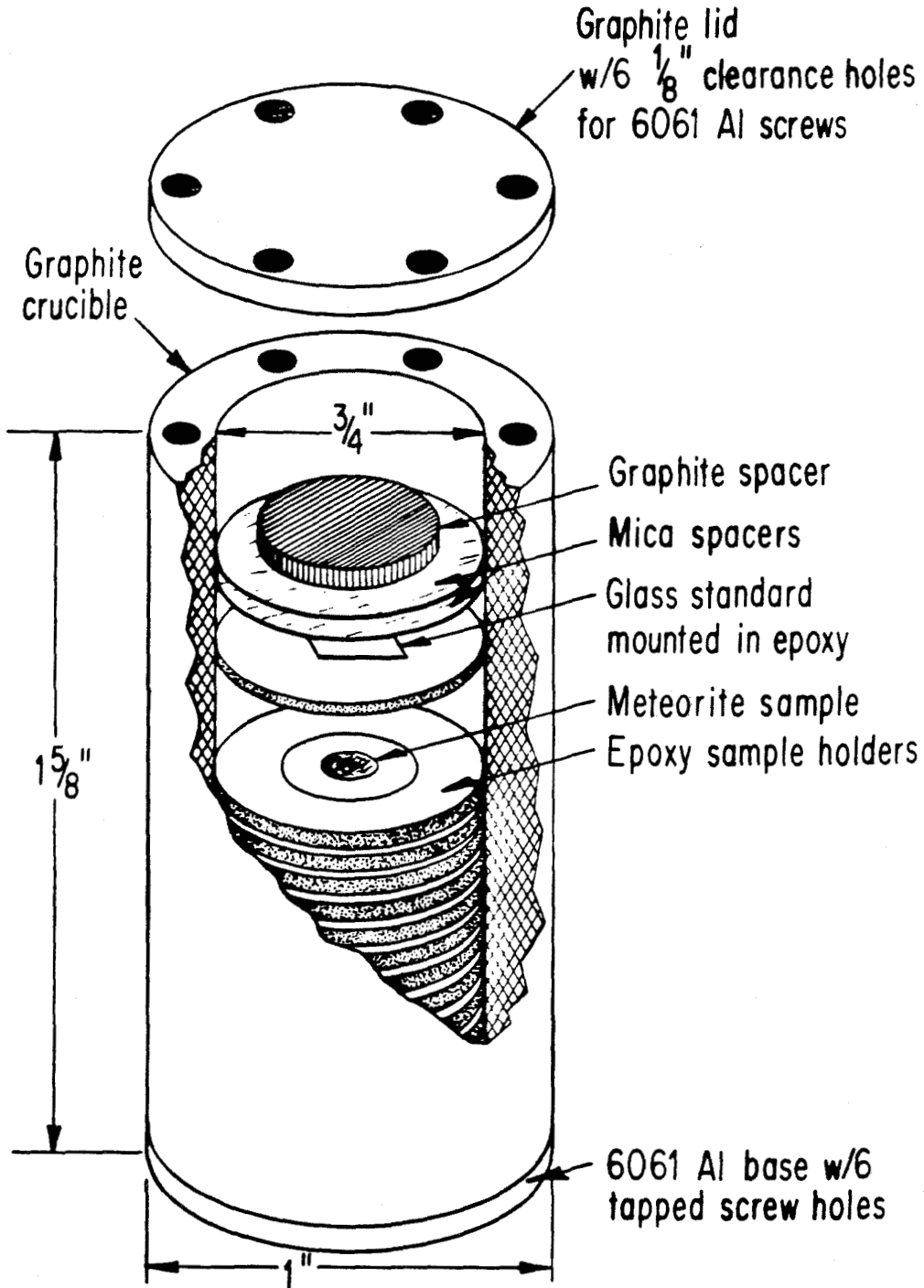
Prior to loading samples and standards into the reactor irradiation crucible the micas are fiducialled. (For the pellets the sample well outline and outer perimeter of the pellet are fiducialled onto the mica).

Figure 5 illustrates the loading of the reactor irradiation graphite crucible. Graphite is used to minimize long-lived induced activity. Samples are stacked one on top of the other with standards typically interspersed after every two. Care must be taken to insure that samples don't get hung up on crucible walls. Small graphite plugs are used to fill up any gaps between the sample/standard

FIGURE 5

Illustrates the stacking of the meteorite samples and standards in the graphite reactor irradiation crucible. Graphite spacers are placed inside the crucible after loading of samples to pack samples in as snugly as possible. The compression provided insures flush sample/mica surface contact. Mica spacers provide cushioning.

REACTOR IRRADIATION CRUCIBLE



stack and the lid of the crucible. Micas can be used to provide some cushioning. The major point is to have the sample stack packed in tightly (i.e., under compression) to insure flush detector mica-sample surface contact for all the samples.

2. Irradiations

Table 4 lists the four reactor meteorite irradiations. Irradiation conditions are essentially the same for all runs with total fluences of $1-2 \times 10^{18} \text{n/cm}^2$. Our graphite crucible is sealed in an aluminum can during the irradiation. Because of the 7 gram epoxy content in Col MS-3, the irradiation was done in three steps with the welded aluminum can opened in between steps to relieve pressure. Readings of 300 mR/h were taken before the can was resealed. To get an idea of the activity levels faced during the analysis phase, readings taken one month after Col MS-3 during unloading of the samples gave 50 mR/hr at the surface of a piece of mica. A CT glass standard without mica was 210 mR/h at the surface. A pellet was 80 mR/h at 1 inch. Three months after the irradiation the sections were unloaded. Readings were ~ 20 mR/h at the sample surface. The predominant long-lived gamma-emitting radioactive nuclei are ^{134}Cs , ^{46}Sc and, for chondritic samples, ^{60}Co .

TABLE 4

LIST OF REACTOR IRRADIATIONS

<u>REACTOR RUN (date)</u>	<u>REFLECTOR POSITION</u>	<u>NOMINAL FLUX (n/cm²-sec)</u>	<u>NOMINAL FLUENCE (n/cm²)</u>
Col MS-1 (7/75)	I-3 (0-4)	5×10^{12}	1×10^{18}
Col MS-2 (6/76)	I-3 (0-4)	5×10^{12}	1.6×10^{18}
Col MS-3 (3/77)			
a. Crucible a	I-3 (26-30)	5×10^{12}	1.7×10^{18}
b. Crucible b	I-3 (0-4)	5×10^{12}	1.7×10^{18}
Col MS-4 (1/79)			
a. Crucible a	I-3 (20-30)	7×10^{12}	1.75×10^{18}
b. Crucible b	J-3 (10-30)	7×10^{12}	1.75×10^{18}

D. Cyclotron Experiments

1. Packaging

Figure 6 illustrates the sample-array holders for the Texas A&M irradiations. They carry seven 1/4 inch diameter samples (at least one of which is a CT standard) and are made of aluminum to aid in heat conduction. Type 6061 aluminum (low Mn,Cu) is used to reduce the induced activity levels. There is a 3/4 inch diameter thin ($\sim .004$ inch) surface layer of Colpot 3501 epoxy over the aluminum through which the individual close-packed sample wells are drilled. This epoxy serves to screen out tracks induced from contaminant Th+U in the aluminum holder from reaching the top detector mica.

Before loading a pellet or 1/4 inch diameter CT glass into their respective sample wells, a bottom detector mica is put into place. Detector micas are $\sim .002$ inch thick. The well depths are machined such that, after loading, the top surface of a sample will sit slightly ($\sim .001$ inch) above the array plate. In some cases a shim mica is necessary below the bottom detector mica to bring the pellet sample up to the desired height. Below the section samples is a foil spring made from 3/4 mil high purity aluminum foil. Typically room is allowed for an 8-fold accordion "spring". Figure 6c shows a cross section of the filled seven sample array. The top detector mica is held in place with E-7 epoxy. A weight is placed across the array plate and top mica, while the epoxy is allowed to cure overnight. The mica is fiducialled before loading the array into the target assembly.

Figure 7 shows the design of the target assembly holding

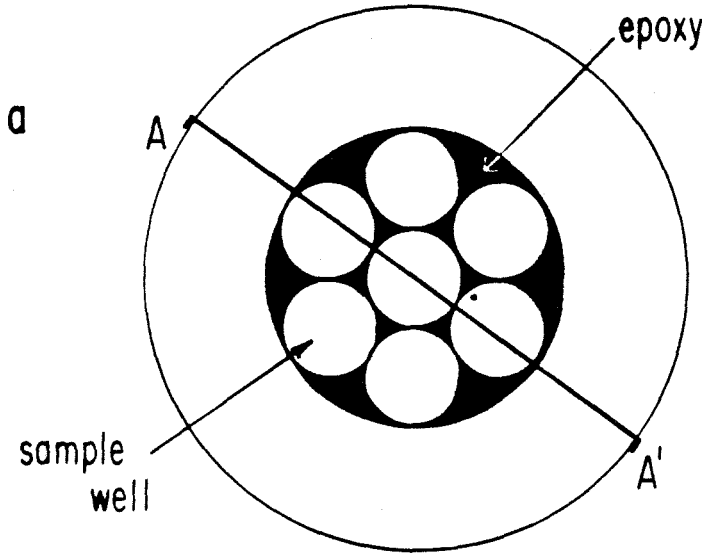
FIGURE 6

a. Illustrates the aluminum seven-sample array holder used in the cyclotron irradiation. Sample wells are machined through a thin surface coating ($\leq .005''$) of Colpot 3501 epoxy.

b. Illustrates sample loading into individual sample wells. Well dimensions chosen to give sample surface clearance of $\sim .001''$ above the holder. First shim micas are placed into the bottom of the well as necessary, followed by the bottom detector mica and the pellet sample. For loading of sections, an Al-foil "spring" is first placed in the bottom of the well to be compressed only after the top detector mica is epoxied into place.

c. Illustrates the fully loaded sample-array holder. The epoxy coating over the $3/4''$ sample area of the holder serves to minimize the top detector mica contact with Al near the area of the samples.

CYCLOTRON SAMPLE HOLDER



(6061)
Aluminum sample-array holder

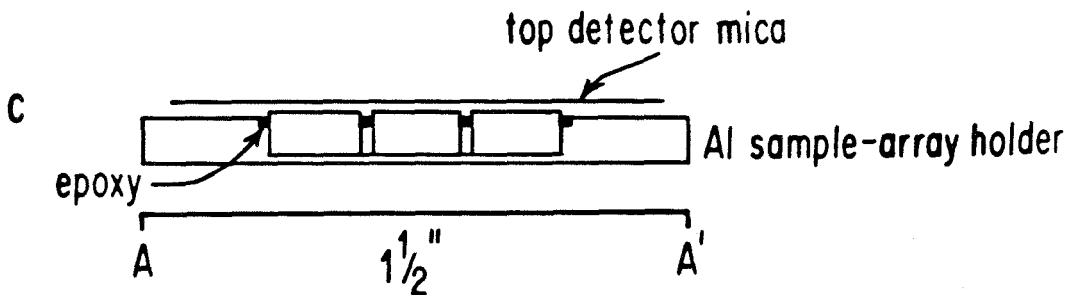
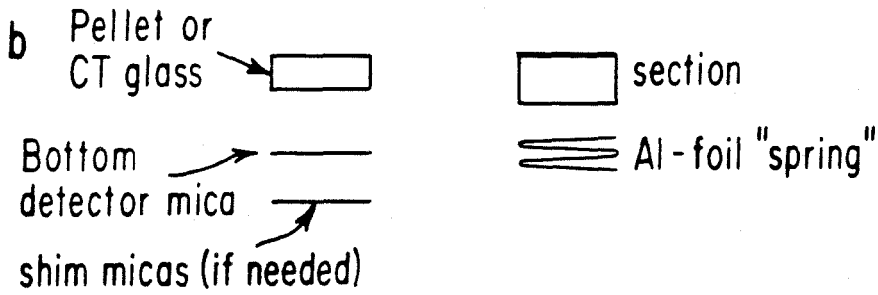
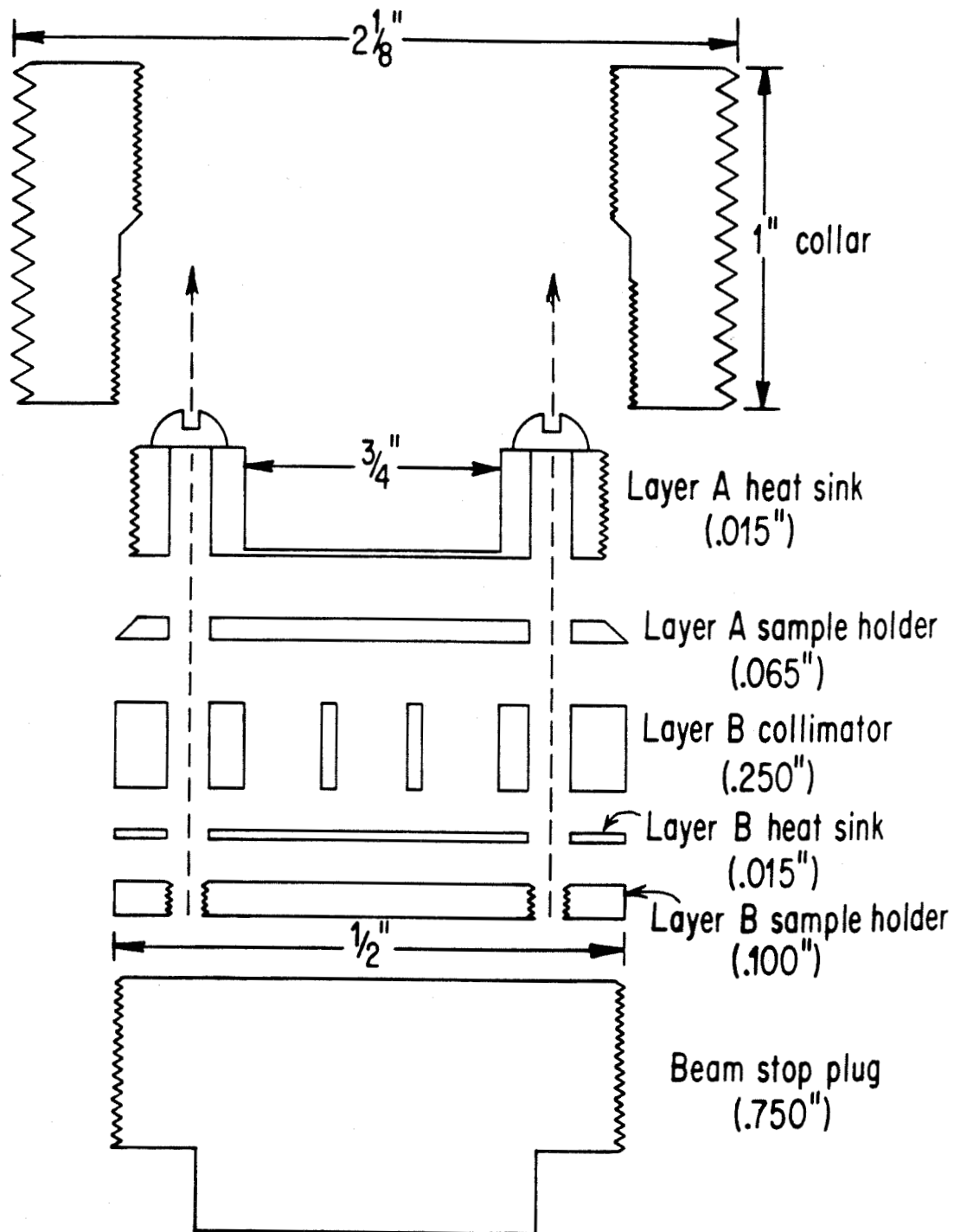


FIGURE 7

This is a diagram of the cyclotron target assembly for the two sample layer target used in TA&M-10. The Layer A (or upstream target layer) and Layer B sample holders are illustrated in Fig. 6(b). These sample holders, their heat sink plates, and collimators form a package which is then screwed into the collar. The beam stop plug screws in separately behind the sample holder package. Tight machining tolerances insure good contact of all the pieces. The outside threads on the collar allow the fully assembled target to be screwed into a water-cooled target holder inside the cyclotron beam line.

CYCLOTRON TARGET ASSEMBLY



two seven-sample arrays (Layers A and B) used for Texas A&M-10. Earlier irradiation targets were similar. Two target layers are permitted because the fission cross sections for both U and Th are essentially energy independent for proton energies above ~20 MeV (see Fig. 3 from Khodai-Joopari[1966] in Basic Physics section). With a dE/dx of ~ 0.1 MeV/.001" for 35 MeV protons, Layer A in TA&M-10 sees a beam of energy 32.5 MeV while Layer B sees a beam of 25.6 MeV. In any case, standards are included in both layers.

The entire assembly is machined under tight tolerances because good thermal contact is essential for the survival of samples and detectors. The .015 inch heat sink plates, placed flush against the top detector micas, aid in detector survival. To minimize beam damage to epoxy associated with the section-samples a collimator was machined to prohibit the beam hitting anything but meteorite. If the meteorite fills the entire 1/4 inch area of its aluminum mounting post, the need for a collimator is eliminated (see Appendix II on sample preparation). No layer A collimators were used to insure full irradiation of all Layer B samples. Thus, when pellets and sections were irradiated in the same target, pellets were always put on the top layer.

The Layer A heat sink, Layer A sample array, Layer B collimator, Layer B heat sink and Layer B sample array form a tight package which is screwed into the 2-1/8 inch O.D. aluminum collar. A beam stop plug fits in last. The outside threads on the collar allow the entire target assembly to be screwed into a water-cooled target holder at the cyclotron.

2. Irradiation Requirements

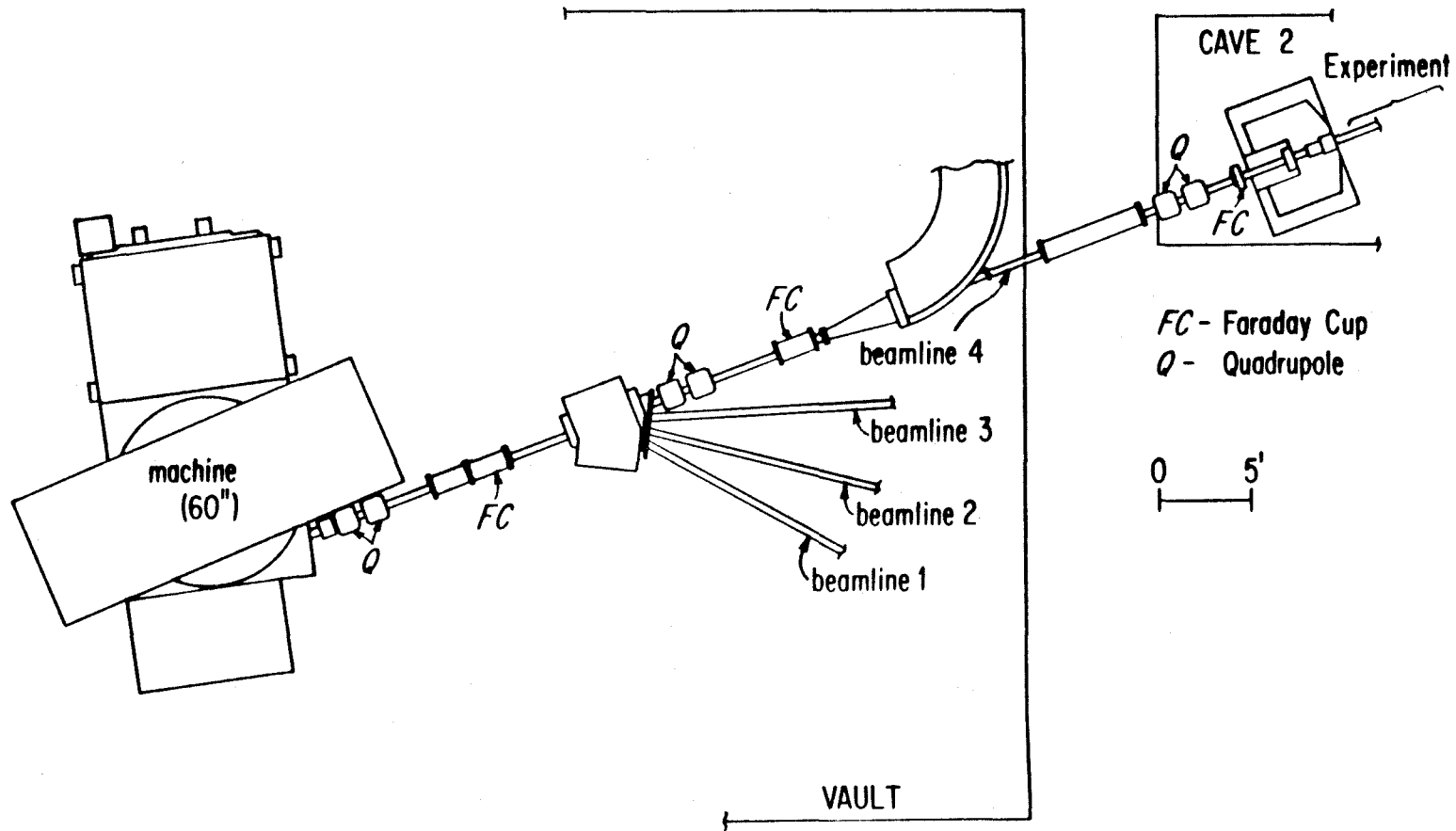
The following calculations are included to illustrate the high dose requirements necessary to obtain statistically useful measurements. The track production rates measured in the TA&M-6 40 MeV proton run will be used. Assuming ~50 ppb Th+U, to obtain track densities from the pellet samples of $\sim 10^5/\text{cm}^2$ (a comfortable 10 tracks per field of view at 1250x magnification) an integrated current of $\sim 90 \mu\text{ah}$ over our 3/4 inch target area is needed ($1 \mu\text{ah} = 2.25 \times 10^{16}$ protons). This is equal to $\sim 30 \mu\text{ah}/\text{cm}^2$ fluence. Setting a "minimum" acceptable criterion of 500 tracks over a 5 mm diameter pellet requires $\sim 1 \mu\text{ah}/\text{cm}^2$. An inclusion irradiation which yields 100 tracks from a 100μ grain containing 250 ppb Th+U needs $63 \mu\text{ah}/\text{cm}^2$. The "minimum" acceptable pellet dose value of $1 \mu\text{ah}/\text{cm}^2$ would give 100 tracks over a 1 mm inclusion containing 250 ppb Th+U. Doses of 1-10 $\mu\text{ah}/\text{cm}^2$ were obtained in the present experiments.

3. On-line Experimental Set-Up

Figure 8 illustrates the basic layout of the cyclotron facility. Most of our experiments were set up in Cave 2. The charged particle beam is first focussed ($\sim 1/8$ inch diameter) and centered to send as much current as possible down line to our experimental set-up. Typically only 1/3 to 1/6 of the internal machine current is extracted for down line use. Of this extracted beam only about 1/2 makes it all the way down to our target position.

FIGURE 8

This schematic of the TA&M cyclotron facility shows the relationship of the machine with our general experimental area. Quadrupole and Faraday cup positions are noted along the beam line upstream of our experiment.



FC - Faraday Cup
 Q - Quadrupole

0 5'

Figure 9 is a schematic of our on-line experiment configuration. Alignment is crucial and much effort was expended with the aid of a transit to insure proper alignment. As discussed in Appendix IV an aluminum scattering foil is placed on a water-cooled retractable probe upstream from the target to disperse the beam. The resultant beam pattern is gaussian in shape. As discussed in Appendix IV on beam scattering, beam homogenization over the target is at the expense of target current. We aimed for ~30-50% beam homogeneity at the target position from center to edge of our 3/4 inch diameter sample arrays, thereby losing no more than half the available on-target beam.

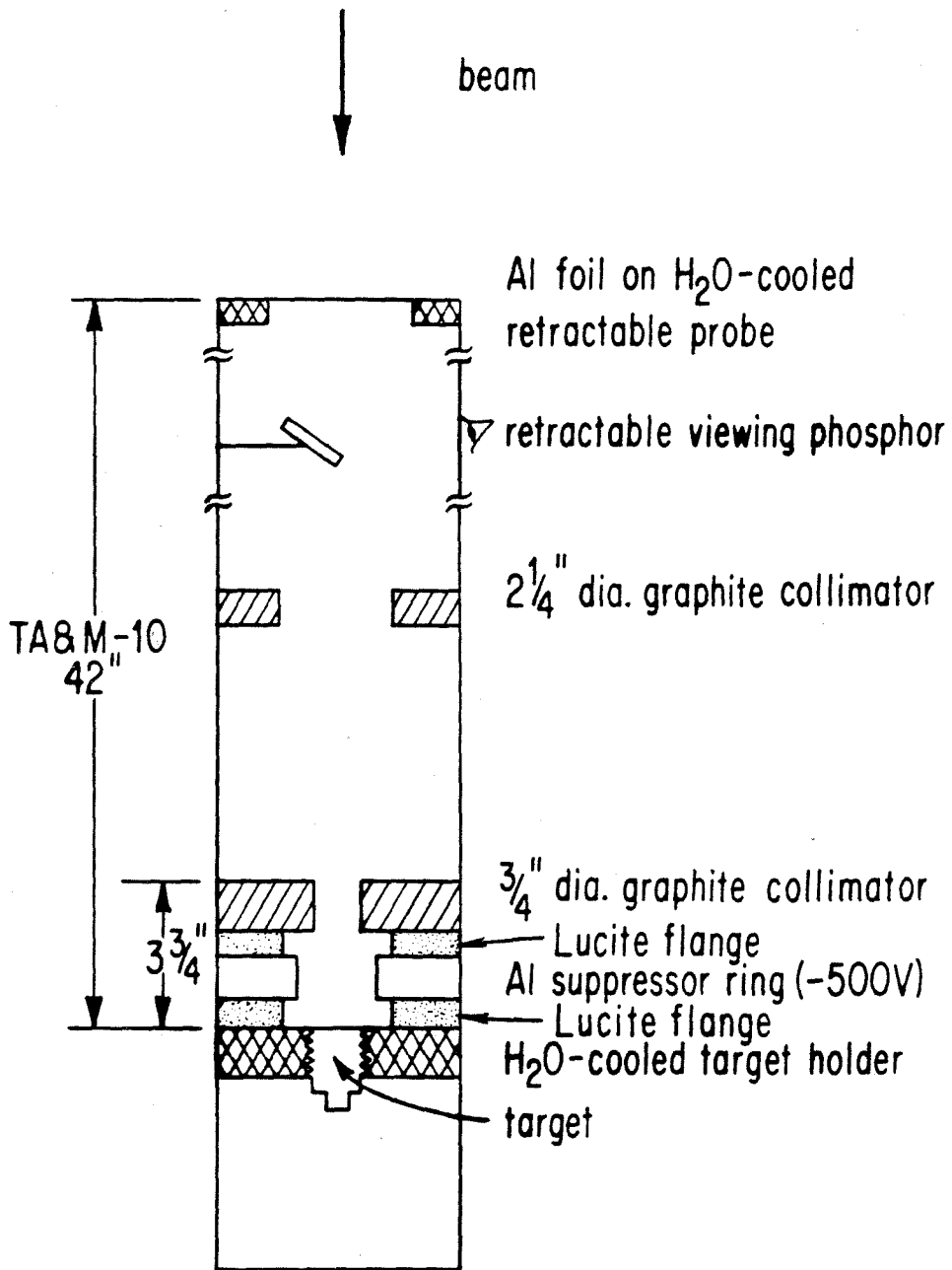
Downstream from the beam dispersing foil is a retractable phosphorescent plate. When swung into the beam, the induced phosphorescence outlines the beam shape and can be viewed from a side port in the beam line. Since the dispersing foil is also on a retractable probe, viewing of the beam with or without the foil is possible. The phosphor is useful during the initial stages of focussing and centering the beam. It can also be used to check for beam drift as the experiment progresses. Downstream from the viewing phosphor is a 2-1/4 inch graphite collimator. It serves to cut down on extraneous beam going downstream that would cause additional unwanted induced activity near the target area. As with the foil, beam current can be read on this collimator, which aids in checking for gross alignment changes.

Another graphite collimator sits 3-3/4 inches upstream from the target. This collimator stops all but the necessary 3/4 inch center area of the beam from reaching the target.

FIGURE 9

This is an on-line schematic of our cyclotron experiment. Breaks in the drawing indicate where distances are not drawn to scale. Most upstream is an Al (beam scattering) foil placed on a water-cooled retractable probe. A retractable viewing phosphor with side beam port aids in beam focussing and centering. Further downstream is a 2-1/4 inch diameter graphite collimator which cuts down on extraneous beam from reaching the target. The last 3-3/4 inches required careful attention to alignment and were bolted together to keep as a reusable package. A 3/4 inch diameter graphite collimator is isolated electrically by a lucite flange from the Al suppressor ring (described in text). A -500 V bias applied to the suppressor ring minimizes electron interference with target current readings. Last in the beam line is the target assembly illustrated in Fig. (7) which has been screwed into a watercooled holder. The beam line is sealed off to allow the experiment to be run in vacuum. Use of a lucite end plate aids in checking alignment.

CYCLOTRON ON-LINE SCHEMATIC



Current readings on target can often prove misleading due to knock-off electrons. For example, electrons can be knocked into the beam (from edge of a collimator) upstream from the target. Also, electrons are knocked out of the target by the impinging particle beam which results in an apparent positive contribution to the target current readings. To suppress the electrons an aluminum ring was placed just upstream from the target and a bias voltage applied. This negative bias serves to keep electrons in the target while preventing electrons knocked into the beam upstream from reaching the target. The voltage used was the minimum necessary to reach a plateau in the on-target current readings.

As mentioned earlier the target is screwed into a watercooled target holder. A lucite flange sealing the beam line behind the target allows viewing access for alignment verification.

4. Irradiations

Table 5 lists information about the Texas A&M irradiations which contained meteorite samples. Five previous irradiations (untabulated) were basically developmental. Continual adjustments were made in the technique through Texas A&M-10.

Although a high intensity beam was available, initial runs with 100 MeV alpha beams proved unacceptable because the interaction track backgrounds could not be handled satisfactorily (see Appendix VI). Preliminary irradiations with 40 MeV protons and 50 MeV deuterons were quite promising on this score, however. The first meteorite run, TA&M-6, used the 40 MeV proton beam. Because of limitations

TABLE 5

LIST OF CYCLOTRON IRRADIATIONS

<u>RUN</u> (<u>date</u>)	<u>BEAM</u>	<u>METEORITE TARGETS</u>	<u>CURRENT ON TARGET</u>	<u>INTEGRATED CURRENT</u>	<u>FLUENCE</u>
1. TA+M-6 (10/16/75)	40 MeVp	a. Incl I	1.7-2 μ a	8.4 μ ah	$6.6 \times 10^{16}/\text{cm}^2$ (2.9 μ ah/cm ²)
		b. Pellet I	2 μ a	10 μ ah	$7.9 \times 10^{16}/\text{cm}^2$ (3.5 μ ah/cm ²)
		c. { Pellet II-Layer A Incl II-Layer B	2.2-2.5 μ a	3 μ ah	$2.4 \times 10^{16}/\text{cm}^2$ (1.1 μ ah/cm ²)
2. TA+M-7 (12/16/75)	50 MeVd	a. Meteorite (1-layer)	4 μ a	2.1 μ ah	$0.92 \times 10^{16}/\text{cm}^2$ (0.41 μ ah/cm ²)
3. TA+M-8 (8/9/76)	40 MeVp	a. { Pellet -Layer A Pellet -Layer B	1.5 μ a	5.5 μ ah	$4.3 \times 10^{16}/\text{cm}^2$ (1.9 μ ah/cm ²)
4. TA+M-9 (11/8/76)	50 MeVd	a. { Pellet -Layer A Incl. -Layer B	2.6-3.2 μ a	23 μ ah	$1.8 \times 10^{17}/\text{cm}^2$ (7.9 μ ah/cm ²)
5. TA+M-10 (12/8/76)	35 MeVp	a. { Met. -Layer A Incl. -Layer B	2 μ a	38 μ ah	$2 \times 10^{17}/\text{cm}^2$ (10 μ ah/cm ²)

in available cyclotron time and the low (~2 micro-amp) proton currents, 50 MeV deuterons appeared a better alternative. Deuteron beam currents were routinely extracted a factor of 2-3 higher than proton beams. Also, the possibility of time sharing with the major cyclotron users who used only the 50 MeV deuteron beam presented less restrictions on time. Mica test runs with deuteron doses up to $9 \times 10^{16}/\text{cm}^2$ indicated the interaction track interference could be handled. TA&M-7 was run in the vault area of the cyclotron as opposed to the end of a beam line but had to be aborted because of high induced activities (a measurement taken after the beam had been on for 1/2 hour read 50 R/h several feet from the target). Poor cyclotron scheduling required that our target be removed immediately to make room for the following experiment. Another deuteron run was tried in TA&M-9 after low proton beam currents were again obtained in TA&M-8. TA&M-9 was run in vacuum at the end of a beam line. The current was dropped down to ~3 micro-amp when pressure problems due to beam heating were encountered. Because of these problems it was necessary to irradiate in cycles with the beam on for 15 minutes and then off for 3 to allow the beam line to pump out. During the run a ceiling monitor 8 feet above the target read 100 R/h gamma-activity. Six hours after the irradiation a target reading of 30 R/h was taken. Eighteen days after this high dose deuteron irradiation the target was disassembled. The Layer B sample array with samples and micas in place measured 20 mR/h at 2 inches. However, the severe irradiation damage sustained by the mica at $1.8 \times 10^{17}/\text{cm}^2$ dose ended further consideration of deuteron irradiations. This was somewhat surprising

in light of an earlier deuteron mica irradiation where the mica easily handled a $4 \times 10^{16}/\text{cm}^2$ dose. Whether this was a unique damage threshold for the particular mica used (Div. Coll. 2969), an error in current measurements, or a general phenomenon encountered at this deuteron dosage is unclear.

Development of a higher current 35 MeV proton beam provided us with an alternative to deuteron bombardments. Using a different muscovite mica (Indian-Washington U.), which, prior to usage, underwent a 15 hour baking at 250°C , we had a highly successful TA&M-10 meteorite run. The dose reached $2 \times 10^{17}/\text{cm}^2$. Top detector micas for both sample layers could be annealed for interaction track suppression and fission tracks counted.

An ominous note, however, was presented in the almost total loss of track information in pellet bottom detector micas due to severe thermal or irradiation damage. From the beginning of these experiments, thermal problems-- mica annealing, sample and mica survivability-- were recognized as incredible challenges to contend with in developing a charged particle induced fission track technique.

During the TA&M-10 run, the ceiling monitor read 10 R/h. One month after the run our target assembly read 20 mR/h at six inches. Three months after the irradiation the Layer A detector mica was ~ 10 mR/h near the surface.

E. Analysis

In this section the step-by-step process of analyzing the detector micas and applying the necessary corrections to obtain [Th+U] and [U] concentrations for a sample is described.

Prior to the irradiation, mica is epoxied flush against the sample surface (see sections on reactor and cyclotron irradiation packaging). Using a fine needle, the sample is outlined and an irregular grid pattern is scratched onto the non-detector side of the mica. Fiducialling is important for the polished section samples in relating positions on a mica to locations on a sample surface. The fiducialling is done under a stereomicroscope to produce a grid system that will be most advantageous in locating interesting features. Post-irradiation, but prior to removal of the mica detector, the sample is photographed (usually at 40x magnification) through the fiducialled mica. Although this overlay photograph is not of high quality, it does provide an absolute, permanent record to relating the mica grid system to the sample.

All track counts were done using a Leitz Ortholux microscope with precision x-y stage.

1. Reactor - [U]

a. Mica etch and track counts

After the post-irradiation fiducial photography is completed, the micas are removed and etched. Etching is done at room temperature in 48% HF. Because track densities are $\sim 1.5 \times 10^7 / \text{cm}^2$ for the CT standards, these micas are etched only 16 minutes. The micas are

then lightly gold coated in an argon-sputter coater and counted in reflected light at 1250x magnification. At these densities counting in transmitted light is difficult because of a high degree of overlap of the tracks. In reflected light only a black dot is seen corresponding to the point of entry of the fission fragment into the mica, and much better resolution is possible.

Track densities of CC pellet samples are $\sim 4 \times 10^5 / \text{cm}^2$. To ease track scanning at these low track densities, pellet detector micas were etched either 32 or 64 minutes. The 32 minute etched samples were counted at 1250x in transmitted light. The 64 minute etched micas were counted at 625x in transmitted light. Counting in reflected light at these densities was found to be imprecise. Pellet micas were typically scanned over a $4 \times 10^{-3} \text{ cm}^2$ area near the center of the sample.

All section sample detector micas were etched 16 minutes with track counts done at 1250x. Transmitted light counts were used except where "star" track densities were so high that individual track identifications were difficult, making reflected light counts necessary. A track star is when fission tracks emanate radially out from a single point, indicating the presence of a point or highly localized source.

b. Track counting efficiency factor (SMI)

In a simplistic sense, the ratio of the measured track density of a sample to that of a standard should equal the ratio of their uranium concentrations. This assumes tracks are counted in a sample

and standard mica with equal efficiency. However, the ability of an observer to identify and count a feature as a track may depend on the actual counting conditions--i.e., the magnitude of the track density, mica etch time, microscope magnification, whether transmitted or reflected light was used. In our experiment, relating pellet track densities to CT standard track densities presented the greatest dichotomy in counting conditions. The $2 \times 10^7/\text{cm}^2$ standard track densities necessitate short etch times to avoid track overlap and counting under reflected light. On the other hand the $4 \times 10^5/\text{cm}^2$ meteorite sample track densities are most easily counted with long etch times and transmitted light.

An additional complication in directly relating standard track density measurements to pellet track densities results from the use of long etch times for the pellet micas. Long etch times (32-64 minutes) revealed a high density of fast neutron recoil tracks. These tracks result from fast neutron collisions with heavy nuclides in the target material, a fraction of which recoil into the mica to form short (~1.5 micron) tracks. The tracks due to these low specific ionization recoils (compared to fission fragments) were suppressed at low etch times (≤ 16 minutes). Unfortunately, all the pellet micas were etched longer, as discussed earlier, in the naive hope of easing the track scanning.

As a result of the standard/meteorite track density differences and the fast neutron recoil tracks in the etched meteorite micas, we experimentally determined a relative track counting efficiency factor (SMI) to be applied to the pellet data (see Appendix III). This SMI

factor is determined from a set of calibration micas with accurately known relative fission track densities close to those observed in our standards and meteorite pellet samples. A strict track length counting criterion was established to handle the recoil track problem. It is then the observed pellet/standard track density ratios divided by the SMI factor which equals the ratio of uranium concentrations:

$$[\rho(\text{sample})/\rho(\text{standard})] \times \text{SMI}^{-1} = \text{U}(\text{sample})/\text{U}(\text{standard}).$$

The SMI factor applied to the 32 minute etch pellet micas equals $1.15_{\pm 0.07}$, while that for the 64 minute etched pellet micas equals $1.08_{\pm 0.07}$; i.e., the sample/standard track density ratio gives high apparent U sample concentrations for the etch conditions used.

c. Dosimetry

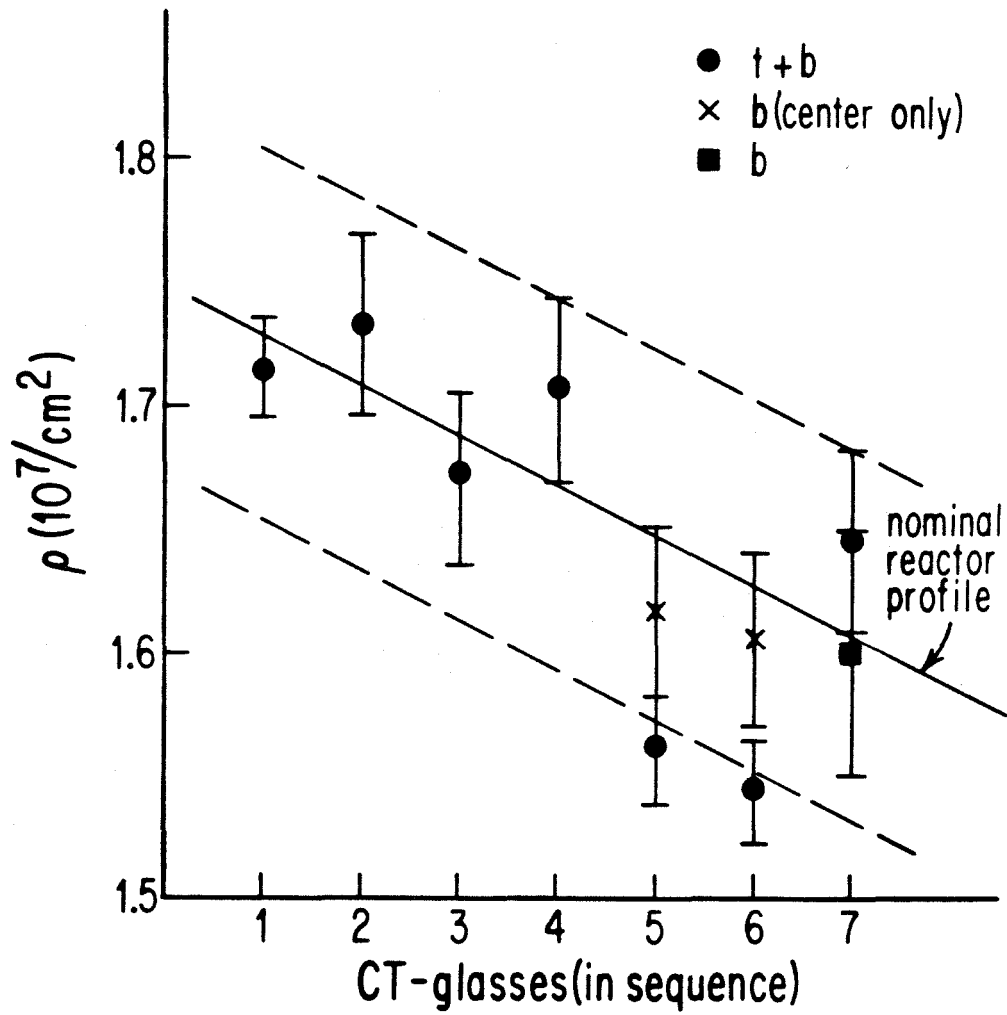
The neutron flux profile along the long axis of the irradiation crucible is obtained from the track density measurements on the CT standards interspersed along the crucible. Typically there is a standard located every 0.18 inch or less in the sample stack. A smooth curve drawn between the track density vs. location points for the CT glasses provides a flux corrected standard track density value for comparison with a sample at any location in the crucible. The CT glass track counts in Col MS-1 and Col MS-2 give monotonic approximately linear profiles from which interpolations were made to correspond with positions of the meteorite samples.

More standards were included in Col MS-3 and these data provide the best information on the flux profile (see Fig. 10). As the diagram also shows, 4% differences (~order of the error of an

FIGURE 10

Track densities are plotted for the CT-glasses irradiated in the Col MS-3-A reactor crucible in the order of their stacking sequence (see Fig. 5). Points labelled t+b indicate the average track density of a glass obtained by counting both its top and bottom surface detector micas. The points labelled b are track counts for the bottom surface only. Points labelled b(center only) are for track counts taken on the bottom detector mica within a single $100\mu \times 100\mu$ field of view at the center of the sample. Typically, scanning is from partial fields of view over a $\sim 300\mu \times 300\mu$ central area. The best fit line to the monotonic nominal reactor profile is plotted for reference. The fluence profile used in our Col MS-3-A analyses is this best fit line with errors which incorporate the scatter in actual CT track measurements (indicated by dashed lines).

COL MS-3 (A)



individual measurement) in the measured track density of a CT glass can be obtained by varying the location on the glass where a track count is taken perhaps indicative of the magnitude of glass homogeneity. To determine a flux profile curve to apply to our meteorite sample analyses, a best fit line was drawn through the CT data points with slope chosen to be equal to the reactor published nominal thermal neutron flux profile at the position of our irradiation. Meteorite track densities are then related to the interpolated standard track density at the location of the sample using this best fit line. The dashed lines in Fig. 10 which bracket the actual CT glass measurements determined the error assigned to this standard profile curve.

d. Range

The measured track density for a sample is directly proportional to the product of the U (or Th+U for cyclotron irradiations) concentration of a sample and the range of a fission fragment through the sample. Thus it is necessary to investigate the relative fission fragment ranges for our CT standard glass and meteoritic material. A good approximation for comparing ranges through different material of atomic weight A is Bragg's Rule: $R \propto A^{0.5}$ for R in g/cm². Calculations using heavy ion range tables for nuclei in the region of most probable fission fragment masses (A= 96, 140) show that the approximation $R \propto Z^{0.5}$ where Z is the atomic number of the absorber gives relative ranges to better than ~5%, typically 1-2%. For a material made up of several elements each of weight fraction w_1 , the total range is calculated with the equation: $(1/R_T) = (w_1/R_1) + (w_2/R_2) + \dots$. Applying the $Z^{0.5}$ and $1/R_T$ equations to typical bulk carbonaceous chondrite compositions (Mason, 1971 cites Wiik, 1956) and the analysis of our standard microscope slide glass, we can derive relative range values. The ratio of the range in the meteorite to the range in the standard CT glass is calculated to be 0.99 for C1 (based on Orgueil composition), 1.02-1.08 for C2 (low value is Mighei, high value is Mokoia), and ~1.07 for C3 chondrites (based on Allende composition, Mason & Martin [1977]). The range in C2 values comes from the differences in bulk composition (largest difference is in bulk water content) for the CM2 Mighei (13 wgt.% water) and the CV2 Mokoia (2 wgt.% water). Since the ratios of ranges tabulated in Table 6 are calculated from ranges in units of mg/cm², the density of the sample does not enter in.

TABLE 6
SUMMARY OF RELATIVE RANGE CALCULATIONS

	$\frac{R}{R_{CT}}^*$
CT glass	1.000
NBS nominal	1.011
^a CV2 (Mokoia)	1.082
^a CM2 (Mighei)	1.021
^a C1 (Orgueil)	0.985 → (1.086, w/o water)
^b Perovskite	1.157
^b Spinel	0.984
^c Melilite	1.061
^c Clinopyroxene	1.036
^d Nepheline	0.993
Olivine [Fo]	0.997
^e Average Type A	1.047
^e Average Type B	1.041
^e Average Type I	1.033
^f Bulk Allende (CV3)	1.067

a. Mason (1971)

b. Allen et al. (1978)

c. Grossman (1975)

d. Grossman and Steele (1976)

e. Wark and Lovering (1978)

f. Mason and Martin (1977)

* Range relative to CT standard glass

It would appear at most an 8% correction could be made in the direction of lowering corresponding meteorite U and [Th+U] values. These maximum corrections are typically within quoted errors in our measurements. None of the data presented in the following sections are range corrected. It should be emphasized that this correction in no way affects our Th/U ratio measurements.

The [U] and [Th+U] values presented for the Allende sections are also not range corrected. Using typical Allende inclusion mineral compositions obtained from Grossman (1975), Grossman & Steele (1976), and Allen et al. (1978), range calculations tabulated in Table 6 indicate less than 4% difference between the range in the CT glass and fission fragment ranges in nepheline, olivine, pyroxene, and Mg-spinel. The range for gehlinite with 3.63 weight % Mg is ~6% higher than the CT glass, while the range in perovskite is 16% higher. As will be discussed in the Allende section results, the fine-grained nature of the major U,Th rich phases makes our concentration measurements lower limits. It is not the quantitative U and Th+U concentrations that this experiment is primarily after, but the Th+U/U (hence Th/U) ratios. Taking a ratio totally circumvents this range problem.

For the record, range calculations were done using Wark & Lovering (1978) composition data for average Allende Type A, Type B, and Type I inclusions. Calculated ranges for these inclusions differed from the CT glass range by less than 5%.

2. Cyclotron - (Th+U)

a. Interaction tracks and pre-etch mica annealing

Background due to interaction tracks has proved a difficult barrier in the use of high dose charged particle irradiations. As the charged particle beam passes through the mica detector, spallation and scattering reactions occur with the atoms in the mica. In particular, collisions with heavy trace elements in the mica can leave the resultant recoil heavy ions in a charge-velocity state above the critical ionization threshold for mica. Short tracks, typically less than 1.5 microns long, result and can literally saturate the mica surface for the fluences used. For an idea of the magnitude of this effect, our highest dose proton run gave typical bulk meteorite fission track densities of $5 \times 10^4 / \text{cm}^2$. Based on previous developmental proton irradiations the interaction track density expected at this dose would be $4 \times 10^9 / \text{cm}^2$. Heavier projectiles would produce larger interaction track densities.

The full range of a fission fragment is approximately 10 microns. However, for a thick source the mica will record a length spectrum of fission fragments from the full 10 microns down to zero microns as a fission fragment barely nudges itself into the mica from a 10 micron path length through the meteorite sample. For track counting to be accomplished the interaction track background must be suppressed while at the same time not losing a large fraction of the fission track spectrum.

As discussed in Appendix VI, mild annealing can be used to preferentially anneal out short interaction tracks

while still leaving a significant fraction of the fission track population. For the required high dose irradiations only the 35-40 MeV proton beam proved suitable for mica thermal and irradiation-damage survivability. Details of the interaction track production rates and the annealing technique are discussed in Appendix VI. Irradiation damage affects the fission track registration efficiency of a mica as well. An experiment, described in Appendix VI, compared the track registration properties of mica receiving a 40 MeV dose of $\sim 7 \times 10^{16}/\text{cm}^2$ with areas that saw no beam. The irradiated mica had at best 80% of the fission track registration efficiency of unirradiated mica. Annealing experiments described in Appendix VI calibrated fission track retention for cyclotron-irradiated micas against mica with no irradiation damage. Retention factors so obtained had to be corrected for the difference in mica fission track registration efficiencies to derive the proper retention factor for fission tracks obtained during cyclotron bombardment. Following the experiments described in Appendix VI, all cyclotron detector micas in our meteorite irradiations were annealed together at 425°C for two hours prior to etching. Under these conditions the interaction track background is greatly subdued while >80% of the fission tracks are retained.

b. Mica etch and track counts

All micas in a cyclotron run are etched either 12 or 16 minutes in 48% HF at room temperature. Because the relative (Th+U) contents are closer, the difference between the CT standard and bulk pellet sample track densities is a factor of three less than encountered in

the reactor irradiations. With typical track densities $<10^7/\text{cm}^2$ for all samples and standards, counting was done at 1250x using transmitted light.

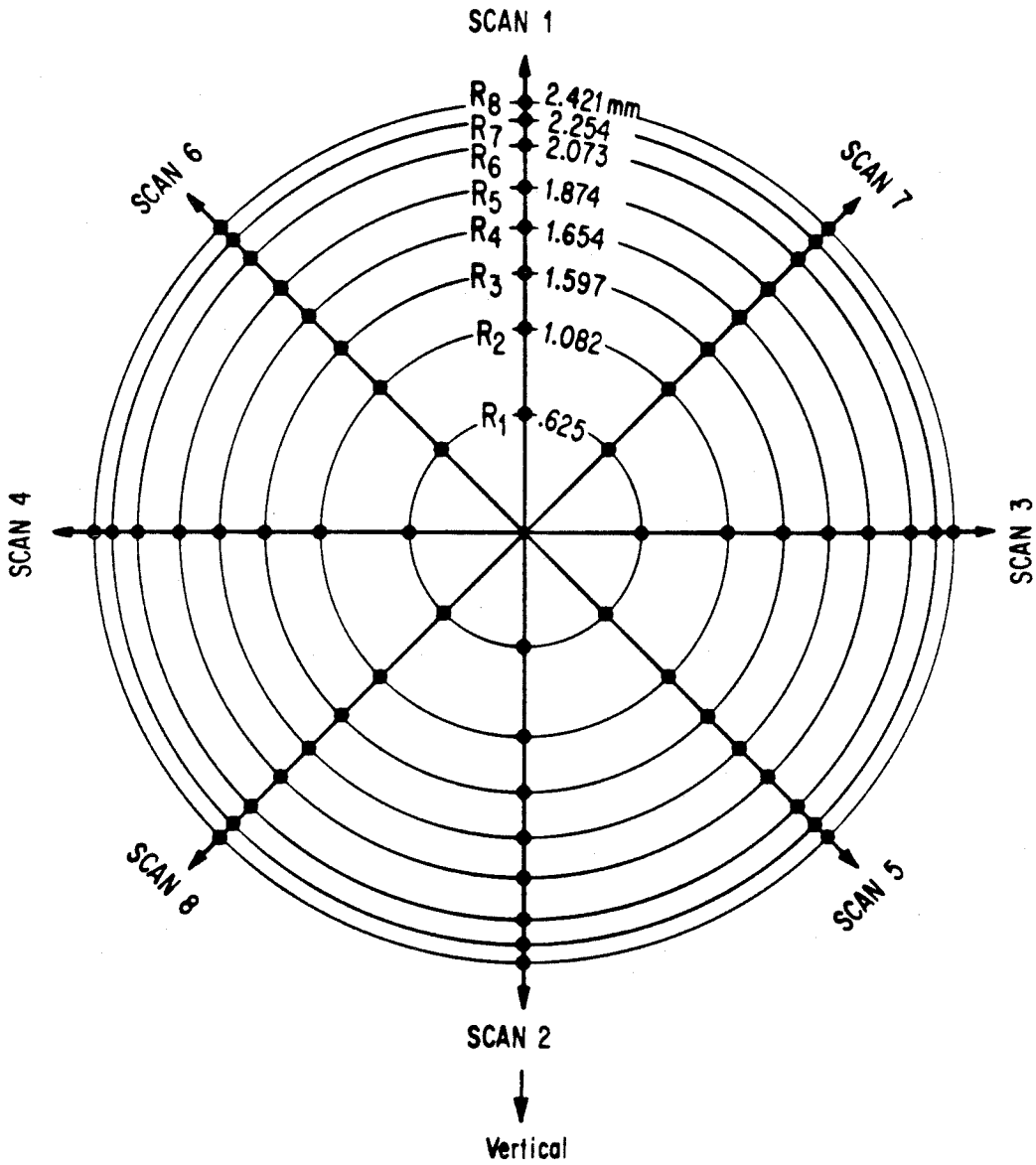
Unlike the reactor irradiations where dose variations across an individual sample are insignificant, dose gradients do exist over a sample in a cyclotron run. A track scan pattern for pellet samples and standards was devised to representatively cover the surface area of the 5mm sample and to provide ~3% counting statistics (~1000 tracks). In this way dose measurements over the total sample (which require much less position control) can be appropriately applied to the scan pattern track measurements without having to count every field of view over the sample. The 5 mm sample area is divided into a concentric series of eight equal area annuli (see Fig. 11). Track counts are taken about the midpoints of these annuli along eight scan directions (45° apart) radiating from the center of the sample. Typically five symmetrically placed fields of view ($\sim.05 \text{ mm}^2$) are counted at the midpoints of each of these annuli lying along the chosen radial scan directions.

As will be described in the next section, we have the ability to map the dose distribution across an entire 1/4 inch sample position. From these dose maps readings can be selected that correspond to the positions of pellet track scan patterns. It turns out that even for dose variations as high as a factor of three across a 1/4 inch surface there is at most a 3% difference in integrated dose obtained by taking readings over the track scan pattern as opposed to averaging readings over the entire 1/4 inch area. This supports the initial

FIGURE 11

Illustrates the track scan pattern used on micas for pellet and glass samples in our cyclotron analyses. Vertical refers to the vertical direction during target irradiation. The 5 mm pellet area is divided into 8 concentric equal area annuli. Starting from the center of the sample, track densities are measured at annuli midpoints along the eight radial scan directions as shown.

PELLET SAMPLE SCAN PATTERN



contention that the scan pattern permits representative sampling.

c. Dosimetry

The cyclotron beam induced beta-activity in the Layer A top detector micas was exploited to make the necessary relative dose measurements. Placed in contact with a photo-emulsion plate the mica provides an image of the beam distribution. A densitometer designed for optical emission spectrograph plates permitted $500\mu \times 40\mu$ spatial resolution. With the internal coordinate control provided by three .015" holes drilled through the outer perimeter of the mica, we were able to make detailed dosimetry maps that could be directly related to positions on the mica and hence to a sample. The slow but fruitful development of this technique is described in detail in Appendix V. Photoemulsion dosimetry permits high spatial resolution measurements to be made without destroying the integrity of the mica. The densitometer measures %Transmission of light through the plate. Under experimentally determined exposure conditions, $\log(100/\% \text{transmission}) \equiv T \propto \text{proton fluence}$. Correlating track density gradients with gradients in T gives a useful internal consistency check.

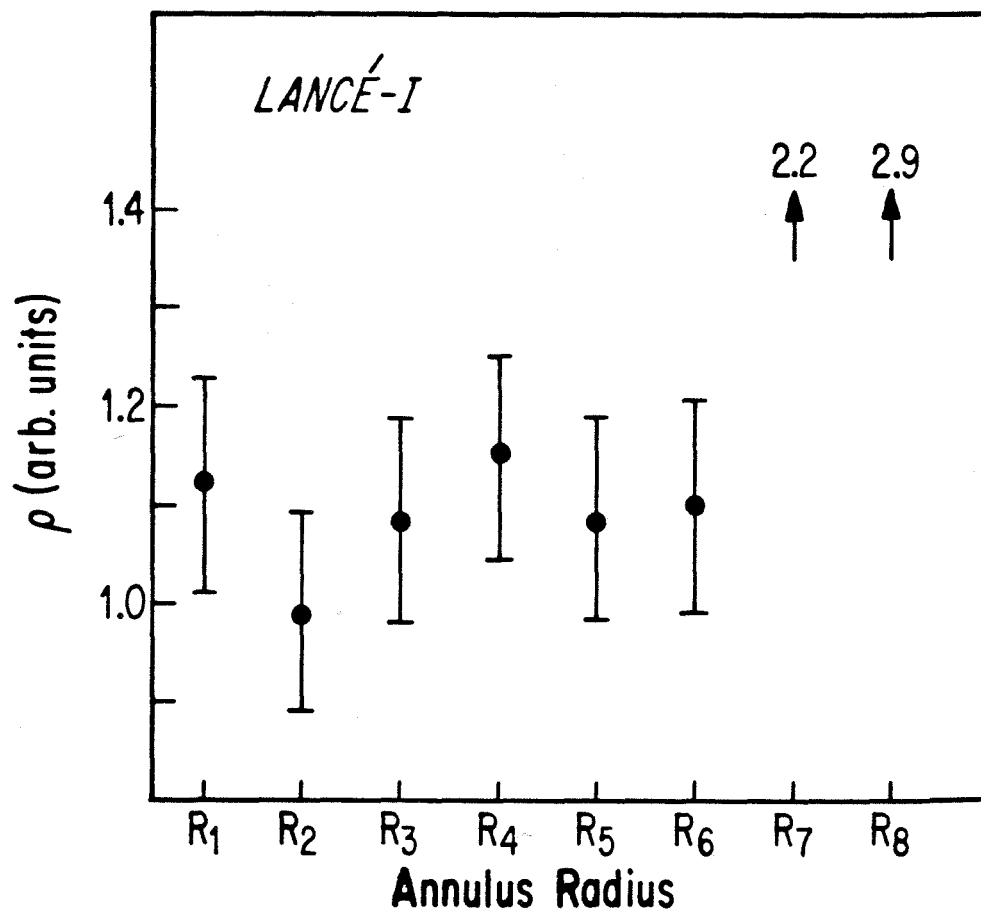
Predictions of the track distribution over a homogenized sample can be made based on the knowledge that the beam distribution is approximately gaussian over the 7-sample cyclotron target array. For a properly centered gaussian shaped beam, the track density over the center sample in the array would be expected to monotonically decrease along a radial scan from sample center to sample edge. The

reader is referred back to Fig. 11 for a diagram of the track scan pattern for homogenized samples. Another way to look at the track data other than as individual points or radial directional scans is as concentric annuli. Integrating the track densities for a fixed radius over all eight directional scans (360° coverage) allows comparisons of the data for equal area concentric annuli. Thus in the case of a sample irradiated in the central position of the target array a plot of annular-averaged track density vs. radial distance out toward the sample edge is expected to be a monotonically decreasing function. A homogenized sample sitting in one of the six perimeter positions in the target array, however, would exhibit a different track pattern. Plots of annulus track density vs. radial distance for these samples would be roughly flat. Each annulus has an area of maximum dosage (sample edge closest to the center of the target array) and a minimum dosage (edge furthest away from the target center). For a given annulus, contributions from the high and low edges will tend to average out. Comparing two annuli, the one at larger radial distance from the center of the sample will show more extreme track densities, but these will still approximately cancel to give an average track density close to the annulus at a smaller radius. In this way, total annulus track densities for each annulus tend to be equalized.

Figure 12 is an annulus total track density versus annulus radius for the Lance I pellet. Lance I was irradiated in an outer perimeter target position in TA&M-8. As can be seen the integrated annulus track distribution within errors is essentially flat out to

FIGURE 12

Plots the track density measurements associated with an annulus (refer back to Fig. 11) vs. the annulus radius- in order of increasing radius- for the Lance I pellet sample. The break in the flat distribution at R_7 and R_8 indicates fission track contributions from contaminants in the aluminum holder surrounding the outer edge of the sample.



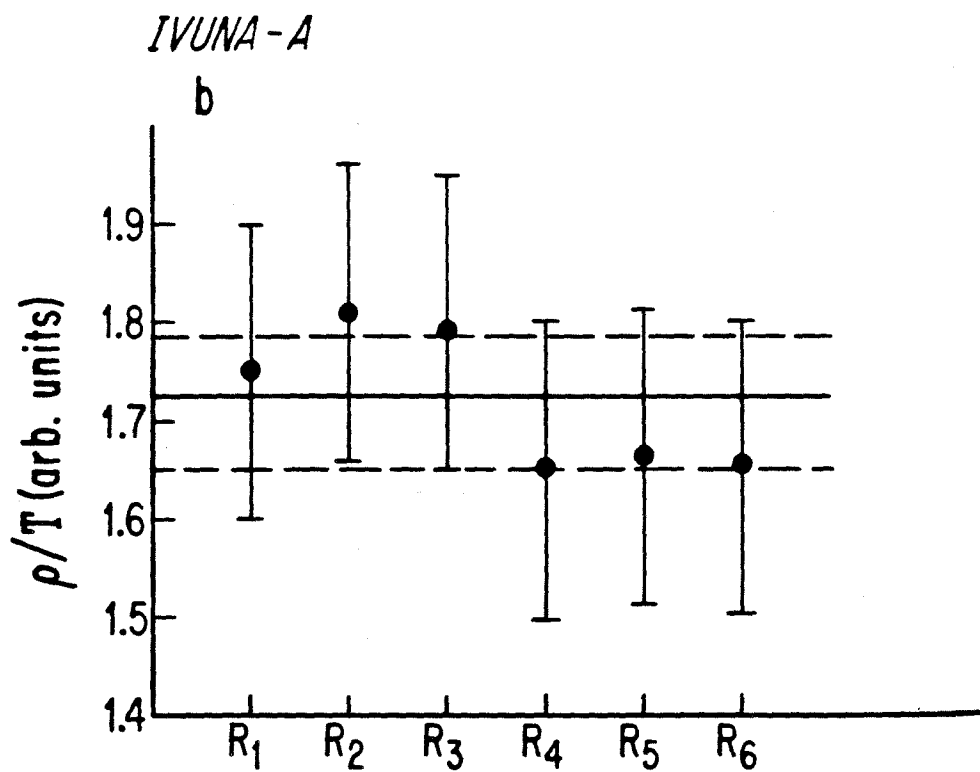
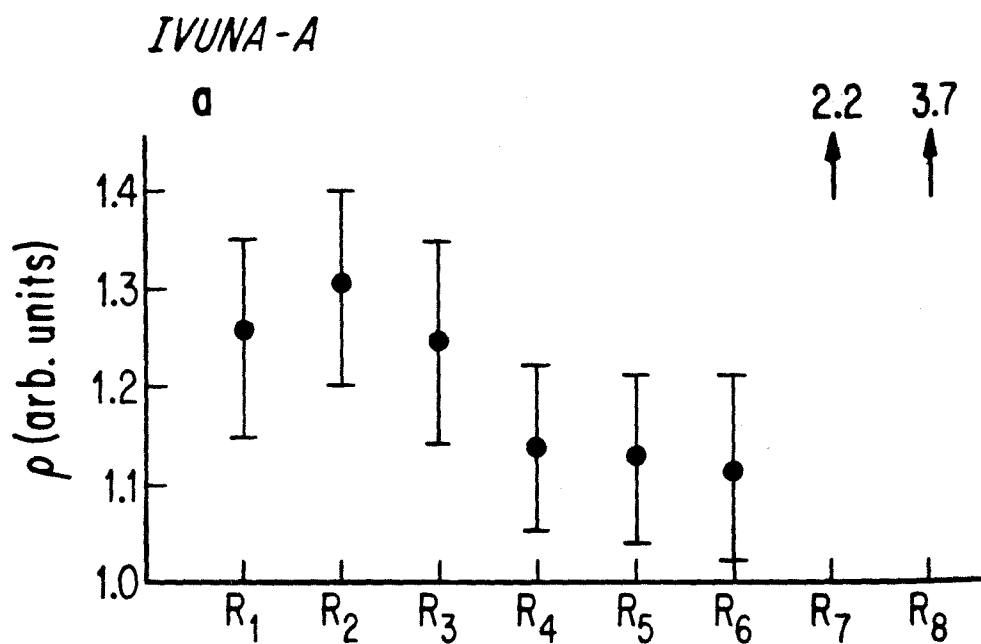
the R_6 annulus located ~ 2 mm from the center of the sample well. The abrupt discontinuity in track density observed at 2.25 mm (R_7) and 2.42 mm (R_8) from the center are indicative of an edge interference. These high track densities around the edge of a sample result from U and Th fission tracks caused by impurities from the walls of the aluminum holder sample well. Because of this interference, only track data out to the R_6 position (~ 2 mm radius) for pellet analyses were used.

Figure 13(a) is the track distribution pattern observed for the Ivuna-a pellet, the center sample in TA&M-8. Excluding the data for the two most exterior annuli as influenced by edge interference, the general trend within errors is consistent with a decreasing track density with increasing distance from the center. The fact that the 5 mm sample was not exactly centered in its 6.25mm sample well may account for some of the discrepancy. This decreasing trend follows what was predicted for the annulus track density vs. radius profile of a center target sample in a gaussian beam.

Comparisons of track density data over a homogenized sample with the dosimetry data serves as a powerful internal consistency check. Direct correlations of track scan positions to points on the dosimetry maps can be made. Dividing the track data by their corresponding dosimetry data compensates for irradiation intensity differences. Figure 13(b) shows the individual annuli track data of the Ivuna-a sample normalized by their corresponding beam dosage plotted against annulus radial position. A flat distribution is expected and within errors is observed. There is some suggestion

FIGURE 13

- a. The Ivuna-a track density measurements associated with an annulus (see Fig. 11) are plotted versus annulus radius, in order of increasing radius. Ivuna-a was located in the center of the target. Points at R₇ and R₈ show fission track interference from contaminants in the aluminum holder surrounding the sample. General trend for the inner six positions is a decrease in track density from the center outward.
- b. The track density for an annulus divided by the dose received by the area associated with an annulus is plotted as a function of annulus radius. Dose-normalization of the track density results in a flat distribution within errors.



of a 7% drop in the dosimetry-normalized track densities in going from the inner three annuli (out to 1.6 mm) to the outer three but it is not statistically significant.

Another method of correlating track and dosimetry data is to analyze the pellet in quarters. This is quicker and requires less position control. Figure 14(a) illustrates the track distribution pattern for the Mighei C-2 pellet, an outside perimeter sample in TA&M-8. Within errors, the track distribution is fairly flat out to the standard R_6 position but with some suggestion of a systematic increase. Figure 14(b) plots the Mighei C-2 data out to 2 mm radius (R_6) in a quarter by quarter analysis. The distribution is flat as predicted, indicating no problems in track vs. dosimetry correlations.

Annulus track density vs. radius plots were done for all pellet samples. Dose-normalized track plots were done for most pellets including all samples which showed irregularities in their un-normalized track plots.

d. Fission cross section corrections

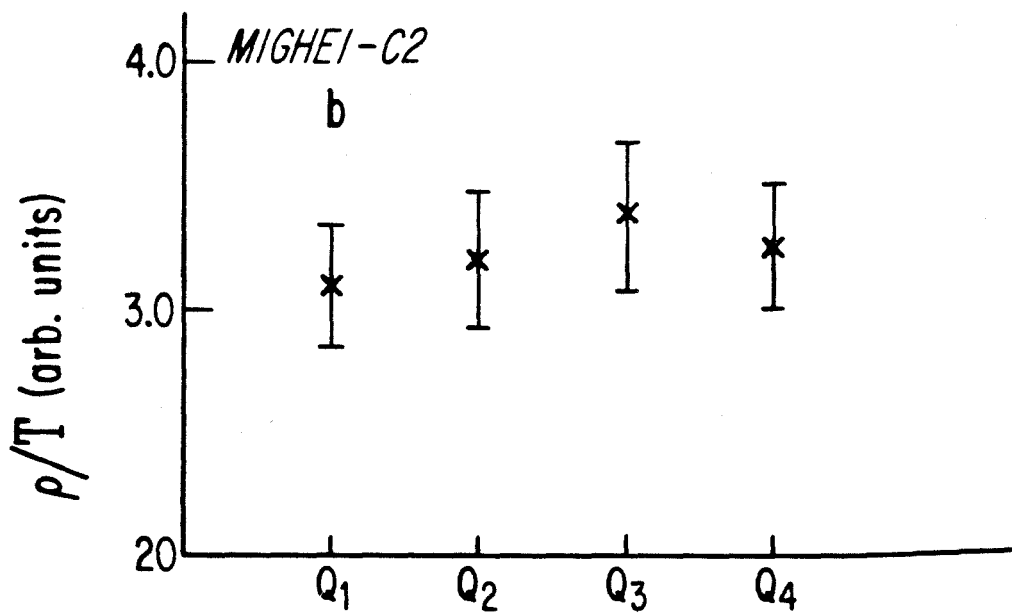
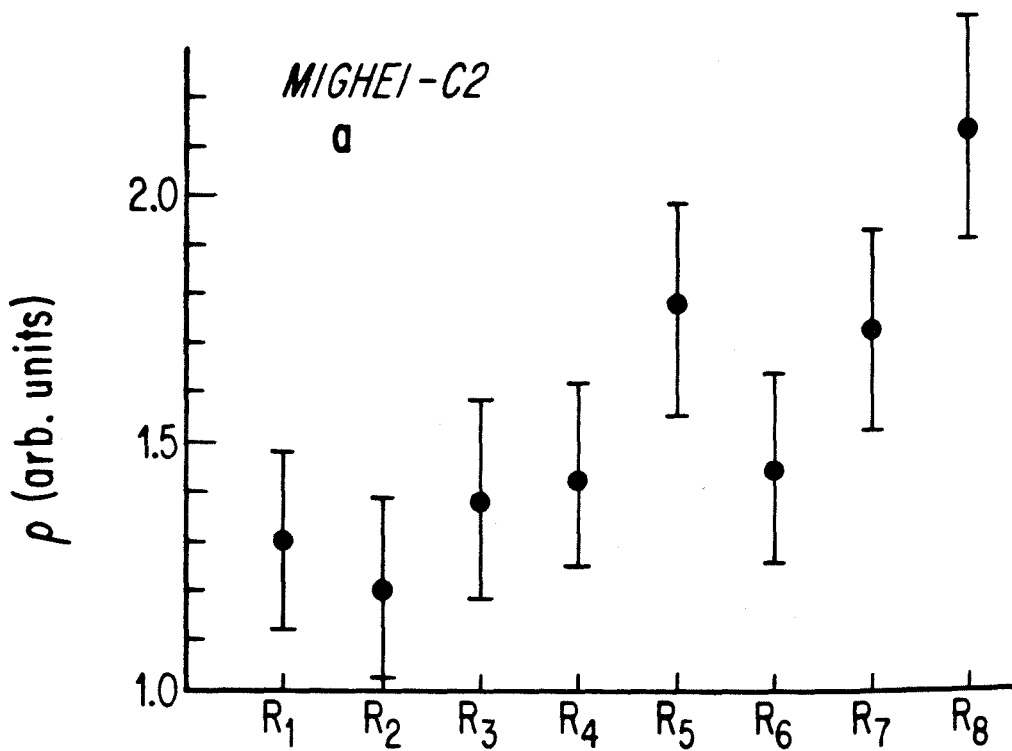
Appendix I derives the equation used to correct for unequal Th,U fission rates in determining a $(Th+U)/U$ ratio for a sample (see section II A-4 in main text, also). The relative Th,U fission cross sections were determined by irradiating pure metal foils with the charged particle beams of interest.

Our best analysis for the relative fission cross sections was obtained in TA&M-8. Although the 40 MeV proton beam was used, passage of the beam through the upstream dispersing foil and the Layer A

FIGURE 14

- a. Plots the track density associated with an annulus versus the annulus radius (refer Fig. 11) for the Mighei C-2 sample.

- b. Illustrates a method for relating track density and dosimetry data that does not require precise position control. The Mighei C-2 pellet track data and dosimetry data are divided into equivalent quarters. The resultant flat distribution for the dose-normalized track density vs. quarter indicates good track count/dosimetry correlation.



heat sink plate caused a sample to see a proton beam of ~ 38 MeV. At this energy track counts on mica over the U and Th foils give $\sigma(\text{Th})/\sigma(\text{U}) = 0.87 \pm .01$. The high track densities involved necessitated counting be done on a scanning electron microscope. Our result agrees quite well with an extrapolation of the fission cross section data tabulated by Khodai-Joopari(1966) [refer to Fig. 3 in section on Basic Physics]. This ratio is expected to be insensitive to proton energy. The correction factor calculated using our measured relative fission cross section value typically changes a (Th+U)/U ratio determined by assuming equal fission rates by $\sim 4\%$ (Appendix I).

A quick check of relative fission rates using 50 MeV deuterons gives $\sigma(\text{Th})/\sigma(\text{U}) \sim 0.83 \pm .07$. Thus, with regard to relative fission rates 50 MeV deuterons and 35-40 MeV proton beams are essentially identical.

e. Fission of other elements

Interference from fissioning of other heavy elements is a point in need of discussion. With the elemental compositions of carbonaceous chondrite material the major interferences are expected from lead and bismuth fission. To determine the Pb fission rate relative to U and Th, a Pb foil was irradiated along with our U and Th metal foils. For 38 MeV protons the relative track production rate ratio for Pb versus Th measures 6×10^{-4} . As discussed earlier in the Basic Physics section, the Pb and Bi fission cross sections drop steeply with energy while Th and U are essentially energy independent in the

region applicable to our experiments (25-40 MeV). No bulk CC total Pb value is reported above 3 ppm (Mason, 1971). Using the 38 MeV proton derived value and an average CC bulk [Th+U] value of 60 ppb gives an upper limit to the Pb fission contribution equal to 3% of the total track density. Pb is expected to present even less of an interference in our Allende inclusion analyses. The concentration of Pb in Allende inclusions (radiogenic in origin) is less than half that measured in whole rock and matrix samples (Tatsumoto et al., 1976).

An accurate relative Pb fission rate measurement for 50 MeV deuterons was never made. Only an upper limit can be set at $\sim 3 \pm 1 \times 10^{-3}$ for the Pb fission rate compared to Th. This would place a maximum upper limit to the Pb fission track contribution of 15%. Thus meteorite data obtained from deuteron irradiations would require careful scrutiny for non-negligible Pb interference. Because of the severe irradiation-damage encountered with high dose deuteron irradiations, deuteron experiments were abandoned. Deuteron analyses were attempted for only three samples, all pellets made from material we received as crushed powders. As will be discussed in the pellet results section, there is evidence for the need of blank corrections unlike those found for samples we crushed ourselves. The Pb interference question in deuteron irradiations is yet unresolved. Fortunately, all but the aforementioned three pellet samples were irradiated in proton irradiations as were all the Allende inclusion samples.

Carbonaceous chondrite Bi concentrations are reported from 40-120 ppb (Mason, 1971). These concentrations are < 25 times less

than bulk C chondrite Pb concentrations. Referring back to Fig. 3, Bi fission cross sections appear enhanced by less than a factor of 10 over Pb fission cross sections. Hence, Pb is expected to cause at least 2.5 times more fission interference than Bi. As such, we consider interference by Bi fission as negligible.

f. Fission Track Annealing during Irradiation

The possibility that detector micas were heated during an irradiation to high enough temperatures for long enough times to cause fission track annealing warrants discussion. Actually what is important is not whether annealing occurred, but whether large temperature gradients were sustained during the irradiation which could cause differential fission track annealing. Significant differences in track annealing experienced by meteorite sample vs. standard glass detector micas would prohibit meaningful concentration measurements to be made. In our reactor irradiations, the maximum flux difference between any samples or standards is only ~10%. The long irradiation times (days) permits thermal equilibration within the irradiation crucible. Thus, differential annealing during reactor runs should be unimportant. The thermal conditions experienced by a target during the cyclotron irradiations, however, presents a quite different situation. A discussion of this issue is presented in Appendix VII. There is evidence from our two-layer cyclotron targets that differential annealing has occurred in the Layer B mica relative to the upstream Layer A detector mica. However, within each mica there is no evidence to support differential annealing greater than

~5% between samples receiving a factor of two difference in dose. Since each layer holds at least one CT standard, all samples irradiated in a particular target layer are always referenced to a standard in the same layer.

3. Blank Corrections

a. Reactor

Contributions to the measured U content due to contamination during the pellet-making process as well as the U content of the mica must be subtracted out. All reactor irradiations used Indian Ruby muscovite (obtained through Washington U.) for the detectors. The U content of the mica, determined from a cleaved internal surface of an irradiated mica, is $(.28 \pm .03)$ ppb.

Crushing a sample with the 4-40 stainless steel mortar and pestle introduces $.74 \pm .09$ ppb U, while use of the hardened steel ball mill gives $.09 \pm .04$ ppb. These crushing blank corrections are probably upper limits since bulk meteorite material is much softer than the SiO_2 glass involved in making the blanks.

b. Cyclotron

In all irradiations except TA&M-10, Caltech Division Collection 2469 mica from Chester County, Pa. was used as the detector. Typically, a detector mica was cleaved over the CT glass standard and track counts done on the internal surface to determine [Th+U] content of the mica. Averaging over runs TA&M 6-9, Div. 2469 has a [Th+U] value of 5 ± 2 ppb. The one standard deviation error is derived from the total range observed in the measured Th+U concentration of individual micas irradiated in the various TA&M runs.

After the severe irradiation damage suffered by the Div. 2469 mica in our TA&M-9 high dose deuteron irradiation (which may have been a damage threshold unique to this mica), mica detectors were changed

to Indian-Washington U. in the following irradiation. The single TA&M-10 run determination of the Indian-Washington U. mica [Th+U] content is $2.7 \pm .3$ ppb. During an early developmental 40 MeV proton run, the measured $[\text{Th+U}]_{\text{Indian}}/[\text{Th+U}]_{2469}$ ratio was 1.5 ± 0.2 . This measurement was determined from single pieces of the two mica types. The differences in these numbers represent (Th+U) inhomogeneities in at least the Div. Coll. 2469.

Analyses on crushed high purity quartz gives a 4-40 stainless steel mortar and pestle crushing blank equal to 6 ± 3 ppb [Th+U] and a hardened-steel ball mill crushing blank of 2 ± 2 ppb. These errors are not simply due to counting statistics, but are predominantly due to the errors on the [Th+U] concentration of the mica detectors for these blank samples which had to be subtracted out before proper crushing blank values could be obtained.

F. Technique Evaluation

1. Sensitivity

The demonstrated sensitivity of our cyclotron technique is based on our highest target-integrated dose irradiation, TA&M-10. For our 5 mm homogenized samples we could see down to 0.4 ppb with 10% counting statistics. Comparing this value to the 2-6 ppb [Th+U] in the micas it would appear the technique is sensitivity limited by the detector. Regarding section analysis, a 100 μ grain with 1 ppm Th+U or similarly a 20 μ grain with 25 ppm Th+U can be analyzed with 10% counting statistics.

For the dosage ($1.6-1.8 \times 10^{18}/\text{cm}^2$) used in our reactor irradiations, 10% counting statistics can be obtained for a 100 μ grain with 20 ppb U or a 20 μ grain with 500 ppb U. The Colpot epoxy used in these irradiations fails at ~ 3 times this fluence. For rock slab samples, where epoxy is not necessary, one is only detector limited.

2. Error Estimates

Precision of the technique is discussed in terms of the bulk analyses. In the reactor runs track counts are done to 3% (1 standard deviation) or better counting statistics for samples and standards. The major source of error in determining a bulk U concentration comes from the SMI track counting efficiency factor known to 6.6%. Multiplication of the track densities by the SMI factor gives blank uncorrected U values within 8%. Subtracting out the blanks adds less than 1% to this 8% error. [Note: Choice of a standard closer to CC uranium levels (e.g., a 50 ppb glass) would obviate the

necessity for an SMI factor, cutting total errors in half.]

In the cyclotron experiments statistics are also 3% or better for pellet samples and standards. No counting efficiency factor was applied since standard track densities rarely exceeded sample track densities by more than a factor of 10. Also, sample and standard micas were counted under identical conditions. The most difficult error to assign concerned the dosimetry correction factor. As discussed in Appendix V, errors can typically vary between under 2% to 10% depending on whether replicate analyses on different plates were made, the precision of fiducial location control, pellet slippage within a sample well, and possible Layer A vs. Layer B sample well position differences. In particular cases each of these effects were investigated providing a basis for assignment of errors to other samples. The resultant blank-uncorrected [Th+U] values are known to 6.5%. Adding blank corrections typically raises this error to 10%. Final errors in (Th+U)/U ratios range from ~12-20%.

Our bulk analyses require comparing track densities from crushed-pressed samples to track densities obtained from polished-slab standards. A check was done to confirm that track densities from a standard glass polished surface do not differ significantly from track densities obtained from a crushed-pressed pellet surface. A series of pellet and polished slice samples were made from an NBS SRM-610 nominal 500 ppm glass. At these concentrations contamination due to crushing is not at issue. Samples were irradiated jointly at the UCLA reactor facility. The average track density for the two glass slices was $262 \pm 2/\text{fov}$ (fov \equiv area of single field of view at

magnification of track scan). By comparison the average for the two pellet samples was $264 \pm 10/\text{fov}$. Thus the slice/pellet data averages reproduce to better than 1%, indicating no fundamental problem in calibrating pressed-pellet concentrations against polished slab standards.

3. Reproducibility

Great effort was expended to maintain a constant track counting criteria throughout the experiment. In the reactor mica analyses, the SMI micas were frequently recounted to ascertain consistency of criteria application over time (see Appendix III). Good reproducibility was demonstrated, assuring uniform track counting over the duration of the analyses. Periodic recounting of select samples and standards were done to insure the meaningfulness of the track counting statistics errors. Reactor pellet micas counted for 3% counting statistics typically reproduced better than 3%, with the largest discrepancy observed equal to 5%. The 5% value was for the sample with the lowest observed track density. Track recounts of a reactor CT glass mica reproduced within 2.8%. A cyclotron irradiated meteorite mica recount gave 2.5% reproducibility, a value comparable to the 3% individual counting statistics. Similarly, the counting statistics error over a CT standard glass was 3% with reproducibility at least as good.

As will be discussed in the section on pellet results, analysis of data from top and bottom micas on a pellet can be regarded as a reproducibility check. Analyses of top and bottom pellet surfaces

give uranium values within 5% or better in all cases. This is well within 8% errors assigned to an individual analysis. There is greater diversity in the cyclotron analyses. Top and bottom [Th+U] values obtained for three different pellets give differences of 15%, 8%, and .2%. It should be noted the high value was obtained for a pellet irradiated in the low dose TA&M-7 deuteron run.

4. NBS Standard Glasses

Two reactor irradiations included pieces of an NBS SRM-617 nominal 0.02 ppm glass. This glass has an isotopic dilution U value of 73 ppb (analysis by Tatsumoto.) Accounting for the ^{235}U depletion factor of this glass ($^{235}/^{238} = 0.616$ atom%), we obtained a U concentration of 75.6 ± 3.5 ppb for the Col MS-2 glass fragment and 73.1 ± 2.8 ppb for the Col MS-4 glass fragment. Going from the center of the glass radially outward to 4 mm and taking measurements every 1 mm for the four perpendicular directions gave a maximum variation in track density of 4.2% compared to a counting statistics standard deviation of 3% for a single measurement.

A sample of the NBS SRM-963 nominal 1 ppm glass was irradiated in TA&M-6II. The isotopic dilution [Th+U] value by Tatsumoto for this glass is $1.569 \pm .008$ ppm (NBS Special Publ. 260-49). By comparison, our analysis gives the glass $1.31 \pm .13$ ppm [Th+U]. The ratio of the two analyses equals $1.19 \pm .12$. Although the difference is two standard deviations, we considered possible sources of systematic error. Dosimetry measurements indicate the glass sample sustained a factor of two dose gradient over its surface. Shifting the glass

position in the sample well, however, changes the average dose by no more than a couple percent. This 1 ppm glass was irradiated in the same 7-sample target layer which included three CT glasses. The agreement of the dose-normalized track-densities of these CT glasses was used to argue strongly against the existence of large scale fission track annealing during irradiation. The possible [Th+U] depletion we observe in the 1 ppm glass relative to isotopic dilution analyses is difficult to reconcile in terms of differential annealing. The integrated dose over the NBS glass was slightly lower than the least irradiated CT glass. The difference, if real, is not understood.

III. Bulk Carbonaceous Chondrite Th/U ratios

A. Results

The results of our bulk pellet analyses of carbonaceous chondrites are listed in Table 7. This table provides all pertinent track density measurements and correction factors that go into calculating a (Th+U)/U ratio. The reactor standard track density values listed ρ_{OL} are the interpolated values for a standard glass as if it were located at the position of the sample of interest (see Section II.F-1(c) on reactor dosimetry). The appropriate track counting efficiency factor (SMI), and blank correction (crushing plus mica background) for determining a uranium concentration from the reactor track counts are also indicated.

The cyclotron track densities, denoted by the subscript H, are those measured for a sample and the CT standard irradiated in the same target layer. The relative sample to standard dose T is obtained from photo-emulsion dosimetry measurements (refer Appendix V). Blank values listed are a sum of the U and Th contamination due to crushing plus the mica background. Tabulated [Th+U] concentrations have been corrected for measured relative U,Th fission rates (see Appendix I).

In both irradiations detectors are always placed against the two surfaces of the pellet. The term top detector mica refers to the upstream mica in a cyclotron run, and in both reactor and cyclotron runs the mica available for sample position fiducialling. This top detector mica was always counted and when warranted (or as time permitted) the bottom detectors were also counted. Though difficult,

TABLE 7

RESULTS OF BULK SAMPLE ANALYSES

Sample	$\rho_L (10^5/cm^2)$	$\rho_{OL} (10^7/cm^2)$	(SMI, BI) U(ppb) *	$\rho_H (10^4/cm^2)$	$\rho_{OH} (10^5/cm^2)$	T	Th+U (ppb) *	Th+U U
1. Ivuna -a	t: 2.43±.07	1.72±.08	4.8±.4 ^{1,3}	t: 3.05±.12	5.89±.04	1.16±3.5%	28±3 ⁷	6.1±.8
	b: 2.38±.07	1.72±.08	4.4±.4 ^{2,3}	b: 3.00±.13			27±3 ⁷	6.5±.9
2. Ivuna -e1	3.65±.10	1.71±.08	7.0±.6 ^{1,3}	2.73±.11	5.89±.04	0.28±4%	117±8 ⁷	17±2
3. Ivuna -e2	3.40±.09	1.61±.08	6.9±.6 ^{1,3}	2.97±.15	3.72±.12	1.15±10%	46±6 ⁷	6.6±1.1
1. Orgueil 2216-a	5.27±.14	1.62±.08	10.8±1.0 ^{1,3}					
2. Orgueil CII-1	2.65±.08	1.36±.03	5.9±.7 ^{1,6}	t: 0.262±.015	0.605±.020	0.49±6%	56±7 ¹¹	9.5±1.6
				b: 0.230±.015			49±6 ¹¹	8.2±1.5
3. Orgueil CII-2	4.65±.12	1.73±.08	8.5±.9 ^{1,6}	2.78±.10	5.89±.04	0.97±4%	26±4 ¹¹	3.1±0.6
4. Orgueil I "stars"				0.683±.026	0.605±.020	0.95±10%	75±10 ¹¹	
1. Murchison -5	3.07±.09	0.837±.019	10.7±.9 ^{2,5}	1.44±.05	1.19±.03	1.22±1.4%	61±5 ⁹	5.7±.7
2. Murchison -5 II	t: 4.33±.03	1.39±.03	9.6±.8 ^{1,5}	1.21±.04	1.19±.03	1.46±7%	39±6 ⁹	4.1±.7
	b: 4.19±.09		10.3±.8 ^{1,5}					

TABLE 7 (continued)

Sample	$\rho_L (10^5/cm^2)$	$\rho_{oL} (10^7/cm^2)$	(SMI, BI) U(ppb)	$\rho_H (10^4/cm^2)$	$\rho_{oH} (10^5/cm^2)$	T	Th+U (ppb)	$\frac{Th+U}{U}$	
3. Murchison -5s	4.48±.11	1.31±.03	10.6±.9 ^{1,5}						
4. Murchison -7	2.71±.08	1.03±.02	7.4±.7 ^{2,5}	1.05±.08	1.19±.03	1.43±7%	33±6 ⁹	4.5±.9	
5. Murchison -M	4.39±.13	1.70±.08	8.4±.8 ^{1,4}	t: 3.98±.16 b: 3.66±.14	4.90±.11	1.17±7%	43±5 ⁸ 39±5 ⁸	5.1±.8	
6. Murchison -T	2.72±.08	0.836±.019	9.4±.8 ^{2,5}						
<hr/>									
1. Murray -I	3.66±.11	0.945±.020	11.4±1.0 ^{2,5}	(0.885±.091)	1.19±.03	.79±7%	57±10 ⁹	5.0±.9	
2. Murray -II	4.15±.13	1.28±.03	10.0±.9 ^{1,5}	0.512±.021	0.809±.030	.69±4%	56±6 ⁹	5.6±.8	
<hr/>									
1. Mokoia -I	4.83±.13	0.962±.020	15.1±1.2 ^{2,5}	2.88±.19	1.19±.03	8±4%	89±9 ⁹	5.9±.8	
2. Mokoia -II	6.34±.16	1.29±.03	15.7±1.3 ^{1,5}	1.44±.04	0.809±.030	1.56±4%	71±7 ⁹	4.5±.6	
<hr/>									
1. Mighel -C1	t: 4.36±.12	1.33±.03	10.5±1.0 ^{1,6}						
	b: 4.32±.13		10.4±1.0 ^{1,6}						
2. Mighel -C2	t: 4.46±.12	1.68±.08	8.4±.9 ^{1,6}	t: 1.54±.08	4.90±.11	.611±.7%	29±4 ¹¹	3.4±.6	
	b: 4.66±.13		8.8±1.0 ^{1,6}	b: 1.56±.14		.611±.7%	29±5 ¹¹	3.3±.7	

TABLE 7 (continued)

Sample	$\rho_L (10^5/cm^2)$	$\rho_{oL} (10^7/cm^2)$	(SMI, B1) U(ppb) *	$\rho_H (10^4/cm^2)$	$\rho_{oH} (10^5/cm^2)$	T	(B1) * Th+U(ppb)	$\frac{Th+U}{U}$
3. Mighei FM-1	t: 4.51±.12 b: 4.58±.13	1.69±.08	8.7±.8 ^{1,4} 8.9±.8 ^{1,4}	2.07±.09	5.89±.04	.55±4%	39±4 ⁸	4.5±.6
4. Mighei FM-2	4.90±.13	1.64±.08	9.8±.9 ^{1,4}	5.27±.18	5.74±.06	1.04 ±2.5%	60±6 ¹⁰	6.1±.8
1. Lance - I	6.28±.16	1.68±.08	12.4±1.1 ^{1,4}	2.80±.11	5.89±.04	.55±4%	56±5 ⁸	4.5±.6
2. Lance -II	5.90±.15	1.66±.08	11.7±1.0 ^{1,4}	1.74±.09	5.89±.04	.33±4%	58±4 ⁸	4.9±.6
3. Lance -9	6.20±.14	1.63±.08	12.6±1.1 ^{1,4}	7.44±.21	5.74±.06	1.15±2.5%	78±5 ¹⁰	6.2±.6
1. Allende -1	4.77±.12	0.89±.019	16.1±1.3 ^{2,5}					
2. Allende -3	3.92±.12	0.841±.019	13.9±1.2 ^{2,5}	1.82±.15	1.19±.03	1.08±10%	92±14 ⁹	6.6±1.2
3. Allende -NWT	3.80±.12	1.01 ±02	11.0±.9 ^{2,5}	0.521±.026	0.809±.030	.91±4%	39±5 ⁹	3.6±.6

* SMI: 1 = 1.08 ± 6.6%
2 = 1.15 ± 6.5%
3 = 0.28 ± .03

[Th+U] Blanks: 7 = 5 ± 2 ppb
8 = 7 ± 2.8 ppb
9 = 11 ± 3.6 ppb
10 = 4.7 ± 2.0 ppb
11 = 8 ± 3 ppb

[U] Blanks: 4 = 0.37 ± .03 ppb
5 = 1.22 ± .09 ppb
6 = 0.7 ± 0.5 ppb

we tried to maintain pellet face identities throughout the multiple irradiations. The two surfaces are denoted by the letters t and b in the data tables.

The Orgueil-CII pellets, Orgueil-I pellet, and the Mighei-C pellets were made from material received by our lab as already crushed powders. As such no exact blank correction could be made. In an attempt to bracket the appropriate blank correction we applied the average of our highest (mortar & pestle plus mica) and lowest (mica only) blank corrections to the measurements.

The discussion of results for individual samples follows. Comparisons with literature values are made and summarized in Table 8. Th/U data will be referenced as high, low, or normal depending on whether it falls in the band 3.8 ± 0.5 .

TABLE 8
 COMPARISON OF U AND Th/U ANALYSES
 IN C CHONDRITES

	<u>U [ppb]</u>	<u>Th/U</u>
<u>Ivuna</u>		
This work	4.6 ± 0.2	5.3 ± 0.4
Other: a	13; 7; 8	2.3; 3.7; 3.6
b	8, 7	
<u>Orgueil</u>		
This work	11 ± 1; (6*, 9*)	-; (8.5*, 2.2*)
Other: a	24; 24; 18; 8	2.7; 2.9; 2.2; 4.3
b	6	
c	8	
e	9	3.1
h	5.2; 18	
j	8	3.5
k	5	3.6
<u>Murchison</u>		
This work	11; 10; 11	4.7; 3.1; -
" "	7; 8; 9	3.5; 4.1; -
Other: h	13.5 ± 2.5	
j	11	
<u>Murray</u>		
This work	11; 10	4.0; 4.6
Other: h	16.5	
i	11	3.7

TABLE 8 (continued)

	<u>U [ppb]</u>	<u>Th/U</u>
<u>Mighei</u>		
This work	9; 10; (11 [*] , 9 [*])	3.5; 5.1; (- [*] , 2.3 [*])
Other: a	17	2.7
b	8	
c	16	
f	15	
h	9.3; 16	
<u>Mokoia</u>		
This work	15; 16	4.9; 3.5
Other: a	14	4.3
<u>Lancé</u>		
This work	12; 12; 13	3.5; 3.9; 5.2
Other: a	20	5.8
b	7	
d	28	
h	25	
<u>Allende</u>		
This work	(16, 14, 11)	(-, 5.6, 2.6)
Other: h	15.5; 16.5	
i	15	4.1
k	16.2	

*Refers to samples received as crushed powders.

Values in () from this study are not optimum, see text.

TABLE 8 (continued)

- a. Morgan and Lovering (1968)
- b. Reed and Allen (1966)
- c. Reed et al. (1960)
- d. Reed (1963)
- e. Wanke (1974)
- f. Goles and Anders (1962)
- g. Fireman et al. (1970)
- h. Fisher (1972)
- i. Tatsumoto et al. (1973)
- j. Tatsumoto et al. (1976)
- k. Tatsumoto - pers. comm. - analysis of Orgueil 2216 fragment
at our request (see text) .

Ivuna: The Ivuna specimen analyzed (USNM 2478) was a single fragment. It was carefully dissected under a stereomicroscope using cleaned stainless steel tools. Pellets were made from completely interior material (grade a) or material containing a significant amount of museum exterior surface (grade e). This exterior surface material is not to be confused with fusion crust. The Ivuna e samples were made by taking exterior surface material (small fragments < 1 mm) and crushing in a plastic vial with plastic ball pestle. Initial crushing was done by simply shaking the plastic ball mill by hand for 2 minutes. The finest sized fraction was used in making Ivuna-e1. Ivuna-e2 was made from the more resilient fraction of this initial crushing plus additional exterior material crushed together in the plastic ball mill but this time using the automatic shaker (Wigl-bug). Comparing the data listed for Ivuna-a with those for Ivuna-e1 and -e2 the absolute concentrations of U and especially Th are significantly enhanced in going from the interior to the exterior of the specimen. Uranium jumps from an average value of 4.6 ppb in the interior to ~7 ppb for both exterior samples. The Th increases are much more variable. Interior (sample a) Th+U measurements are 28 ppb giving (Th+U)/U equal to an average value of 6.2 and Th ~23 ppb. For sample Ivuna-e2 the inferred Th concentration (~39 ppb) is directly proportional to its U enhancement over grade a material. As such the sample has (Th+U)/U = 6.6, a value comparable to that determined for the grade a sample. The Ivuna-e1 sample, however, exhibits a much higher Th content (~110) and (Th+U)/U = 17.

The most obvious explanation for the U and Th enhancements seen in the grade e samples as opposed to grade a samples is contamination with Th apparently much more variable than U. There is precedent for observing problems with Th contamination. Morgan and Lovering (1968) in discussing contamination problems with Orgueil samples found at least one instance of suspected thorium contamination. The alternative to interpreting the difference in inferred Th concentration levels of Ivuna-e2 and Ivuna-e1 is interference by Pb surface contamination. A 70 ppb difference in Th corresponds to a ~140 ppm difference in Pb, which seems implausibly high.

To put our measurements in the context of other studies, Morgan & Lovering (1968), herein referred to as M&L, measured $U \sim 8$ ppb and $Th/U \sim 3.7$ for two Ivuna samples. Their U value, though comparable to our Ivuna-e samples, is a factor of two higher than the U measurements on our grade a samples. The activation analysis determination by Reed and Allen (1966) also obtained U values twice as high as our grade a measurements. In contrast another M&L (1968) Ivuna sample has $[U] = 12.6$ ppb and $Th/U = 2.3$. With $[Th]$ contents of all three M&L samples close to 29 ppb it would appear the U abundance controls the Th/U ratio variations observed in their study. Our Ivuna-a data imply a Th content of ~28 ppb which agrees well with the M&L analyses. The fact we observe a higher Th/U ratio in our grade a samples (5.3 ± 0.3) than the M&L analyses is because we measure a factor of two lower U concentration. The 4.6 ppb Ivuna-a U value is the lowest observed for this meteorite. As Table 8 shows, however, similar low U values have been observed in the Cl, Orgueil. It may

be that we have the only "clean" U Ivuna sample analysis to date.

Orgueil: As mentioned earlier, most of our Orgueil analyses were done on samples we received as crushed powders. Proper blank corrections could not be made for these samples so we used a blank correction equal to the average of our highest and lowest blank corrections for samples we crushed ourselves. One Orgueil sample, Orgueil I, obtained through UCLA from Montalban, France, was so peppered with U fission track "stars" that the reactor irradiated mica detector was not even counted. From our cyclotron irradiation analysis the Orgueil I sample has a Th+U value of ~75 ppb with tracks not obviously located in stars. Thus, had the U analysis been done on this apparently contaminated sample it would have undoubtedly exhibited a low Th/U ratio. Two of the M&L(1968) Orgueil samples have [U]~24 ppb, [Th]~65 ppb and Th/U~2.8. Since the combined U and Th concentrations of these M&L samples is greater than our probable contaminated sample, these data may be suspect.

Another M&L (1968) Orgueil sample contained [U]~18 ppb and [Th]~41 ppb to give Th/U = 2.2. This can be compared to a fourth Orgueil sample they measured with U~8 ppb, Th~34 ppb, and Th/U~4.3. The factor of 2 difference in U content between these two Orgueil samples is mainly responsible for the observed Th/U variability. The sample with the lowest measured U gives the most "normal" Th/U ratio.

Wanke (1974) measured an Orgueil whole rock U concentration of

9.1 ppb. Reed et al. (1960) and Reed & Allen (1966) measure 8 ppb and 6 ppb uranium respectively. This range in U values is also observed in our Orgueil CII samples. Even though no exact blank correction can be made for the CII samples (material received as a single vial of crushed powder) there is a difference in Th concentrations between the two samples of almost a factor of 3. This factor is responsible for the wide difference in their measured Th/U ratios: ~2 vs. ~8.

Unfortunately our cleanest and most controlled Orgueil sample, Orgueil 2216-a, made entirely of interior material, was in the cyclotron run with deuteron irradiation and heat damage to the mica detectors. A uranium concentration of 10.8 ± 1.0 ppb was determined for this sample. The remaining ~20 mg reservoir of crushed grade-a Orgueil 2216 material, from which our pellet's 30 mg was taken, was sent to M. Tatsumoto (USGS, Denver) for isotopic dilution analysis. His uranium measurement of 10.2 ppb agrees well with our analysis. The thorium content measures 31.73 ppb giving the sample a Th/U ratio of 2.98.

An untouched interior ~40 mg chip of Orgueil 2216 sent to Tatsumoto for analysis gave a low value for uranium of 5.13 ppb. This value is a factor of 2 less than the value measured by Tatsumoto and us on crushed material of this specimen. As listed in Table 8 similar low U values have been observed for Orgueil among the wide range of U values reported. Although the crushing blank for Orgueil should be negligible, the possibility we may have introduced some unaccounted for contamination during the crushing of this sample can not be excluded. On the other hand, inhomogeneities on a ~50 mg

scale may indeed exist. Tatsumoto also measured a low Th concentration (=18.6 ppb) for the interior chip of Orgueil 2216 resulting in a "normal" Th/U ratio equal to 3.63. These numbers can be compared to a whole rock isotopic dilution analysis by Tatsumoto et al. (1976) for Orgueil where U=8.2 ppb, Th=28.6 ppb and Th/U=3.49. These U and Th concentrations are roughly a factor of 1.5 higher than those measured on that interior chip of Orgueil 2216 by Tatsumoto. There would thus appear to be strong indications of U and Th heterogeneity in Orgueil. The high hydrous phyllosilicate content of C1 material could be suggestive of a means for U and Th mobility. The two high precision Tatsumoto analyses of 3.49 and 3.63, however, give strong support for a "normal" Orgueil Th/U ratio, although there is no good reason for rejecting the 2.98 value.

Murchison: The Murchison fall in 1969 (Fuchs et al., 1973) makes this meteorite the freshest available carbonaceous chondrite. Within errors, our measurements on four samples from this CM2 meteorite give Th/U ratios lying in the "normal" band of 3.8 ± 0.5 . Uranium concentrations on six samples show a relatively small range from 7.4 ppb to 10.7 ppb. An 11 ppb whole rock uranium value is quoted in Tatsumoto et al.(1976). [Th+U] concentrations range from 33 ppb to 61 ppb.

Murray: The pellets Murray I and II are actual splits from a reservoir of crushed powder. The entire Murray II 5mm area on the TA&M mica was scanned. A 250 μ star with 12 times the track density of the rest of the sample observed in the [Th+U] track scan was attributed to contamination and excluded from the statistics. The two pellet samples for this CM2 meteorite appear quite uniform. If the star were included, the [Th+U] for Murray II would increase by 12%. On the average this meteorite has [U]=10.7 ppb, [Th+U]=56 ppb, and Th/U \sim 4.3. These numbers compare well to an isotopic dilution analysis of Murray by Tatsumoto et al.(1973) where [U]=10.8 ppb, [Th+U]=50.4 ppb and Th/U = 3.67.

Mighei: Our best values for the CM2 meteorite Mighei come from analysis of Field Museum specimen ME-1456 (pellets FM-1 and FM-2). Pellet FM-1 is a 30 mg split taken from \sim 130 mg of crushed Mighei ME-1456. Pellet FM-2 is simply 30 mg poured out from the remaining 100 mg of crushed material. The two surfaces of the FM-1 pellet give identical uranium concentrations of 8.8 ppb. The FM-2 pellet gives a 10% higher value of 9.8 ppb. When comparing [Th+U] concentrations, the samples differ by a factor of 1.5 (39 ppb for FM-1 compared to 60 ppb for FM-2). FM-1, the properly homogenized sample, gives a "normal" Th/U ratio of $3.5 \pm .6$. In contrast, FM-2, the more [Th+U] rich sample, gives a Th/U ratio slightly higher than normal at $5.1 \pm .7$. As can be seen, sampling criteria can make a difference. The average of these two samples gives Mighei a

Th/U ratio of 4.3, a value within the "normal" band. Because of the more proper sampling of crushed material represented by FM-1, the ratio 3.5 ± 0.6 is the better whole rock value.

The remaining two pellets, Mighei C-1 and C-2, were made from material received as a crushed powder. The uranium values seem to agree with those obtained from the samples we crushed. The [Th+U] values, however, are significantly lower and even with our lowest blank correction give Th/U ratios near 2.5.

Literature U values of 8 ppb (Reed and Allen, 1966), 15 ppb (Goles and Anders, 1962), 16 ppb (Reed et al., 1960) and 17 ppb (M&L, 1968) are reported. Thus, U measurements compiled on this meteorite range over a factor of two. M&L report [Th+U] = 62.5, similar to our FM-2 pellet, but because their U concentration is a factor of two higher they determined a low Th/U ratio equal to 2.7.

For the reasons outlined earlier, we believe the best whole rock Mighei value is the 3.5 ± 0.6 value of pellet FM-1. This value and the error associated with it support a "normal" Th/U ratio for Mighei.

Mokoia: The Mokoia CV2 samples are splits of the same crushed material. The uranium values are identical within errors at ~15 ppb. Although, with error, their [Th+U] values differ by a factor of 1.25 (71 ppb compared to 89 ppb). The sample with the lower [Th+U] concentration gives a "normal" Th/U ratio of 3.5. The higher [Th+U] sample gives a ratio slightly above, but, within errors, just inside the normal range. As discussed later, the Mokoia I cyclotron mica was scanned

in a non-standard manner. The scan pattern used makes dosimetry calibration less straightforward and we may have underestimated the assigned dose correction factor error. Averaging the two pellet ratios gives a Th/U ratio for Mokoia equal to 4.2. By comparison M&L (1968) obtain a Mokoia uranium concentration of 14.0 ppb and [Th+U] = 74.5 ppb. The resultant Th/U ratio of 4.3 similar to our pellet average reflects their [Th+U] value being midway between our sample measurements. Thus, there is no evidence to suggest a Mokoia Th/U ratio outside of the normal range.

Lance: Two of the three Lance CO3 meteorite analyses (I and II) are splits of the same crushed powder. Uranium values for all pellets I and II are nearly identical at ~ 12 ppb. They both have [Th+U] ~ 57 ppb. Their resultant Th/U ratios of 3.5 ± 0.5 and 4.2 ± 0.6 give an average "normal" Th/U ratio of 3.9.

Though the uranium value for the Lance-9 pellet is similar to the other two pellets, the [Th+U] value is ~78 ppb compared to ~57 ppb. As such the Th/U ratio for this pellet is $5.2 \pm .5$. Averaging all three ratios gives a Th/U ratio of 4.2 for Lance.

For comparison Reed(1963) reports a Lance uranium concentration of 28 ppb; Reed and Allen(1966), 7 ppb; and Morgan and Lovering(1968), 20 ppb. Our three 12 ppb measurements fall within the previously reported factor of four spread in U values. M&L(1968) report a Lance [Th+U] value near 138 ppb--a factor of two higher than any of our measurements. This high [Th+U] value and their U determination of 20 ppb results in a high Lance Th/U ratio of 5.8. M&L do note

that their sample was not prepared especially for their experiment and, as such, a more controlled analysis would be warranted. It should be noted that Lance does contain Ca-Al inclusions similar to Allende which could explain the high U and Th variability reported in the literature. (Further elaboration will be made in the Allende discussion). They are rarer in Lance than Allende, allowing a greater chance for more homogeneous sampling to happen on a smaller scale in Lance rather than Allende. Our data indicate that Lance does indeed fall within the "normal" Th/U ratio band.

Allende: Comparatively little attention has been given to Allende in our bulk sample analyses because it was recognized that the presence of abundant Ca-Al-rich inclusions, rich in U and Th, were a complication to any homogenization and to the interpretation of results. Pellet analyses for bulk Allende illustrate the complex inhomogeneity of the meteorite. We obtained uranium abundances ranging from 11 ppb up to 16 ppb. On the two Allende pellets where [Th+U] measurements were made a factor of two difference was observed. The sample with Th+U~87 ppb has a Th/U ratio of 5.6, while the sample with anomalously low Th+U of ~38 ppb has a ratio of 2.6.

The sample with the high Th/U ratio may indicate that a significant amount of the pellet material sampled was "white" inclusion material with high Th/U ratios. Tatsumoto et al.(1976) and Chen & Tilton (1976), for example, report many Ca-Al rich inclusions with Th/U ratios ranging from 5 to 11. However, Tatsumoto et al. also report a

calcium-aluminum rich chondrule with uniquely low Th/U ratio of 2.68 and some highly uncertain ratios for three magnesium-rich chondrules with Th/U ratios below 2. From the Allende inclusion work in this study (see Table 15 in Allende Disc. Section) two of four matrix analyses gave non-normal Th/U ratios at values of ~ 2 . Thus while there are large inclusions with high Th/U ratios in Allende there is widespread low ratio material as well.

Tatsumoto et al. (1973) and Tatsumoto et al. (1976) report whole rock Allende Th/U ratios of 4.07 and 4.2 respectively. This would suggest that even though large Th/U fractionations are present within Allende, proper bulk sampling might lead to a "normal" ratio.

B. Accuracy of the data

1. Internal Reproducibility

Questions of reproducibility of our experimental data fall into three categories: (1) track recounts on a given sample or standard; (2) agreement of measurements taken on two faces of a pellet; (3) agreement between pellets that are splits from the same reservoir of crushed material. Discussion of error estimates is given in section II-G-2.

(1) Track recount reproducibility has already been discussed in section II-G-3 and Appendix III. General reproducibility is well within track counting statistics for both samples and standards.

(2) Measurements taken on the top and bottom surfaces of a meteorite pellet for very heterogeneous samples can be subject to fractionation effects, e.g. due to pouring or settling. However, for well homogenized samples, comparison of top and bottom pellet surfaces should be a valid reproducibility check. For the five pellets where top and bottom surface uranium analyses were done, the uranium values all agreed to better than ~9%, roughly the 8% error assigned to an individual surface uranium value. In the three cases where top and bottom surface [Th+U] concentrations were measured two reproduced to better than 1% and the third within 10%. The 10% reproducibility between the surfaces of this last pellet is satisfactory considering the individual top and bottom values have assigned errors greater than 10% ($\pm 13\%$).

(3) When effort is taken to sample a powder reservoir representatively, the fractions may properly be called splits. The Murray I and II, Mokoia I and II, and Lance I and II pellets provide three cases for comparison. Table 9 summarizes the pertinent information for each sample. The Murray and Mokoia splits provide an especially good test of the technique. Both of these pairs consist of samples run in different cyclotron targets as well as different reactor runs involving different SMI factors. The Lance samples on the other hand were both irradiated in the same reactor run and in the same cyclotron target.

Graphic comparison of split U and Th+U measurements is presented in Fig. 15. As can immediately be seen from these plots, the U analyses for split pairs overlap within the errors of the individual analyses. The difference in U between the Murray I and II pellets is about twice as large as the other split pairs but is still less than 2σ (1.4σ).

Both the [Th+U] values for the Murray I and II and Lance I and II splits agree to within 2 ppb (better than 0.5σ). The Mokoia I and II [Th+U] values do not reproduce as well. The 18 ppb difference is about a 2σ difference. Although the difference is not statistically significant, there is a possible cause for the discrepancy because a non-standard method was used in the track scanning of Mokoia I. This sample was the first pellet sample track counted in this study. Rather than using the equal area sector scan pattern described in an earlier section, the Mokoia I cyclotron-irradiated mica was scanned in three radial 300μ wide strips. Thus the proper dosimetry

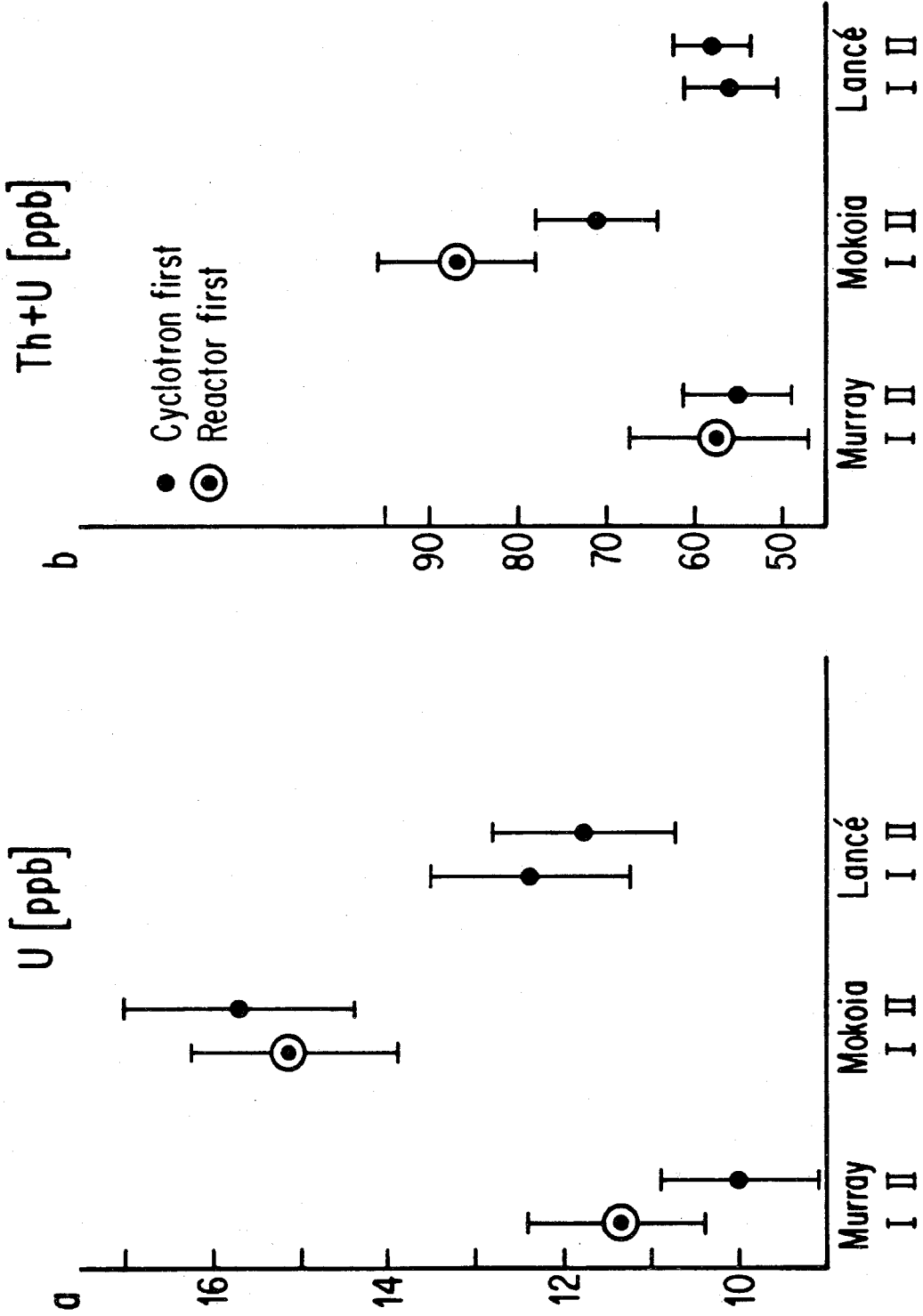
TABLE 9
BULK SPLIT ANALYSES

	<u>Irradiations</u> <u>(in sequence)</u>	<u>U (ppb)</u>	<u>Th + U (ppb)</u>
Murray I	Col-1; T-6I	11.4 ± 1.0	57 ± 10
II	T-6II; Col-2	10.0 ± .9	56 ± 6
Mokoia I	Col-1; T-6I	15.1 ± 1.2	89 ± 9
II	T-6II; Col-2	15.7 ± 1.3	71 ± 7
Lancé I	T-8; Col-3	12.4 ± 1.1	56 ± 5
II	T-8; Col-3	11.7 ± 1.0	58 ± 4

FIGURE 15

- a. Compares uranium measurements between splits of Murray, Mokoia, and Lance. Within one standard deviation errors all splits give identical U concentrations.
- b. Compares Th+U measurements between splits. Again, within 1σ errors all split pair analyses agree. (The largest discrepancy is observed for the Mokoia split samples. See text for discussion.) Data points are referenced as to whether the pellet was irradiated in the cyclotron or reactor first. No effect due to irradiation order is seen.

SPLIT COMPARISONS



correction factor equal to the average over the sample area is not applicable. The dose readings must be strictly over the area scanned. The tight mica/photo-emulsion coordinate fiducial system to relate positioning was not developed at this time. Thus it is possible that the error assigned to the dosimetry correction used in determining a [Th+U] concentration for Mokoia I is underestimated. The overall agreement of the sample pairs is strong reinforcement for the correctness of the track counting and dosimetry techniques. This is especially true for the Murray I and II samples irradiated in different cyclotron targets.

The data plotted in Figure 15 are identified as to whether the sample was irradiated in the reactor or the cyclotron first. No consistent effect is observed. As such no consistent effect due to irradiation contamination or volatilization is apparent.

2. Comparison with Isotopic Dilution Measurements

The instrumental nature of the fission track method permitted isotopic dilution measurements to be made on the same pellet samples. Three pellets-- Ivuna-a, Mighei C-2, and Murchison-5--for which we had measured respectively a high, low, and ~normal Th/U ratio were sent to M. Tatsumoto (USGS, Denver) for isotopic dilution analysis. The first three items in Table 10 show the comparison results. Here values reflect the sum of meteorite plus crushing blank (i.e., no mica contribution to the blank). A cursory glance suffices to show the agreement between the measurements by the two techniques is rather disappointing.

TABLE 10

FISSION TRACK/ISOTOPIC DILUTION COMPARISONS

SAMPLE	FISSION TRACK		ISOTOPIC DILUTION (Tatsumoto)	
	$\frac{U^* \text{ (ppb)}}{(Th + U)^* \text{ (ppb)}}$	$\frac{Th + U}{U}^*$	$\frac{U^* \text{ (ppb)}}{(Th + U)^* \text{ (ppb)}}$	$\frac{Th + U}{U}^*$
1. Ivuna - a	t: 4.5±.4 b: 4.2±.4	28 ± 3 27 ± 3	6.84	3.81
2. Mighe1 C-2	t: 8.8±.8 b: 9.2±.8	32 ± 3 32 ± 4	9.95	4.53
3. Murchison - 5	11.4±.9	66 ± 4	15.76	3.45
4. Mighe1 ME1456				
1) Mighe1 FM-1	1) 8.8±.8	41 ± 4		
2) Mighe1 FM-2	2) 9.9±.9	61 ± 5		
3) Reservoir			3) 8.46	5.52

TABLE 10 (continued)

SAMPLE	FISSION TRACK		ISOTOPIIC DILUTION (Tatsumoto)	
	$\frac{U^*}{U}$ (ppb)	$\frac{(Th + U)^*}{U}$ (ppb)	$\frac{U^*}{U}$ (ppb)	$\frac{(Th + U)^*}{U}$ (ppb)
5. Murchison-Melbourne				
1) Murchison - M	1) 8.5±.8	1t) 45 ± 5		5.3 ± .8
		1b) 42 ± 5		(4.9 ± .7)
2) Reservoir			2) 10.96	51.15
				4.67
6. Orgueil - 2216a				
1) Orgueil -2215a	1) 10.8±1.0	-----		-----
2) Reservoir			2) 10.20	41.93
				4.11

* Values listed are for meteorite plus crushing blank.

Table 11 summarizes the fission track-isotopic dilution comparison data of the three pellets as percentage differences. Any concentration difference larger than ~10% or (Th+U)/U ratio difference larger than ~15% exceeds the precisions of our fission track measurements. A positive percentage error value indicates the isotopic dilution number (I.D.) is greater than the induced fission track number (F.T.).

For the three pellet samples analyzed by both labs, two have measured U abundances that did not reproduce at the 2σ level, and in all cases the I.D. numbers are higher. The largest percentage difference in U values is for the Ivuna-a pellet where both sides of the pellet were F.T. analyzed. In actual concentration the 55% difference amounts to ~2.4 ppb. For Murchison-5 the 38% difference is equivalent to 4.4 ppb uranium. Overall these discrepancies are not understood, but the simplest explanation for the discrepancy in U measurements is contamination. The I.D. analyses were done after the F.T. analyses were completed, making the I.D. measurements more susceptible to contamination interference, although it would seem the F.T. analyses would be more susceptible to contamination since only the surface (10μ) of a pellet is analyzed. It is plausible that radiation damaged surfaces are more easily contaminated; but then some Th/U might be expected with regard to whether the cyclotron or reactor irradiation was done first. No such correlation is apparent.

The last three meteorite listings in Table 10 show I.D. measurements on crushed powder that was never pressed or irradiated. It should be noted that this reservoir powder material and the associated pellets are not true splits. Rather they simply have the common

TABLE 11
 FISSION TRACK/ISOTOPIC DILUTION
 MEASUREMENT DIFFERENCES

<u>Sample</u>	<u>ΔU</u>	<u>$\Delta [Th + U]$</u>	<u>$\Delta \left[\frac{Th + U}{U} \right]$</u>
Ivuna - a	+55% (2.4ppb)	-3.70 (1ppb)	-39%
Mighei C-2	+11% (1ppb)	+41% (13ppb)	+26%
Murchison - 5	+38% (4.4ppb)	-18% (12ppb)	-40%

$$\left(\Delta = \left(\frac{I.D.-F.T.}{F.T.} \right) \times 100\% \right)$$

heritage of coming from the same vial of crushed meteorite material with no attempt at further homogenization. The U results tend to lend some support to the contamination theory suggested above. For two out of the three powder to pellet comparisons the agreement is within the errors of the measurements. The Murchison-Melbourne I.D. analysis of the powder gives a higher U measurement than the F.T. pellet analysis.

The SMI correction factor applied to all pellet F.T. analyses for track counting efficiency systematically lowers all U concentrations by ~10%. If we are overcorrecting, the F.T. U values would increase by 10%--a factor not large enough to account for the F.T.-I.D. discrepancies.

In contrast to the large difference in uranium measurements, the [Th+U] values obtained by the two labs for the Ivuna-a pellet are identical. It is thus the difference in measured U that accounts for the higher F.T. compared to I.D. measured (Th+U)/U ratio. Because of the lower F.T. U value, F.T. analysis gives 20% (~4 ppb) more Th to the Ivuna sample than I.D. analysis. For the Murchison-5 pellet the F.T. [Th+U] concentration is higher (~20%) than the I.D. determined value. Combining these values with the U data for the Murchison-5 pellet implies the F.T. analysis saw 16 ppb more Th. The reverse trend in Th enrichment, however, is observed for the Mighei pellet where, although the U measurements are close for the two analyses, the I.D. [Th+U] value is 41% higher than the F.T. value. In this case the I.D. analysis measured 8 ppb more Th in the sample. Thus, there is no systematic differences between I.D. and

F.T. analyses for either (Th+U) or Th.

It should be recalled that an alternative explanation for apparent Th contamination in F.T. analysis is Pb contamination. The 4 ppb Th enhancement in the F.T. analysis of Ivuna-a could be explained by 10^{14} atoms/cm² of surface Pb contamination. For a sample containing 50 micron grains this would be equivalent to about 10 ppm Pb contamination. This seems large, but it cannot be totally excluded. The 16 ppb Th difference in Murchison-5 data requires 4×10^{14} atoms/cm² of surface Pb contamination. Pb contamination, however, cannot be the rule, since the I.D. Th measurement for the Mighei pellet was higher than the F.T. value.

Although the prime purpose of the I.D. measurements of the reservoir samples was to check the possibility of systematic differences in U concentration, comparisons of the [Th+U] data for two of the three vials of reservoir material can be made with pellet data. The two Mighei Me 1456 pellet samples give [Th+U] values of ~40 ppb and 60 ppb. The I.D. powder analysis at ~46 ppb falls within this rather wide range. The top and bottom pellet analyses for Murchison-Melbourne give [Th+U]~45 ppb, agreeing satisfactorily with the reservoir material analysis of [Th+U]~51 ppb.

The powder to pellet comparisons show either comparable Th abundances as measured by the two labs, or higher Th abundance for the I.D. analysis. Therefore, there is no consistent evidence for Th (or alternatively Pb) contamination systematically affecting the fission track analyses.

Up to now we have focussed on contamination as the possible

explanation for the observed F.T.-I.D. differences. If it did occur, it was not systematic in Th (or Pb). A stronger case could be made for post-F.T. analysis U contamination. It is the F.T. analyses, however, which are more sensitive to surface contamination.

Powder settling during the process of pellet making could lead to pellet compositional stratification. The discrepancies between I.D. and F.T. analyses would be expected to be systematic, however. Also, if settling had occurred, pellet top and bottom surface analyses should not reproduce well. As discussed in the previous section, excellent F.T. reproducibility was observed in pellet surface comparisons.

Migration of volatiles in the pellet (with the interior the hottest) due to irradiation heating could affect observed concentrations. If this were the case, a correlation with irradiation order (i.e., reactor or cyclotron irradiation first) would be expected. As discussed in the previous section (Fig. 15) and as will be seen in the following data summary (Fig. 16), no systematic irradiation order effect has been observed.

F.T. U values are based on assuming a normal U isotopic composition in the samples. The fact the F.T. U values are never higher than the I.D. measurements suggests the possibility of chondritic $^{238}/^{235}$ ratios higher than the normal terrestrial value. The F.T. measurement is on ^{235}U ; the I.D. measurement is on ^{238}U . In the case of the Ivuna-a pellet, the I.D./F.T measured uranium ratio is 1.6. Explanation of this difference by U isotopic variations requires a significant fraction of this meteorite to have a high $^{238}/^{235}$ ratio. This is

difficult to reconcile with bulk sample analyses in the literature. The reader is referred to Appendix VIII for a full discussion of meteoritic U isotopic variation measurements in the literature to date.

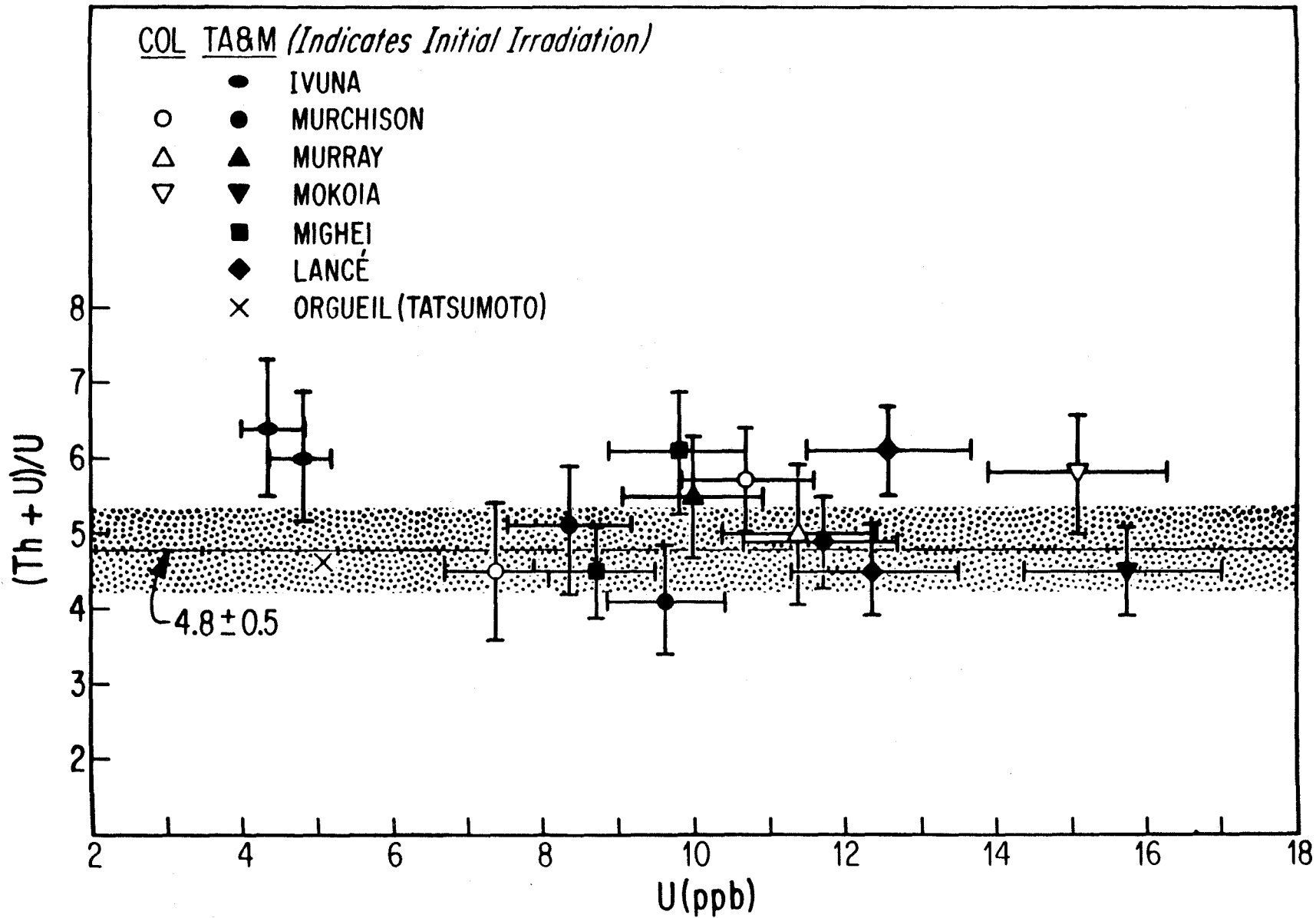
In summary, although relatively large differences were found between the isotopic dilution and fission track measurements, these do not appear to be systematic and are not easily explained. Some sources of error, e.g. the track counting efficiency (SMI) and cyclotron beam homogeneity, which are larger than originally hoped, have been evaluated and discussed in detail (see Sections II-F-1(b),(c); II-F-2(c); II-G-2; Appendix III ; Appendix V). A variety of tests of precision (Sections II-G-3,4; III-B-1) have been made and have indicated that error estimates are reasonable. The present data will be accepted at face value in the following discussion.

C. Summary of Bulk Sample Results

Figure 16 plots $(\text{Th}+\text{U})/\text{U}$ ratios against U concentrations for our "best value" suite of carbonaceous chondrite samples. Since our analyses measure $(\text{Th}+\text{U})/\text{U}$ ratios we shall use this quantity rather than Th/U in the discussion. The following samples have been excluded from figure 16: (1) All Ivuna grade e samples, i.e., those containing significant material from a fragment exterior surface, have been excluded. We have shown that exterior surface contamination can lead to apparently severely fractionated high ratios. A case presented for an Ivuna grade-e sample suggests either large Th contamination levels or, alternatively, Pb contamination. (2) Our two Allende pellet analyses have also been excluded from Fig.16. As discussed in the previous section, because of the difficulty encountered in proper bulk sampling of Allende on our pellet size-scale, our Allende data do not reflect true bulk $(\text{Th}+\text{U})/\text{U}$ ratios. Rather, the 3.5 to 6.5 range in the observed Allende pellet ratios suggests only a specialized sampling of this heterogeneous meteorite. Most importantly, it is unlikely that the bulk Allende Th/U has any significance in terms of defining the average solar system ratio. (3) Fig. 16 excludes all pellet samples made from samples our lab received as crushed powders. Our analyses of these pre-crushed samples cover the extremes (~ 3 to 9) in the range of $(\text{Th}+\text{U})/\text{U}$ ratios we measured. It is possible that the actual blank corrections for these samples may be outside the range of our own crushing blanks. The preliminary results presented in Stapanian et al. (1978) included the analyses of these pre-crushed samples. As such, the conclusion that the Morgan & Lovering (1968)

FIGURE 16

The bulk carbonaceous chondrite data are summarized in a plot of $(\text{Th}+\text{U})/\text{U}$ vs. U (ppb) [see text for samples excluded]. All but two of the 15 samples lie within 1 standard deviation of the normal terrestrial $(\text{Th}+\text{U})/\text{U}$ band. The remaining Ivuna and Lance samples plot less than two standard deviations from the normal band. The Tatsumoto isotopic dilution measurement of our Orgueil fragment lies well inside the normal band. Data points are identified as to reactor or cyclotron irradiation first. No effect due to irradiation order is observed.



2-6 spread in carbonaceous chondrite Th/U ratios (i.e., 3-7 spread in (Th+U)/U ratios) had been confirmed requires re-examination.

In Fig. 16 the "normal" range in (Th+U)/U ratios of 4.8 ± 0.5 has been dashed in for reference. Within their individual errors ($=1$ standard deviation $= 1\sigma$), thirteen of our fifteen CC analyses fall inside the "normal" band. One Lance sample out of the three measured lies 1.3σ above the "normal" band. Although rarer, Lance-like Allende- contains refractory Ca-Al rich inclusions. If the analogy to Allende applies, unrepresentatively high sampling of these inclusions in a Lance pellet could account for the slightly high ratio.

The other analysis which lies outside the "normal" band is an Ivuna sample. The measured ratio of 6.4 lies 1.2σ outside the normal band. Averaging the two Ivuna analyses (the top and bottom surfaces of a single pellet) gives a ratio of 6.3 ± 0.5 , a 2σ value from the "normal" band. The only other CI data point we have for comparison is an isotopic dilution analysis of our Orgueil fragment we requested from Tatsumoto. That Orgueil ratio of 4.63 lies well inside the "normal" band.

Because of the limits in precision of the fission track technique the goal of our bulk analyses was to confirm or refute the wide (2-6) range in Th/U ratios previously observed (M&L, 1968). Our "best value" results do not confirm this spread. Our results combined with recent high precision isotopic dilution measurements of CC's (Tatsumoto et al., 1976; Chen & Tilton, 1976), in fact, indicate strong coherence to the accepted "normal" range.

IV. Review of Allende Inclusions

Careful characterization of inclusions has been increasingly important for putting new information into a cohesive context amidst a rapidly growing data base. For this reason a brief summary is given here to familiarize the reader with the characteristics of the major inclusion types. This will help toward recognition of where the inclusions studied fit into already recognized categories, and where perhaps new or intermediate populations have been found.

The Allende meteorite is composed of ~60% matrix (largely Fe-rich olivine), ~30% Mg-rich chondrules, and ~10% Ca-Al rich inclusions (Clarke et al., 1970). Within each category classes and subclasses have been recognized based on refined knowledge of chemistry, mineralogy, and texture. Based on bulk chemistry, McSween (1977b) and Simon & Haggerty (1980) have defined chondrule classification schemes. Following McSween (1977b) inclusions fall into two basic categories: amoeboid aggregates (Grossman & Steele, 1976.) and the refractory-enriched Ca-Al rich inclusions (CAI). The CAI are categorized as coarse-grained or fine-grained (Grossman, 1975). Coarse-grained is used only in the relative sense since the grain size in these CAI seldom exceeds 1 mm, with typical grain sizes $<100 \mu$ (Wark & Lovering, 1978). As discussed in the Introduction, the coarse-grained inclusions, because of their refractory-rich bulk chemistry, mineralogy, and apparent primitiveness ($^{87}\text{Sr}/^{86}\text{Sr}$ age; presence of in situ ^{26}Al decay), have been the main focus for studies investigating early solar nebula condensation.

A. Coarse-grained CAI

For an excellent review article on Allende coarse-grained inclusions, the reader is referred to Grossman (1980). Table 12 (from Grossman, 1980) lists the chemical formulae of the minerals encountered in CAI. The coarse-grained CAI are classified as Type A or Type B (an intermediate population is defined as Type I). These classifications were originally based on mineralogical grounds mainly (Grossman, 1975) but have continued to be a workable scheme as continued chemical and petrographic information accumulates. Each CAI type has a distinctive rim sequence associated with it (Wark & Lovering 1977,1978), and inclusion classification can be made by rim identification alone. Because of the importance of rim structures observed in this thesis study we shall return to a more detailed rim discussion later.

Type A inclusions are made up of 80-90% melilite with spinel and perovskite as the other major phases. MacPherson & Grossman (1979) distinguish two Type A subtypes. The more abundant are termed "fluffy" Type A's. They are highly irregular in shape, heavily altered (as inferred from obscuration of textural relations between primary phases by veins of apparent secondary alteration products), and contain abundant cavities. "Compact" Type A's are more spherical in shape, less altered, and as the name implies, contain less void space. Grossman (1980) presents a detailed discussion of the textural and slight compositional differences between the two Type A subclasses. The textural features and intense alteration found in the "fluffy" Type A's lead MacPherson & Grossman (1979) to propose that these inclusions are the best candidates for gas to solid nebular condensates which have never

TABLE 12

CHEMICAL FORMULAE OF MINERALS MENTIONED IN THE TEXT*

<u>Oxides</u>	Corundum	Al_2O_3
	Hibonite	$CaO \cdot 6Al_2O_3$
	Perovskite	$CaTiO_3$
	Spinel	$MgAl_2O_4$
	Thorianite	ThO_2
	Baddeleyite	ZrO_2
	Magnetite	Fe_3O_4
<u>Silicates</u>	Wollastonite	$CaSiO_3$
	Rhönite	$Ca_4(Mg, Al, Ti)_{12}(Si, Al)_{12}O_{40}$
Melilite Series	Gehlenite	$Ca_2Al_2SiO_7$
	Akermanite	$Ca_2MgSi_2O_7$
Plagioclase Series	Anorthite	$CaAl_2Si_2O_8$
	Albite	$NaAlSi_3O_8$
Clinopyroxenes	Diopside	$CaMgSi_2O_6$
	Hedenbergite	$CaFeSi_2O_6$
	Fassaite	$Ca(Mg, Al, Ti)(Si, Al)_2O_6$
Olivine Series	Forsterite	Mg_2SiO_4
	Fayalite	Fe_2SiO_4
Garnets	Grossular	$Ca_2Al_2Si_3O_{12}$
	Andradite	$Ca_3Fe_2Si_3O_{12}$
Feldspathoids	Nepheline	$NaAlSiO_4$
	Sodalite	$3NaAlSiO_4 \cdot NaCl$

* Table from Grossman (1980)

been molten since accretion. The texture of the compact A's does not rule out a molten stage.

Most coarse-grained inclusion studies have been done on Type B inclusions. Grossman (1980) argues the abundance of Type B's relative to Type A's is not greater but, because a significant fraction of Type A's are only several tenths of a millimeter in size, sampling is biased toward the Type B's. Type B's are distinguished by high Ti-Al rich pyroxene (fassaite) content which makes up ~35-60% of the inclusion with melilite, spinel and anorthite as the other major phases. In contrast, ~50% of a Type I inclusion is anorthite. Melilite, Ti-pyroxene and spinel make up the rest of a Type I inclusion.

Type A's are medium-grained and often altered while Type B's are coarser-grained and often texturally zoned (distinguishing the B1 and B2 subclasses of Wark & Lovering, 1977). Type I inclusions are more fine-grained with a "chilled" texture (Wark & Lovering, 1978).

The SEM has introduced a new dimension to Allende petrographic work. Mineralogy studies have become micro-mineralogy (Hutcheon, 1977) as individual grains are part of a delicate complex local environment on a micron and sub-micron scale.

A major question is whether these inclusions have ever undergone a molten stage and to what degree. Under the physical conditions proposed for the solar nebula (Cameron & Pine, 1973) the liquid stability field is bypassed and direct gas to solid condensation occurs. Grossman & Clarke (1973) indicate that partial melting can be accomplished for pressures slightly above 10^{-3} and temperatures slightly above minimum solidus temperatures for these compositions.

The gaseous envelopes of giant protoplanets have been proposed as sites where pressure can be high enough to allow total melt condensation to occur (Podalak & Cameron, 1974). Blander & Fuchs (1975), on the other hand, argue that metastable, subcooled liquids could condense out as droplets under low pressure nebular conditions. The reader is again referred to Grossman (1980) for details of the textural arguments presented in this debate. Grossman, a vigorous advocate of direct solid condensation, concedes a partially molten stage for the coarse-grained CAI's may have been prevalent. In a trace element study of the coarse-grained inclusions Grossman & Ganapathy (1976a) find similar bulk REE abundances in Type A and Type B inclusions. Mineral separate analysis, however, indicates an internal partitioning of the REE between coexisting melilite and pyroxene that may be crystal structure controlled (Mason & Martin, 1974; Onuma et al., 1974). It was observed that melilites have a trend of decreasing REE enrichment with increasing atomic number and large positive Eu anomalies while the coexisting pyroxenes have a trend of increasing enrichment and negative Eu anomalies. The typical mean bulk coarse-grained inclusion REE pattern, however, is flat (Group I pattern of Martin & Mason, 1974; Mason & Martin, 1977). The average enrichment (~17 times chondritic Cl) is identical to that for a large suite of other refractory elements leading Grossman & Ganapathy (1976a) to propose a two stage model for REE distribution. The REE entered the inclusions as trace, refractory condensate phases but were subsequently redistributed among the major crystallizing phases after a melting event. It should be emphasized, however, that the rare earth distributions by themselves do not require the inclusions to be molten.

Models to explain the heterogeneous and exotic oxygen isotopic composition in CAI (Clayton et al., 1973; Clayton et al., 1977) are pertinent to the molten vs. anti-molten controversy. Clayton et al. (1977) propose that the observed non-equilibration of pyroxene and/or spinel oxygen composition with that of melilite in Type B's need not rule out total melting. Differential relative oxygen diffusion rates between the coexisting phases during alteration could explain the observed isotopic heterogeneity.

Trace element analysis has been of key importance in supporting views for high temperature origins of inclusions. Palme & Wlotzka (1976) found an Fe-Ni-S particle in a Type B inclusion which contained high concentrations of Mo, Ru, Rh, W, Os, Ir and Pt. Taken literally, the Grossman (1973) calculations predict that Pt metals and some refractory oxides (MoO_2 , ZrO_2) would condense at high temperatures. Interpretation of the particle as high temperature in origin was debatable because of the Fe-Ni-S affiliation. A stronger case for refractory condensates could be made from the SEM analyses of four trace phases in Type B inclusions, all less than 2 microns in size and enriched in the rare earth elements (REE), Th, U, Nb and Zr (Lovering et al. 1976, 1979). In a Type A, Wark & Lovering (1976) analyzed ten refractory siderophile-rich alloys ranging in size from 0.5-3 microns. El Goresy et al. (1977, 1978) determined two modes of refractory trace metal occurrence. They can occur as individual 1-2 micron metal nuggets, some as single pure phase (e.g., Ir, Pt, Os), or as "Fremdlinge", a complex aggregate ~3-15 microns in size consisting of smaller grains (down to submicron-sized) of metal

alloys, sulfides, phosphates, oxides and silicates. Wark & Lovering (1978) observed that nuggets found in the same host melilite crystal in a Type A inclusion are closer in composition to each other than nuggets from different host crystals. This can be used to argue against a molten stage in the inclusion history. Interpretation of the Fremdlinge compositions as primary condensate (El Goresy et al., 1978) necessitates chemically distinct reservoirs, possibly even pre-solar. Alternatively, the Fremdlinge could be primary condensate altered after enclosure in the host phase (Wark & Lovering, 1978). Both El Goresy et al. (1978) and Wark & Lovering (1978) find that within an individual metal nugget, Mo, Ru, Rh, W, Re, Os, Ir and Pt relative abundances are roughly chondritic. Blander et al. (1980), however, found Pt-metal nuggets in a Type B inclusion where this was not true for the refractory siderophiles.

B. Fine-grained CAI

Because of the extremely fine-grained nature of these inclusions, mineral identifications for the most part are made using X-ray powder diffraction techniques. Following the discussion in Grossman & Ganapathy (1976b) spinel and pyroxene have been recognized in all fine-grained inclusions. Sodalite and nepheline, on the average make up ~20% by mass of the fine-grained inclusions. Grossular is also a common phase as is possibly melilite. Plagioclase and olivine are rarely detectable. The CAI are often referred to as white inclusions. Reference to pink or purple fine-grained inclusions reflects coloration

from higher concentrations of spinel and/or grossular doped with trace amounts of transition metals (Grossman & Ganapathy, 1976b).

The origin of nepheline & sodalite are unclear. Following the discussion presented in Grossman (1980), neither nepheline nor sodalite can condense from a gas of solar composition at equilibrium. If nepheline and sodalite are condensates, the reacting gas was not solar. On the other hand, if nepheline and sodalite are alteration products, the alteration process was not an equilibrium one. The alkali content and high mean Fe content of the inclusions (=6.1%, presumably as FeO in spinel and pyroxene due to absence of metallic Fe-Ni and troilite) suggest a lower temperature origin for the fine-grained CAI than the coarse-grained CAI (Grossman & Ganapathy, 1976b).

As mentioned in the introduction and touched upon in the previous section, coarse-grained inclusions show a fairly uniform enrichment (factor of ~17 over Cl levels) in the refractory lithophile and siderophile elements. Also the majority have a flat REE distribution pattern (Grossman & Ganapathy, 1976 ; Grossman et al., 1977). In contrast the fine-grained CAI's show complex enrichments in the lithophile elements (Grossman & Ganapathy, 1976b). Refractory lithophile element abundances (Ca, Sc, Ta, and REE) are a factor of 5-30 higher than Cl chondritic levels. In addition volatile lithophiles (Na, Mn, Fe, Zn, Chlorine) are enriched by factor of 4-14 in the fine-grained inclusions relative to the coarse-grained ones. The coarse-grained inclusion Cl and Zn, however, are based on a single analysis (Wanke et al., 1974). Unlike the Group I (Mason & Martin, 1977) flat REE patterns of coarse-grained CAI, fine-grained inclusions typically

exhibit the Group II fractionated patterns. The light REE are more enriched in fine-grained than in coarse-grained inclusions, while the heavy REE are less enriched (See Fig. 1 in Introduction).

The observation of low temperature mineralogy (nepheline, sodalite) with refractory element enrichments might suggest that fine-grained inclusions are a mixture of high and low temperature materials (absence of abundant olivine indicates a temperature hiatus if the condensation sequence is taken literally). It is difficult, however, to reconcile the fractionated refractory element contents with this model, assuming the coarse-grained inclusion patterns are not fractionated. As an alternative Grossman & Ganapathy (1976b) suggest the fine-grained inclusions resulted from incomplete non-equilibrium condensation. If the cooling rate was rapid compared to diffusion and reaction rates (as the fine-grained texture might suggest), or if early formed phases were buried, incomplete and non-equilibrium condensation could occur.

Boynton (1975) models the fractionated REE pattern observed in a single fine-grained inclusion by removal from the gas of an early high temperature phase enriched in the heavy REE. To mimic the REE pattern observed, Boynton's model requires highly non-ideal solid solution of the REE during condensation. In contrast, Davis & Grossman (1979) developed models for REE condensation which can explain the fractionated REE patterns of 20 fine-grained inclusions under ideal solid solution condensation. They favor a two component model where one component is the gas remaining after removal of an early high temperature phase, and the second component is a material

uniformly enriched in all REE.

Citing a consortium study (to be published, in Allende Meteorite Reference Sample, eds. E. Jarosewich & R.S. Clarke, Jr., Smithsonian Contrib. Earth Sci.), Grossman et al. (1979) discuss the finding that bulk Allende has a fractionated REE pattern, with light REE slightly more enriched than many of the heavy REE. This indicates fine-grained inclusions may contain a large fraction of the total Allende REE, and argues against a model where the fine grained inclusion REE components are a small residual fraction, left behind after the condensation and loss of a very high temperature (heavy REE-rich) fraction.

C. Amoeboid olivine aggregates

Following the description presented in Grossman et al. (1979) the major amoeboid inclusion constituent is olivine of variable composition (Fo₆₄-Fo₉₉). Nepheline and sodalite are common. Characteristic coarse-grained inclusion phases such as spinel, perovskite, Ti-Al rich pyroxene and anorthite can also be found surrounded by coarser-grained olivine. The conglomeratic structure and heterogeneous composition of adjacent grains suggests these inclusions may never have been molten (Grossman et al., 1979; McSween, 1977 b).

Most amoeboids have high Os, Ir and Ru abundances compared to Cl chondritic, nevertheless they are a factor of 5.4 less than the levels found in coarse-grained inclusions (Grossman et al., 1979). Out of 10 amoeboid aggregates studied, Grossman et al. find 7 have average refractory element abundances depleted by a factor of 0.212 ± 0.029

relative to coarse-grained refractory elements abundances.

Most amoeboid inclusions show Group I REE patterns similar to coarse-grained inclusion patterns, but there are some amoeboid inclusions which exhibit the more fractionated patterns indicative of most fine-grained inclusions. These observations led Grossman et al. (1979) to propose that amoeboid inclusions accreted from fractions of coarse-grained and fine-grained inclusion material. These fractions remained finely subdivided and suspended in the nebula until the temperatures fell to where FeO-rich olivine became stable.

D. Olivine and Pyroxene-rich Chondrules

Simon & Haggerty (1980) recognize six types of Mg-rich chondrules. In order of decreasing abundance they are: anhedral olivine chondrules, recrystallized olivine chondrules, euhedral olivine chondrules, glassy-skeletal olivine chondrules, barred olivine chondrules, and pyroxene-rich chondrules. In all except one of the chondrules they analyzed, the olivine compositions ranged from $Fa_{1.1}$ - $Fa_{9.8}$. The exceptional case had $Fa_{24.1}$. Compositional zoning of olivine within individual chondrules is typical with core olivines $\sim Fa_{2.0}$ and rim olivines $\sim Fa_{6.0}$ (Simon & Haggerty, 1979). Except for one chondrule in the Simon & Haggerty (1980) study, the pyroxenes are clinoenstatite confined to a narrow compositional range. The exception contained Ca-rich pyroxenes. Variations in the glassy mesostasis compositions and differences in total inclusion modal abundances accounted for

most of the observed variations in bulk chemistry. Pyroxene chondrules have the highest Na_2O content of all the chondrule classes, low MgO , high Al_2O_3 , and because clinoenstatite was usually observed, and, relative to the other Mg-rich chondrule types, an intermediate CaO content. Because of their higher glass content, barred chondrules exhibited the highest TiO_2 , Al_2O_3 , and CaO contents.

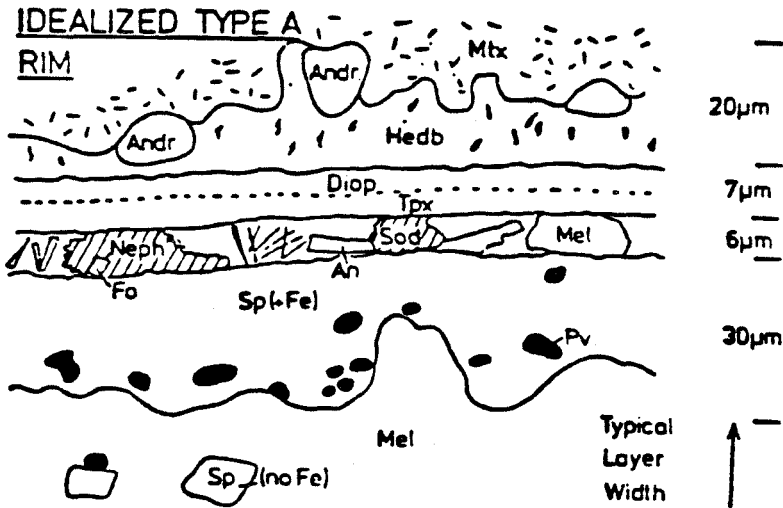
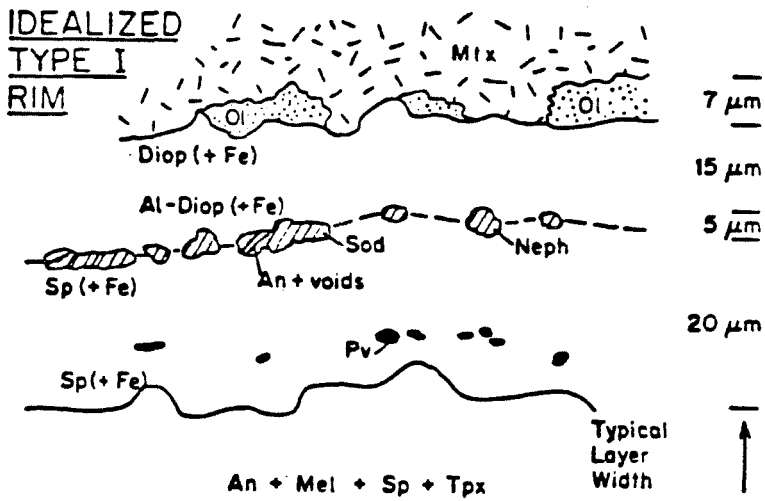
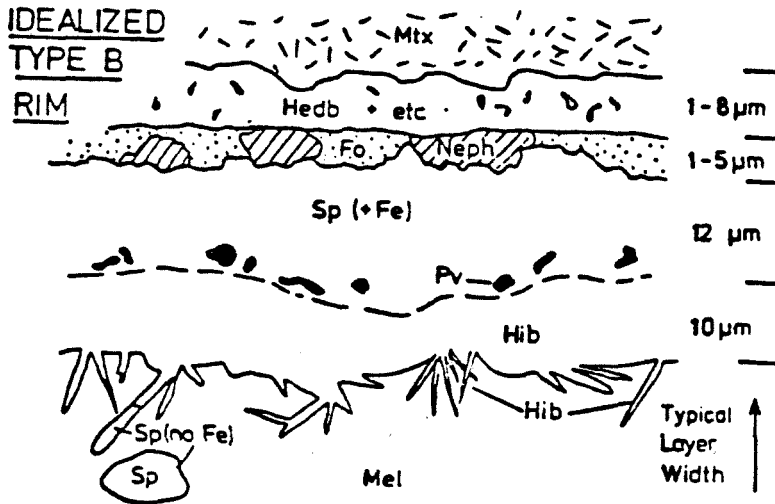
Based on good correlations in two element plots, Simon & Haggerty (1980) propose that the chondrule suite, omitting the barred chondrules, represents a possible fractional crystallization or partial melting sequence with pyroxene chondrules the most highly evolved. Because the inferred parent liquid for barred chondrules would be quite refractory (i.e., Ca-Al-Ti-rich), Simon & Haggerty (1980) suggest a more primitive and totally independent petrogenesis history for the barred chondrules. As such, barred chondrules may be an important component in linking early (CAI) to late stage (olivine chondrule) nebular condensation.

E. CAI Rims

Wark & Lovering (1977, 1978, 1980b) present evidence for the apparently universal rimming of all coarse-grained CAI. They observe rims covering rounded inclusion surfaces and note their absence on fractured angular surfaces. This would imply that the CAI were originally completely rimmed. Distinctive rim sequences are associated with Type A, B, and I inclusions that allow identifications to be made based on rim descriptions alone. Figure 17, taken from

FIGURE 17

This sequence of illustrations shows the idealized rim structures associated with the different types of coarse-grained Ca-Al-rich inclusions (figure taken from Wark & Lovering, 1978).



from Wark and Lovering (1978)

Wark & Lovering (1978), summarizes the rim sequences for each coarse-grained CAI type. Textural and chemical evidence is presented in Wark & Lovering (1977) that argues strongly against these rims resulting from matrix reaction. Type A inclusions exhibit the most clearly defined rims. The rim order, going outwards from the interior, is: Fe-bearing spinel → nepheline + sodalite + voids → Ti-Al pyroxene → diopside → hedenbergite + andradite. This order violates the sequence predicted by thermodynamic equilibrium models indicating that successive layers are not condensates from a progressively cooling nebula. The position of the nepheline-sodalite plus void layer is particularly hard to understand since these minerals are not stable above 1100°K while the outer layer pyroxenes are. Wark & Lovering (1977) argue that the crystal-void texture of the feldspathoid rim layer suggests vapor deposition. They later revised their thinking and reinterpret this layer as having been originally melilite which was altered to the presently observed mixture of secondary phases and voids (Wark & Lovering, 1980b). This alteration, they suggest, could explain the the Fe-enrichment in the interior spinel layer.

Within 50 microns of the rims of almost all Type A's and B's the melilite composition becomes more refractory (i.e., gehlenitic) in composition (Wark & Lovering, 1980b). Unless the compositional change reflects an inward crystallization, alternative explanations (solid condensate or subsolidus metamorphism) would require an increase in the nebular T or some corresponding decrease in pressure.

Wark & Lovering (1980b) suggest the differences between the Type A and B rim sequences, relate to differences in the T,P conditions

during formation. Wark & Lovering (1980b) discover two composite CAI's where in each case a Type A encloses a Type B inclusion. They propose this as "unequivocal" evidence for an increase in T (or decrease in P) during condensation. The consistent A,B rim dichotomy suggests the different CAI types were formed and kept separate until after rimming.

A fascinating link between fine-grained aggregates and coarse-grained inclusion rims is presented in Wark & Lovering (1977,1979). They observe that the fine-grained inclusions themselves are not rimmed but the individual 10-100 micron grains which make up the inclusions are. The individual microscopic layering of these grains, so-called Type F bodies, is essentially identical in composition (except for an underabundance of hedenbergite and andradite) and sequence to the Type A rims. Wark & Lovering (1980b) argue that assuming Type A inclusions condensed before their rims and hence before Type F bodies, they would have depleted the condensing reservoirs of refractory trace elements. This could account for the fractionated Group II patterns observed in fine-grained inclusions. This should have serious implications for refractory trace elements in the CAI rims as well. We shall pursue this point during the discussion of our Th/U Allende results.

V. Allende Inclusion Results

A. Remarks on Allende Inclusion Analysis

Because of the refractory nature of the Ca-Al rich inclusions (e.g., Marvin et al.(1970), Martin & Mason (1974), Grossman (1975)) candidates for these inclusions were singled out for analysis by pre-irradiation visual inspection. Post-irradiation low magnification inspection of the etched section micas for areas of fission track enrichment was used to target other inclusions for study. This proved enormously satisfying in broadening the categories of refractory inclusions.

Track scanning was done on a Leitz Ortholux microscope with a precision x-y stage which gives position readings in 1 micron units. Actual point relocation capability using stage coordinate readings alone is better than 25 microns. Coordinates of at least three fiducial scratch locations near the inclusion of interest (based on sample/mica fiducial photography) were recorded to serve as the reference points for mica/sample position control. Scanning was done at 1250x. A 20 x 20 eyepiece grid allowed mapping of track structures within each ~115 micron field of view. A single scan would always begin on a fiducial line and usually end on one, with each start and stop position recorded. Typically position readings were recorded at intervals of no less than every 5 fields of view (575 microns). The fiducial photography was used to correlate the cyclotron mica track scan maps with the reactor track scan maps. The fine detail in the track maps, e.g., distinctive track "star" patterns, that could be correlated between the two track maps was

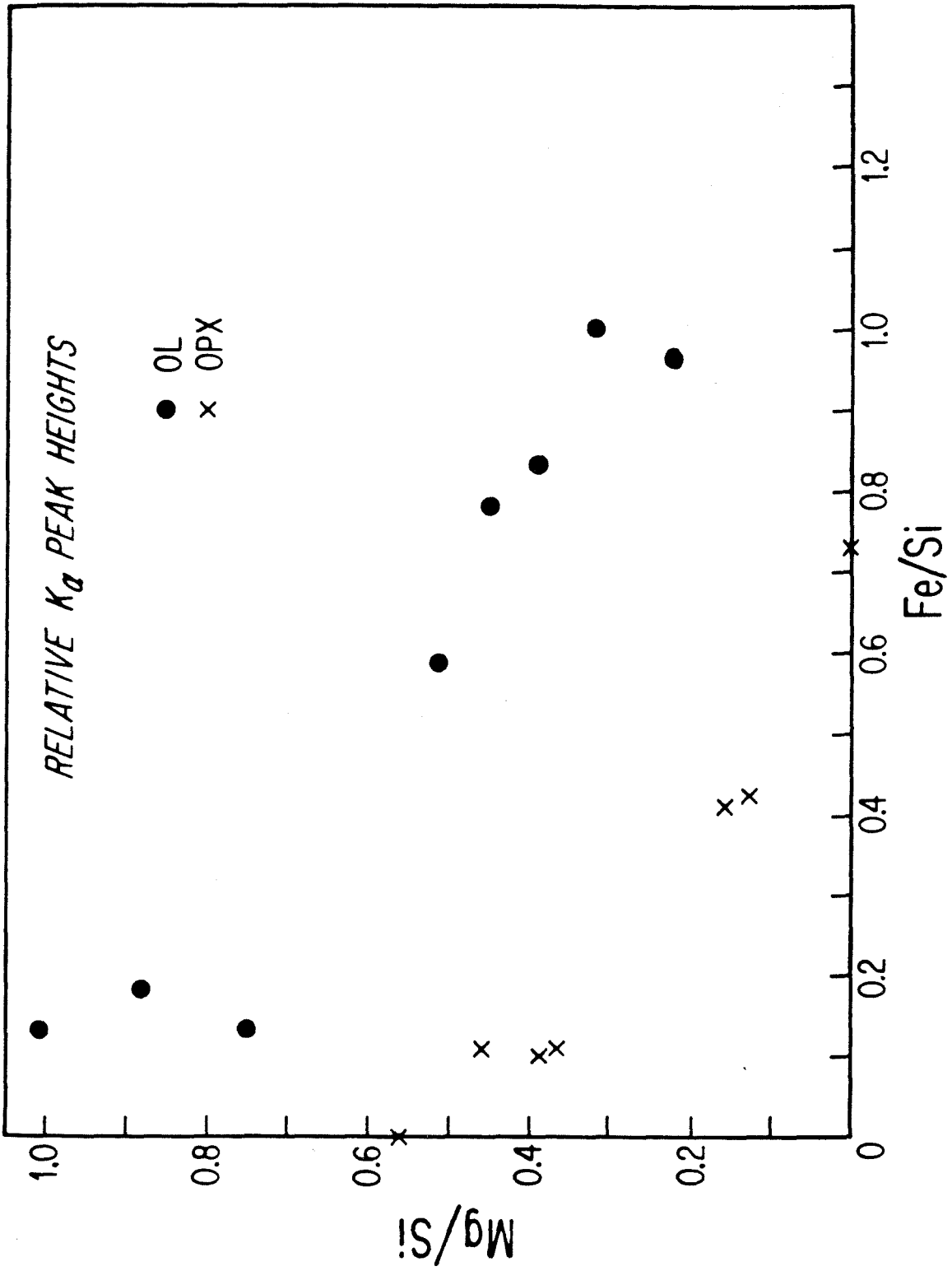
used to refine the alignment. Correlation of more than one star can theoretically lead to location controls better than the range of a fission fragment.

Location control in our dosimetry maps was excellent. A flat 4% uncertainty in the dose correction factor was applied based on average uncertainties for the pellet samples. The only blank correction applied to section sample data analysis is the U,Th content of the micas. Quantitative U and Th analysis is only possible for grains large compared to the range of a fission fragment ($\sim 10\mu$).

Mineral identifications were made from X-ray spectra obtained with an SEM. The 15 keV electron beam has a penetration depth of ~ 3 microns. Positive mineral identifications were made by referencing spectra to mineral standard spectra. J. Woodhead (Caltech) provided us with a suite of synthetic melilite glasses of varying composition to catalogue melilite X-ray line peak ratios. In addition an Allende melilite grain separate (Ak₅₀) was provided by J. Huneke & G. Wasserburg. In order to distinguish olivine from orthopyroxene, relative X-ray spectral peak heights were measured for a range of compositions and plotted in Fig. 18. The plots show distinctive olivine and orthopyroxene trends against which unknowns can be compared. Element beam scans were used to aid in defining the inclusion boundaries as well as areas of compositional zoning within the inclusion. Electron microprobe analyses were performed on selected areas for quantitative compositional measurements. Small grain size ruled out general probe use. The SEM 15 keV electron beam has a penetration depth of $\sim 3\mu$. Therefore, grain size must be at least $\sim 3\mu$ to obtain

FIGURE 18

In order to distinguish olivine from orthopyroxene based on SEM X-ray spectra, the relative peak heights for Mg/Si vs. Fe/Si are plotted for olivine and orthopyroxene samples of known composition. Within the scatter of the data, distinct olivine and orthopyroxene fields are observed.



clean spectra using the 15 keV beam. The fine-grained nature of many of the U,Th rich regions and the complicated compositional variability in what visually appear to be single grains (see e.g., Hutcheon,1977) often made precise identification difficult. Also for inclusions such as the Type B's described by Lovering et al. (1979), where the carrier actinide phases are in the 1.5 micron range, definite identifications of the carrier phase may be difficult. Rather, statements of the mineralogy associated with U or Th enrichments can be made.

In the following section, each inclusion is individually discussed. Petrographic descriptions are accompanied with results from our track analyses. The inclusion names are of the form All X-n-Y, with All representing Allende, X-n referring to the section and Y to the individual inclusion.

B. Allende Inclusion Descriptions and Th/U Results

1. Allende C-5-A: This is a broken 500 micron barred olivine inclusion, probably a chondrule fragment, rectangular in shape, with an 80 micron wide blocky rim surrounding a barred rectangular core (see fig. 19a). Electron microprobe analysis reveals a rim composition of Fog_4 olivine with patches of low Ca-pyroxene. In reflected light the barred core appears as alternating ~7 micron wide light bands and ~3 micron dark bands. Light lamellae are typically Fog_2 olivine with some intergrowth of low Ca-clinopyroxene. By analogy to features described by Simon & Haggerty (1980) and McSween (1977b) the dark lamellae are probably glass, the composition of which is Ca-Al rich and low in Na. There is possibly some sodalite in the dark lamellae. Table 13 lists electron microprobe analyses for several points taken on the dark lamellae. Lamellae compositions are not homogeneous across the entire inclusion as indicated by the dashed lines in Fig. 19. In the right hand side of the inclusion this band structure is frequently obscured by overgrowths of a low Al, high Ca silicate phase with a garnet-like X-ray spectrum. Because of the lamellar context, however, this low Al, high Ca silicate phase is probably a glass. Peppered throughout the core are 10 micron trapezoidal iron-chromium rich spinels wedged between or incorporated along the lamellae. Table 13 lists a microprobe analysis for one of these spinels.

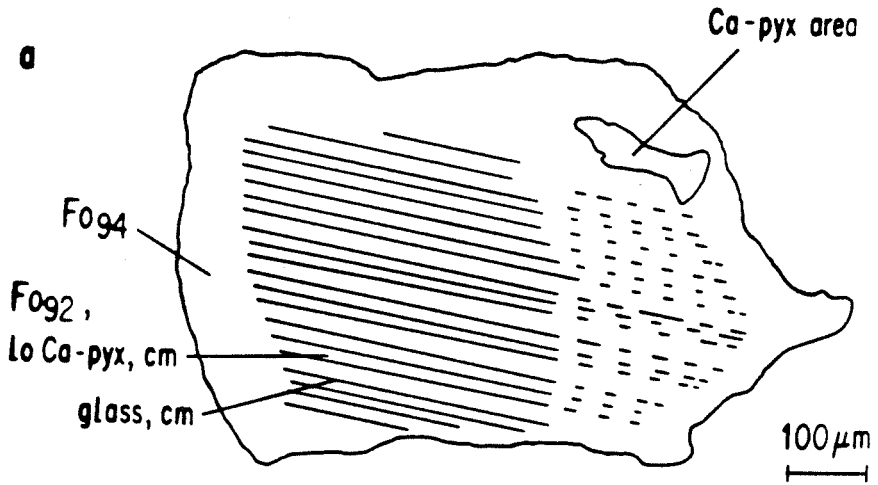
Fig. 19b illustrates the overall uranium fission track pattern over the inclusion. The track densities over the cyclotron-irradiated micas are too low to permit low magnification mica to section correlation.

FIGURE 19

a. Illustrates the general configuration of this barred olivine fragment. The rim is mostly olivine with one corner containing diopside and sodalite. The interior is composed of alternating lamellae of a Ca-Al-rich, Na-poor glass and bands of olivine with low Ca-pyroxene. Chromite grains, often trapezoidal in shape, are associated with both lamellae. The dashed lines indicate a region where the lamellae are ill-defined.

b. Illustrates the U track distribution pattern over inclusion All-C-5-A. Th and U enrichments are observed in the barred core. Because of the fine size of the lamellae, the U,Th carrier cannot be specifically identified, but the glass is the most probable carrier. The Ca-Al-rich corner of the rim, although enriched in U, does not show a comparable Th enrichment.

Allende C-5-A



Allende C-5-A

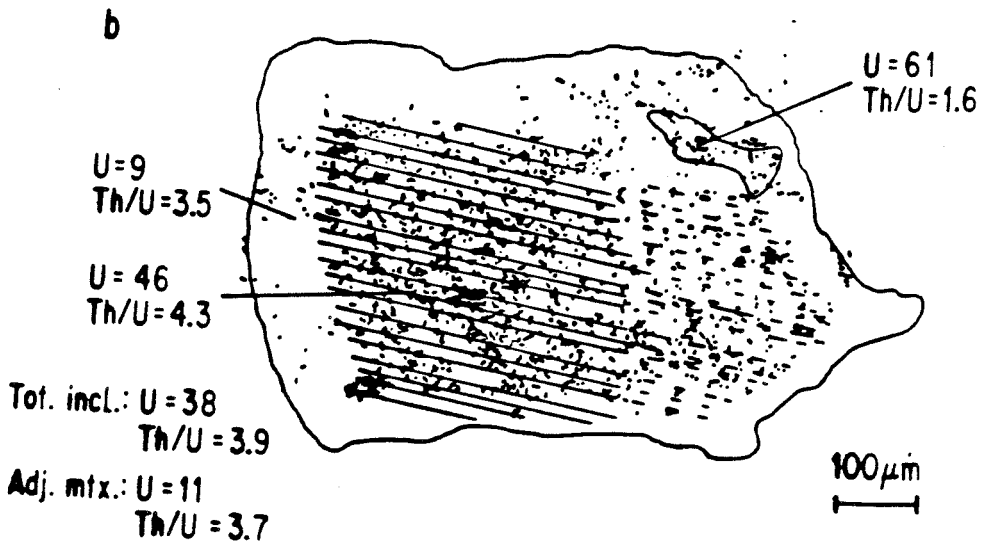


TABLE 13
ELECTRON MICROPROBE ALLENDE C-5-A

ANALYSES (WEIGHT %)

a. Dark Lamellae

	<u>1</u>	<u>2</u>	<u>3</u>
Na ₂ O	0.28	0.36	0.49
MgO	15.5	15.0	6.52
Al ₂ O ₃	10.97	29.23	30.90
SiO ₂	50.49	45.65	45.39
CaO	12.78	11.05	16.08
TiO ₂	0.76	0.24	0.08
Cr ₂ O ₃	0.55	0.53	0.07
MnO	0.08	0.05	0.00
FeO	<u>0.67</u>	<u>3.48</u>	<u>0.57</u>
TOTAL	92.08	105.56	100.10

b. Spinel

MgO	23.11
Al ₂ O ₃	53.6
SiO ₂	0.27
K ₂ O	0.016
CaO	0.10
TiO ₂	0.57
Cr ₂ O ₃	17.67
MnO	0.10
FeO	<u>6.78</u>
TOTAL	102.22

No stars are observed in the track patterns, nor, because of the scale of the lamellar structure, is any lamellar structure seen in the uranium enriched core. A "clean" olivine rim area has a uranium content of 8 ± 1 ppb with $\text{Th/U} = 4.3 \pm 1.3$. A $150 \mu \times 40 \mu$ fine-grained Ca-Al rich corner of the rim contains pyroxene grains ($< 7 \mu$), some with pure diopside spectra, and sodalite. The identification of sodalite is based on comparison of the observed X-ray spectra with the Cl-rich phase found in our Ca-Al rich inclusions. Sodalite has been documented as the Cl-bearing phase in literature descriptions of CAI of the same type. To our knowledge, this is the first occurrence of sodalite in what would normally be regarded as an olivine chondrule fragment. In U and Th content this Ca-Al rich rim area is distinctive with $\text{U} = 61 \pm 6$ ppb and $\text{Th/U} = 1.6 \pm 0.5$. The barred core has $\text{U} = 46 \pm 2$ ppb and $\text{Th/U} = 4.3 \pm 0.4$ with the glass being the most probable actinide carrier. Total inclusion values are $\text{U} = 38 \pm 1$ ppb and $\text{Th/U} = 3.9 \pm 0.3$. The adjacent matrix has $\text{U} = 11 \pm 1$ ppb and $\text{Th/U} = 3.7 \pm 0.7$.

2. Allende C-5-B is a 250 micron fragment composed primarily of Ca-rich pyroxene, possibly a broken chondrule (fig. 20). Angular to subrounded 30-150 micron long diopside grains are situated in a fine-grained, and, in places, porous matrix. Electron microprobe analyses of eight large diopside grains are tabulated in Table 14. Figure 21 plots these pyroxene analyses with pyroxene analyses from other Allende inclusions and other chondrites. The compositional variation in Figure 21 reflects real differences in the Ca/Mg ratio, as shown by Table 14, rather than the effects of other pyroxene components.

FIGURE 20

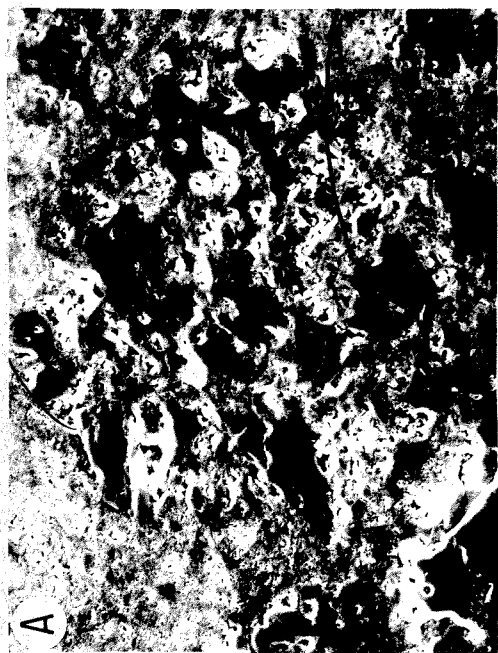
- a. This SEM secondary electron photograph of the inclusion All C-5-B shows coarse pyroxene crystals in a fine-grained porous matrix.

- b. The All C-5-B diopside grains are defined by this Ca X-ray beam scan of figure (a).

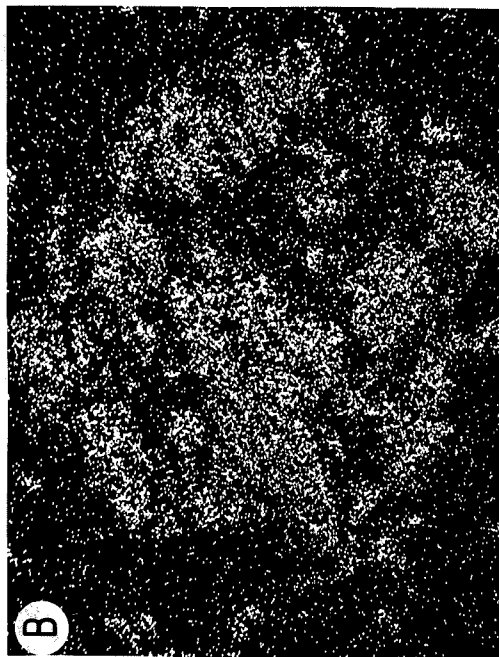
- c. The Fe X-ray beam scan photo of figure (a) shows Fe enrichment in the fine-grained interstitial material.

- d. This sketch of the inclusion shows the diopside grains and the outline of the inclusion boundary superimposed on the U track distribution pattern. The track-rich areas are correlated with the fine-grained, Fe-rich interstitial material.

ALLende C-5-B



Ca



Fe

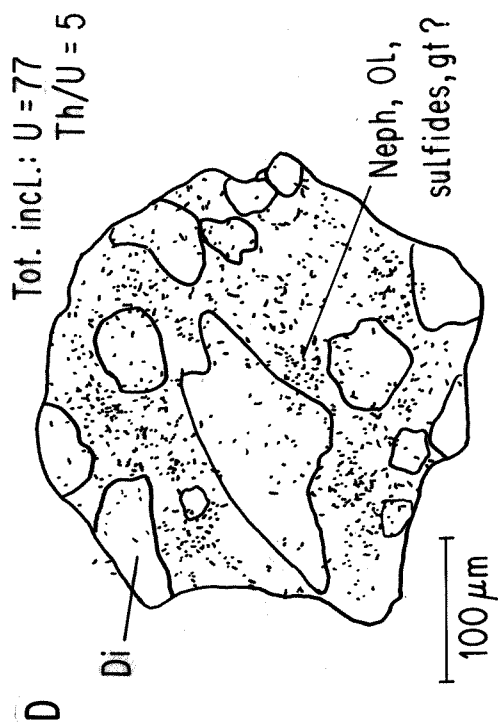
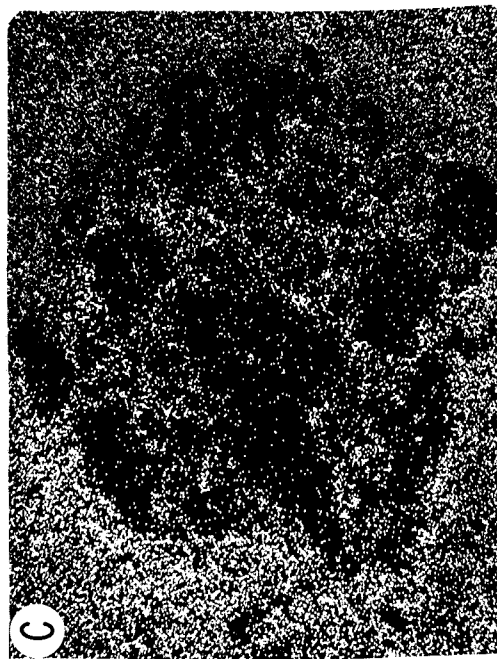
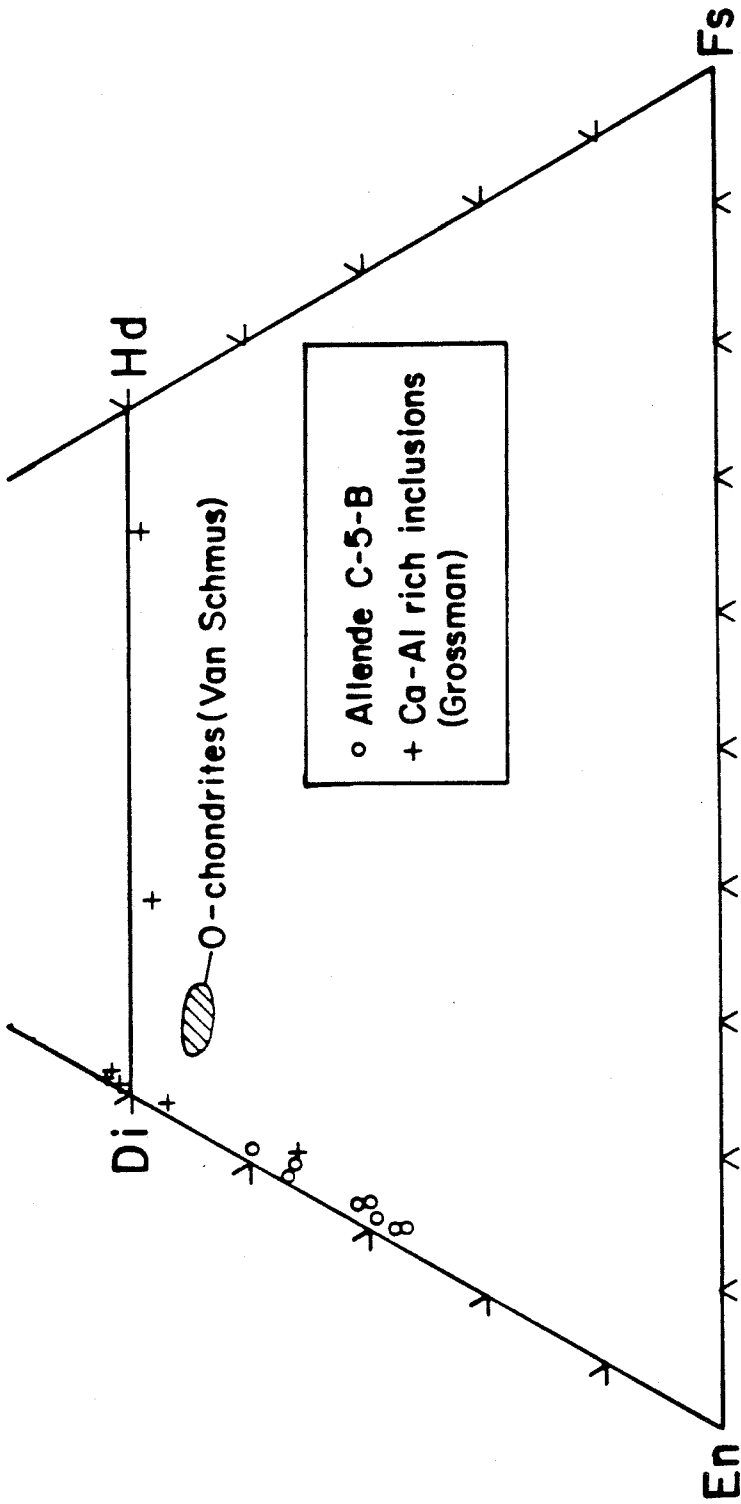


TABLE 14
 ELECTRON MICROPROBE ANALYSES
 OF ALLENDE C-5-B CLINOPYROXENES (WEIGHT %)

	<u>1</u>	<u>2</u>	<u>3</u>	<u>4</u>	<u>5</u>	<u>6</u>	<u>7</u>	<u>8</u>
Na ₂ O	0.026	0.003	0.034	0.009	0.000	0.055	0.000	0.000
MgO	25.442	20.858	24.337	25.570	22.115	26.333	24.721	22.320
Al ₂ O ₃	1.624	2.500	2.048	2.290	2.506	1.623	1.989	2.560
SiO ₂	56.555	54.447	55.043	56.127	55.410	56.230	56.533	56.261
CaO	15.955	20.799	16.138	15.095	19.687	14.692	16.967	19.576
TiO ₂	0.597	0.955	0.999	0.731	0.813	0.546	0.678	0.808
Cr ₂ O ₃	0.724	0.532	0.942	0.554	0.617	0.656	0.578	0.549
MnO	0.293	0.198	0.517	0.134	0.210	0.180	0.144	0.150
FeO	<u>0.544</u>	<u>0.482</u>	<u>0.611</u>	<u>0.518</u>	<u>.500</u>	<u>1.065</u>	<u>0.672</u>	<u>0.676</u>
TOTAL:	101.760	100.773	100.670	101.030	101.858	101.380	102.281	102.901

FIGURE 21

The pyroxene compositions observed in All C-5-B are plotted on a pyroxene quadrilateral. For comparison pyroxene analyses from other studies are also plotted illustrating the rarity of chondrite pyroxene compositions similar to All C-5-B.



Although more closely related to clinopyroxenes from Allende CAI's, the All C-5-B diopside grains appear to be fairly unique. We shall return to this point in the discussion section. Analysis of the interstitial material is difficult. SEM spectra for nepheline, Fe-Ni sulfides, olivine, possibly two garnets (pyrope, and Ca-rich garnet), as well as an unidentified highly aluminous phase are present in this interstitial material.

Fig. 20d shows the track distribution pattern over the chondrule. In fact it was the observed track enrichment which drew our attention to this chondrule. The U and Th track maps exhibit a patchy pattern that can be definitely correlated with the fine-grained material. Total inclusion values are $U=77\pm 3$ ppb and $Th/U=5\pm 1$.

3. Allende C-5-E is a millimeter-sized amoeboid inclusion (see Grossman & Steele (1976), fig. 1, for illustration of inclusions of similar type) with abundant olivine ranging from 100 micron subrounded fragments to fine-grained matrix material. Pyroxene is also abundant, with a wide range in composition (diopside, enstatite, Fe-rich, and low Ca-pyroxenes). Fe-Ni sulfides (sometimes with accompanying Cr) are found in the fine-grained matrix as well as incorporated in olivine grains. Nepheline and, less frequently, sodalite can be found in the matrix but are more often found as dark veinlets in pyroxene complexes (probably altered pyroxene crystals).

No stars were observed in the track maps, but there is structure. Areas of Th and U enrichment are associated with the above described

feldspathoid- and pyroxene-complexes. One 4 micron Ca-phosphate rich area was discovered, but there was no outstanding corresponding feature in the track map. Total inclusion values are $U=12.5\pm0.4$ ppb and $Th/U=4.2\pm0.3$. Adjacent matrix has $U=11\pm1$ ppb and $Th/U=4\pm1$.

4. Allende D-2-A would have never been singled out for study had the track maps not shown a U,Th enriched feature. Because of its overall finegrained nature, it is difficult to visually distinguish from matrix. Fig. 22a is a SEM backscattered electron photograph of the inclusion. We had to use a Ca x-ray scan of the area (Fig. 22b) to outline the inclusion boundaries. These inclusion boundaries are also drawn in the Al and Fe beam scan photos (Figs. 22 c and d).

A schematic of the inclusion is drawn in Fig. 23a. All D-2-A is a 500 micron broken inclusion exhibiting a definite layered structure. The 50 micron outermost lobate rim has a typical grain size of ~5 microns and is composed of Ca-rich pyroxenes (Ca-Fe pyroxene and diopside) with accessory nepheline and olivine.

The next layer is a well-defined scalloped-shaped high-Al rim. Fig. 23b is the companion U track map to Fig. 23a. As can be seen it is in this Al-rich rim that the U and Th are concentrated. Nepheline is the major aluminous phase. Also present are very small grains of an unidentified high aluminum phase. Fe-Ti-oxide grains up to 4 microns in size are abundant in this rim, but are rare elsewhere. In several cases these grains exhibit a small Ca peak which may suggest a past perovskite association.

FIGURE 22

- a. This back scattered electron SEM photo of All-D-2-A shows the general fine-grained nature of this inclusion. The inclusion is outlined to aid identification.

- b. Ca X-ray beam scan of figure (a) outlines the inclusion and indicates compositional layering.

- c. Al X-ray beam scan of figure (a) reveals a distinct Al-rich rim. The discontinuity in contrast near the top of the photo is due to one of the multiple beam scan repetitions not starting at the upper edge of the photo.

- d. Fe X-ray beam scan of figure (a) suggests an Fe-enriched core.

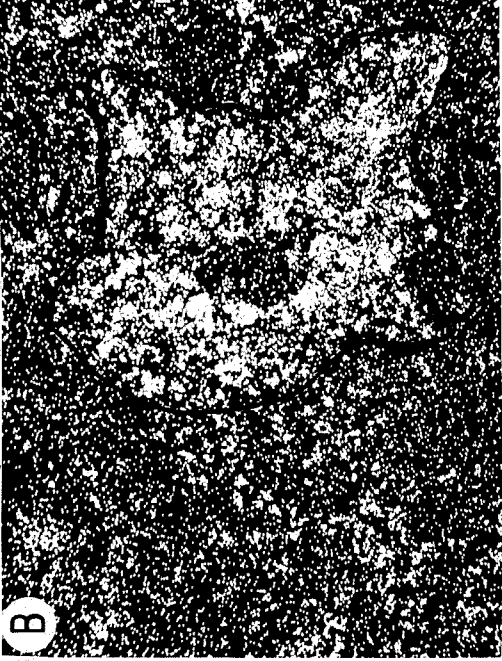
Allende D-2-A



Al



Ca



Fe

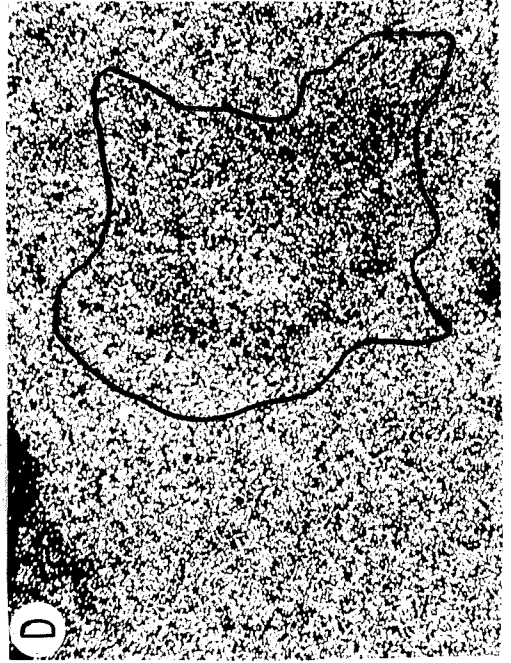


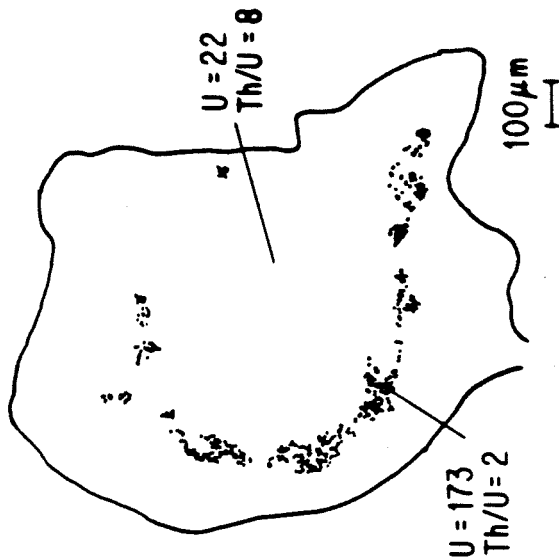
FIGURE 23

a. Based on SEM X-ray spectral mineral identifications, this drawing depicts the mineralogically distinct zones in All D-2-A. The striped band follows a highly distinct Al-rich layer composed mostly of nepheline. The Fe-Ti oxide component of this layer mineralogically sets it apart from other areas of the inclusion.

b. This figure shows the U-track distribution pattern over inclusion All D-2-A. The track pattern follows closely the Al-rich rim structure, and appears correlated with the Fe-Ti oxides.

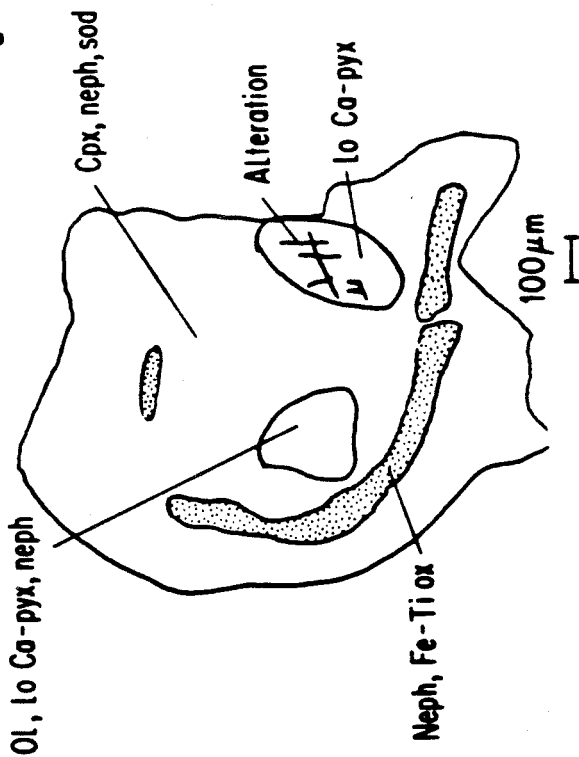
Allende D-2-A

b



Allende D-2-A

a



Abutting and terminating the Al rim on one edge (lower right) is a complex (100 x 200 μ) grain. This grain is basically low Ca-pyroxene criss-crossed by a series of 10 micron, probably alteration, channels. Fine-grained low-Ca pyroxene and Fe-Ni sulfide fill these channels.

Interior to the Al-rich rim is a patchy Ca-rich, U-Th-poor layer approximately 150 microns wide. Grain size is typically 5 microns, but may go up to 18 microns. In this layer, Ca-rich pyroxene (wollastonite?), nepheline, sodalite, sulfides, olivine and an Fe-Ni metal grain were found.

The comparatively consolidated core is ~75 microns wide. The core is distinguished in the element beam scan photos as an area relatively low in Ca and Al but high in Fe. Olivine is the main component with accessory low-Ca pyroxene and nepheline.

The aluminium rich rim has $U=173\pm 6$ ppb and $Th/U=2.1\pm 1.1$. In contrast the area interior to the Al-rim has $U=22\pm 1$ ppb and $Th/U=8.5\pm 1.1$. In the discussion section we will pursue the implications of the observed wide variation in Th/U ratio over this apparently highly altered inclusion.

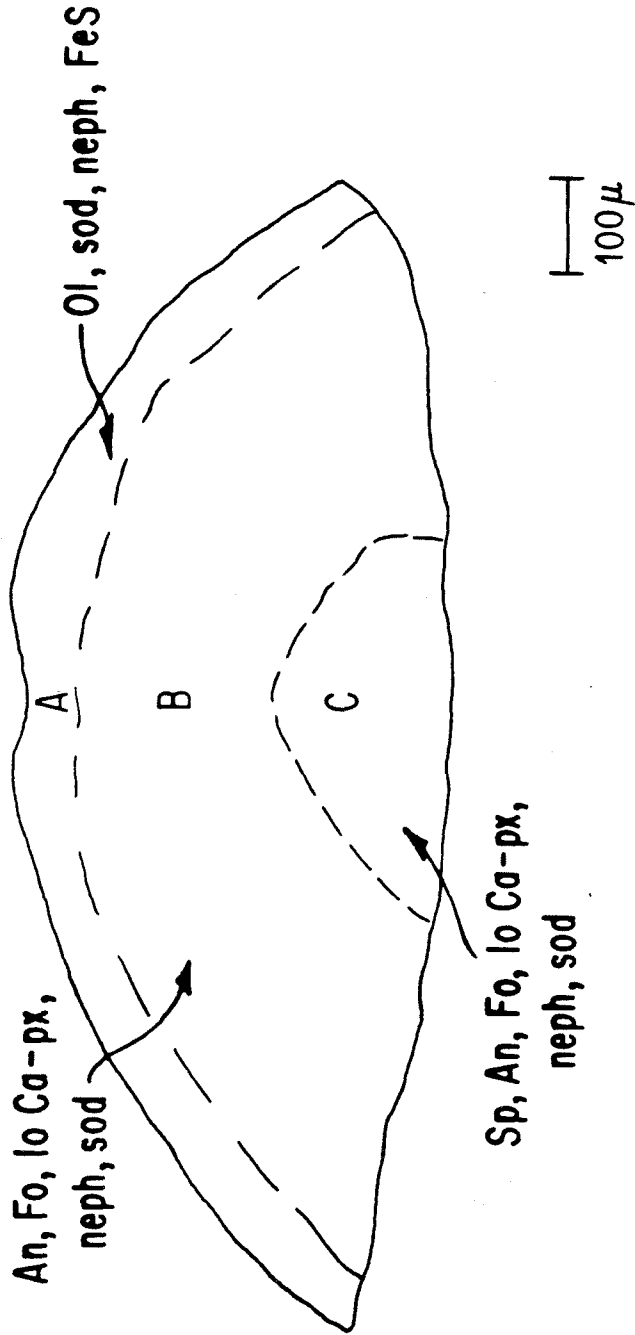
5. Allende D-2-E is a pinkish white hemisphere 500 microns in radius situated at the edge of a section (Figure 24). At first observation the inclusion appears to be coarse-grained, but the grains are microscopically heterogeneous. The outer 50 microns (Rim A) has a highly porous texture, with grain size typically 15 microns. Interior

FIGURE 24

This sketch of All D-2-E shows the inclusion can be divided into three mineralogical and textural zones. The porous rim is Fe-enriched with respect to the rest of the inclusion. The interior zone and core are Ca-Al-rich. Their mineralogy is similar except for the notable addition and dominance of spinel in the core.

ALLENDE D-2-E

- A = "porous rim"
- B = "cemented" interior zone
- C = inequigranular mosaic core



to this porous rim the grain size increases up to 50 microns. Ovoid- to irregular-shaped grains are cemented together by a dark (reflected light) interstitial material (zone B). This cemented texture, which composes the bulk of the inclusion, grades into a compact inequigranular mosaic texture for the 250 micron core (C). The porous rim is Fe-rich relative to the rest of the inclusion, but Fe-poor relative to the surrounding matrix. Olivine is abundant with sodalite and nepheline found interstitially. FeS is also observed. The inclusion interior is highly Al-enriched relative to the outer rim (A). The 200 micron zone B immediately interior to this rim has abundant anorthite, intermixed with low Ca-pyroxene, and Mg-rich olivine. Nepheline and sodalite are found both in veins and as small grains. In the core, the same mineralogy is found with the notable addition of $MgAl_2O_4$ spinel.

The track maps show no layering. Instead, high track areas occur as clumps, typically 25 microns wide, throughout the inclusion. Nothing unique was discovered in the SEM analyses of these high track areas, thus the U,Th enriched phase(s) were not identified. Values for a suite of the U,Th-rich clumps range from U=374 ppb, Th/U=5 to U=97 ppb, Th/U=19. The total inclusion has U=49±2 ppb and Th/U=7.3±.4. Adjacent matrix has U=15±1 ppb and Th/U=2.1±.3.

6. Allende A-5-A is a 650 micron, pink, coarse-grained, broken subrounded inclusion with a well-ordered rim sequence (see Figs. 25-top and 26). The rim sequence is reminiscent of a Wark and Lovering (1978)

FIGURE 25

Top: This is an SEM secondary electron photograph of the compact Type A fragment, All A-5-A which sits at the edge of a section. A void-rich band and compact interior composed of lath-like melilite grains can be seen.

Bottom: This is a sketch of the U track distribution pattern superimposed on the outline of inclusion All A-5-A. The Th+U map mimics the U pattern. U and Th are concentrated in the outer rim layers. An area where the track pattern forms a definite scalloped-shape is bracketed as being illustrative of most of the inclusion (see fig. 26). The track-rich band appears enriched in its most interior edge. It should be noted, however, that this pattern breaks down into a more complicated structure for the lower-left-hand corner of the illustration.

Allende A-5-A

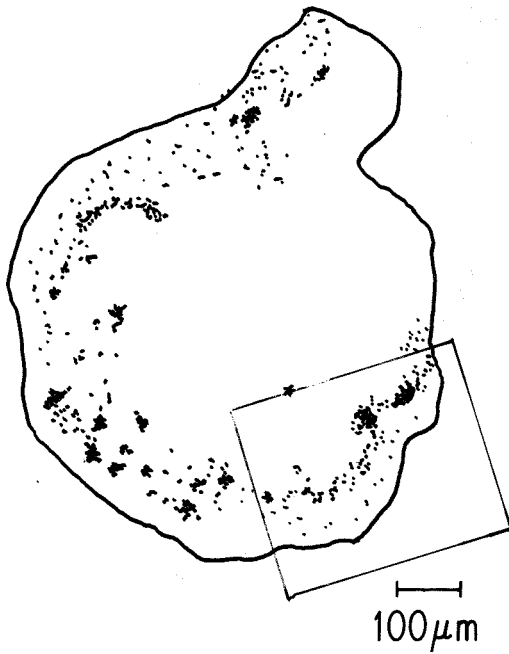
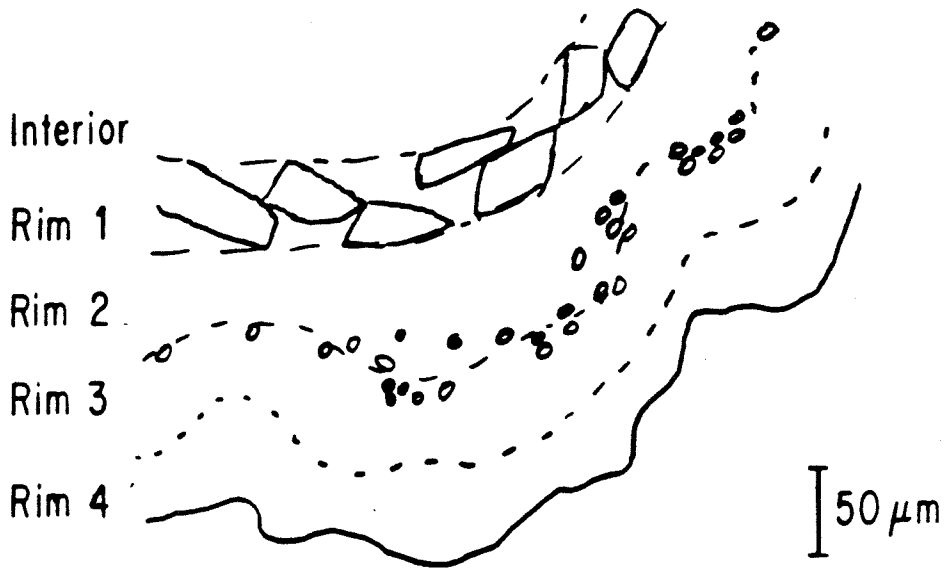


FIGURE 26

Illustrates the $\sim 450\mu$ rim area bracketed in figure 25 of the compact Type A inclusion All A-5-A. Four distinct rim layers are observed in this region. The rims are identified by their major mineral components and measured U and Th/U values are listed. Perovskite is the major U,Th carrier.

Allende A-5-A



	<u>U(ppb)</u>	<u>Th/U</u>
Interior: Mel, sp, An, Ti-pyx, Pv individual grains (perovskite?)	23±2 {639 }260	15±2 {31 }82
Rim 1: Mel, An, sod, voids	9±2	7±2
Rim 2: Mel, sp, Ti-pyx individual grains (perovskite?)	81±4 206 52	3.2±.5 22 83
Rim 3: Sp, pv individual perovskite grains	417±13 {424 }502 {570 }551	21±1 {23 }19 {17 }40
Rim 4: Ca-pyx, access. sod + gt?	99±4	3±.4
Total Inclusion	105±3	9.1±.3
Adjacent Matrix	19±1	2±1

Type A rim structure though the exact ordering differs somewhat (compare figure 17 in section IV). We shall return to this point in the Discussion section. Fig. 25(bottom) illustrates the U track distribution over the inclusion. As can be seen U enrichment is confined to the rim layers. The area of greatest enhancement forms a well-defined narrow scallop-shaped band 50 microns from the edge of the inclusion. The ~300 micron area bracketed in Fig. 25, which includes a segment of this track pattern, is illustrated in Fig. 26.

The 20-40 micron outermost rim (designated rim 4 in Fig. 26) is composed of Ca-rich pyroxene with accessory sodalite and possibly garnet. This rim has $U=99\pm 4$ ppb and $Th/U=3\pm 0.4$. Rim 3 is a scalloped band of Mg-Al spinel 60 microns wide. Chains of discrete 20 micron euhedral perovskite grains define the inside border of this spinel rim. The U and Th of the inclusion is concentrated in rim 3. Clumps of U,Th tracks, embedded in a diffuse high track band, mimic the pattern of the perovskite chains. Rim 3 has $U=417\pm 13$ ppb and $Th/U=21\pm 1$. Individual (presumably perovskite) grains in rim 2 have U values ranging from 424 to 570 ppb with average $Th/U\sim 20\pm 2$. Only one grain analyzed has a Th/U ratio (=40) which differed from this range.

Rim 2 is a 30 micron band of melilite, spinel, and accessory fassaite. Rim 2 has $U=81\pm 4$ ppb and $Th/U= 3.2\pm .5$. An isolated rim 2 grain analysis, which most likely is a perovskite, has $U=206$ ppb and $Th/U=22$. An unidentified grain of more questionable correlation between the two track maps has $U=52$ ppb and $Th/U=83$. Rim 1 is a 40 micron void-filled band of anorthite, sodalite and melilite. Including

void areas, this rim has $U=9\pm 2$ ppb and $Th/U=7\pm 2$. The interior of the inclusion is a complex intergrowth of melilite laths, ranging from almost pure gehlinitite to more Mg-rich melilite. Spinel, minor anorthite and fassaite, as well as a few highly dispersed perovskite grains are also present. The interior a U content is 23 ± 2 ppb and $Th/U=15\pm 2$. A well defined isolated interior U,Th enriched grain has $U=639$ ppb and $Th/U=31$. A grain of less certain definition has $U=260$ and $Th/U=82$. Total inclusion values are $U=105\pm 3$ ppb and $Th/U=9.1\pm .3$. Adjacent matrix values are $U=19\pm 1$ ppb and $Th/U=2\pm 1$. This total inclusion value was derived from reactor and cyclotron track counts over the entire inclusion except for the $\sim 200\mu \times 200\mu$ "panhandle" at the broken upper edge of the inclusion (see Fig. 25) where the cyclotron mica was scratched. Rim values were determined for restricted areas where clear definition existed and unambiguous correlation between the reactor and cyclotron micas was possible. Interior values were obtained from as much of the mutually countable areas identified as interior on the cyclotron and reactor micas as possible. Taking these rim and interior values and a rough estimate of their respective total areas in the inclusion one calculates a "total" inclusion Th/U ratio of ~ 11.6 . This crude estimate actually agrees quite well with our measured "total" inclusion value.

7. Allende A-5-B is a 3 mm irregular dumbbell-shaped Ca-Al rich inclusion enclosed by a 50-250 micron U,Th rich rim (Fig. 27).

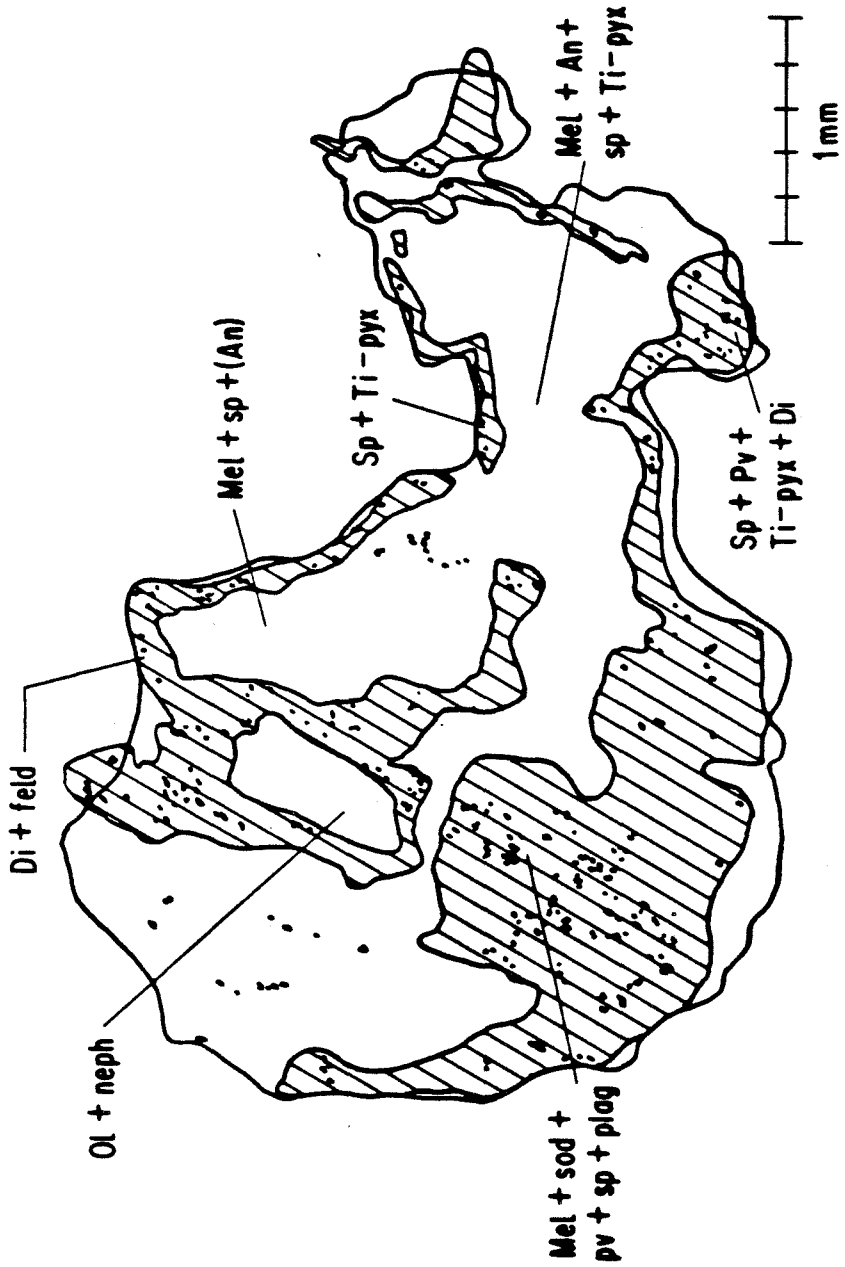
FIGURE 27

Outlines the irregular shape of the 3mm white inclusion

All A-5-B. Mineral identifications are based on SEM X-ray spectra.

Superimposed is a very complex U,Th track pattern. Areas of enrichment can be identified as individual clumps or as a general swath of closely packed track clumps and high track background. This track-rich swath is defined by the cross-hatched area. In one case, perovskite has been identified as the U,Th carrier. Because of the highly irregular shape it is difficult to distinguish whether the cross-hatched areas define a single U,Th-rich rim or whether the inclusion is actually an aggregate, the components of which each had their own rim. On the basis of overall morphology, texture and mineralogy, All A-5-B has been tentatively classified as a "fluffy" Type A.

Allende A-5-B



Based on the texture and mineralogy this inclusion can tentatively be classified as a fluffy Type A (MacPherson & Grossman, 1979).

The U and Th are located mostly in discrete ~30 micron localizations embedded in a diffuse, relatively track-rich band. These discrete U,Th localizations are often associated with perovskite. Detailed SEM investigation of a 150 micron area positively correlated the pattern of these track localizations with the pattern of perovskite distribution. One star has $U=373\pm 22$ ppb and $Th/U=18\pm 2$.

Another star has $U=1352\pm 78$ ppb and $Th/U=20\pm 2$. Accompanying rim mineralogy consists of spinel, diopside, trace anorthite, sodalite, and fassaite. The major interior component is melilite with spinel and anorthite.

8. Allende D-2-C is a white fine-grained Ca-Al rich inclusion (Grossman, 1975; Grossman & Ganapathy, 1976b) roughly 1mm x 100 μ . Because of the fine-grained nature of the inclusion no individual phase identifications could be accomplished. Element beam scans verified the inclusion to be Ca and Al-rich. Track maps indicate the entire inclusion is U- and Th-rich, but some localizations can be discerned. One such "star" has $U=59\pm 13$ ppb and $Th/U=54\pm 16$. Total inclusion values are $U=68\pm 2$ ppb and $Th/U=3.0\pm 2$.

9. Allende D-2-D is a dumb bell-shaped fine-grained Ca-Al rich inclusion, 800 μ x 350 μ . This inclusion is peppered with small

stars embedded in a bulk U,Th-enriched material. The U-Th-rich regions have high Th/U ratios (10-30), whereas the total inclusion has $U=123\pm 10$ ppb and $Th/U=4.4\pm 0.4$.

VI. Discussion of Allende Th/U Results

A. Discussion

A summary of our Allende Th/U analyses is presented in Table 15. In light of the fact that most coarse-grained CAI analyses have been done on Type B inclusions, the compact Type A (All A-5-A) and the fluffy Type A (All A-5-B) inclusions are particularly important.

Equilibrium condensation sequence calculations predict that the earliest condensing pure actinide phases reach saturation at temperatures below those of the major Type A mineral phases, i.e., perovskite, melilite, and spinel (refer back to Table 1 [from Grossman & Larimer (1974)] and Table 2 [from Ganapathy & Grossman (1976) in Introduction]. Earlier condensation of these elements as solid solution in previously formed phases could have occurred (Grossman, 1973; Grossman & Larimer, 1974). Because of the magnitude of actinide element enrichments over Cl levels in the CAI's, perovskite structurally appeared to be the most likely candidate for an early condensing actinide carrier phase (e.g., see Grossman & Ganapathy, 1976; Grossman et al., 1977; and Boynton, 1978). Lovering et al. (1976, 1979) and Wark & Lovering (1978) found perovskite as the sole U carrier in Type A CAI's. This is in contrast to Type B's where in addition to perovskite six accessory micron-sized refractory oxide, titanate, niobate, and silicate U,Th enriched phases were discovered. Our study of All A-5-A supports perovskite as the major carrier for both U and Th.

What is particularly fascinating in our U,Th study is that the highest levels of U,Th enrichment are observed in the outermost rims rather than the inclusion interior. The typical Th/U ratio of

TABLE 15
SUMMARY ALLENDE INCLUSION

U AND Th/U

		<u>U(pbb)</u>	<u>Th/U</u>
1.	All C-5-A Barred chondrule "clean" olivine rim:	7.8±1	4.3±1.3
	Ca-Al rim corner :	61±6	1.6±0.5
	Total Rim :	9.3±.8	3.5±0.9
	Barred core :	46±2	4.3±0.4
	Total Incl. :	38±1	3.9±0.3
	(Adj. matrix) :	(11±1	3.7±0.7)
2.	All C-5-B Diopside chondrule Total Incl. :	77±3	5.3±1
3.	All C-5-E Amoeboid Incl. Total Incl. :	12.5±.4	4.2±0.4
	(Adj. matrix) :	(11±1	4±1)
4.	All D-2-A "altered" Incl. Al-rich rim :	173±6	2.1±0.1
	Interior :	22±1	8.5±1.1
5.	All D-2-E Layered Pink- 25 μ U,Th clumps :	374	5
	white chondrule	↓	↓
		97	19
	Total Incl. :	49±2	7.3±0.4
	(Adj. matrix) :	(15±1	2.1±0.3)
6.	All D-2-C f.g. inclusion "*" :	59±13	54±16
	Total Incl. :	68±2	3.0±0.2
7.	All D-2-D f.g. inclusion Total Incl. :	123±10	4.4±0.4

TABLE15 (continued)

		<u>U(ppb)</u>	<u>Th/U</u>
8. All A-5-A Compact Type A	{ Interior	: 23±2	15±2
		{ isol. grains	: 639
		260	82
	rim 1	: "9±2"	7±2
	{ rim 2	: 81±4	3.2±0.5
		{ isol. grains	: 206
		52	83
	{ rim 3	: 417±13	21±1
		{ isol. grains-pv	: 424
		502	19
		570	17
		551	40
	rim 4	: 99±4	3±0.4
	Total Incl.	: 105±3	9.1±.3
(Adj. matrix)	: (19±1	2±1)	
9. All A-5-B "Fluffy" Type A	outer rim "*"	: 373±13	18±2
	outer rim "*"	: 1352±78	20±2

individual perovskite grains in Rim 3 is ~20 with U contents varying from 424-570 ppb. In contrast, one grain with similar U content has a Th/U ratio of 40. Positive identification of individual grains as perovskite in areas other than rim 3 is more questionable. However, it can be seen from Table 15 that all individual U,Th enriched grain analyses have $Th/U > 20$. The perovskite and possibly other phases exhibit highly fractionated Th/U ratios relative to a "normal" ratio of 4. In the correlation studies, mostly on Type B inclusions, presented in Grossman et al. (1977) U is found to generally correlate with REE abundances (excluding Eu) and therefore some of the REE could be associated with perovskite. However, because there is a reasonable amount of scatter ($\pm 20\%$) about a constant Sm/U ratio, other phases are also important. Evidence for REE fractionation was found in laboratory perovskite/ melt experiments (Ringwood, 1975; Nagasawa et al., 1976) where light REE-enriched over heavy REE patterns were observed. Because the fractionation trends are essentially smooth functions of ionic radius, if an actinide/lanthanide analogy can be made, preferential Th^{+4} partitioning into perovskite over the larger U^{+4} ion might be possible depending on the phases competing for Th and U. To explain a ratio of 20 perovskite would need to incorporate Th^{+4} five times more preferentially than U^{+4} .

Since trace element substitutions in calcium minerals are usually believed to be into Ca sites, trivalent elements are usually observed to be incorporated more readily than tetravalent elements into the host structure due to the easier charge balance. This behavior is observed experimentally in partition coefficients for clinopyroxene and Ca-phosphate (Benjamin, 1979). Consequently, if the high perovskite Th/U ratios

indicate preferential Th incorporation into perovskite, it may mean that U isn't trivalent under conditions (nebular condensation) in which CAI formed.

One might ask instead whether the high Th/U ratios in perovskite indicate incomplete U condensation relative to Th. Boynton (1978) has argued that high bulk CAI Th/U ratios measured by Tatsumoto (1976) and Chen & Tilton (1976) are indicative of incomplete U condensation relative to Th due to higher volatility of U. Again what is especially bothersome with this relatively simple scenario is the fact that in All A-5-A the majority of perovskites are located in an outer rim. Rims are secondary features in an inclusion. Wark & Lovering (1977, 1980b) suggest a link between the fine-grained inclusions and Type A rims. They explain the observed fractionated Group II REE patterns observed in fine-grained inclusions by having these inclusions form from the depleted residual reservoir left after the Type A inclusions (minus rims presumably) condensed. If rims share a common origin with fine-grained inclusions and rim order indicates some time sequence (Wark & Lovering, 1977, 1980b), Th would have to be more volatile than the heavy REE if Boynton is correct. However, this is consistent with his calculations. Also, one might then expect on the average lower Th/U ratios in Rim 3 perovskites compared to any found inwards of this rim. Since positive identifications for grains interior to Rim 3 could not be made and since the overall statistics are not good, it is difficult to address this question. In the next rim inward (2), a grain has half the U but a Th/U ratio still near 20. The other rim 2 grain

analyzed with 1/10 of the U of a rim 3 perovskite has a Th/U ratio of 83. A similar ratio of ~82 is obtained on a grain in the inclusion interior which has ~1/2 the U of a rim 3 perovskite. An explanation of U variability could simply hinge on grain size, i.e., for grains $\leq 20 \mu$, U concentrations may be low. It is, however, the similarity of the two extremely high ratios (~82) which suggests a phase other than perovskite is also present which is exceedingly Th enriched--possibly one of the Lovering et al. (1976,1979) Type B trace carrier phases. In contrast, another interior grain has a U value slightly higher than a rim 3 perovskite with Th/U ratio of 31. Thus, if two out of the three high Th/U interior grains are a phase other than perovskite, there is only the weakest case for an increase in Th/U ratio of the perovskites inward.

Another alternative to a volatility argument or host phase structural preference to explain high Th/U ratios is that perovskite quantitatively incorporates U and Th and that the high perovskite ratio is actually preserving the ratio of the reservoir from which the phase condensed. This means the source (nebular gas?) from which the perovskite originated had a high Th/U ratio. Preferential incorporation of U relative to Th in an early condensing phase which was not sampled (to any great extent) by the CAI could explain this. Jones & Burnett (1980) have observed the remarkable ability of U to be reduced from a silicate melt and alloy with Pt. Fairly reducing conditions are necessary, contrary to the relatively oxidizing conditions proposed for some CAI formation (Boynton, 1978; Grossman et al., 1979), and particularly the CAI Fremdlinge (El Goresy et al., 1978).

The failure to observe U in CAI Pt nuggets (Wark, pers. comm.) makes the application of this mechanism for U depletion, however, less than straightforward.

As mentioned in the results section, the observed rim sequence (refer back to Fig. 26) is highly reminiscent of the idealized Type A Wark & Lovering (1978) rim (Fig 17) although the exact ordering differs somewhat. In particular the melilite and feldspathoid void-rich rim in All A-5-A is located immediately adjacent to the mainly melilite interior. Wark & Lovering (1980b) suggested that this rim was originally melilite which had been subsequently altered and this seems better supported in the observed All A-5-A sequence. Detailed quantitative analysis of the melilite grains observed in this rim and the melilite immediately interior could perhaps aid in distinguishing whether this rim is some type of reaction rim or actually a separately deposited layer that was subsequently altered. The differences in the measured Th/U ratios for the void-rich rim 1 and the inclusion interior (7 ± 2 compared to 15 ± 2) would imply differential mobilization of Th and U if alteration of interior material formed rim 1. Alternatively, the lower rim ratio could imply condensation or reaction exchange conditions at lower T (or higher P) during rim 1 formation compared with the conditions during original interior condensation.

The U concentration obtained for the A-5-A inclusion interior (23 ppb) is only a factor of ~ 3 higher than C1 chondritic levels. In contrast the total U concentration (105 ppb) is ~ 13 times C1 chondritic. Grossman et al. (1977) report similar U concentrations

for a Type A inclusion. We have shown that the incorporation of the rimming material appears crucial if this inclusion is to show a U enrichment factor close to the ~ 17 mean enrichment factor for the refractory elements in coarse-grained inclusions of Grossman et al. (1977), and even when the rim is incorporated, U seems somewhat depleted. In order for U to be part of a "total" refractory element condensate, rim material can not simply be viewed as secondary residua after major refractory mineral condensation, but as a major refractory trace element carrier. In contrast to U, the inferred Th concentration in the inclusion interior is ~ 15 times CI chondritic. With the bulk inclusion Th/U ratio measured at 9.1, the inferred bulk Th content is ~ 22 times chondritic. Therefore, unlike U, the incorporation of the rim phases is not crucial for obtaining Th enrichment levels near the Grossman & Ganapathy (1976) and Grossman et al. (1977) uniform refractory element enrichment factor of ~ 17 . Even if the difference between 13 and 17 is not important, the need to incorporate the rim in order to obtain the full complement (17) of U in our compact Type A would seem to support the Boynton (1978) contention of a higher U volatility relative to Th during CAI condensation. It is not until after the process of CAI rimming does the U enrichment level in the inclusion reach a value comparable with the other refractory elements.

All A-5-B, tentatively identified as a "fluffy" Type A, exhibits a Th, U enrichment pattern similar to the well-studied compact Type A (A-5-A). As in our compact Type A, the U and Th are enriched in an outer rim with perovskite identified as a carrier phase. Although

not the exact track stars identified as perovskite, track counts on two other grains, presumably perovskite, gave Th/U ratios ~ 20 while their U values differed by a factor of 4. One is immediately struck by the rim carrier phases (almost certainly perovskite) in both a compact Type A and a fluffy Type A exhibiting Th/U ratios of 20. Even though the petrogenesis (molten vs. non-molten) of their interiors may differ, the rim histories may be similar.

Returning to the analysis of the compact Type A, two rims have perhaps slightly low Th/U ratios: the melilite-spinel rim 2 with $\text{Th/U} = 3.2 \pm 0.5$ and the outermost Ca-pyroxene rich rim 4 with $\text{Th/U} = 3.0 \pm 0.4$. The mineralogy of rims 2 and 4 are quite different, but in addition to their near identical Th/U ratios, their U contents are both roughly 10-12 times CI chondritic levels. The complexities in understanding a single rim are encountered in rim 2. This rim has a near normal Th/U ratio, but there are isolated grains of high Th/U ratios (20 and 83). Whether these differences in ratios are due to different phases for the actinides or due to differences in the conditions at the time of the formation of the same phase has not been resolved.

Because of the proposed link between fine-grained inclusions and Type A rim material (Wark & Lovering, 1977, 1979) we turn next to our two fine-grained inclusion analyses. All D-2-C exhibits a bulk Th/U ratio slightly below normal at 3.0 ± 0.2 while All D-2-D is perhaps slightly high at 4.4 ± 0.4 . There is a factor of two difference in their bulk U contents, with All D-2-C at concentrations ~ 8 times chondritic and All D-2-D at concentrations ~ 15 times chondritic.

It is interesting to note the two rim layers in All A-5-A with near normal Th/U ratios (rims 2 and 4) have bulk U enrichments in between these two inclusions. Rim 2 is composed mostly of melilite, spinel, and Ti-pyroxene while rim 4 is predominantly Ca-pyroxene with accessory sodalite and garnet. Fine-grained inclusions, on the other hand, are composed of spinel, pyroxene, 20% nepheline and sodalite, with grossular and possibly melilite (Grossman & Ganapathy, 1976b). Compositionally, rim 4 seems a better match to fine-grained inclusion material in attempts to link fine-grained inclusions with Type A rims (Wark & Lovering, 1977, 1980b). Unfortunately, no mineral identifications for our specific fine-grained inclusions were done.

Two Ca-Al-rich inclusions do not fit neatly into the established classification scheme. In the description of All D-2-A there is presented textural and mineralogical evidence to suggest this inclusion has undergone extensive alteration. The inclusion has a layered structure which may be primary. The U,Th enrichment is associated with an Al-rich primarily nepheline rim. The complex fine-grained texture prohibited positive identification of the U,Th carrier phase. Within this rim the U concentration is ~21 times chondritic but the resultant Th/U ratio is only ~2. While nepheline is found throughout the inclusion, only in this rim are there found Fe-Ti-oxide grains. The overall Ca-Al rich nature of this altered inclusion suggests the possibility that these Fe-Ti oxide grains might have been originally perovskite. In a study of a carbonaceous xenolith in the Plainview H5 chondrite, Nozette & Wilkening (1980) discovered an inclusion which resembles a fine-grained amoeboid aggregate juxtaposed with an

inclusion resembling a coarse-grained inclusion. The major minerals found were an Al-rich clay, an Al-poor clay, and an Fe-Ti oxide. Compositions indicate the parent material was rich in Ca, Al, and Ti. A model was proposed where original CAI material was hydrothermally altered resulting in the mineral assemblages observed. If the link with CAI material is justified, the Fe-Ti oxide may have at one time corresponded to perovskite.

If the All D-2-A Fe-Ti oxide had similarly originally been perovskite, the low observed Th/U ratio is different than the observed Th/U in perovskite grains in the Type A inclusions studied. Either these proposed original perovskites for All D-2-A were formed from a gas depleted in Th or the alteration process preferentially depleted Th over U or alternatively added U. If inclusion alteration were a closed system process for Th and U, rim Th depletion could mean interior Th enrichment. Indeed the interior does exhibit a high Th/U ratio equal to ~9. Coincidentally or not the interior of All D-2-A has a U concentration almost identical to the interior of the compact Type A, All A-5-A. In Th content, however, All D-2-A falls short of the All A-5-A levels by a factor of 3. Thus the attempt to correlate the two inclusions by a closed system alteration process with regard to refractory elements seems difficult. In order to view the low Th/U ratios in the All D-2-A rim as due to Th depletion, the Th apparently did not go into the interior.

The extremely fractionated Th/U ratios observed—a factor of two below and a factor of two above "normal"—are intriguing in this altered inclusion. It will be difficult to resolve whether the

fractionations are the result of the alteration process or whether the fractionations were established during an earlier condensation stage.

The model proposed by Grossman et al (1979) for amoeboid olivine aggregates was discussed in the Introduction to Allende Inclusions section. Based mainly on observed REE patterns and mineralogy it is suggested they are a mixture of fine-grained and coarse-grained fractions left suspended in the solar nebula until temperatures fell to where Fe-rich olivine became stable. One can then explain the bulk U concentration measured for the amoeboid inclusion All C-5-E, which is near chondritic levels, as due to the dilution of CAI enriched material by U-poor olivine.

The near normal Th/U ratio (4.2 ± 0.4) observed for this inclusion may indicate a wider range in condensation temperatures was sampled, and, considering the CAI models proposed, perhaps also a range of source materials. In deciding good candidate material for measurements of solar system averages, amoeboids may give more representative average solar system sampling than coarse-grained or fine-grained CAI individually. Both Group I and Group II patterns are observed in bulk amoeboid inclusion REE analyses. This suggests the mixture of coarse-grained CAI, fine-grained CAI and olivine components are not mixed in constant proportions from inclusion to inclusion. As such the composition for the amoeboid inclusion C-5-E could be atypical for this inclusion type.

Another olivine-rich inclusion is the barred olivine chondrule All C-5-A. Because barred chondrules do not lie on major element variation

trends defined by other olivine/pyroxene chondrule types, Simon & Haggerty (1980) suggest that barred chondrule origins may be a totally separate group. The presence of glass is strong evidence for a molten stage. Referring to summary table 15, the olivine rich rim, while extremely low in its Th,U content, exhibits a normal Th/U ratio (although the errors are large due to poor counting statistics). The Ca-Al rich corner of the rim, composed mainly of diopside and sodalite, has a U content ~8 times chondritic levels. This corner, however, exhibits no comparable Th enrichment resulting in a Th/U ratio of 1.6. The mineralogy of the Ca-Al rich rim corner is reminiscent of the compact Type A (A-5-A) outermost rim (4) which is composed of Ca-pyroxene with accessory sodalite and possibly garnet. U enrichments ~12 times higher than chondritic were observed and the A-5-A rim has a Th/U ratio at best slightly below normal ($3 \pm .4$). In a laboratory partitioning study Benjamin et al. (1978) did not find large differences in U and Th crystal/liquid partition coefficients in diopside. Their experiments were run such that U and Th were probably both tetravalent. The diopside partition coefficient for Pu, however, indicated a strong preference for trivalent over tetravalent ions. If conditions were such that U was trivalent, very low Th/U ratios (<1) in clinopyroxene may be expected. However, clinopyroxene has not positively been identified as the U,Th carrier in the two inclusions discussed.

The glassy lamellae in the barred core of C-5-A are the most probable carriers of the U and Th. As can be seen in Table 13 (in results section) the glass is extremely alkali-poor. The low Na_2O , K_2O ,

and FeO content of the glass resembles Murchison C2 glasses (Fuchs et al., 1973; Olsen & Grossman, 1978), although the All C-5-A glass is more Al-rich on the average. Compared with the average of C3-0 chondrule glasses analyzed by McSween (1977_a) or the Yamato 74191 unequilibrated chondrite glass (Kimura & Yagi, 1980) the alkali contents observed in the All C-5-A glass are an order of magnitude less. The CaO content of All C-5-A is almost a factor of two higher than that found in the Yamato chondrite glass. Grossman & Clarke (1973) tabulate glass analyses from Allende chondrules which show affinities to CAI compositions. The best match of our All C-5-A glass is with a glass associated with Ca-Al rich material from Marvin et al. (1970). Grossman & Clarke (1973) calculate "normative" mineralogies based on CAI minerals. For the Marvin et al. glass they calculate a composition of 67% anorthite, 26% diopside, 3% forsterite, and 4% Ca-Al pyroxene.

Because of the size, individual lamella could not be resolved in the track pattern. The bulk core contains a U concentration enriched by a factor of 6 relative to C1 chondrites. If this U is actually coming from half the area of the interior then the enrichment factor in the glass could be ~12. The Th/U ratio (4.3 ± 0.4) is in the "normal band". The apparent U,Th enrichments in the glass are reminiscent of CAI enrichment levels. Thus, our work supports the Simon & Haggerty (1980) scenario for a separate petrogenesis of the barred chondrules. We suggest these barred chondrules may have had a history closely associated with the CAI's and may have been an intermediate population between the CAI's and the Mg-rich chondrules.

A rare inclusion find is the diopside chondrule All A-5-B. The uniqueness of the pyroxene grain compositions was illustrated in Fig. 21 (Result Section). Theoretical calculations, lacking the relevant thermodynamic information on Ti-pyroxene (fassaite), predicted diopside to be the high temperature pyroxene phase (Grossman, 1972). The U,Th enriched areas in this diopside chondrule, however, are associated with the porous interstitial material. Similarly, Benjamin (1979) found low crystal/melt partition coefficients for U and Th in diopsidic clinopyroxene. The fine-grained texture of this material made mineral identifications difficult. Along with relatively low temperature minerals such as olivine and Fe-Ni sulfides, minerals such as nepheline and a Ca-rich garnet, which are seen in CAI, were also observed interstitially. If the diopside were indeed a high temperature condensate phase and since U and Th are early condensing elements, then it is difficult to reconcile the association of U and Th with the low temperature interstitial phases unless they represent alteration products of high temperature phases. Actually the mineralogy observed in the interstitial areas is similar to phases observed in amoeboid inclusions minus the high temperature CAI phases. The total inclusion is enriched in U by a factor of ~ 10 above C1 chondritic levels with a possibly high Th/U ratio of 5.3 ± 1.0 . Because of the mineralogy and of the U and Th enrichment, the diopside chondrule may have some tie with CAI material. But the rarity of this inclusion type suggests very specialized conditions of formation.

The majority of our Allende inclusions exhibit high (relative to normal terrestrial) Th/U ratios. If more extensive sampling should

bear this out, there could be possible intriguing repercussions for the interpretation of ordinary (O) and enstatite (E) chondrite data. Larimer (1979) found what he interprets as two distinct fractionation trends in plots of Si/Al vs. Mg/Al (and Cr/Al vs. Mg/Al) involving various classes of meteorites. One linear trend is defined by O and E chondrites and the second linear trend is defined by the C chondrites, lunar, and eucrite parent body measurements. Allende inclusions lie very close to this second fractionation trend at the Al-enriched end. Larimer interprets these lines as mixing lines. He argues the C2's C3's and lunar compositions result from progressive enrichment relative to the C1 composition in a component composed essentially of Allende inclusion material plus olivine. Alternatively, the eucrite parent body is depleted in this component relative to C1 material. Because the O and E chondrites lie on a different fractionation trend, they require mixing with a component of quite different composition. Larimer calculates the O and E trend is consistent with a 40-56% depletion relative to C1 of a highly aluminous and as such a high temperature phase enriched component. Loss of a high temperature component could also mean lack of a full refractory complement. If in general the Allende inclusions have high Th/U ratios and this can be extrapolated to the high temperature component depleted in O and E compositions, this may mean O and E chondrites are composed of material which has a Th/U ratio too low relative to an average solar system value. Similarly, fractionated $^{244}\text{Pu}/^{238}\text{U}$ ratios might be expected in the O and E chondrites. The sparse available Th/U data on E's are unclear (Morgan & Lovering, 1968), but the fact O chondrites

exhibit ~ normal Th/U ratios (e.g., see Morgan & Lovering, 1968) indicates a possible inconsistency with the model as proposed. The fact the high temperature fractionation component in the O,E trend must contain more olivine than the fractionation component in the CC-lunar trend, and also covers a temperature range extending to lower temperatures than the component in the CC-lunar trend, may explain the observance of unfractionated O-chondrite Th/U ratios. Thus, these meteorites could exhibit unfractionated ^{244}Pu ratios as well. It is possible that materials such as the barred chondrule C-5-A match the required properties of the component missing from O and E chondrites. But C-5-A has a normal Th/U ratio and loss of such material would leave the O and E chondrite Th/U (and probably Pu/U) unaffected.

B. Inclusion Summary Statement

The unique perspective gained from an insitu Th,U mapping study emphasizes the importance of rimming in CAI petrogenesis. It is difficult to relegate the rims to a position of interesting, but unimportant, secondary features when the Type A rims studied contain the bulk of the Th and U and possibly the bulk of many of the other refractory trace elements (REE?) as well. As such, what is observed in the refractory element component of the rims must constrain the models for the nebular condensation process at its very earliest stages. There is also the intriguing role rimming played in ending CAI growth. Type A rims are incredibly U and Th rich and, especially for U, are important in the classification of U and Th as refractory (i.e., early condensing) elements on par with the REE.

The link between fine-grained CAI and rim material must also be re-examined. Our bulk fine-grained CAI did not exhibit the highly fractionated Th/U ratios exhibited in specific CAI rim layers. This may be the result of limited sampling or a fine-grained CAI association with only particular Type A rim layers. To test whether a correlation of the fine-grained inclusions and rim material existed it would be useful to determine possible rim mixtures required to match the observed fine-grained inclusion Th/U ratios. The implied bulk chemistry of the rim mixture could then be compared to actual bulk fine-grained chemical analyses. Complementary REE analyses would be appropriate. It could be determined whether the rim REE patterns are like the typical highly fractionated fine-grained inclusion patterns and if the pattern changed from each individual rim layer.

The significance of the rims in overall bulk inclusion REE patterns and enrichments could be examined as well. An obvious result of our U,Th study is the significance of proper inclusion sampling in the determination of inclusion compositions. In trace element analyses, incorporation of rim material or not could affect the concentrations measured and therefore the proper interpretation of measurements.

The experimental technique used in this study permitted us to discover interesting inclusions which may have otherwise been overlooked. Some of these inclusions may play a key role in understanding alteration processes of CAI material. Some may be intermediate populations in a petrogenetic sequence. Clearly other techniques can do the quantitative measurements to a much higher precision. The real strength of our fission track radiography technique is the capability to map Th and U over an inclusion. With the map as a guide subsequent ion probe or charged particle X-ray analyses could then be used to give grain by grain analyses for other elements. It is fascinating to find that the pieces of the puzzle in understanding how our solar system formed have now become micron and submicron in size.

VII. Conclusions

A. Bulk Carbonaceous Chondrites

The results of our bulk sample analyses do not confirm the large fractionations in carbonaceous chondrite Th/U ratios observed by Morgan & Lovering (1968). The large variations seen were possibly due to contamination. The precision of the present induced fission track study allowed Th/U ratios to be measured to $\pm 10-20\%$. Our data fall within errors into the nominal solar system Th/U of 3.8 ± 0.5 . The majority of samples were C2 chondrites. The average of ten C2 chondrites gave a value of 4.1 ± 0.6 where the quoted error measures the average deviation for individual sample analyses. We were able to obtain only a single measurement for a clean C1 sample. This Ivuna sample has a Th/U equal to 5.2 ± 0.5 . A high quality Orgueil sample, provided by us to Tatsumoto for analysis, has Th/U = 3.64. Observed variability of Th/U ratios between analyses of different fragments of the same meteorite is, however, suggestive of subgram (20-30 mg) level Th/U fractionations.

Incorporation of high precision isotopic dilution analyses of the C1 chondrite Orgueil (Tatsumoto et al., 1976) supports our contention against large bulk Th/U fractionations among the carbonaceous chondrites. Thus CC material still appears to be a good source for the determination of nonvolatile solar system average abundances. With regard to nucleosynthesis models the lack of large deviations (i.e., Th/U ratios as low as 2 or as high as 6) from the band of "normal" Th/U ratios can not give strong support for or against the necessity of any major contribution to actinide nucleosynthesis on a time scale less

or greater than ~6 billion years prior to solar system formation. Within the error of the nominal solar system Th/U ratio (3.8 ± 0.5) models of r-process nucleosynthesis can differ by a factor of 4 in their time scales (see Introduction). In terms of the Schramm & Wasserburg (1970) mean age of the elements, this band covers a range of a factor of 6 in time. Refinement of the solar system value can only hope to be made via a systematic CC survey with a high precision technique, but would probably also require greater quantities of high quality Cl material than are presently available for study.

B. Allende Inclusions

1. CAI rim material must be considered when calculating total inclusion U and Th abundances in terms of average refractory element enrichment factors relative to Cl chondritic abundances, e.g. as done by Grossman et al. (1977).
2. As a consequence of the high U,Th contents in CAI rims, the determination of bulk inclusion compositions requires careful attention to sampling.
3. Volatility and the ability to substitute into a host phase govern the condensation of a trace element. According to the calculation of Boynton (1978), U is much more volatile than Th at the temperatures considered for CAI condensation ($>1450^{\circ}\text{K}$). Interpretation of the high Th/U ratios (~ 20) observed in compact and fluffy Type A rim perovskites, however, is unclear. The predominantly melilite interior

of the compact Type A also exhibits a high ratio ($\text{Th}/\text{U} \sim 15$). There is only a weak case for interior-located perovskites having Th/U ratios greater than 20. Thus it can not be resolved whether the rim perovskite ratio is mainly a crystal structure controlled fractionation (i.e., mineral preference for one ionic species over another), or instead is indicative of the actinide condensation conditions (i.e., U volatility or Th/U ratio in the gas) at the time of rim perovskite formation.

4. The general pattern in this study has been to observe high Th/U ratios in Ca-Al rich material, in particular for Type A coarse-grained inclusions. This seems to support the Boynton (1978) view that U is more volatile than Th at the temperatures proposed for CAI condensation. The contention of Grossman and Ganapathy (1976) that Th and U are both uniformly enriched in coarse-grained CAI at levels equal to other refractory elements, however, may still be valid if a larger sampling of inclusions is taken to average out any individual fractionations, or if many past total inclusion Th/U analyses were biased against rim material. Grossman and Ganapathy base their argument on analyses of mostly Type B inclusions, and, as such, they may be correct for this particular subgroup of coarse-grained inclusions at least.

5. Severe Type A CAI Th/U fractionation on both a macro- (bulk inclusion) and micro-scale have been observed. As such, the proposal of Ganapathy & Grossman (1976) to determine a solar system $^{244}\text{Pu}/\text{U}$ ratio from measurements on a large suite of coarse-grained CAI, must

be approached with caution. It is may be better to measure other chondrite materials for ^{244}Pu /actinide solar system abundances. However, it must be noted that for Type B CAI the analyses could still be valid.

6. Our U,Th study supports the proposal of Simon & Haggerty (1980) that barred chondrules have a separate origin from other Mg-rich chondrules. The suggestion is made they may be an intermediate population linking CAI with ordinary olivine chondrules.

7. The discovery of a rare diopside chondrule revealed U,Th enhancements in the fine-grained interstitial material. The pyroxene composition, interstitial material mineralogy, and Th,U enrichments suggest affinities to the CAI. Their rarity suggests formation (condensation?) under specialized conditions.

Appendix I: U,Th Relative Fission Cross Section Correction

Because the relative fission rates of Th and U are not exactly equal for the particle beam energies used in our cyclotron irradiations, the ratio of the measured track density of a sample to a standard does not directly equal the ratio of their respective [Th+U] contents. In this section the necessary correction term is derived to incorporate the more generalized condition of unequal Th and U fission cross-sections. The following notation is used:

- ρ = measured track density (tracks/cm²)
 σ_i = fission cross-section of element i for the particular cyclotron beam used
i = Th or U
 ϕ_H = cyclotron fluence
T = ratio of cyclotron sample fluence to standard fluence (= ϕ_{HS}/ϕ_{Ho})
[] = concentration in atoms/gm
R = mean range (g/cm²) of single fission fragment
subscripts: s = sample (i.e. unknown)
o = standard (i.e. known; same for both irradiations)
L = reactor irradiation
H = cyclotron irradiation

Thus,

$$(1) \quad \rho_{Ho} = (\sigma_{Th}[Th]_o + \sigma_U[U]_o) \phi_{Ho} (R/2)$$

$$(2) \quad \rho_{Hs} = (\sigma_{Th}[Th]_s + \sigma_U[U]_s) \phi_{Hs} (R/2)$$

$$(3) \quad \rho_{Lo} = F[U]_o (R/2)$$

$$(4) \quad \rho_{Ls} = F[U]_s (R/2) = \rho_{Lo} ([U]_s/[U]_o)$$

Where, ρ_{Lo} is the track density for a standard located at the position of the sample of interest and $F \equiv$ (thermal fission cross section ²³⁵U) x (total reactor neutron fluence). Dividing equation (2) by equations (1) and (4) and solving for $[Th]_s/[U]_s$ gives the formula:

$$(5) \quad \frac{[Th]_s}{[U]_s} = \frac{\rho_{Hs} \rho_{Lo}}{\rho_{Ls} \rho_{Ho}} \frac{1}{T} \left\{ \frac{[Th]_o}{[U]_o} + \frac{\sigma_U}{\sigma_{Th}} \right\} - \left(\frac{\sigma_U}{\sigma_{Th}} \right)$$

Solving equation (5) for the special case of $\sigma_{Th} = \sigma_U$ we calculate

a ($[\text{Th}/\text{U}]_s$)^{*}:

$$(6) \quad \left(\frac{\text{Th}}{\text{U}}\right)_s^* = \frac{\rho_{\text{Hs}}\rho_{\text{Lo}}}{\rho_{\text{Ls}}\rho_{\text{Ho}}} \frac{1}{T} \left\{ \left(\frac{\text{Th}}{\text{U}}\right)_o + 1 \right\} - 1$$

From equation (6) we can derive the substitution,

$$(7) \quad \frac{\rho_{\text{Hs}}\rho_{\text{Lo}}}{\rho_{\text{Ls}}\rho_{\text{Ho}}} \frac{1}{T} = \left\{ \left(\frac{\text{Th}}{\text{U}}\right)_o + 1 \right\}^{-1} \left[\left(\frac{\text{Th}}{\text{U}}\right)_s^* + 1 \right]$$

For convenient data analysis, it is easiest to handle the data as if $\sigma_{\text{Th}} = \sigma_{\text{U}}$. Simplifying the notation so that $[\text{Th}/\text{U}] \equiv [\text{Th}/\text{U}]_s$ and $[\text{Th}/\text{U}]^* \equiv ([\text{Th}/\text{U}]_s)^*$, the difference between the Th/U ratio of a sample where fission cross sections are properly incorporated and the Th/U ratio where equal fission cross sections are assumed can be calculated by subtracting equation (6) from equation (5) and using the substitution defined in (7):

$$(8) \quad \left[\frac{\text{Th}}{\text{U}} \right] - \left[\frac{\text{Th}}{\text{U}} \right]^* = \left(\frac{\sigma_{\text{U}}}{\sigma_{\text{Th}}} - 1 \right) \left\{ \left[\frac{\text{Th}}{\text{U}} \right]^* + 1 \right\} \left(\left[\frac{\text{Th}}{\text{U}} \right]_o + 1 \right)^{-1} - 1 \left\{ \right.$$

In our cyclotron irradiations we are really measuring the $[\text{Th}+\text{U}]$ concentration of a sample. Adding and subtracting 1 to the left side of equation (8) gives:

$$(9) \quad \left[\frac{\text{Th}+\text{U}}{\text{U}} \right] - \left[\frac{\text{Th}+\text{U}}{\text{U}} \right]^* = \left\{ \left[\frac{\text{Th}+\text{U}}{\text{U}} \right]^* \left[\frac{\text{Th}+\text{U}}{\text{U}} \right]_o^{-1} C \right\} - C$$

where $C \equiv [(\sigma_{\text{U}}/\sigma_{\text{Th}})-1]$. Δ is defined as this difference

factor calculated in equation (9). Using the experimentally determined value of $\sigma_{\text{Th}}/\sigma_{\text{U}} = 0.87 \pm 0.01$ for 40 MeV protons, for example, the correction factor becomes:

$$(10) \quad \Delta = ([\text{Th}+\text{U}]/\text{U})^*(0.080) - 0.15$$

Converting from atomic ratios to weight ratios changes the correction factor only slightly to

$$(11) \quad \Delta_w = ([\text{Th}+\text{U}]/\text{U})^*(0.078) - 0.15$$

Using equation (11), when $([Th+U]/U)^*=5$, the relative fission cross-section correction is $\Delta_w=0.24$ and $([Th+U]/U)=5.2$. For $([Th+U]/U)^*=15$, $\Delta_w=1.0$.

Appendix II: Sample/Standard Preparation

A. Bulk sample pellets

To determine bulk meteorite Th/U ratios meteorite material was crushed and then pressed into 5mm diameter, 30mg pellets. In the early stages of the project, meteorites were crushed by hand using a stainless steel mortar and pestle. Later a mechanical ball mill was obtained. Most C2's and C3's were then crushed using a hardened steel vial with hardened steel ball in the automatized mill. The more friable C1's were crushed using a polystyrene vial with polyethylene cap and methacrylate ball-pestle to reduce blanks.

1. Mortar and Pestle Crushed Bulk Samples

The mortar, pestle, and confining sleeve assembly is made of 4-40 stainless steel. Initial clean up involves scrubbing with 600 grit SiC paper and a 1 micron to 0.3 micron alumina-ethanol slurry on a cotton swab. The equipment then undergoes a series of multiple ultrasonic cleanings in trichlorethylene, acetone, 100% ethanol, ending with spectroscopic quality methanol. Spectroscopic quality methanol is always used in the final cleaning stage. Meteorite fragments to be crushed are located away from any fusion crust. 600 grit SiC paper is used to remove the outside layer and then the sample is ultrasonically cleaned in Spec quality methanol. The NMNH Orgueil and Ivuna C1 meteorite samples were treated differently because they contain components soluble in organic solvents, and because they are friable enough to be easily dissected. Single fragments were carefully dissected under a stereomicroscope until all museum-exterior material had been removed. After crushing, the meteorite material is

passed through a 37μ nylon seive. The material is viewed under a binoc to remove any obvious foreign material, e.g., nylon mesh, and then weighed. Powder fractions of 30-40 mg are pressed in a die (Beckman Instruments # D-0 which has been cleaned in a procedure similar to the mortar and pestle) for 30 seconds at 3,000lb. pressure. The resultant pellet is 5mm in diameter and roughly 1mm thick. Blanks are made from T-21 Suprasil quartz glass. The glass is cleaned for 1 hour in a solution of 1 part HNO_3 to 2 parts distilled water. It is then rinsed in distilled water and undergoes a series of ultrasonic cleanings. The processes of crushing, sifting, splitting, and pressing of a blank pellet are identical to a meteorite sample.

2. Ball Mill Crushed Samples

For C2, C3 and SiO_2 glass blank pellets a hardened steel (HS) vial and ball are used for the crushing. A new ball and vial are initially ultrasonically cleaned in trichlorethylene, acetone, and several times in 100% ethanol. Then to "season" or "age" the HS vessel clean quartz is run through the automatized mill (Spex Industries, No. 5100) for about 4 minutes, the powder removed, and the vial and ball cleaned with a cotton swab and 100% ethanol and air dried. This process is repeated several times for a new vial. Each time the crushed powder lightens in color compared to the dark grey color of the first crushed aliquot. The process is repeated several more times with the intermediate cleaning step now involving use of 0.3-1 micron alumina and a cotton swab with 100% ethanol followed by an ultrasonic rinse in 100% ethanol. In total it may take up to 10 runs of quartz through the ball mill

before the quartz powder comes out looking white in color. With a final swabbing of the vial and ball with the alumina and cotton swab dipped in ethanol an ultrasonic rinse in 100% ethanol and two ultrasonic rinses in spec quality methanol the meteorite samples and blanks are ready to be crushed. Typically, 150 mg of material is crushed at a time. If the mill is run for 1.5 minutes, all material will pass through a 200 mesh nylon sieve.

Between each mill run for different meteorite samples, the ball and vial are swabbed with alumina and 100% ethanol on a cotton swab, ultrasonically rinsed in 100% ethanol and several times in spec quality methanol, and finally air dried. From this crushed powder stage to the final pressed pellet, the samples are handled the same as the mortar and pestle crushed samples.

For extremely soft samples, in particular some samples of Ivuna and Orgueil, a methacrylate ball and vial were used instead of the hardened steel.

B. Polished Section Preparation

The extremely friable nature of the carbonaceous chondrites made polished section preparation a challenge. Essentially we had to learn as we went. The meteorite section samples began as .5 - 1 mm thick slabs. These were obtained by slicing a meteorite fragment on a Buehler Isomet saw with either a .006 or .012 inch thick diamond wafering blade. Slicing was done under a 100% ethanol slurry to avoid meteorite contact with water. These slices and, in some cases, small fragments which contained inclusions of interest,

were then epoxy-impregnated to help prevent crumbling during the grinding stages of section making. Following the procedure of Moreland (1968) impregnations were done under vacuum with the sample immersed in a mixture of 3:1 toluene and epoxy. Colpot epoxy was used in all stages of our section preparation. The vacuum was broken approximately every 15 minutes during the 2 - 3 hour impregnation process to allow the intruding air to aid in forcing the epoxy solution into these porous samples (Moreland, 1968). After impregnation the sample was extracted from the impregnation solution and the surface gently wiped with a Kimwipe to remove excess impregnation fluid. The sample was now ready to be epoxied to a 1/4 inch diameter aluminum post. Pre-epoxying, the mounting surface of the posts were lightly roughed with 400 grit SiC paper and cleaned. This rougher surface helped to strengthen the Al-epoxy bond and thereby decreased the chance of a meteorite sample tearing off the aluminum post during polishing. Full strength Colpot epoxy was used to bind the sample to the post. The thickness of the binding epoxy was held to a minimum for irradiation reasons. With the addition of a small weight to press the sample-post assembly together the epoxy was allowed to cure overnight in a ~90°C oven.

Thick samples were put on the lathe to be thinned down to ~600 microns. This was a slow process but insured against gross wedging of a sample in the early grinding stages. A clean carbide tool was used and 100% ethanol from a squirt bottle bathed the meteorite surface continuously. The sample edges were also trimmed down on the lathe to exactly cover the 1/4 inch diameter area of the aluminum post.

The remaining grinding steps were done on a Buehler lap wheel. A Buehler AB Whirlimet polishing attachment provided the option for simultaneous automatic polishing of multiple samples. This attachment moved the samples in a restricted circular direction opposite to the rotation of the lap. Samples under moderate weight to insure even surface pressure were ground down to ~200 microns with 600 grit SiC paper covering the lap wheel. The lap was run at 600 rpm with continuous feed of 100% ethanol over the SiC paper. Care was taken throughout this grinding process to rotate the sample periodically with respect to the direction of lap rotation to prevent sample wedging.

The next step involved thinning the 200 micron sample down to 60 - 90 microns. This was accomplished by using a few dabs of 3 micron diamond paste placed on a lap wheel covered by two layers of Kraft heavy duty wrapping paper (use of this Kraft paper is suggested by Moreland, 1968). Just enough Buehler AB automet lap oil to moisten the paper is then added. The wheel was run at 600 rpm with moderate weight applied to the samples. After every three minutes the sample surfaces were cleaned with 100% ethanol and then rotated 90° with respect to the lap rotation direction before continuation of grinding. Again this was to insure against gross sample wedging. Lap oil was added as the Kraft paper dried out and the paper itself was changed as it wore rough. Total lap time during this 3 micron diamond grinding stage was typically 40 minutes. Upon completion of this procedure the samples were ultrasonically cleaned in 100% ethanol.

The polishing process was done one sample at a time. This

allowed us to individually tailor the polishing procedure to sample surface response. Use of 0.3 alumina with 100% ethanol often proved hit or miss as to whether the surface polished up before plucking occurred. Rather, what seemed to work consistently the best was 1 micron diamond paste with Buehler lap oil on Texmet paper. Sometimes the initial polishing was done with the aid of the lap wheel. The sample was held by both hands and moved perpendicularly across the direction of rotation of the wheel in several quick swiping motions. The sample was rotated between each swipe. In all cases, however, the final polishing was done totally by hand. Polishing progress was checked continually by ultrasonically cleaning the sample in 100% ethanol and making detailed inspections under a reflected light microscope.

To clean the polished section mounts an extremely soft toothbrush or a cotton swab is used with Alconox detergent (Alconox Inc., N.Y.) in 100% ethanol and the surface carefully scrubbed. This is followed by an ultrasonic cleaning in Alconox and 100% ethanol and several 100% ethanol rinses (the alconox does not dissolve well in the 100% ethanol. It is made for use with water but at no stage are our samples put in contact with water.) There are then two more ultrasonic cleanings in 100% ethanol and two final ultrasonic cleanings in spec quality methanol. Care is taken to never have drops of the cleaning solvent dry leaving a residue on the sample surfaces.

C. Standards

Glasses used as standards in this experiment are from a 370ppb uranium microscope slide glass (Gold Seal micro-slides A-1458, Clay Adams, Inc., N.Y.). The Gold Seal slides used are 50 x 75 mm and $1.21 \pm .05$ mm thick according to the manufacturer's specifications. By using a dental drill, the slide can be cut into a large number of small square pieces which in turn can have their corners rounded into 1/4 inch or 5 mm diameter disks for use in the cyclotron irradiations. In our reactor runs, where the restrictions are greatly relaxed as regards thermal and irradiation damage, glass standards in any shape are mounted in 5/8 inch diameter Colpot epoxy. Details are discussed in section II-C-1 on reactor experiment packaging in the main text. At times various NBS standard glasses are also included in an irradiation as an additional internal check. Slices ~ 25 mils thick are cut with a diamond wafer blade from the 1 centimeter diameter NBS glass rods. From these slices 5mm to 1/4inch diameter sized pieces are fashioned with a dental drill using SiC and diamond-tipped tools for use in the cyclotron and reactor irradiations.

Cleaning procedure for the glasses is similar to that described for the polished sections. It was found, however, that the final polish was best when an alumina-water slurry is used. Tiny residual pitting with alumina-ethanol slurries could be a result of a chemical interaction with the glass but is probably a result of more alumina clumping in the ethanol slurry compared to the water slurry.

Appendix III: Relative Track Counting Efficiencies at High and Low Density: The SMI Factor

Before one measured track density can be directly related to another track density from a different sample, various factors relating to track counting efficiency must be considered. For example, how long a mica was etched, what magnification the tracks were counted, whether reflected or transmitted light was used, and the magnitude of the track density itself all affect how an observer recognizes and counts a feature as a track. Hence, when circumstances allow, samples and standard micas should be etched and counted under as identical conditions as possible, but in our reactor experiments involving the CC bulk pellets this was not possible. In these experiments the standards used have close to 40 times the uranium content as the average bulk meteorite sample. As such this factor of 40 is reflected in the track densities observed: $1.6 \times 10^7 / \text{cm}^2$ for standards and $4 \times 10^5 / \text{cm}^2$ for bulk meteorites. At 1250x magnification this means an observer sees about 40 tracks per field of view for a meteorite detector mica while he sees 1600 per field of view for a standard mica. Using transmitted light, counting 1600 tracks of 10 microns length in a field of view $100 \mu \times 100 \mu$ is difficult. Under these high track density conditions, low etch-high magnification reflected light counts are necessitated. This way only the surface expression of the track (a characteristic diamond-shape for mica detectors) is observed and the isolation of individual tracks is possible. For the low track densities encountered in the reactor irradiated CC pellet micas, however, long etch times and transmitted light counts

are called for since tracks need ideally to be large high contrast features to avoid being omitted.

In order to get wider tracks, the mica etch time for the meteorites was increased from 12-16 minutes to 32 or 64 minutes; however, this increase in etch time was enough to cause a previously unknown track background to emerge. We interpret these tracks as due to heavy nuclide recoils from fast neutrons. They appear to have a much higher density over (Fe-bearing) meteorite samples; consequently, it is not possible to make a simple background subtraction from an interior mica surface. As with the charged particle recoil tracks in our cyclotron irradiations, these fast neutron recoil tracks are short (<1 micron), but at 64 minutes etch they can be as wide (~ 3.5 microns) as some fission tracks. Several pellet micas had been counted after a 12 minute etch prior to being etched the full 64 minutes. Comparison of these track counts can give an idea of the magnitude of the interference these wide recoil tracks can make on accurate fission track counts. Both the 12 minute and 64 minute etched micas were counted in transmitted light at 1250x magnification. Although standard track counting practice has always been to discriminate against anything <1 micron in length, out of four micas counted the track density for three increased by $\sim 30\%$ in going from the 12 minute to the 64 minute etch time and one increased by $\sim 45\%$. Switching from transmitted to reflected light adds an additional $\sim 2-4\%$ in the track density measured for the 64 minute etched micas. What had to be developed was a strict track counting criterion that would discriminate against recoil tracks without biting into too

much of the short fission track population. Using transmitted light, only tracks with width >3.5 microns and enough contrast to indicate depth (i.e., ≥ 1.5 microns) were counted. For the 64 minute etched pellet micas, transmitted light counts applying the counting criterion were most comfortably done at 625x magnification. The pellet micas etched 32 minutes were counted at 1250x.

To ascertain that criterion judgments would not vary over time, a set of calibration micas was established. These calibration micas, designated SMI, were irradiated in a neutron howitzer with a ^{235}U foil which produces a fission track density of $\sim 2 \times 10^5/\text{cm}^2/\text{hr}$. A two hour howitzer irradiation would approximate the fission track densities encountered in our reactor irradiated CC pellet samples. In these SMI micas all tracks are fission tracks. Applying the CC pellet counting criterion to a 64 minute etched, 2 hour-irradiated SMI mica under transmitted light at 625x magnification results in the omission of roughly 4% of the fission track population. For micas etched 32 minutes and counted in transmitted light at 1250x magnification a similar number of 4-5% fission track omission is obtained with application of the counting criterion. (Theoretically, discrimination against tracks $< 1.5\mu$ should omit $\sim 10\%$ of the total fission track population. However, it is consistency in counting that really matters.)

Depending on whether a reactor irradiated pellet mica had been etched 64 minutes or 32 minutes, a corresponding SMI mica was periodically re-counted under the exact same conditions to assure counting criteria judgments held constant with time. For example, the results of

periodic recounting of one SMI mica, etched 64 minutes are presented in Figure 28 and Table 16 (C). Track recounts for this SMI mica with track density $\sim 5 \times 10^5/\text{cm}^2$ (simulating the fission track density for a reactor irradiated meteorite pellet sample) over one month's time reproduced within 3.4%. Over a four month period of time, which included a 2 month hiatus, recounts reproduced within 4.1%.

To handle the problem of comparing the low track density-long etch time meteorite samples with high track density-short etch time standards an independent set of calibration micas, part of the SMI series, was created to determine a track counting efficiency factor which we designated as the SMI factor. A series of irradiations with the neutron-howitzer for varying times were made to give fission track densities (ρ_{Lo}) comparable to those observed in the CC micas or, alternatively, track densities (ρ_{Hi}) close to standard glass values. These micas were then etched and counted in the manner of a bulk sample or standard using both 32 and 64 minute etches for the low density SMI micas. Since great care was taken to replicate as closely as possible the howitzer irradiation geometry from run to run and exact exposure times were recorded, a track production rate (tracks/cm²/hour) for each SMI mica was determined. The individual SMI data are tabulated in Table 16. Nominally this track production rate should be a constant regardless of howitzer exposure time. Any differences between track production rates for short exposure and long exposure times should thus reflect differences in the efficiency of track counting.

FIGURE 28

This graph illustrates the consistency of application of the fission track counting criterion over time. Track density versus date of track density measurement is plotted for the SMI-1 (see text) mica. This mica was etched 64 minutes.

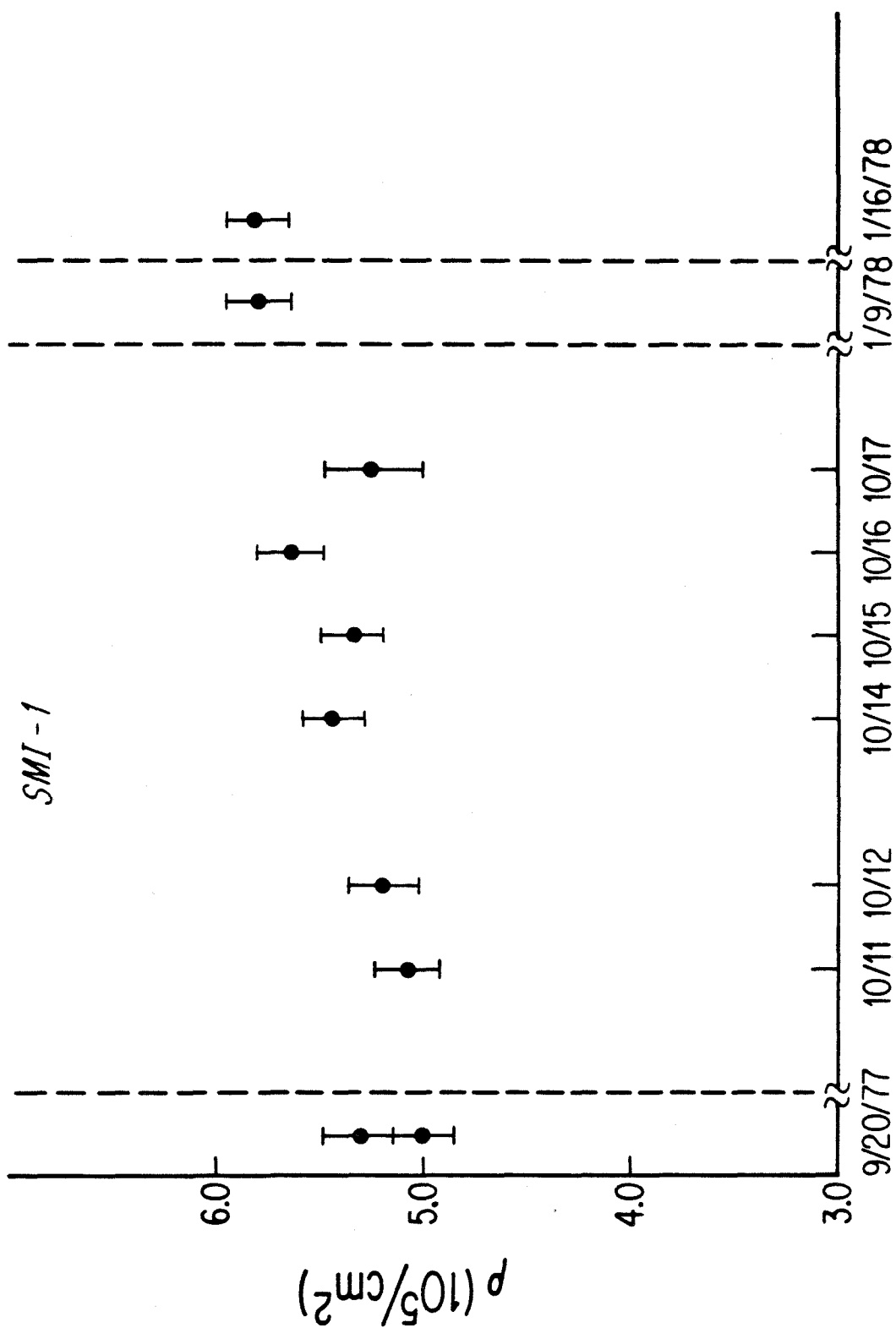


TABLE 16

SMI NEUTRON-HOWITZER IRRADIATED FISSION TRACK PRODUCTION RATES

A. High fission track density SMI micas - 16 minute etch
(1250 x reflected light counts)

<u>SMI</u>	<u>Δt (howitzer)</u>	<u>Date of track count</u>	<u>Fission track production rate ($10^5/cm^2/hr$)</u>
7	65.80 hr	12/9/77	$2.14 \pm .08$
10	52.95 hr	12/9/77a	$2.49 \pm .08$
10	"	12/9/77b	$2.23 \pm .08$
6	63.90 hr	8/22/77	$2.22 \pm .05$
2	68.80 hr	8/15/77	$2.24 \pm .04$
2	"	1/16/78	$2.33 \pm .07$
			Av. = $2.28 \pm .12$

B. Low fission track density SMI micas - 32 minute etch
(1250 x transmitted light counts)

<u>SMI</u>	<u>Δt (howitzer)</u>	<u>Date of track count</u>	<u>Fission track production rate ($10^5/cm^2/hr$)</u>
8	1.85 hr	12/6/77a	$2.54 \pm .11$
"		12/6/77b	$2.59 \pm .11$
"		12/8/77a	$2.74 \pm .11$
"		12/8/77b	$2.66 \pm .11$
"		12/9/77	$2.72 \pm .11$
9	1.97 hr	12/6/77	$2.46 \pm .10$
12	2.00 hr	1/7/78	$2.69 \pm .10$
			Av. = $2.63 \pm .10$

C. Low fission track density SMI mica - 64 minute etch
(625 x transmitted light counts)

<u>SMI</u>	<u>Δt (howitzer)</u>	<u>Date of track count</u>	<u>Fission track production rate ($10^5/cm^2/hr$)</u>
1	2.17 hr	9/20/77a	$2.30 \pm .06$
"		9/20/77b	$2.46 \pm .07$
"		10/11/77	$2.31 \pm .06$
"		10/12/77	$2.41 \pm .06$
"		10/14/77a	$2.51 \pm .07$
"		10/14/77b	$2.47 \pm .07$
"		10/16/77	$2.52 \pm .07$
"		10/17/77	$2.42 \pm .06$
"		1/9/78	$2.59 \pm .07$
"		1/16/78	$2.59 \pm .07$
			Av. = $2.46 \pm .10$

For reactor run Col MS-1 the CC pellet micas were etched 32 minutes and counted at 1250x in transmitted light. The corresponding track counts on SMI micas give the ratio of average track production rates (calculated from the data presented in Table 16) as:

$\langle \dot{\rho} \rangle_{Lo} / \langle \dot{\rho} \rangle_{Hi} = 1.15 \pm 0.07$. The errors (1 σ mean) are derived from the observed deviation in the individual analyses from the mean production rate. Thus, before meteorite track data can be directly related to standard glass track data the meteorite data must be divided by an SMI factor of 1.15.

For pellet samples in reactor runs Col MS-2 and Col MS-3 the micas were etched 64 minutes and counted at 625x in transmitted light. Micas for standards in these runs were etched 16 minutes and counted at 1250x in reflected light. Under these conditions the SMI factor becomes: $\langle \dot{\rho} \rangle_{Lo} / \langle \dot{\rho} \rangle_{Hi} = 1.08 \pm 0.07$ where the average track production rates are determined from the data presented in Table 16 and the SMI error calculated from the standard deviations from the mean of each average track production rate. Again it is the ratio of the pellet sample mica track density to the standard glass mica track density multiplied by the reciprocal of the SMI factor that has direct meaning for the ratio of U contents between sample and standard.

In summary, for long etch low track density micas, application of the strict track length criterion to help discriminate against recoil tracks in the meteorite micas omits 4% of the fission tracks. However, under the differences in etching conditions and reflected vs. transmitted light counts, low track density ($10^5/\text{cm}^2$) micas

are still counted at ~10% higher efficiency than high track density ($10^7/\text{cm}^2$) micas. Thus, incorporation of this track counting efficiency factor (SMI) is important for proper analysis of our meteorite track data.

Appendix IV: Small Angle Scattering

Multiple scattering theory shows that a beam of medium energy protons which passes through a material of moderate thickness is scattered into an approximately Gaussian distribution (Marion & Young, 1968). That is, $F(x) \approx \exp -[0.5(x/x_0)^2]$ where x is the angular distance from the center of the beam and $2^{0.5}x_0$ is the angular distance at which the gaussian beam distribution has fallen to $1/e$ of its value for zero deflection. In our cyclotron irradiations we use an aluminum foil upstream of the target to disperse the 1/8 inch diameter focussed particle beam over the 3/4 inch target. The determination of foil thickness and foil-target distance cannot just hinge on maximizing beam homogeneity over the target, because the extracted cyclotron beam currents would necessitate long irradiations to obtain the minimal dosage requirements. Trade-off criteria between homogeneity and acceptable beam loss had to be established.

The pertinent equations for the calculation of the dispersing angle at which the angular distribution has fallen to $1/e$ of its value at zero degrees deflection are presented in Marion & Young(1968). These equations are somewhat awkward to use for they are most easily solved with the thickness of the scattering foils as initial input. A more utilitarian approach gives foil thickness as the output value.

Following Fano (1964),

$$\langle 1 - \cos\theta \rangle \sim k Z (m/M) \ln[(E_0[E+2Mc^2])/(E[E_0+2Mc^2])] \quad (1)$$

where θ = scattering angle,

k = dimensionless coefficient with minor residual dependence
 on both material and energy
 Z = atomic number of the dispersing foil
 m = mass of electron
 M = projectile mass, i.e. cyclotron beam particle
 E_0 = initial particle kinetic energy
 E = particle kinetic energy after passing through the foil

A non-relativistic form of the equation gives,

$$\langle 1 - \cos\theta \rangle \sim k Z (m/M) \ln(E_0/E). \quad (2)$$

Doing a first order Taylor expansion of $\ln(E_0/E)$ about E_0 gives,

$$\ln(E_0/E) = (E - E_0)/E_0 = \Delta E/E_0. \quad (3)$$

Therefore,

$$\langle 1 - \cos\theta \rangle \sim k Z (m/M) (\Delta E/E_0). \quad (4)$$

The angle θ is defined such that $\tan \theta = x/s$, where x is a radial distance measured from the center of the target toward the target perimeter, and s is the foil-target distance. For small angles $\tan \theta \sim \theta$. Thus equation (4) becomes

$$\langle 1 - \cos\theta \rangle \sim \langle \theta^2/2 \rangle \sim k Z (m/M) (\Delta E/E_0) \quad (5)$$

$$\text{or, } \langle (x/s)^2 \rangle \sim K [Z(m/M)(\Delta E/E_0)] \text{ , where } K = 2k. \quad (6)$$

$$\text{Thus, } \langle (x^2) \rangle^{0.5} = [KZ(m/M)(1/E_0)]^{0.5} [(\Delta E)^{0.5} s] \text{ for } s = \text{cons.} \quad (7)$$

Since $\Delta E = (dE/dx)_E t$, where dE/dx equals the stopping power of a beam particle (e.g. see Northcliffe & Schilling, 1970) and t = the thickness of the foil, then

$$\langle (x^2) \rangle^{0.5} \propto st^{0.5}. \quad (8)$$

With these relations, we shall follow a calculation for a realistic situation for our experiments. In TA&M-10 the extracted proton beam was 6 micro-amps with 4 microamps actually making it down beam-line to our experimental area. Dispersal of the beam should allow at least 2 microamperes on target to obtain a

comfortable dosage in a reasonable amount of time (at 2 micro-amps we get ~10 microampere-hour/cm² in 20 hours). For

$$I/I_0 = \exp - [0.5(x/x_0)^2] \quad (9)$$

the requirement that half the intensity be included within our 3/4 inch target area implies $x_0 = 0.552$ inches. With this x_0 we have,

$$\frac{I(x=.375)}{I(x=0)} = 0.79.$$

In other words, we expect ~ 80% beam homogeneity from center to edge over our 3/4 inch target. In TA&M-10 we used 40 MeV protons and an aluminum dispersing foil. Referring to the tables in Fano(19xx) $k \sim 0.9$. Since $x_0 = (\langle x^2 \rangle)^{0.5}$ for a gaussian distribution, we obtain:

$$\Delta E^{0.5s} = .552([40/1.8][2000/13])^{0.5} = 33 \text{ MeV}^{1/2}\text{-inch.}$$

With a foil-target distance $s = 42$ inches in TA&M-10, $\Delta E \sim 0.9$ MeV. The dE/dx for 40-35 MeV protons is ~ 0.1 MeV/.001 inch. Use of a .009 inch foil is therefore indicated to meet the beam loss and homogeneity criteria established. Because our foils came in .004 inch sheets, we used a total thickness of .008 inch. Comparison of foil-in/foil-out target beam current readings were used to monitor the amount of beam loss due to foil beam dispersal. For Texas A&M 10, the dispersing foil produced about a factor of two attenuation, as planned; however, the actual post-irradiation dosimetry measurements revealed a center to edge homogeneity of 50%, significantly less than the 80% expected from the above calculations. The reason for this difference is not understood. Possibly electrons from the dispersing foil produced a higher attenuation of beam current than the actual proton beam attenuation.

Appendix V: Cyclotron Dosimetry

An initial attempt to measure relative doses between positions in the seven-sample cyclotron target array involved measuring the induced gamma-activity variations across the aluminum array holder. (Refer back to Fig. 6a.) This induced activity results from cyclotron beam spallation reactions with constituent nuclei of the sample holder. The bottoms of the seven 1/4-inch diameter sample wells were punched out of the holder and individually gamma-counted using a NaI crystal detector with a multichannel analyzer. It was thought that comparing specific peak intensities between the holder pieces would give the relative dose measurements. It soon became evident, however, that there were problems with the interpretation of these data. Slight shifts in the beam energy due to passage through different types of samples (e.g., pellet vs. section) or around slightly undersized samples changed the amounts of gamma activity in the aluminum below the meteorite samples. As a result of this finding, only the Layer A (upstream layer in a two layer target) heat sink plate or Layer A top detector mica could be used for dosimetry. Both of these target pieces were irradiated with mono-energetic particle beams. Layer A detector micas were preferentially used for the dosimetry because more accurate comparisons of dosimetry and areas scanned for tracks could be made.

The prospect of trying to cut the detector mica precisely along fiducial lines to isolate the individual sample positions for gamma counting seemed difficult at best. Also, since edge to edge dose variations over a single 1/4 inch position could be as high as a factor of two, use of average dosimetry readings for a particular

sample position would be unacceptable for our inclusion microdistribution studies. Thus, an alternative to direct gamma-counting was sought that would circumvent the need to cut up the detector mica for inter-sample relative dose measurements plus provide the resolution to permit detailed intra-sample dosimetry mapping.

Dosimetry by beta radiography was done by placing the Layer A detector mica in contact with a photo-emulsion plate, Kodak spectroscopic Type III-O. [Developing recipe is as follows. Developer: Kodak DK-50, 2 minutes and 35 seconds with agitation at $\sim 20^{\circ}\text{C}$; Short Stop: 1 oz. acetic acid to 16 oz. water; Hypo: Kodak Fixer, 6.5 minutes at $\sim 20^{\circ}\text{C}$ with agitation; Rinse: ~ 1 hour under running water, final rinse with distilled water to prevent spotting; Dry: air dry room temperature].

Quantitative readings of percent transmission (100% corresponds to a transparent plate, 0% to total opaqueness) were made with a densitometer (for general ref. see Methods for Emission Spectrochemical Analyses (1971), Am. Soc. for Testing & Materials, Philadelphia, Pa.). The densitometer used (designed to analyze spectral lines) made readings through a 500 x 40 micron slit, which could be scanned across an entire plate. To be able to relate positions on the mica with positions on the emulsion plate three 0.015 inch holes were drilled through the mica from which to reference a coordinate system. Precision dial indicators placed along the x-y drive of the densitometer stage permitted the position of each percent transmission reading to be recorded as well as the three fiducial holes. In this way densitometry maps were made. The detector mica was scratch-fiducialled while

still in place over the meteorite sample array to outline sample positions as well as grid each sample surface. Photos were taken of the samples through the scratched mica. This photo-documentation permits mica to meteorite position correlations to be made. This fiducial scratch system can be referenced to the three-hole dosimetry fiducial system by using a precision x-y stage with coordinate read-out capability on the optical microscope. Thus dosimetry readings over any area on a meteorite sample can be obtained. It should be noted that because the sample positions for targets with two layers were machined to be directly aligned one on top of the other, bottom layer sample dosimetries can be determined from the top layer mica dosimetry map.

The details of emulsion response to a flux of incident charged particles or photons are not completely understood. In the most simplistic sense, the photographic process involves the dissociation of silver halide grains to form Ag metal grains with the incident particle providing the energy of the reaction (for general reference see James, 1977). The quantity measured by the photo-densitometer is the %transmission through the exposed emulsion plate ($\%T = (I/I_0) \times 100$, where I_0 is the incident light intensity). Similar to equations for light scattering through a medium, an optical density can be defined as $D = -\ln(I/I_0)$, a quantity proportional to the number of scatters, i.e., the number of Ag grains in the emulsion. The rate of Ag production is not constant with time during the plate exposure, however, due to the continued depletion of available Ag-halide grains. Thus, at some point an essentially linear relationship between $\log\%T$ vs. length of exposure

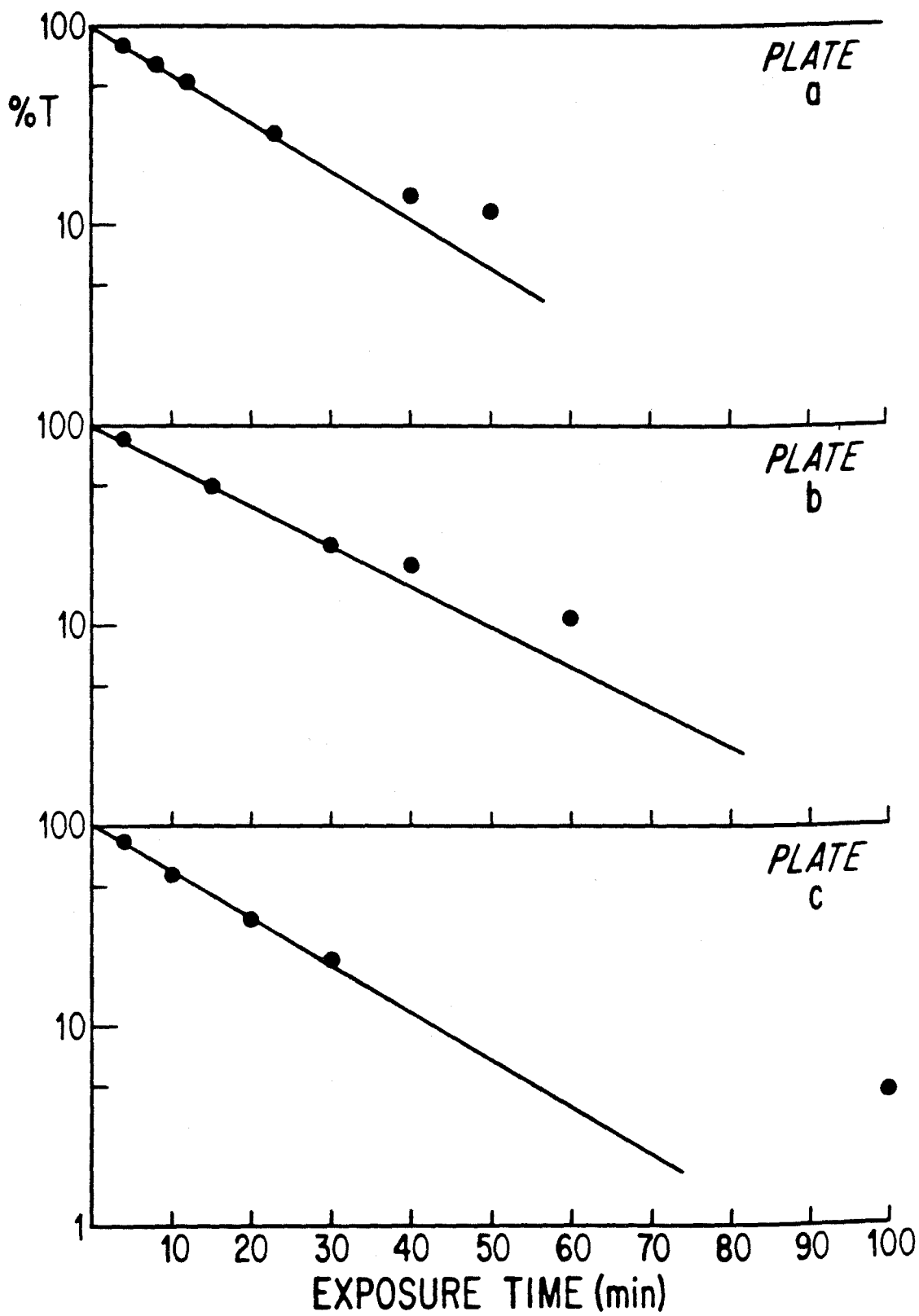
(i.e., dose) is terminated as saturation effects dominate. It thus becomes necessary to define the limits that exposures should be made to retain linearity under the conditions of our experiment.

In order to calibrate plate response, four exposures of a ^{151}Sm beta-source of varying times, were done on three different plates. The longest exposures on a plate were always done first. Conditions of exposure (e.g., pressure on the emulsion, room temperature) were kept as constant as practically possible. Similarly, all three plates were developed under as identical conditions as possible.

Figures 29-a, b, and c illustrate the response curves for the three plates. Plotted on a logarithmic scale is the % transmission reading vs. the linearly scaled exposure time. For all three plates a straight line with a 0 minute-100% transmission axis intercept can be drawn through the data points for %Transmission > 30%, indicating an inverse linear relationship between $\log(\%T)$ and dose for $\%T > 30\%$. The major source of beta activity in the cyclotron-irradiated micas is from the decay of ^{22}Na . ^{22}Na beta energies are 0.54 MeV and 1.83 MeV in contrast to the 0.076 MeV betas from ^{151}Sm . For a given number of Ag grains (total) along the light beam path (which determines %T), the ^{151}Sm low energy betas have produced Ag at a higher concentration in the emulsion than the higher energy ^{22}Na betas. Higher Ag concentration means a higher AgBr depletion, and accepting that saturation is due to depletion of [AgBr] in the region developed, saturation would be expected to occur at higher %T for ^{151}Sm than ^{22}Na . As such exposure criteria derived from the ^{151}Sm emulsion response curves are even more restrictive than need be for

FIGURE 29

A ^{151}Sm beta source is used to calibrate photo-emulsion response to dose. A series of exposures of varying lengths of time (to vary dosage) were carried out on three separate plates. Percent transmission vs. exposure time is presented on a semi-logarithmic plot for plates (a), (b), and (c). In all cases, a linear relation between $\log(\%T)$ and exposure time is observed for $\%T > 30\%$.



our mica exposures. For practical reasons (i.e., to be able to visually identify an exposed plate area), no plate data were taken for $T > 90\%$. Therefore, mica photoemulsion dosimetry analysis was restricted to exposures in the range $30\% < T < 90\%$. This range covers a factor of 10 difference in dose.

Prior to drilling the three 0.015 inch holes in the mica for coordinate control, reproducibility from plate to plate in dosimetry measurements of ratios between two 1/4 inch sample areas hinged on being able to determine accurate plate locations. Before drilling the holes, reproducibility of the ratio of % transmission readings for the same two sample positions were as poor as 7.5%, but post-hole reproducibility measurements were 1.5% or better. In TA&M-10 (which includes all our Allende inclusion analyses) all samples were systematically analyzed with the high precision fiducial method, as were select samples from TA&M-6 and TA&M-8. Slippage of a 5 mm pellet sample within a 1/4 inch sample well can add 2.5-3.5% in the dosimetry measurements. Uncertainties in the measured dosimetry ratio of a sample to a standard could, in rare cases, be as high as 10%. These cases involved friable meteorite pellet samples that through breakage in handling were not full-sized, and, as such, required an increased error from position uncertainty within the target sample well.

The Texas A&M-6 pellet II target contained three CT standard glasses. Table 17 shows the correlation between the measured dosimetry ratios and the observed track ratios for these standard glasses. If our method of determining the dose is accurate, the relative track

TABLE 17
 TA+M-6 CT-GLASS TRACK DENSITY RATIOS
 VS
 PHOTOEMULSION DOSIMETRY RATIOS

(a) $\frac{CT_i}{CT_j}$	(b) $\frac{\rho_i}{\rho_j}$	(c) $\frac{T_i}{T_j}$
CT_4/CT_8	0.517 ± 0.031	0.538 ± 0.008
CT_8/CT_{10}	1.091 ± 0.054	1.081 ± 0.016
CT_4/CT_{10}	0.564 ± 0.035	0.581 ± 0.009

(a) i, j refer to position of CT-glass in TA+M sample target array

(b) ρ = tracks/cm²

(c) $T = \log [\% \text{ Transmission}/100]^{-1}$

densities measured should directly reflect the relative integrated dose each standard glass received. As can be seen, within the statistics of the track measurements the dosimetry ratios do indeed equal the track ratios between the standards.

Appendix VI: Interaction and Fission Track Registration and Annealing
in Cyclotron-Irradiated Mica

A. Interaction Tracks

A difficulty to overcome in using high energy particle induced fission for low-level Th+U abundance measurements is the interference from interaction tracks. Beam particles passing through the mica detectors scatter elastically and inelastically with constituent mica nuclei. Recoiling nuclei with $Z > 13$ (Croaz, 1969) can have sufficient energy to surmount the specific ionization threshold for track formation in mica. Because of their low energy and low specific ionization compared to fission fragments these interaction tracks are short, < 1.5 microns (Croaz et al., 1969) compared with 10μ full range fission tracks.

Table 18 lists the interaction track production rates measured for the various beams used in our cyclotron experiments and from other studies. We determined these rates by attempting to count interaction track pits on an interior surface of a cleaved and etched mica or a mica surface which was irradiated against another sheet of mica. The interaction track production rates measured by us are probably good to no better than a factor of two mainly because of the uncertainty in beam integration. The data show for $\sim 10^{17}/\text{cm}^2$ dose irradiations bulk CC sample fission track densities of $\sim 2 \times 10^4/\text{cm}^2$ must be discerned from an interaction track population of $10^8 - 10^{10}/\text{cm}^2$ in our cyclotron runs.

Croaz(1969), Maurette(1970) and Haines(1976) have demonstrated that alpha, heavy ion, and fast neutron induced interaction tracks

TABLE 18

INTERACTION TRACK PRODUCTION RATES

<u>Beam</u>	<u>Dose</u>	<u>Interaction Track Production rate</u>	<u>Study</u>
100 MeV α	$10^{14}/\text{cm}^2$	$\sim 2.2 \times 10^{-7}/\alpha$	This work
30 MeV α	$10^{15}/\text{cm}^2$	$6.5 \times 10^{-7}/\alpha$	Crozaz et al. (1969)
40 MeV p	$4 \times 10^{16}/\text{cm}^2$	$\sim 2 \times 10^{-9}/p$	This work
11 MeV p	$10^{16}/\text{cm}^2$	$< 6.5 \times 10^{-10}/p$	Crozaz et al. (1969)
50 MeV d	$4 \times 10^{15}/\text{cm}^2$	$\sim 3 \times 10^{-8}/d$	This work
Fast n	$10^{15}/\text{cm}^2$	$10^{-9}/n$	Haines et al. (1976)

Note: Numbers from this work based on 8 minute etch times

can be preferentially annealed relative to fission tracks. Previous fission track annealing studies, as cited in FPW(1975, p.82) indicate no fission track loss has been observed in mica for temperatures below 275°C for one hour. The important consideration in setting the annealing conditions in our experiments was that suppression of the interaction track background not be at a major cost to the fission track population.

In order to initially establish the limits for the annealing of interaction tracks as defined by an acceptable loss of fission tracks, a batch of 0.1% U glasses and mica detectors were sent to the Northrop reactor. This was a simple way to get large areas of mica with homogeneous fission track densities. Hughes-Liberty (H-L) and Indian-Washington U. (I) micas were irradiated. A neutron dose of $2.5 \times 10^{12}/\text{cm}^2$ produced fission track densities of $\sim 3 \times 10^4/\text{cm}^2$. Annealing experiments were carried out under controlled conditions. Post-irradiation, but pre-annealing, micas were "dried" for 12 hours at $\sim 130^\circ\text{C}$ to drive off any loosely bound water.

The annealing was done in a tube furnace with mica samples and monitoring thermocouple wrapped together in a thin (.001 inch) titanium foil. Samples and furnace reached an equilibrium temperature in less than 5 minutes. All annealing results will be given in terms of a retention factor, R.F.. The R.F. is equal to the ratio of the measured track densities in annealed mica to the measured track density in unannealed mica. Fission track counts are done for tracks $> 1.5\mu$.

The results for the Northrop irradiated H-L micas and I micas are presented in Figs. 30 and 31 respectively. All annealing

FIGURE 30

This figure summarizes the fission track annealing experiments on Hughes-Liberty mica irradiated in the Northrop reactor with a 0.1% U glass (see text). In this case the fission track retention factor (R.F.) is defined as the fission track density measured on an annealed mica relative to an unannealed piece of the same mica. R.F. is plotted against annealing temperature. Data points are identified by batch corresponding to pre-annealing "drying" run (see text). All micas were etched 8 minutes.

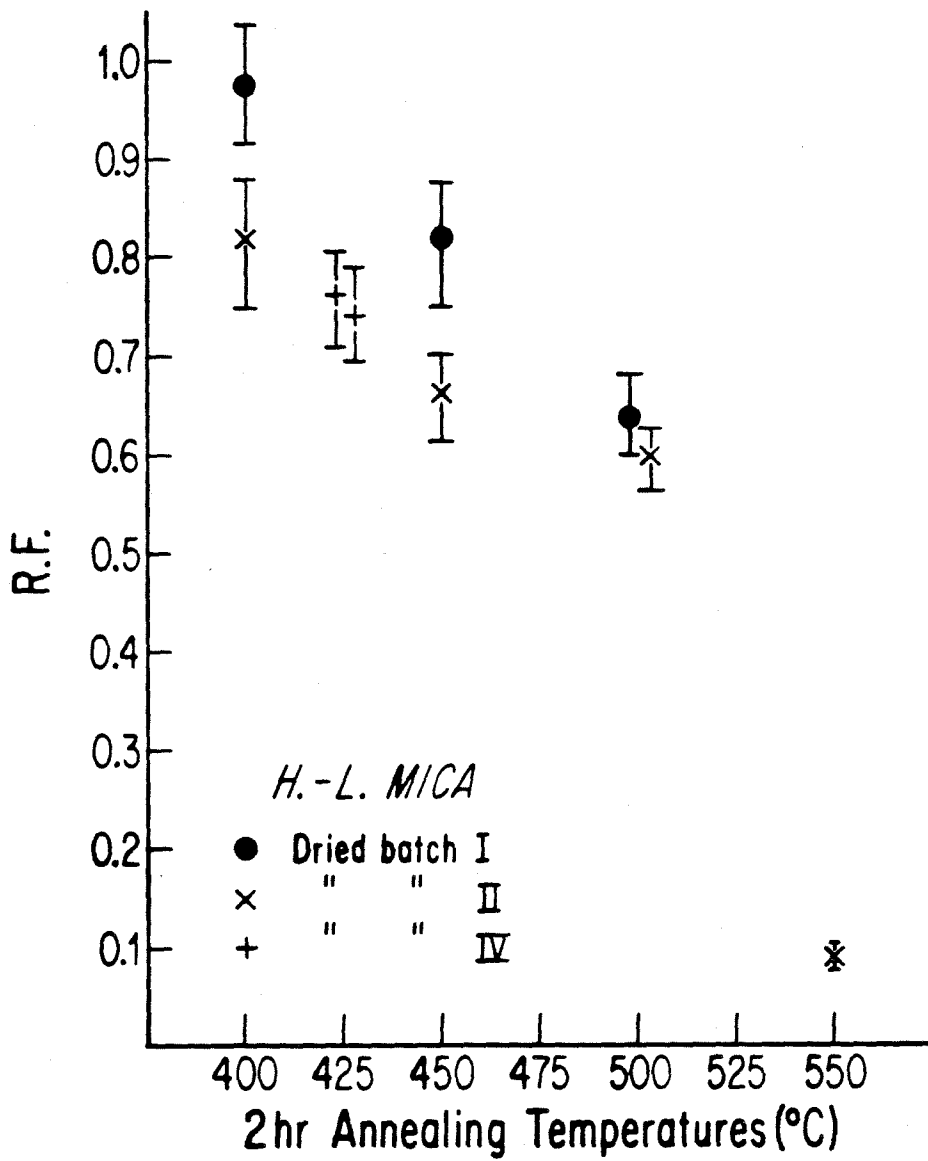
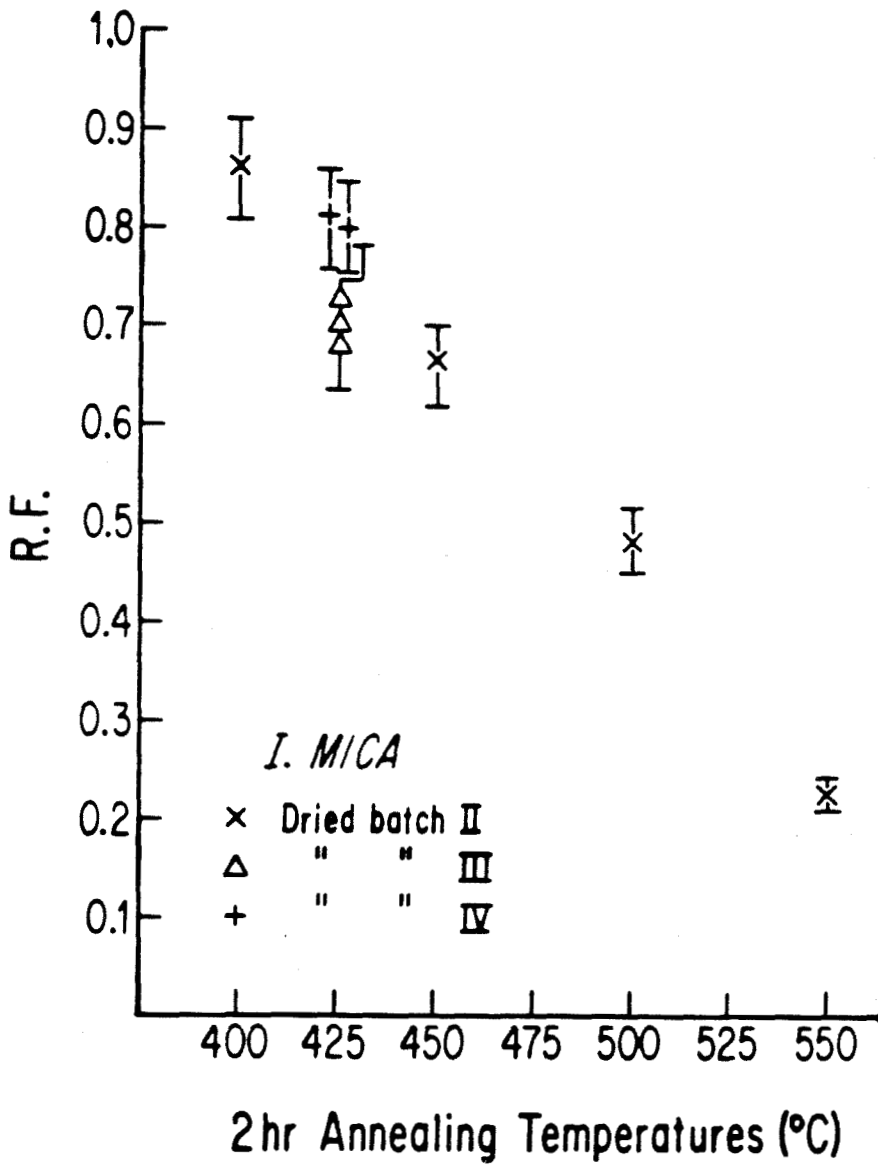


FIGURE 31

This figure summarizes the fission track annealing data for Indian-Washington U. mica irradiated in the Northrop reactor with a 0.1% U glass (see text). Fission track retention factor, R.F., relative to an unannealed piece of the same mica is plotted against annealing temperature. Data points are identified as to batch for pre-annealing "drying" (see text). All micas were etched 64 minutes.



times were two hours-- long compared to the time of initial furnace temperature stabilization but short enough for a practical laboratory timescale. Annealing temperatures chosen were 400°C, 425°C, 450°C, 500°C and 550°C with temperature variances kept to $\sim \pm 30^\circ\text{C}$.

Data points are distinguished as to the batch in which they were dried. Batch drying oven temperatures ranged from 128.9°C to 139.5°C. All fission track retention factors are determined based on an unannealed mica from the same drying batch. When the figures 30 and 31 are compared, it is seen that the fission track R.F. profiles for the two types of mica are not identical. There also appears to be some variability within the H-L micas. The H-L mica R.F. profile drops slowly up to 500°C and then changes slope, dropping steeply for higher temperatures. The Indian mica, on the other hand, shows almost a uniform straight line decreasing profile with temperature. For both H-L and I micas the fission track R.F. is ~ 0.75 after 2 hours at 425°C which is an acceptable fission track retention factor for our meteorite analyses.

To investigate how the alpha-interaction tracks respond to two hours at 425°C, micas from the TA&M-I 100 MeV alpha irradiation receiving various alpha-doses were annealed. The $\sim 10^7/\text{cm}^2$ interaction track population $\leq 1.5\mu$ accompanying a mica which received $\sim 10^{14}/\text{cm}^2$ alpha dose annealed out almost totally. However, for micas in targets receiving 10^{15} alphas/ cm^2 and 0.5×10^{16} alphas/ cm^2 the 425°C annealing failed to significantly improve the recoil situation.

What is especially disturbing in the alpha irradiations is the

surprisingly large population of long recoil tracks, larger than our cut-off criterion of 1.5 microns. A target consisting of an NBS "1 ppm" glass and its accompanying detector mica were irradiated in TA&M-I with a dose of 0.5×10^{16} alphas/cm². Track counts were done on both sides of the Indian mica detector. The side against the glass contains fission tracks from the Th+U in the glass as well as interaction tracks, while the reverse side which was against another piece of mica contains only interaction tracks. For a piece of this mica which was dried at ~130°C but not annealed, the interaction track density for tracks >1.5 micron on the back side of the mica was 0.55 of the track density observed on the side flush against the NBS 1 ppm glass. The combined Th+U content of the 1 ppm glass is ~1.6 ppm, making the long recoil track background as counted on the backside of the mica comparable to ~1.9 ppm Th+U. (Note: An upper limit of 10 ppb Th+U is attributable to the mica composition.) The effective cross section for such hard collisions is $\sim 10^{-6}$ barns/mica atom. These long recoil tracks are also highly resistant to annealing. Annealing for 2 hours at 425°C, retains ~75% of the long recoil tracks. It is precisely because of this unacceptable long recoil track interference that further use of the 100 MeV alpha beam for meteorite high dose irradiations had to be abandoned. [Note: An alternative to the theory that these interference tracks are long recoil tracks is the possibility that they represent heavy ion contaminants in the 100 MeV alpha beam.]

In an attempt to circumvent the unacceptable long recoil population of the 100 MeV alpha irradiations, samples of I and H-L micas were irradiated with a dose of $\sim 4 \times 10^{16}/\text{cm}^2$ of 40 MeV protons at a current of 3 micro-amperes. This dose would be adequate to obtain minimally acceptable statistics from the bulk CC samples. From track counts at 8 minutes etch an interaction track production rate of $2 \times 10^{-9}/\text{proton}$ was determined. By removing any minimum track length restrictions an attempt was made to count on interior mica surfaces an interaction track retention factor. Results from annealing micas two hours at 425°C gave an interaction track retention factor of $\sim 0.54 \pm 0.04$. For these proton irradiated micas, however, this recoil background is essentially entirely composed of highly subdued ≤ 1 micron pits. There is no longer the problem of a large population of long recoil tracks encountered in the alpha irradiations.

Because high extraction currents could be obtained routinely and quickly, the 50 MeV deuteron beam was investigated. The possibility of parasitic irradiations also existed. On H-L micas receiving a $4 \times 10^{15}/\text{cm}^2$ deuteron dose, an interaction track production rate of $\sim 3 \times 10^{-8}/\text{deuteron}$ was obtained. Test runs with deuteron doses up to $4 \times 10^{16}/\text{cm}^2$ seemed quite satisfactory. Micas remained transparent and annealing for two hours at 425°C suppressed the interaction tracks at least as well as found in the proton irradiations described above. A subsequent run using a 3 micro-ampere current in which the dosage was increased to $1.8 \times 10^{17}/\text{cm}^2$ ended consideration of any future use of the 50 MeV deuteron beam for our meteorite experiments.

The micas in this run sustained irradiation damage so severe that mica transparency was lost. It is unclear whether this was a unique damage threshold for the mica used (Div. Coll. 2469) or a more general phenomenon at the deuteron dosage.

As a result of the high dose deuteron experiment our attention was refocused on proton irradiations. Development of a high current 35 MeV proton beam proved a workable alternative. In TA&M-10, Indian-Washington U. mica baked for 15 hours at 250°C prior to the irradiation was used. The dose reached $2 \times 10^{17}/\text{cm}^2$ and the upstream detector micas for the two sample layers survived well. The subsequent two hour 425°C annealing of the irradiated micas suppressed the interaction track background allowing fission track counts to be easily made.

B. Fission Tracks in Irradiation-Damaged Mica

The experiment described in the previous section, which defined a 75% fission track retention factor for 2 hour annealing at 425°C, was based on fission tracks in non-irradiation damaged micas. The applicability of these R.F. results to fission tracks in irradiation damaged micas must be investigated. In particular, experiments investigating (1) the fission track registration efficiency in irradiation damaged micas and (2) fission track annealing in irradiation damaged micas are discussed.

1. A unique opportunity to study the effect of irradiation damage on the track registration properties of mica was afforded by our cyclotron target assembly. As discussed in the main text (section II D-1)

a seven-hole collimator is placed directly over polished sections to minimize the amount of epoxy hit by the beam (refer to fig. 7). A single layer target of sections irradiated in TA&M-6 received a 40 MeV proton dose of $6.6 \times 10^{16}/\text{cm}^2$. A mica spacer had been sandwiched between the seven-hole collimator and the detector mica for the sections. In areas exposed to the beam the downstream face of the spacer mica recorded interaction tracks and background fission tracks due to the U,Th impurities of the mica. Alternatively, areas on the mica not sitting directly under the collimator holes were totally shielded from the beam. Thus on one sheet of mica there are irradiation damaged areas (in this context referring to the presence of interaction tracks) adjacent to undamaged no-track areas. The characteristic discoloration of the irradiation damaged mica provides easy definition of the areas which saw the beam.

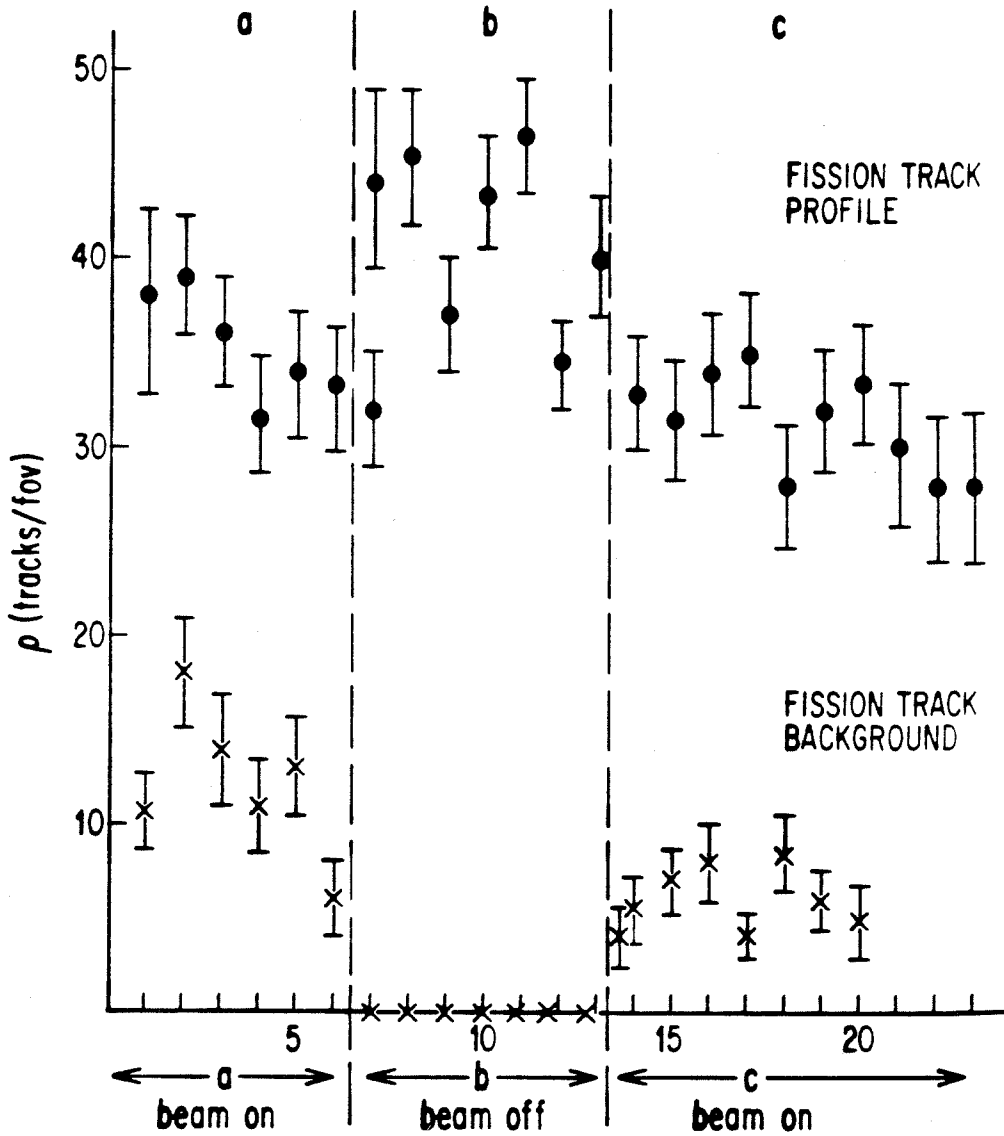
A quick experiment was done on this mica to see how and if the fission track registration properties of this mica are altered with irradiation damage. The cyclotron downstream face of a piece of the spacer mica containing damaged and undamaged areas was placed against a ^{235}U foil and irradiated in a Pu-Be neutron howitzer for two hours producing $\sim 5 \times 10^5/\text{cm}^2$ of implanted fission tracks. The mica was etched without annealing for 8 minutes in 48% HF.

Figure 32 shows the fission track densities (i.e., tracks >1.5 microns to discriminate against interaction tracks) observed along a scan which goes from a cyclotron beam irradiated area (area a) to an unirradiated area (area b) and back to an

FIGURE 32 .

This figure illustrates the relative fission track registration efficiencies of irradiation-damaged (beam on) and undamaged (beam off) areas of a mica situated downstream from a collimator which received a proton dose of $6.6 \times 10^{16}/\text{cm}^2$. There is an apparent 20% loss of registration efficiency with irradiation-damage. Background subtraction (as determined from track counts on the back side of the mica) serves to increase the difference in the registration efficiencies. See text for full discussion.

*TRACK REGISTRATION EFFICIENCY
IN IRRADIATION DAMAGED MICA*



irradiated area (area c) on the mica. The immediate observation is made that the fission track density observed over the beam shielded area b is greater than the track densities observed over the unshielded areas a and c. The lower profile in Fig. 32 is the background due to cyclotron-induced fission tracks from U,Th impurities as determined from track counts made on the upstream surface of the mica. The counts were done over areas near those scanned in the upper profile but far enough from the collimator walls to avoid counting tracks from U+Th in the aluminum. The background correction over area a is twice the background over area c as would be expected from relative dosimetry measurements made over these areas. Correction of the upper profile for the background contribution serves only to enhance the radiation damage effect.

One can conclude from this plot that the track registration efficiency of the mica has been lowered by ~20% upon subjection to an average proton dose of $\sim 7 \times 10^{16}/\text{cm}^2$. This is consistent with the differences in annealing behavior for damaged and undamaged mica as shown in figure 33. Although areas a and c received roughly a factor of two difference in dose, within errors their registration properties are identical.

2. Our first annealing experiments used Hughes-Liberty (H-L) micas irradiated upstream of the 0.1% U glass detector mica in TA&M-1. These micas received a 100 MeV alpha dose of $\sim 10^{14}/\text{cm}^2$ and have an interaction track population of $\sim 2 \times 10^7/\text{cm}^2$. Because these low U,Th micas were against other micas during the cyclotron

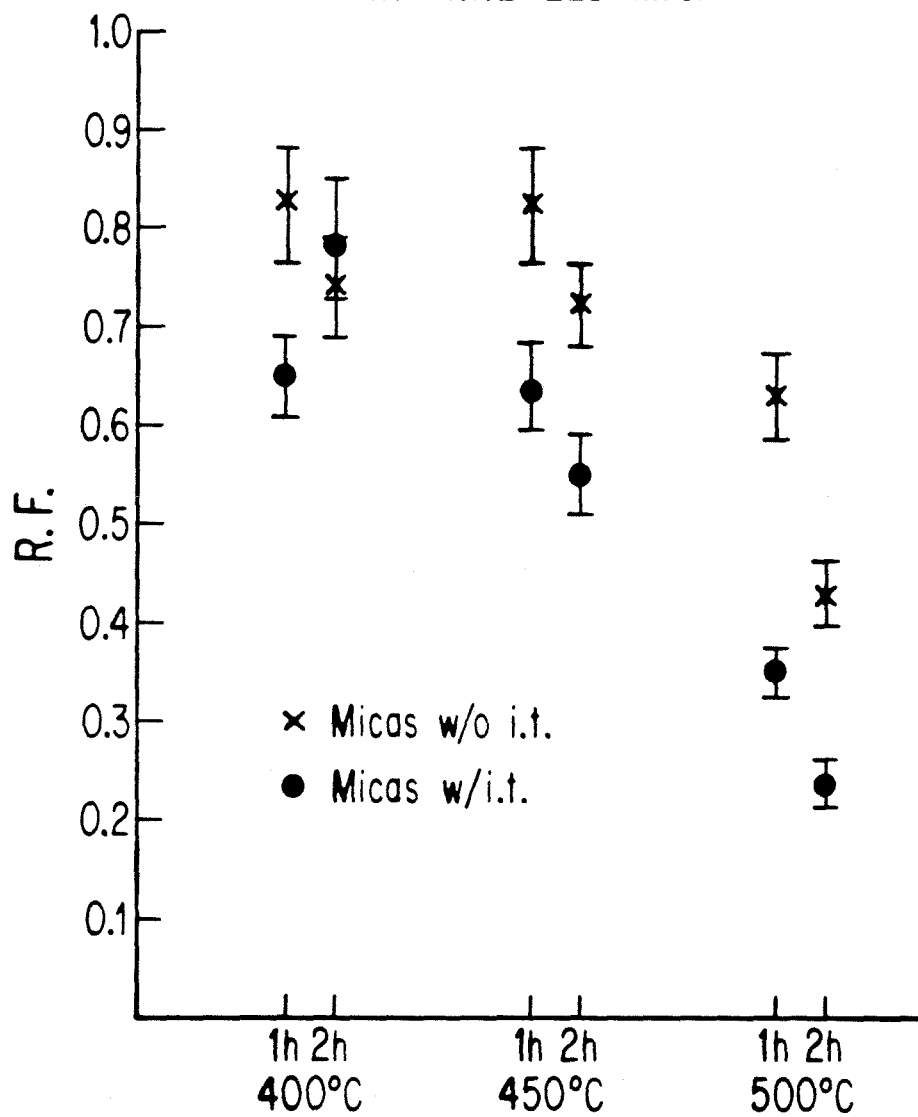
run all tracks observed are interaction tracks at this low dose. In order to compare interaction track suppression with fission track retention fission tracks had to be implanted post-cyclotron irradiation. This was done by placing micas flush against a HNO_3 -cleaned ^{235}U foil and inducing U fission in a Pu-Be neutron howitzer. Typical induced fission track densities were $\sim 10^6/\text{cm}^2$. Pieces of H-L mica never exposed to charged particle irradiation were in each howitzer irradiation along with the TA&M-I micas. One of these pieces was designated as the calibration mica. It remained as an unannealed reference mica against which to measure fission track retention factors in the annealing experiments. The other non-cyclotron irradiated pieces accompanied the TA&M micas in all the annealing runs.

Results of annealing the TA&M-I micas at 400°C , 450°C , and 500°C for one and two hours are illustrated in Fig. 33. The track retention factor, R.F., is the ratio of measured track densities (tracks >1.5 micron) in the annealed micas to the measured fission track densities in the unannealed calibration mica. The general trend is a decrease in the R.F. for increases both in temperature and time. The reverse trend for the 400°C one hour and two hour points is difficult to understand and may indicate a problem with applying the track length counting criterion uniformly. It might be expected that with a higher recoil track population an observer would tend to overdiscriminate against short tracks while in a lower recoil track environment the strict application of a length criterion might be relaxed.

FIGURE 33

This illustration plots the fission track retention factor (R.F.) for Hughes-Liberty mica vs. annealing temperature for annealing times of 1 and 2 hours. Data for mica with interaction tracks and without are shown. The cyclotron irradiated mica received a 100 MeV alpha dose of $10^{14}/\text{cm}^2$. Retention factors in both cases were made relative to unirradiated micas. All micas were etched 8 minutes.

*FISSION TRACK RETENTION FACTOR
IN ANNEALED MICA*



In any case, a one to two hour annealing at 400°C appears to retain ~70% of the fission tracks. At 450°C the retention factor is 55 - 65% and drops steeply for temperatures above this.

Comparison data of the fission track retention profile for micas without interaction tracks that were annealed along with the TA&M-I micas are also plotted in Fig 33. The R.F. profile is essentially flat out to 450°C dropping steeply at higher temperatures. For one to two hour annealings at 400°C and 450°C the retention factor averages ~78%.

In our cyclotron irradiation measurements interpretation of the affect of annealing must also allow for the loss of fission track registration efficiency of the mica due to charged particle produced irradiation damage. From Figure 32, irradiation-damaged mica has at best 80% the fission track registration efficiency of undamaged mica. The R.F. = 0.7 for the Texas A&M-I mica in Figure 33 was determined relative to the fission track density in an unirradiated mica. The fission track retention factor for fission tracks recorded during the cyclotron irradiation, therefore, is: $R.F. = 0.7/0.8 = 0.9$ for a two hour annealing at 400°C. Similarly, at 450°C, the cyclotron charged particle induced fission track registration efficiency is: $R.F. = 0.6/0.8 = 0.75$. Thus, the irradiation-damaged mica dealt with in our meteorite analyses is equal, or even better, at fission track retention under annealing than unirradiated mica.

Appendix VII: Differential Fission Track Annealing of Mica during Cyclotron Irradiation

Of major concern in the success of our experiments is whether thermal gradients existed in the cyclotron target which were large enough to cause differential fission track annealing in the detector micas. Uniform annealing of all micas in a target still preserves the proportionality of sample/standard track density ratios with their respective (Th+U) concentrations. Differential annealing, however, destroys this relation. In this section we will discuss thermal gradients along the beam direction and perpendicular to it. Referring back to Fig. 7, an illustration of the two layer target, we shall redefine the gradient directions with respect to the individual target 7-sample layers. Gradients along the beam and hence through a layer will be designated vertical gradients. Gradients perpendicular to the beam and parallel to the sample plane of an individual layer are designated horizontal. A horizontal gradient is thus parallel to the mica detector cleavage plane.

Experimental evidence strongly suggests a (vertical) gradient existed between Layers A and B, the upstream and downstream target layers. In TA&M-10 CT standard glasses were irradiated in both layers in positions not directly behind each other. Normalizing their respective track densities by their relative doses results in a dose-normalized track density ratio of $(CT, \text{Layer A}) / (CT, \text{Layer B})$ equal to 1.30 ± 0.06 .

Other than differential annealing, beam absorption or beam scattering are possible explanations for the apparent relative depletion of fission tracks in layer B compared to layer A. A simple calculation

can be done to check the magnitude of beam absorption by assuming a nuclear absorption cross section σ equal to 1 barn (10^{-24}cm^2) and a beam flux function for passage through an absorbing medium, i.e., $\phi(x) = \phi_0 \exp(-\sigma x)$. Using the layer A and heat sink thicknesses given in Fig. 7 (in II D-1) and assuming the density of samples and standards are roughly the density of aluminum, we calculate $\phi(\text{Layer A})/\phi(\text{Layer B}) = 0.986$. Thus, beam absorption cannot account for the 30% track depletion factor of Layer B relative to Layer A.

The magnitude of beam scattering can be calculated using equations similar to those used in determining our foil-target parameters for homogenization of a focussed beam over our target (see Appendix IV). For 35 MeV protons the $1/e$ angle of scattering is only 2.35° . With beam absorption and beam scattering apparently unable to account for the magnitude of the Layer A/Layer B discrepancy, differential annealing seems to be the most likely explanation. It would thus appear that a beam-aligned thermal gradient existed in the target with the higher temperatures in Layer B, the downstream layer. Existence of such a gradient, however, does not obviate a successful experiment. Each target layer in all our two-layer cyclotron runs has at least one standard glass. Barring any large thermal gradient within an individual layer, referencing samples only to a standard irradiated in the same target layer will eliminate errors from interlayer temperature gradients.

Thus, the existence of a large horizontal thermal gradient is of prime concern. In TA&M-6II, three CT standard glasses were irradiated

in the same 7-sample target layer. From photo-emulsion dosimetry measurements (see Appx.V) there was almost a factor of two spread in their integrated beam doses. If serious differential annealing had occurred across this sample layer, there should be obvious discrepancies between the CT glass relative track density ratios and their dosimetry ratios. In all cases the agreement between the track ratios and the dosimetry ratios was well within the statistical errors (3-4%) of the track measurements (see Table 17 in Dosimetry Appendix V). Thus, no strong support for horizontal large-scale fission track annealing in mica has been observed.

Target design for meteorite irradiations post-TA&M-6 were identical or improved (regarding thermal conductivity and target cooling) as refinements to the experimental technique were made. Therefore, we expected TA&M-6 to be a "worst case" differential annealing example compared to any of the following proton irradiations.

Appendix VIII: Uranium Isotopic Variations

Prior to Arden (1977) there had been no reason to doubt the applicability of the terrestrial value of $^{238}\text{U}/^{235}\text{U} = 137.88 \pm 0.14$ (atom ratio) [Shields, 1960; Cowan & Adler, 1976] to meteorite work. U isotopic measurements of lunar samples (e.g., Rosholt & Tatsumoto, 1970; Fields et al., 1972; Barnes et al., 1972) were identical to the terrestrial value within its 0.1% error.

Arden performed uranium isotopic analyses on residues of acid-treated chondrites. The magnitude and frequency of isotopic variations, all indicating ^{235}U enrichment relative to ^{238}U , were totally unanticipated. Eleven samples from five meteorites were analyzed. The most extreme deviations observed were in a final residue fraction of an Allende and a Barwell sample. In both cases the $^{238}\text{U}/^{235}\text{U}$ ratios are lower than normal terrestrial by ~500% (Allende#1c = 46 ± 6 , Barwell#1c = 40 ± 1). In both meteorites, this highly anomalous fraction accounts for 10^{-3} of the total sample U. The Allende bulk sample $^{238}\text{U}/^{235}\text{U}$ ratio is 136.9 ± 0.3 , and the Barwell bulk value is 137.5 ± 0.4 . Another Allende sample (Arden sample# 2) has 43% of the total U with an isotopic composition 4% below normal terrestrial. The bulk $^{238}\text{U}/^{235}\text{U}$ ratio for this sample is 136.1 ± 0.4 .

A sample of the Richardton H5 meteorite stands out as unique in the Arden study because of the fraction of anomalous uranium and magnitude of the isotopic variations. In this sample nearly one-half of the total uranium has a $^{238}\text{U}/^{235}\text{U}$ ratio ~92. The bulk ratio for this sample is 106.8 ± 0.4 --over 20% lower than the accepted terrestrial isotopic ratio.

In bulk sample analyses, only 2 out of the 11 Arden (1977) measurements are within twice their quoted error of the normal terrestrial value. The rest of the bulk numbers give 238/235 ratios 1-3% below the "normal" value. Two notable Richardton analyses give ratios ~12% and ~20% below "normal".

Since the Arden (1977) study many studies have been done to verify the results. Unruh et al.(1979) report preliminary isotopic analyses of several chondrites which fail to observe the large uranium isotopic anomalies reported by Arden(1977). Within error they find the uranium in Allende matrix to be isotopically identical to terrestrial. Deviations of 1% from normal were observed in two Allende inclusion measurements. Analyses of an Allende "pink-white aggregate" with Th/U=11 and "white aggregate" with Th/U=5 give 238/235 values of $136.2 \pm .5$ and $136.6 \pm .5$ respectively.

Preliminary studies by Chen & Tilton (1979) give 238/235 ratios for two Allende white aggregates of 127 ± 10 and 136 ± 6 respectively. An Allende bulk ratio determination give $238/235 = 136.0 \pm 2.1$. Thus, within errors all their Allende measurements are identical to the terrestrial value. Ratios for four ordinary chondrites also give nothing anomalous. Similarly, three terrestrial basalt analyses fall within the accepted terrestrial value.

The first post-Arden (1977) study to observe significant isotopic fractionations in meteoritic material from the normal terrestrial value was Tatsumoto and Shimamura(1979). While still unable to observe Arden's low 238/235 ratios, they report isotopic variations up to 7% in Allende and for the first time ratios higher than normal

were also reported. The 238/235 ratios from a suite of Allende inclusions give values ranging from 132.4 to 142.6 with a $\pm 0.5\%$ error for each individual analysis. A Ca-Al rich inclusion found not to lie on an Allende $^{207}\text{Pb}/^{206}\text{Pb}$ isochron (Tatsumoto, 1976) showed near normal U isotopic ratios.

Allende acid residue experiments were also performed by Tatsumoto & Shimamura (1979). Ratios measured were all near the terrestrial value except for a single high ratio measurement of 145.3. Bulk analyses of the carbonaceous chondrites Orgueil, Mighei and Murchison gave 238/235 ratios ~ 136.5 .

Acid etching experiments on Allende matrix were reported in Tatsumoto et al. (1980a). A high 238/235 ratio of 164 is observed in a chromite-rich (and perhaps MgAl_2O_4 spinel-rich) residue. In contrast, a carbon-rich residue gives a low value of 90. This is the first low ratio reported comparable to the ^{235}U enrichments observed by Arden. In a companion study, Tatsumoto et al. (1980b) report St. Severin whitlockite 238/235 ratios of 129, a value fully 7% lower than normal terrestrial.

Chen & Wasserburg (1980a, 1980b) have carried out a systematic, high precision U isotopic survey in search of U anomalies. For samples as small as 2 ng, they can resolve isotopic variations on the 0.5% level at least. Mean bulk 238/235 determinations were made for nine chondrites. All values were indistinguishable from normal terrestrial U to within the 0.2-0.4% limits of the error. Leaching experiments were carried out on Allende and Richardton-- the two meteorites where Arden (1977) found his most spectacular

fractionations. As Chen & Wasserburg discuss, the Allende sample with the largest fraction of anomalous U in the Arden study (Allende#2) has 43% of the total U with 238/235 ratio ~4% below normal. If just 10% of this material had been present in their leaches, they would have seen shifts of ~1.2%. Instead no shift greater than ~0.2% was observed. Similarly, a Richardton leach analysis was done on material originating from the same parent sample as the Arden (1977) analysis which found ~57% of the total sample U with isotopic composition ~33% lower than normal terrestrial. Chen & Wasserburg (1980a) calculate if only 10% of this material were present in their acid leaches, shifts of 4.5-20% should be observed. On the contrary, no shift larger than 0.2% was measured.

In an effort to maximize the possibility of observing U isotopic variations, Chen & Wasserburg (1980b) analyzed five Allende inclusions many of which had shown ^{26}Mg excesses. Again, within the 0.5% error of their measurements, all samples were found to have normal terrestrial U isotopic compositions. St. Severin whitlockite samples were also analyzed with results indistinguishable from normal. This is in sharp contradiction to the results of Tatsumoto et al. (1980b) where St. Severin whitlockite 238/235 ratios 7% lower than normal were reported. It is difficult to believe that sampling differences could account for the discrepancies between the Chen & Wasserburg (1980b) and Tatsumoto et al. (1980b) for St. Severin whitlockite 238/235 ratios. Because the acid-leach experimental procedure in Chen & Wasserburg (1980a) was not identical to that of Arden (1977), Chen & Wasserburg concede the existence of highly anomalous fractions is still

a possibility.

In the light of overwhelming evidence against bulk chondrite U isotopic variations outside the 0.5% error of the Chen & Wasserburg (1980a) measurements, we feel assumption of normal isotopic composition in our bulk sample determinations is justified. Since our experiments determine U concentrations relative to a glass of normal isotopic composition, a 10% overestimate in U would be consistent, for example, with 50% of the total meteorite U having a $^{238}/^{235}$ ratio of 110. A 10% underestimate in the U content of a meteorite sample is consistent with 50% of the total U having a $^{238}/^{235}$ ratio of 165. In regard to inclusion analyses, sampling could have controlled whether U isotopic variations were present or not.

Finally, the correlation of Pb isotopic measurements with U isotopic variations deserves some comment. Chen & Tilton (1976) and Tatsumoto et al. (1976) did independent Pb isotopic analyses of various Allende inclusion and matrix samples. Plotted as $^{207}\text{Pb}/^{204}\text{Pb}$ vs. $^{206}\text{Pb}/^{204}\text{Pb}$, the Chen & Tilton data define a straight line isochron inferring no $^{238}/^{235}$ variations greater than 0.2%. All data except one inclusion in the Tatsumoto et al. study define a straight line isochron to within 0.3%. Direct measurements of the $^{238}/^{235}$ ratio of the inclusion not lying on the isochron, however revealed a normal $^{238}/^{235}$ ratio (Tatsumoto & Shimamura, 1979). Thus, there would appear to be some inconsistency between the interpretation of Pb isotopic data with observations of U isotopic variations as high as 7% from normal in bulk inclusions. In this study, we have assumed a normal U isotopic composition in the Allende inclusions. It is in the individual grain

analyses within an inclusion that this assumption could be least valid. Thus, grains with highly fractionated Th/U ratios as determined in this study could be good candidates for verification of U isotopic variations.

REFERENCES

- Allen, J.M., Grossman, L., Davis, A.M., Hutcheon, I.D. (1978) Mineralogy, textures and mode of formation of a hibonite-bearing Allende inclusion. In Proc. Lunar Planet. Sci. Conf., 9th, pp. 1209-1233 Pergamon.
- Anders, E. (1971) How well do we know "cosmic" abundances?, *Geochim. Cosmochim. Acta* 35, 516-522.
- Arden, J. W. (1977) Isotopic composition of uranium in chondritic meteorites, *Nature* 269, 788-789.
- Barnes, I. L., Carpenter, B. S., Garner, E. L., Gramlich, J. W., Kuehner, E. C., Machlan, L. A., Maienthal, E. J., Moody, J. R., Moore, L. J., Murphy, T. J., Paulsen, P. J., Sappenfield, K. M., and Shields, W. R. (1972) Isotopic abundance ratios and concentrations of selected elements in Apollo 14 samples, Proc. Third Lunar Sci. Conf., 1465-1472. Suppl. 3, *Geochim. Cosmochim. Acta*, MIT press.
- Benjamin, T. M. (1979) Experimental actinide element partitioning between whitlockite, apatite, diopsidic clinopyroxene, and anhydrous melt at one bar and 20 kilobars pressure, Ph.D. Thesis, California Institute of Technology, Pasadena.
- Benjamin, T. M., Heuser, W. R., and Burnett, D. S. (1978) Laboratory studies of actinide partitioning relevant to ^{244}Pu chronometry, 9th Lunar and Planetary Science Conference, *Geochim. Cosmochim. Acta*, Suppl. 10, 1, 1393-1406. Pergamon, New York.
- Berzina, I.G., Gurvich, M.Yu., and Khelbnik, G.I. (1971) Determination of thorium concentration and spatial distribution in minerals and rocks from tracks of fission fragments, Tr., Vses. Nauch.--Issled. Inst. Yad. Geofiz. Geokhim. No. 9, 158-161.

- Bimbot, R., Maurette, M., and Pellas, P. (1967) A new method for measuring the ratio of the atomic concentrations of thorium and uranium in minerals and natural glasses; preliminary application to tektites, *Geochim. Cosmochim. Acta* 31, 263-274.
- Blander, M. and Fuchs, L. H. (1975) Calcium-aluminum-rich inclusions in the Allende meteorite: Evidence for a liquid origin, *Geochim. Cosmochim. Acta* 39, 1605-1619.
- Blander, M., Fuchs, L. H., Horowitz, C., and Land, R. (1980) Primordial refractory metal particles in the Allende meteorite, *Geochim. Cosmochim. Acta*, in press.
- Boynton, W. V. (1975) Fractionation in the solar nebula: Condensation of yttrium and the rare earth elements, *Geochim. Cosmochim. Acta* 39, 569-584.
- Boynton, W. V. (1977) Fractionation of Th, U, Pu and Cm in the early history of the solar system; implications for dating techniques. In *Lunar Sci. VIII*, 136-138, Lunar Sci. Inst., Houston.
- Boynton, W. V. (1978) Fractionation in the solar nebula II, Condensation of Th, U, Pu, and Cm, *Earth Planet. Sci. Lett.* 40, 63-70.
- Burbidge, E. M., Burbidge G. R., Fowler, W. A., and Hoyle, F. (1957) Synthesis of the elements in stars, *Rev. Mod. Phys.* 29, 547-650.
- Burnett, D., Monnin, M., Seitz, M., Walker, R., and Yuhas, D. (1971) "Lunar Astrology - U-Th Distributions and Fission-Track Dating of Lunar Samples," *Proc. Second Lunar Sci. Conf.* 2, 1503-1519. Cambridge: MIT Press.
- Burnett, D. S., Stapanian, M. I., and Jones, J. H. (1980) Meteorite actinide chemistry and cosmochronology, to be published.

- Cameron, A. G. W. and Pine, M. R. (1973) Numerical models of the primitive solar nebula, *Icarus* 18, 377-406.
- Chen, J. H. and Tilton, G. R. (1976) Isotopic lead investigations of the Allende carbonaceous chondrite, *Geochim. Cosmochim. Acta* 40, 635-643.
- Chen, J. H. and Tilton, G. R. (1979) Preliminary studies of uranium isotopic composition in chondritic meteorites, *Lunar and Planet. Sci. X*, 192-194.
- Chen, J. H. and Wasserburg, G. J. (1980a) The isotopic composition of U in meteorites and lunar samples, *Lunar and Planet. Sci. XI*, 131-133.
- Chen, J. H. and Wasserburg, G. J. (1980b) A search for isotopic anomalies in uranium, *Geophys. Res. Lett.* 7, No. 4, 275-278.
- Christophe Michel-Lévy, M. (1968) Un chondrite exceptionnel dans la météorite de Vigararo, *Bull. Soc. fr. Mineral. Cristallogr.* 91, 212-214.
- Clarke, R. S., Jr., Jarosewich, E., Mason, B., Nelen, J., Gomez, M., and Hyde, J. R. (1970) The Allende Mexico meteorite shower, *Smithsonian Contrib. Earth Sci.* 5, 1-53.
- Clayton, R. N., Grossman, L., and Mayeda, T. K. (1973) A component of primitive nuclear composition in carbonaceous meteorites, *Science* 182, 485-488.
- Clayton, R. N., Onuma, N., Grossman, L., and Mayeda, T. K. (1977) Distribution of the pre-solar component in Allende and other carbonaceous chondrites, *Earth Planet. Sci. Lett.* 34, 209-224.
- Cowan, G. A. and Adler, H. H. (1976) The variability of the natural abundance of ^{235}U , *Geochim. Cosmochim. Acta* 40, 1487-1490.

- Crozaz, G. (1974) U, Th and extinct ^{244}Pu in the phosphates of the St. Severin meteorite, *Earth Planet. Sci. Lett.* 23, 164-169.
- Crozaz, G. (1979) Uranium and thorium microdistributions in stony meteorites, *Geochim. et Cosmochim. Acta* 43, 127-136.
- Crozaz, G., Hair, M., Maurette M., and Walker, R. (1969) Nuclear interaction tracks in minerals and their implications for extra-terrestrial materials, *Proc. Inter. Conf. Nucl. Track Registration in Insulating Solids*, Clermont-Ferrand, Sect. VII, 41-53.
- Davis, A. M. and Grossman, L. (1979) Condensation and fractionation of rare earths in the solar nebula, *Geochim. Cosmochim. Acta* 43, 1611-32.
- Drozd, R. J., Morgan, C. J., Podosek, F. A., Poupeau, G., Shirck, J. R., and Taylor, G. J. (1977) ^{244}Pu in the early solar system?, *Ap. J.* 212, 567-580.
- El Goresy, A., Nagel, K., Dominik, B., and Ramdohr, P. (1977) Fremdlinge: Potential pre-solar material in Ca-Al-rich inclusions of Allende (abstr.) *Meteoritics* 12, 215.
- El Goresy, A., Nagel, K., and Ramdohr, P. (1978) Fremdlinge and their noble relatives, in *Proc. Lunar Planet. Sci. Conf.*, 9th, pp. 1279-1303. Pergamon.
- Fano, U. (1964) Penetration of protons, alpha particles, and mesons in studies in penetration of charged particles in matter, *Nucl. Sci. Series Report No. 39*, 287-352, National Academy of Sciences--National Research Council Publ. 1133.
- Fields, P. R., Diamond, H., Metta, D. N., Rokop, D. J., and Stevens, C. M. (1972) ^{237}Np , ^{236}U , and other actinides on the moon, *Proc. Third Lunar Sci. Conf.*, 1637-1644. Suppl. 3, *Geochim. Cosmochim. Acta*, MIT press.

- Fireman, E. L., De Felice, J., and Norton, E. (1970) Ages of the Allende meteorite, *Geochim. Cosmochim. Acta* 34, 873-881.
- Fisher, D. E. (1972) Uranium content and radiogenic ages of hypersthene, bronzite, amphoterite and carbonaceous chondrites, *Geochim. Cosmochim. Acta* 36, 15-33.
- Fleischer, R. L., Price, P. B., and Walker, R. M. (1975) *Nuclear Tracks in Solids: Principles and Applications*. U. of California Press, Berkeley.
- Fowler, W. A. (1972) New Observations and Old Nucleo-cosmochronologies, in *Cosmology, Fusion and Other Matters* (ed. F. Reines) pp. 67-123. Associated U. Press, Boulder.
- Fowler, W. A. (1977) Nuclear Cosmochronology. In, *Proceedings of the Robert A. Welch Foundation Conferences on Chemical Research--XXI Cosmochemistry*, Chapt. III, pp. 61-133, Houston, Texas, Nov. 7-9, 1977.
- Fowler, W. A. and Hoyle, F. (1960), Nuclear Cosmochronology, *Annals of Physics* 10, No. 2, 280-301.
- Frost, M. J. and Symes, R. F. (1970) A zoned perovskite-bearing chondrule from the Lance meteorite, *Mineral Mag.* 37, 724-726.
- Fuchs, L. H., Olsen, E., and Jensen, K. J. (1973) Mineralogy, mineral chemistry and composition of the Murchison (C2) meteorite, *Smithsonian Contrib. Earth Sci.* 10, 39 pp.
- Ganapathy, R. and Grossman, L. (1976) The case for an unfractionated $^{244}\text{Pu}/^{238}\text{U}$ ratio in high temperature condensates, *Earth Planet. Sci. Lett.* 31, 386-392.
- Glasstone, S. and Edlund, M. C. (1966) *The Elements of Nuclear Reactor Theory*. D. Van Nostrand Co. Inc., Princeton, N.J.

- Goles, G. G. and Anders, E. (1962) Abundances of iodine tellurium and uranium in meteorites, *Geochim. Cosmochim. Acta* 26, 723-737.
- Gray, C. M., Papanastassiou, D. A., and Wasserburg, G. J. (1973) The identification of early condensates from the solar nebula, *Icarus* 20, 213-239.
- Grevesse, N. (1969) Abundances of heavy elements in the sun, *Solar Phys.* 6, 381-389.
- Grossman, L. (1972) Condensation in the primitive solar nebula, *Geochim. Cosmochim. Acta* 36, 597-619.
- Grossman, L. (1975) Petrography and mineral chemistry of Ca-rich inclusions in the Allende meteorite, *Geochim. Cosmochim. Acta* 39, 433-454.
- Grossman, L. (1980) Refractory inclusions in the Allende meteorite, submitted to *Ann. Rev. Earth Planet. Sci.*
- Grossman, L. and Clarke, S. P. (1973) High-temperature condensates in chondrites and the environment in which they formed, *Geochim. Cosmochim. Acta* 37, 635-649.
- Grossman, L. and Ganapathy, R. (1976a) Trace elements in the Allende meteorite - I. Coarse-grained, Ca-rich inclusions, *Geochim. Cosmochim. Acta* 40, 331-344.
- Grossman, L., and Ganapathy, R. (1976b) Trace elements in the Allende meteorite - II. Fine-grained, Ca-rich inclusions, *Geochim. Cosmochim. Acta* 40, 967-977.
- Grossman, L. Ganapathy, R., Davis, A.M. (1977) Trace elements in the Allende meteorite-III. Coarse-grained inclusions revisited. *Geochim. Cosmochim. Acta* 41, 1647-1664.

- Grossman, L., Ganapathy, R., Methot, R.L., and Davis, A.M. (1979) Trace elements in the Allende meteorite-IV. Amoeboid olivine aggregates. *Geochim. Cosmochim. Acta* 43, 817-829.
- Grossman, L. and Larimer, J. W. (1974) Early chemical history of the solar system, *Revs. Geophys. and Space Phys.* 12, 71-101.
- Grossman, L. and Steele, I. M. (1976) Amoeboid olivine aggregates in the Allende meteorite, *Geochim. Cosmochim. Acta* 40, 149-155.
- Haines, E., Weiss, J. R., Burnett, D. S., and Woolum, D. S. (1976) Th-U fission radiography, *Nuclear Instruments and Methods* 135, 125-131.
- Hair, M. W., Kaufhold, J., Maurette, M. and Walker, R. M. (1971) Th microanalyses using fission tracks, *Rad. Effects* 7, 285-287.
- Haissinsky, M. (1964) *Nuclear Chemistry and its Applications*. Addison-Wesley Publ. Co., Inc., Reading, Mass.
- Heckman, H.H, Perkins, B.L., Simon, W.G., Smith, F.M., and Barkas, W. (1960) Ranges and energy loss processes of heavy ions in emulsion, *Phys. Rev.* 117, 544-556.
- Holweger, H. (1977) The solar Na/Ca and S/Ca ratios: a close comparison with carbonaceous chondrites, *Earth Planet. Sci. Lett.* 34, 152-154.
- Hutcheon, I. D. (1977) Micro-mineralogy of calcium-aluminum-rich inclusions from Allende (abstr.) in *Lunar Sci. VIII*, 1, 487-489.
- Hyde, E. K. (1964) *The Nuclear Properties of the Heavy Elements*, vol. III. Prentice-Hall, Inc., Englewood Cliffs, N.J.
- Jaffey, A. H., Flynn, K. F., Glendenin, L. E., Bentley, W. C., and Essling, A. M. (1971) Precision measurement of the half-lives and specific activities of U^{235} and U^{238} , *Phys. Rev.* C4, 1889-1906.

- James, T.H. (1977) *The Theory of the Photographic Process*, 4th edn. Macmillan Publ. Co., Inc., N.Y.
- Jones, J. H. and Burnett, D. S. (1980) Laboratory studies of actinide metal-silicate fractionation, submitted for publication in Proc. 11th Lunar and Planet. Sci. Conf.
- Kaiser, T., Kelly, W. R., and Wasserburg, G. J. (1980) Isotopically anomalous silver in the Santa Clara and Piñon iron meteorites, *Geophys. Res. Lett.* 7, No. 4, 271-274.
- Keil, K. (1968) Mineralogical and chemical relationships among enstatite chondrites, *J. Geophys. Res.* 73, 6945-6976.
- Kelly, W.R. and Wasserburg, G.J. (1978) Evidence for the existence of ^{107}Pd in the early solar system, *Geophys. Res. Lett.* 5, 1079-1082.
- Khodai-Jóopari, A. (1966) Fission properties of some elements below radium, Ph.D. Thesis, Univ. of California, Berkeley, Lawrence Radiation Laboratory Report UCRL-16489.
- Kimura, M. and Yagi, K. (1980) Crystallization of chondrules in ordinary chondrites, *Geochim. Cosmochim. Acta* 44, 589-602.
- King, E. A., Jr., Schonfeld, E., Richardson, K. A., and Eldridge, J. S. (1969) Meteorite fall at Pueblito de Allende, Chihuahua, Mexico: Preliminary information, *Science* 163, 928-929.
- Kurat, G. (1970) Zur Genese der Ca-Al-reichen Einschlüsse im chondriten von Lance, *Earth Planet. Sci. Lett.* 9, 225-231.
- Larimer, J.W. (1967) Chemical fractionations in meteorites--I. Condensation of the elements, *Geochim. Cosmochim. Acta* 31, 1215-1238.
- Larimer, J. W. (1979) The condensation and fractionation of refractory lithophile elements, *Icarus* 40, 446-454.

- Larimer, J. W. and Anders, E. (1970) Chemical fractionation in meteorites - III. Major element fractionations in chondrites, *Geochim. Cosmochim. Acta* 34, 367-387.
- Lattimer, J. M. and Grossman, L. (1978) Chemical condensation sequences in supernova ejecta, *The Moon and the Planets* 19, 169-184.
- Lee, T., Papanastassiou, D. A., and Wasserburg, G. J. (1976) ^{26}Mg excess in Allende and evidence for ^{26}Al , *Geophys. Res. Lett.* 3, 109-112.
- Lee, T., Papanastassiou, D. A., and Wasserburg, G. J. (1977) ^{26}Al in the early solar system: fossil or fuel?, *Ap. J. (Letters)* 211, L107-L110.
- LeRoux, L. J. and Glendenin, L. E. (1963) Half-life of thorium-232, *Proc. Nat. Mtg. Nucl. Energy, Pretoria, S. Africa*, pp. 83-94.
- Lord, H. C. III (1965) Molecular equilibria and condensation in a solar nebula and cool stellar atmospheres, *Icarus* 4, 279-288.
- Lovering, J. F., Hinthorne, J. R., and Conrad, R. L. (1976) Direct $^{207}\text{Pb}/^{206}\text{Pb}$ dating by ion microprobe of uranium-thorium rich phases in Allende calcium-aluminum rich clasts (CARC's)(abstr.) in *Lun. Sci. VII*, 504-506. Lunar Sci. Inst., Houston.
- Lovering, J. F., Wark, D. A., and Sewell, D. K. B. (1979) Refractory oxide, titanate, niobate and silicate accessory mineralogy of some Type B Ca-Al-rich inclusions in the Allende meteorite (abstr.) in *Lunar Planet. Sci. X* 2, 745-747. Lunar and Planet. Inst., Houston.
- MacPherson, G. J. and Grossman, L. (1979) Melted and non-melted coarse-grained Ca-Al-rich inclusions in Allende, *Meteoritics* 14, No. 4, 479-480.

- Marion, J. B. and Young, F. C. (1968) Nuclear Reaction Analysis. North-Holland Publ. Co., Amsterdam.
- Martin, P. M. and Mason, B. (1974) Major and trace elements in the Allende meteorite, *Nature* 249, 333-334.
- Marvin, U. B., Wood, J. A., and Dickey, J. S., Jr. (1970) Ca-Al-rich phases in the Allende meteorite, *Earth Planet. Sci. Lett.* 7, 346-350.
- Mason, B. (1971) Handbook of Elemental Abundances in Meteorites. Gordon and Breach Science Publishers, N.Y.
- Mason, B. and Martin, P. M. (1974) Minor and trace element distribution in melilite and pyroxene from the Allende meteorite, *Earth Planet. Sci. Lett.* 22, 141-144.
- Mason, B. and Martin, P. M. (1977) Geochemical differences among components of the Allende meteorite, *Smithsonian Contrib. Earth Sci.* 19, 84-95.
- Maurette, M. (1970) On some annealing characteristics of heavy ions in silicate minerals, *Radiation Effects* 5, 15-19.
- McSween, H. Y. (1977a) On the nature and origin of isolated olivine grains in carbonaceous chondrites, *Geochim. Cosmochim. Acta* 41, 411-418.
- McSween, H. Y. (1977b) Petrographic variations among carbonaceous chondrites of the Vigarano type, *Geochim. Cosmochim. Acta* 41, 1777-1790.
- McSween, H. Y. (1979) Are carbonaceous chondrites primitive or processed? A review, *Revs. Geophys. Space Phys.* 17, No. 5, 1059-1078.

- Moreland, G. C. (1968) Polished thin sections, *Am. Mineralogist* 53, 2070-2074.
- Morgan, J. W. and Lovering, J. F. (1967) Uranium and thorium abundances in carbonaceous chondrites, *Nature* 213, 873-875.
- Morgan, J. W. and Lovering, J. F. (1968) U and Th abundances in chondritic meteorites, *Talanta* 15, 1079-1095.
- Murthy, V. R. and Patterson, C. C. (1962) Primary isochron of zero age for meteorites and the earth, *J. Geophys. Res.* 67, 1161-1167.
- Nagasawa, H., Schreiber, H. D., and Blanchard, D. P. (1976) Partition coefficients of REE and Sc in perovskite, melilite, and spinel and their implications for Allende inclusions (abstr.) in *Lunar Science VII*, 588-590. Lunar Sci. Inst., Houston.
- Northcliffe, L. C. and Schilling, R. F. (1970) Range and stopping-power tables for heavy ions, *Nuclear Data Tables* A7, Nos. 3-4, 233-463.
- Nozette, S. and Wilkening, L. L. (1980) Evidence for hydrothermal alteration in a carbonaceous xenolith from the Plainview (HS) chondrite, *Lunar Planet. Sci.* XI, 2, 824-826. Lunar and Planet. Inst., Houston.
- Olsen, E. and Grossman, L. (1978) On the origin of isolated olivine grains in Type 2 carbonaceous chondrites, *Earth Planet. Sci. Lett.* 41, 111.
- Onuma, N., Tanaka, T., and Masuda, A. (1974) Rare-earth abundances in two mineral separates with distinct oxygen isotopic composition from an Allende inclusion (abstr.) *Meteoritics* 9, 387-388.

- Palme, H. and Wlotzka, F. (1976) A metal particle from a Ca,Al-rich inclusion from the meteorite Allende, and condensation of refractory siderophile elements, *Earth Planet. Sci. Lett.* 33, 45-60.
- Papanastassiou, D. A., Lee, T., and Wasserburg, G. J. (1977) Evidence for ^{26}Al in the solar system, in *Comets, Asteroids, Meteorites* (ed. A. H. Delsemme), 343-349.
- Podalak, M. and Cameron, A. G. W. (1974) Possible formation of meteoritic chondrules and inclusions in the precollapse Jovian protoplanetary atmosphere, *Icarus* 23, 326-333.
- Podosek, F. A. (1970a) The abundance of ^{244}Pu in the early solar system, *Earth Planet. Sci. Lett.* 8, 183-187.
- Podosek, F. A. (1970b) Dating of meteorites by the high-temperature release of iodine correlated ^{129}Xe , *Geochim. Cosmochim. Acta* 34, 341-365.
- Podosek, F. A. (1978) Isotopic structures in solar system materials, *Ann. Rev. Astron. Astrophys.* 16, 293-334.
- Podosek, F.A. and Lewis, R.S. (1972) ^{129}I and ^{244}Pu abundances in white inclusions of the Allende meteorite, *Earth Planet Sci. Lett.* 15, 101-109.
- Price, P. B., Lal, D., Tamhane, A. S., and Pereygin, V. P. (1973) Characteristics of tracks of ions of $14 < Z < 36$ in common rock silicates, *Earth and Planet. Sci. Lett.* 19, 377-395.
- Reed, G. W. (1963) Heavy elements in the Pantar meteorite, *J. Geophys. Res.* 68, 3531-3535.
- Reed, G. W. and Allen, R. O. (1966) Hologens in chondrites, *Geochim. Cosmochim. Acta* 30, 779-800.

- Reed, G. W., Kigoshi, K., and Turkevich, A. (1960) Determination of concentrations of heavy elements in meteorites by activation analysis, *Geochim. Cosmochim. Acta* 20, 122-140.
- Reimer, G.M. and Carpenter, B.S. (1973) Fission track analyses for thorium in glasses and minerals, *Geochronology Conference*, "ECOG II", Oxford, 3-8 Sept. 1973.
- Ringwood, A. E. (1975) Some aspects of the minor element chemistry of lunar mare basalts, *The Moon* 12, 127-157.
- Rosholt, J. N. and Tatsumoto, M. (1970) Isotopic composition of uranium and thorium in Apollo 11 samples, *Proc. Apollo 11 Lunar Sci. Conf.* 2, *Geochim. Cosmochim. Acta*, Suppl. 1, 1499-1502.
- Schramm, D. M. and Wasserburg, G. J. (1970) Nucleochronologies and the mean age of the elements, *Ap. J.* 162, 57-69.
- Shields, W. R. (1960) Comparison of Belgian Congo and synthetic "normal" samples, Report No. 8, U.S. National Bureau of Standards Meeting of the Advisory Committee, May 17 and 18, 37 pp.
- Shirck, J. (1974) Fission tracks in a white inclusion of Allende - evidence for ^{244}Pu , *Earth Planet. Sci. Lett.* 23, 305-317.
- Shirck, J. R. (1975) Fission track studies of Pu-244 in white inclusions of the Allende meteorite, Ph.D. Thesis, Washington U., St. Louis, Missouri.
- Silver, L. T. (1976) Thorium/Uranium fractionation as an indicator of petrogenetic processes, *EOS (Trans. AGU)* 57, 351.
- Simon, S.B. and Haggerty, S.E. (1979) Petrography and olivine mineral chemistry of chondrules and inclusions in the Allende meteorite (abstr.) in *Lunar and Planet. Sci. X*, 1119-1121. Lunar and Planet. Inst., Houston.

- Simon, S.B. and Haggerty, S.E. (1980) Bulk chemistry of a diverse chondrule suite in the Allende meteorite (abstr.) in Lunar and Planet. Sci. XI, 3, 1036-1038. Lunar and Planet. Inst., Houston.
- Stapanian, M. I., Burnett, D. S., Eggers, R., and Namboodiri, N. (1978) Solar system actinide abundances: III. Th/U fractionation in carbonaceous chondrites (abstr.) in Lunar Planet. Sci. IX, 1095-1097. Lunar and Planet. Inst., Houston.
- Stapanian, M. I., Burnett, D. S., and Furst, M. J. (1980) Meteorite actinide chemistry: Th-U microdistributions (abstr.) in Lunar and Planet. Sci. XI, 3, 1082-1084. Lunar and Planet. Inst., Houston.
- Tatsumoto, M., Knight, R. J., and Allègre, C. J. (1973) Time differences in the formation of meteorites as determined by $^{207}\text{Pb}/^{206}\text{Pb}$, Science 180, 1279-1283.
- Tatsumoto, M. and Shimamura, T. (1979) Isotopic composition of uranium in Allende and other chondrites, Meteoritics 14, No. 4, 543-544.
- Tatsumoto, M., Shimamura, T., Manuel, O. K., Unruh, D. M., and Pellas, P. (1980a) Cm-U and Pu-Xe chronology of meteoritic whitlockite: confirmation of live ^{247}Cm in early solar system, Lunar and Planet. Sci. XI, 1125-1127. Lunar and Planet. Inst., Houston.
- Tatsumoto, M., Shimamura, T., Patchett, P. J., and White, W. M. (1980b) Ages of the Galaxy: Isotopic composition of U, Sr, Sm and Nd in Allende meteorite (abstr.) in Lunar Planet. Sci. XI, 3, 1128-1130. Lunar and Planet. Inst., Houston.

- Tatsumoto, M., Unruh, D. M., and Desborough, G. A. (1976) U-Th-Pb and Rb-Sr systematics of Allende and U-Th-Pb systematics of Orgueil, *Geochim. Cosmochim. Acta* 40, 617-634.
- Töksoz, M. N. and Johnston, D. H. (1977) The evolution of the moon and the terrestrial planets, in *The Soviet-American Conference on Cosmochemistry of the Moon and Planets* (eds. J. Pomeroy and N. Hubbard), pp. 295-328. NASA, Washington, D.C.
- Unruh, D. M., Hutchison, R., and Tatsumoto, M. (1979) U-Th-Pb systematics and uranium isotopic composition of chondrites, *Lunar and Planet. Sci. X*, 1256-1258.
- Vandenbosch, R. and Huizenga, J. R. (1973) *Nuclear Fission*. Academic Press, N.Y.
- Van Schmus, W. R. (1969) The mineralogy and petrology of chondritic meteorites, *Earth Sci. Rev.* 5, 145-184.
- Van Schmus, W. R. and Wood, J. A. (1967) A chemical-petrologic classification for the chondritic meteorites, *Geochim. Cosmochim. Acta* 31, 747-765.
- Wänke, H., Baddenhausen, H., Palme, H., and Spettel, B. (1974) On the chemistry of the Allende inclusions and their origin as high temperature condensates, *Earth Planet. Sci. Lett.* 23, 1-7.
- Wark, D. A. (1978) Early solar system stratigraphy: The condensation sequence from Allende to chondrites, and the origin of chondrules (abstr.) in *Lunar Planet. Sci. IX* 2, 1208-1210. Lunar and Planet. Sci. Inst., Houston.

- Wark, D. A., Hughes, T. C., Lucas, M., and McKenzie, C. D. (1980) Proton microprobe analysis of perovskite in Allende Ca-Al-rich inclusions (abstr.) in Lunar and Planet. Sci. XI, 3, 1205-1207. Lunar and Planet. Inst., Houston.
- Wark, D. A. and Lovering, J. F. (1976) Refractory/platinum metal grains in Allende calcium-aluminum-rich clasts (CARC's): Possible exotic pre-solar material? (abstr.) in Lunar Sci. VII, 2, 912-914. Lunar Sci. Inst., Houston.
- Wark, D. A. and Lovering, J. F. (1977) Marker events in the early evolution of the solar system: Evidence from rims on Ca-Al-rich inclusions in carbonaceous chondrites, Proc. Lunar Sci. Conf. 8th, 1, 95-112, Pergamon.
- Wark, D. A. and Lovering, J. F. (1978) Classification of Allende coarse-grained Ca-Al-rich inclusions (abstr.) in Lunar Planet. Sci. IX, 2, 1211-1213. Lunar and Planet. Inst., Houston.
- Wark, D. A. and Lovering, J. F. (1980a) More early solar system stratigraphy: Coarse-grained CAI's (abstr.) in Lunar and Planet. Sci. XI, 3, 1208-1210. Lunar and Planet. Inst., Houston.
- Wark, D. A. and Lovering, J. F. (1980b) Second thoughts about rims (abstr.) in Lunar and Planet. Sci. XI, 3, 1211-1213. Lunar and Planet. Inst., Houston.
- Wark, D. A. and Sewell, D. K. B. (1979) Total U-Th-Pb mineral ages of three Ca-Al-rich inclusions in the Allende meteorite (abstr.) in Lunar and Planet. Sci. X, 3, 1289-1291. Lunar and Planet. Inst., Houston.

- Wark, D. A. and Wasserburg, G. J. (1980) Anomalous mineral chemistry of Allende FUN inclusions Cl, EK-141 and Egg-3 (abstr.) in Lunar and Planet. Sci. XI, 3, 1214-1216. Lunar and Planet. Inst., Houston.
- Wark, D. A., Wasserburg, G. J., and Lovering, J. F. (1979) Structural features of some Allende coarse-grained Ca-Al-rich inclusions: chondrules within chondrules? (abstr.) in Lunar Planet. Sci. X, 3, 1292-1294. Lunar and Planet. Inst., Houston.
- Wasserburg, G. J., Huneke, J. C., and Burnett, D. C. (1979) Correlation between fission tracks and fission type xenon in meteoritic whitlockite, J. Geophys. Res. 74, 4221-4232.
- Wasserburg, G. J., Lee, T., and Papanastassiou, D. A. (1976) ^{26}Mg excesses in Allende and a ^{26}Al - ^{26}Mg isochron, Meteorites 11, 384.
- Wasserburg, G. J., MacDonald, G. J. F., Hoyle, F., and Fowler, W. A. (1964) Relative contributions of uranium, thorium and potassium to heat production in the earth, Science 143, 465-467.
- Wasserburg, G. J., Schramm, D. N., and Huneke, J. C. (1969) Nuclear chronologies for the galaxy, Astrophys. J. 157, L91-L96.
- Wasserburg, G. J., Tera, F., Papanastassiou, D. A., and Huneke, J. C. (1977) Isotopic and chemical investigations on Angra dos Reis, Earth Planet. Sci. Lett 35, 294-316.
- Wiik, H. B. (1956) The chemical composition of some stony meteorites, Geochim. Cosmochim. Acta 9, 279-289.